



Development of high performance P-type sodium cobaltate and N-type strontium titanate thermoelectric materials

Author:

Chen, Cong

Publication Date:

2015

DOI:

<https://doi.org/10.26190/unsworks/17348>

License:

<https://creativecommons.org/licenses/by-nc-nd/3.0/au/>

Link to license to see what you are allowed to do with this resource.

Downloaded from <http://hdl.handle.net/1959.4/54226> in <https://unsworks.unsw.edu.au> on 2024-05-01

**Development of High Performance
P-type Sodium Cobaltate and N-type Strontium Titanate
Thermoelectric Materials**

Cong Chen

A thesis in fulfilment of the requirements for the degree of
Doctor of Philosophy



School of Materials Science and Engineering

Faculty of Science

The University of New South Wales

March 2015

Originality statement

‘I hereby declare that this submission is my own work and to the best of my knowledge it contains no materials previously published or written by another person, or substantial proportions of material which have been accepted for the award of any other degree or diploma at UNSW or any other educational institution, except where due acknowledgement is made in the thesis. Any contribution made to the research by others, with whom I have worked at UNSW or elsewhere, is explicitly acknowledged in the thesis. I also declare that the intellectual content of this thesis is the product of my own work, except to the extent that assistance from others in the project’s design and conception or in style, presentation and linguistic expression is acknowledged.’

Signed.....

Date.....

Acknowledgements

I would like to thank my supervisors, Prof. Sean Li, Dr. Tianshu Zhang, and Mr. Richard Donelson, for continuous guidance and support throughout the course of my PhD study. Sean introduced me to the field of thermoelectrics and has always been kind. He has given me the freedom to venture into various projects without objection and always been supportive and provided valuable suggestions. Tianshu taught and advised me from the very basic literature review and material synthesis all the way up to data interpretation and journal publication. He helped me find the way when I felt lost and cheered me up when I was down. I am impressed by his extreme patience and kindness to students. Richard has provided scientific advice and insightful discussion and has taught me to think critically and comprehensively about research findings. His sharp mind and enthusiasms for research have inspired me.

I express my sincere thanks to Dr. Thiam Teck Tan for his selfless time and care for all the laboratory instruments. He has been always there to help me fix the instrumental problems. I am indebted to Dr. Dewei Chu for his insightful comments on both research and life, Dr. Yu Wang for the valuable discussions on XRD analysis, Mr. Sean Lim and Dr. Quadir Md Zakaria for the assistance in TEM training, Dr. George Yang and Dr. Rahmat Kartono for maintaining laboratory instruments. Many thanks go to my labmates, Dr. Ruoming Tian, Beibei Zhu, and Md Rezaul Kabir. I would also like to thank all my group members and my office co-workers, especially Qi Zhang for sitting next to me in the same office for 3.5 years. The friendship between us lightened my PhD life and made it a wonderful and memorable journey.

I am deeply indebted to my parents, Shancai Chen and Jiafeng Guo, for raising me with generous love and endless support. They tried their best to give me both financial and spiritual support in order to give me the chance to do whatever I wanted in life. My boyfriend, Ruoyu Li, has been with me for 5 years through all the ups and downs of my undergraduate and postgraduate studies. He kept me sane and encouraged me when I was overwhelmed by stress and celebrated when research went smoothly. I love you all.

Abstract

Oxide thermoelectric materials have been drawing extensive attention as substitutes for conventional thermoelectric materials due to their low cost, nontoxicity, and high stability. Currently, the most promising p-type and n-type oxides are layered cobaltates (including Na_xCoO_2 and $\text{Ca}_3\text{Co}_4\text{O}_9$) and donor-doped SrTiO_3 , respectively. Major enhancement of the thermoelectric properties of these materials relies on the reduction of thermal conductivity and the improvement of electrical conductivity through doping technology, compositing, nanotechnology, etc. We demonstrated the successful fabrication of p-type $\text{Na}_{0.8}\text{Co}_{1-x}\text{Fe}_x\text{O}_2$ and $(1-x)\text{Na}_{0.77}\text{CoO}_2/x\text{Ca}_3\text{Co}_4\text{O}_9$ composites by means of spark plasma sintering (SPS) technique. The thermoelectric properties were improved with small amount of Fe doping ($x \leq 0.01$). A significant enhancement of Seebeck coefficient was achieved in $(1-x)\text{Na}_{0.77}\text{CoO}_2/x\text{Ca}_3\text{Co}_4\text{O}_9$ composites, approximately 17% higher than that of $\text{Ca}_3\text{Co}_4\text{O}_9$ at 680 °C. The electrical resistivities of the composites were higher than the theoretical values. The increase in the Seebeck coefficient and the electrical resistivity of the composites is most likely associated with the compressive strain in $\text{Ca}_3\text{Co}_4\text{O}_9$ grains due to the mismatch of thermal expansion coefficients between $\text{Na}_{0.77}\text{CoO}_2$ and $\text{Ca}_3\text{Co}_4\text{O}_9$. Most importantly, the chemical stability of $\text{Na}_{0.77}\text{CoO}_2$ was improved by adding up to a 30 vol.% fraction of $\text{Ca}_3\text{Co}_4\text{O}_9$ without deteriorating its thermoelectric performance.

A typical thermoelectric generator consists of p-type and n-type semiconductors which form p-n junctions to convert the wasted heat from exhaust gases to useful electricity. Therefore, apart from the p-type thermoelectric oxides, we also investigated the thermoelectric performance of n-type SrTiO_3 . We examined the solubility of Y and La in $\text{Sr}_{1-1.5x}\text{M}_x\text{TiO}_3$ ($M = \text{Y}, \text{La}$) and the corresponding thermoelectric properties. After determination of the proper amount of dopants (Y and La), the effects of Sr content on the phase composition, microstructure, and thermoelectric properties of $\text{Sr}_x\text{Y}_{0.04}\text{TiO}_3$ ($0.92 \leq x \leq 1$) and $\text{Sr}_x\text{La}_{0.12}\text{TiO}_3$ ($0.82 \leq x \leq 0.90$) were studied. Finally, the effects of Y and Nb co-doping on the thermoelectric properties of stoichiometric or TiO_2 excess in the formula $\text{Sr}_{0.96}\text{Y}_{0.04}\text{Ti}_{1+z-x}\text{Nb}_x\text{O}_3$ were determined. SrO Ruddlesden-Popper phases that existed in $\text{Sr}_{0.96}\text{Y}_{0.04}\text{TiO}_3$ and $\text{Sr}_{0.88}\text{La}_{0.12}\text{TiO}_3$ could be eliminated by decreasing Sr content and increasing oxygen deficiency, thus achieving improved electrical conductivity. A further decrease in Sr content resulted in the formation of TiO_2 Magnéli

phases, which blocked the electrical conduction path. The absolute value of the Seebeck coefficient of $\text{Sr}_{0.96}\text{Y}_{0.04}\text{TiO}_3$ with excess Sr was increased due to the decreased carrier concentration, whereas that of $\text{Sr}_{0.88}\text{La}_{0.12}\text{TiO}_3$ with excess Sr was reduced possibly due to the deterioration of band degeneracy. The electrical conductivity and the Seebeck coefficient of both stoichiometric and TiO_2 excess $\text{Sr}_{0.96}\text{Y}_{0.04}\text{Ti}_{1-x}\text{Nb}_x\text{O}_3$ increased with increasing Nb content. For a certain doping content, excess TiO_2 improved the electrical conductivity, but showed no obvious influence on the Seebeck coefficient possibly due to its minor amount.

List of publications

1. Cong Chen, Tianshu Zhang, Richard Donelson, Dewei Chu, Ruoming Tian, Thiam Teck Tan, and Sean Li, “Thermopower and chemical stability of $\text{Na}_{0.77}\text{CoO}_2/\text{Ca}_3\text{Co}_4\text{O}_9$ composites.” *Acta Materialia*, 63 (2014) 99-106.
2. Cong Chen, Tianshu Zhang, Richard Donelson, Thiam Teck Tan, and Sean Li, “Effects of yttrium substitution and oxygen deficiency on the crystal phase, microstructure, and thermoelectric properties of $\text{Sr}_{1-1.5x}\text{Y}_x\text{TiO}_{3-\delta}$ ($0 \leq x \leq 0.15$).”, *Journal of Alloys and Compounds*, 629 (2015) 49-54.
3. Cong Chen, Tianshu Zhang, Richard Donelson, Dewei Chu, Thiam Teck Tan, and Sean Li, “Thermoelectric properties of $\text{Na}_{0.8}\text{Co}_{1-x}\text{Fe}_x\text{O}_2$ ceramic prepared by spark plasma sintering.” in: *Ceramic Materials for Energy Applications IV*, John Wiley & Sons, Inc., 2014, pp. 35-41.

Table of contents

Originality statement.....	i
Acknowledgements.....	ii
Abstract	iii
List of publications.....	v
Table of contents.....	vi
List of Figures	ix
List of Tables	xiv
Chapter 1 Introduction.....	1
1.1 Background.....	1
1.2 Objectives and overview.....	3
Chapter 2 Literature review	5
2.1 Thermoelectric phenomena	5
2.1.1 Thermoelectric effects	5
2.1.2 Thermoelectric devices	8
2.1.3 Requirements for thermoelectric materials.....	11
2.1.4 Thermoelectric materials	20
2.2 Na_xCoO_2 and $\text{Ca}_3\text{Co}_4\text{O}_9$	23
2.2.1 Crystal structure	23
2.2.2 Electronic structure	25
2.2.3 Thermoelectric properties of single-crystalline Na_xCoO_2 and $\text{Ca}_3\text{Co}_4\text{O}_9$	26
2.2.4 Thermoelectric properties of polycrystalline Na_xCoO_2 and $\text{Ca}_3\text{Co}_4\text{O}_9$	29
2.3 SrTiO_3	31
2.3.1 Crystal structure	31
2.3.2 Electronic structure	33
2.3.3 Defect chemistry of donor doped SrTiO_3	35
2.3.4 Thermoelectric properties of SrTiO_3	37
Chapter 3 Experimental methods.....	39
3.1 Sample preparation	39
3.1.1 $\text{Na}_{0.77}\text{CoO}_2$	39
3.1.2 SrTiO_3	39
3.1.3 Spark plasma sintering.....	40
3.2 Structural characterization	42

	3.2.1	X-ray diffraction	42
	3.2.2	Scanning electron microscopy	42
	3.2.3	Transmission electron microcopy	42
	3.3	Electrical resistivity and thermopower measurement.....	43
	3.4	Thermal conductivity characterization	44
	3.4.1	Dilatometry	45
	3.4.2	Differential scanning calorimetry	46
	3.4.3	Thermal diffusivity measured by laser flash method.....	48
	3.5	Thermogravimetric analysis	49
Chapter 4		Thermoelectric properties of $\text{Na}_{0.8}\text{Co}_{1-x}\text{Fe}_x\text{O}_2$ prepared by spark plasma sintering	51
	4.1	Introduction.....	51
	4.2	Experimental procedure.....	52
	4.3	Results and discussion	53
	4.4	Summary	58
Chapter 5		Thermopower and chemical stability of $\text{Na}_{0.77}\text{CoO}_2/\text{Ca}_3\text{Co}_4\text{O}_9$ composites	59
	5.1	Introduction.....	59
	5.2	Experimental procedure.....	60
	5.3	Results and discussion	62
	5.3.1	Phase and Structural characterization	62
	5.3.2	Effects of sintering temperature and dwell time on $0.5\text{Na}_{0.77}\text{CoO}_2/0.5\text{Ca}_3\text{Co}_4\text{O}_9$	65
	5.3.3	Effects of different compositions on $(1-x)\text{Na}_{0.77}\text{CoO}_2/x\text{Ca}_3\text{Co}_4\text{O}_9$	67
	5.3.4	Chemical stability	77
	5.4	Summary	78
Chapter 6		Effects of Y and La content on the crystal phase, microstructure, and thermoelectric properties of Sr-deficient $\text{Sr}_{1-1.5x}\text{M}_x\text{TiO}_3$ ($M = \text{Y, La}$).....	79
	6.1	Introduction.....	79
	6.2	Experimental procedure.....	80
	6.3	Results and discussion	81
	6.3.1	Effects of Y content and Sr deficiency on the crystal phase, microstructure, and thermoelectric properties of $\text{Sr}_{1-1.5x}\text{Y}_x\text{TiO}_3$ ($0 \leq x \leq 0.15$).....	81
	6.3.2	Effects of La content and Sr deficiency on the crystal phase, microstructure, and	

	thermoelectric properties of $\text{Sr}_{1-1.5x}\text{La}_x\text{TiO}_3$ ($0 \leq x \leq 0.4$)	90
	6.4 Summary	100
Chapter 7	Thermoelectric properties of $\text{Sr}_x\text{Y}_{0.04}\text{TiO}_3$ ($0.92 \leq x \leq 1$) and $\text{Sr}_x\text{La}_{0.12}\text{TiO}_3$ ($0.82 \leq x \leq 0.9$).....	101
	7.1 Introduction.....	101
	7.2 Experimental procedure.....	102
	7.3 Results and Discussion	103
	7.3.1 Thermoelectric properties of $\text{Sr}_x\text{Y}_{0.04}\text{TiO}_3$ ($0.92 \leq x \leq 1$).....	103
	7.3.2 Thermoelectric properties of $\text{Sr}_x\text{La}_{0.12}\text{TiO}_3$ ($0.82 \leq x \leq 0.9$)	116
	7.4 Summary	129
Chapter 8	Effects of Y and Nb co-doping on the thermoelectric properties of SrTiO_3 and $\text{SrTi}_{1.01}\text{O}_3$: a comparative study	130
	8.1 Introduction.....	130
	8.2 Experimental procedure.....	130
	8.3 Results and discussion	131
	8.4 Summary	140
Chapter 9	Conclusions and future work	141
	9.1 Conclusions.....	141
	9.2 Future work.....	143
References	145

List of Figures

Figure 2-1 A metal subject to a temperature gradient.....	5
Figure 2-2 The Seebeck effect. A thermoelectric circuit composed of two different materials, A and B.....	6
Figure 2-3 The Peltier effect. A thermoelectric circuit composed of two different materials, A and B.....	6
Figure 2-4 Illustration of thermoelectric devices. (a) A cooler and (b) a power generator.	8
Figure 2-5 Schematic of a thermoelectric cooler or power generator [31].	9
Figure 2-6 Temperature dependence of ZT for (a) n-type and (b) p-type thermoelectric materials [51].	21
Figure 2-7 Schematic illustration of crystal structure of (a) γ -phase Na_xCoO_2 and (b) $\text{Ca}_3\text{Co}_4\text{O}_9$ [72].	24
Figure 2-8 (a) Local density approximation (LDA) paramagnetic band structure and (b) the magnification of T_{2g} manifold of $\text{Na}_{0.5}\text{CoO}_2$ [73].	25
Figure 2-9 Temperature dependence of the (a) electrical resistivity (ρ) of Na_xCoO_2 along in-plane (ab) and out-of-plane (c) direction, ρ of $\text{Ca}_3\text{Co}_4\text{O}_9$ along ab direction and (b) Seebeck coefficient (S) of Na_xCoO_2 and $\text{Ca}_3\text{Co}_4\text{O}_9$ along ab direction [12,18].	27
Figure 2-10 Thermal conductivity of Na_xCoO_2 and $\text{Ca}_3\text{Co}_4\text{O}_9$ along the in-plane direction measured by the Harman method [81].	28
Figure 2-11 Temperature dependence of the (a) electrical resistivity (ρ), (b) Seebeck coefficient (S) of single-crystalline (in-plane) Na_xCoO_2 , and polycrystalline Na_xCoO_2 and $\text{Ca}_3\text{Co}_4\text{O}_9$ [13,22], and (c) thermal conductivity (κ) of polycrystalline Na_xCoO_2 and $\text{Ca}_3\text{Co}_4\text{O}_9$ [13,22].	30
Figure 2-12 Schematic crystal structure of SrTiO_3	32
Figure 2-13 Schematic crystal structures of $\text{SrO}(\text{SrTiO}_3)_n$ [97]. (a) $n = 1$, Sr_2TiO_4 and (b) $n = 2$, $\text{Sr}_3\text{Ti}_2\text{O}_7$	33
Figure 2-14 (a) Total density of states (DOS), Partial DOS (PDOS) of Ti d and O p in SrTiO_3 . (b) PDOS of Ti d , O p , and empty sphere (ES) in $\text{SrTiO}_{2.875}$. (c) PDOS of Ti d , O p , and La in $\text{Sr}_{0.875}\text{La}_{0.125}\text{TiO}_3$. [98].	34
Figure 2-15 Phase diagram of SrO-TiO ₂ binary system [102].	35
Figure 2-16 Temperature dependence of the (a) electrical conductivity (σ), (b) Seebeck coefficient (S), and (c) thermal conductivity (κ) of polycrystalline $\text{Sr}_{0.9}M_{0.1}\text{TiO}_3$ ($M = \text{La}, \text{Sm}, \text{Gd}, \text{Dy}, \text{Y}$) [25]. Two extra lines in (b) are κ of single-crystalline SrTiO_3 and $\text{Sr}_{0.95}\text{La}_{0.05}\text{TiO}_3$ [110]. Only one curve is present in (b) due to the similarity between different dopants.....	38
Figure 3-1 Schematic illustration of experimental procedure for (a) $\text{Na}_{0.77}\text{CoO}_2$ and (b) SrTiO_3 . 40	
Figure 3-2 Schematic of spark plasma sintering (SPS).	41
Figure 3-3 Schematic of ULVAC-ZEM3 system.	44

Figure 3-4 Schematic of NETZSCH DIL402C.....	46
Figure 3-5 Schematic of NETZSCH DSC 404C [121].....	47
Figure 3-6 Schematic of NETZSCH LFA427.	48
Figure 3-7 Schematic of NETZSCH STA 449 [122].....	49
Figure 4-1 XRD patterns of $\text{Na}_{0.8}\text{Co}_{1-x}\text{Fe}_x\text{O}_2$ ($x = 0, 0.25\%, 0.5\%, 1\%, 3\%$). The star (*) and cross (x) indicate unknown peaks.	53
Figure 4-2 SEM micrographs of $\text{Na}_{0.8}\text{Co}_{1-x}\text{Fe}_x\text{O}_2$. (a) $x = 0$, (b) $x = 0.25\%$, and (c) $x = 1\%$	54
Figure 4-3 Temperature dependence of the (a) electrical resistivity (ρ) and (b) Seebeck coefficient (S) of $\text{Na}_{0.8}\text{Co}_{1-x}\text{Fe}_x\text{O}_2$ ($x = 0, 0.25\%, 0.5\%, 1\%, 3\%$).	55
Figure 4-4 Temperature dependence of the (a) measured thermal conductivity (κ), (b) calculated thermal conductivity for dense $\text{Na}_{0.8}\text{Co}_{1-x}\text{Fe}_x\text{O}_2$ (κ_{Dense}), and (c) ZT of $\text{Na}_{0.8}\text{Co}_{1-x}\text{Fe}_x\text{O}_2$ ($x = 0, 0.25\%, 0.5\%, 1\%, 3\%$).	57
Figure 5-1 XRD patterns of $\text{Na}_{0.77}\text{CoO}_2$ and $\text{Ca}_3\text{Co}_4\text{O}_9$ after solid-state reaction, the mixture of $0.5\text{Na}_{0.77}\text{CoO}_2/0.5\text{Ca}_3\text{Co}_4\text{O}_9$ after mixing by ball milling, $0.5\text{Na}_{0.77}\text{CoO}_2/0.5\text{Ca}_3\text{Co}_4\text{O}_9$ sintered by SPS at various temperatures for different durations, $0.5\text{Na}_{0.77}\text{CoO}_2/0.5\text{Ca}_3\text{Co}_4\text{O}_9$ sintered by the CS method at $700\text{ }^\circ\text{C}$ for 12 h in air.	63
Figure 5-2 XRD patterns of $(1-x)\text{Na}_{0.77}\text{CoO}_2/x\text{Ca}_3\text{Co}_4\text{O}_9$ ($x = 0, 0.3, 0.5, 0.7, 1$) sintered by SPS at $700\text{ }^\circ\text{C}$ for 10 min.	64
Figure 5-3 SEM micrographs of (a) $\text{Na}_{0.77}\text{CoO}_2$, (b) $0.5\text{Na}_{0.77}\text{CoO}_2/0.5\text{Ca}_3\text{Co}_4\text{O}_9$ composite, (c) $\text{Ca}_3\text{Co}_4\text{O}_9$, sintered by SPS at $700\text{ }^\circ\text{C}$ for 10 min, and (d) $0.5\text{Na}_{0.77}\text{CoO}_2/0.5\text{Ca}_3\text{Co}_4\text{O}_9$ sintered by SPS at $700\text{ }^\circ\text{C}$ for 60 min.	65
Figure 5-4 Temperature dependence of figure-of-merit (ZT) for $0.5\text{Na}_{0.77}\text{CoO}_2/0.5\text{Ca}_3\text{Co}_4\text{O}_9$ sintered at $500, 600, 700\text{ }^\circ\text{C}$ for 10 min and at $700\text{ }^\circ\text{C}$ for 30 and 60 min.	65
Figure 5-5 Temperature dependence of electrical resistivity (ρ) for $0.5\text{Na}_{0.77}\text{CoO}_2/0.5\text{Ca}_3\text{Co}_4\text{O}_9$ sintered at $500, 600, 700\text{ }^\circ\text{C}$ for 10 min and at $700\text{ }^\circ\text{C}$ for 30 and 60 min.	66
Figure 5-6 (a) Electrical resistivity (ρ) of $(1-x)\text{Na}_{0.77}\text{CoO}_2/x\text{Ca}_3\text{Co}_4\text{O}_9$ ($x = 0, 0.3, 0.5, 0.7, 1$) versus temperature, and (b) ρ of $(1-x)\text{Na}_{0.77}\text{CoO}_2/x\text{Ca}_3\text{Co}_4\text{O}_9$ versus nominal composition x at $480\text{ }^\circ\text{C}$ and $580\text{ }^\circ\text{C}$, respectively.	68
Figure 5-7 (a) Schematic diagram of a resistor network representing $(1-x)\text{Na}_{0.77}\text{CoO}_2/x\text{Ca}_3\text{Co}_4\text{O}_9$ samples and (b) the experimental and calculated electrical resistivity (ρ) of $(1-x)\text{Na}_{0.77}\text{CoO}_2/x\text{Ca}_3\text{Co}_4\text{O}_9$ versus nominal composition (x) at $580\text{ }^\circ\text{C}$	70
Figure 5-8 (a) Seebeck coefficient (S) of $(1-x)\text{Na}_{0.77}\text{CoO}_2/x\text{Ca}_3\text{Co}_4\text{O}_9$ ($x = 0, 0.3, 0.5, 0.7, 1$) versus temperature (b) S of $(1-x)\text{Na}_{0.77}\text{CoO}_2/x\text{Ca}_3\text{Co}_4\text{O}_9$ versus nominal composition x measured at $480\text{ }^\circ\text{C}$ and $580\text{ }^\circ\text{C}$, respectively.	72
Figure 5-9 (a) Theoretical and experimental Seebeck coefficient (S) versus temperature for $0.3\text{Na}_{0.77}\text{CoO}_2/0.7\text{Ca}_3\text{Co}_4\text{O}_9$. (b) Thermal expansion dL/L_0 of single-phase $\text{Na}_{0.77}\text{CoO}_2$ and $\text{Ca}_3\text{Co}_4\text{O}_9$ versus temperature.	73

Figure 5-10 (a) Thermal conductivity κ of $(1-x)\text{Na}_{0.77}\text{CoO}_2/x\text{Ca}_3\text{Co}_4\text{O}_9$ ($x = 0, 0.3, 0.5, 0.7, 1$) versus temperature and (b) κ of $(1-x)\text{Na}_{0.77}\text{CoO}_2/x\text{Ca}_3\text{Co}_4\text{O}_9$ versus nominal composition x measured at 480 °C and 580 °C, respectively.	75
Figure 5-11 (a) ZT of $(1-x)\text{Na}_{0.77}\text{CoO}_2/x\text{Ca}_3\text{Co}_4\text{O}_9$ ($x = 0, 0.3, 0.5, 0.7, 1$) versus temperature, and (b) ZT of $(1-x)\text{Na}_{0.77}\text{CoO}_2/x\text{Ca}_3\text{Co}_4\text{O}_9$ versus nominal composition x at 480 °C and 580 °C, respectively.	76
Figure 5-12 XRD patterns of pellets of (a) $\text{Na}_{0.77}\text{CoO}_2$ and (b) $0.7\text{Na}_{0.77}\text{CoO}_2/0.3\text{Ca}_3\text{Co}_4\text{O}_9$ before stability test, after testing for 7 days and after testing for 14 days, respectively.	77
Figure 6-1 (a) XRD patterns and (b) lattice parameter a versus x , for $\text{Sr}_{1-1.5x}\text{Y}_x\text{TiO}_3$ ($x = 0, 0.02, 0.03, 0.04, 0.06, 0.08, 0.15$). Insert in Figure 6-1a shows the XRD pattern over 25 ° to 45 ° for the composition with $x = 0.08$	82
Figure 6-2 SEM micrograph and elemental distribution of Sr, Y, and Ti from EDS mapping of $\text{Sr}_{1-1.5x}\text{Y}_x\text{TiO}_3$ with $x = 0.15$. The scale bar indicates 5 μm	82
Figure 6-3 (a) Bright-field image, (b) SAED pattern of grain 1, and (c) SAED pattern of grain 2 of $\text{Sr}_{1-1.5x}\text{Y}_x\text{TiO}_3$ with $x = 0.15$	83
Figure 6-4 (a) Electrical conductivity (σ) versus temperature and (b) electrical resistivity (ρ) versus the square of the temperature (T) for $\text{Sr}_{1-1.5x}\text{Y}_x\text{TiO}_3$ ($x = 0.02, 0.03, 0.04, 0.06, 0.08, 0.15$).	84
Figure 6-5 Oxygen deficiency δ , concentration of Ti^{3+} , and the electrical conductivity (σ) at 680 °C of $\text{Sr}_{1-1.5x}\text{Y}_x\text{TiO}_3$ ($x = 0.02, 0.03, 0.04, 0.06, 0.08, 0.15$).	85
Figure 6-6 (a) Seebeck coefficient (S) versus temperature and (b) concentration of Ti^{3+} and the absolute values of S ($ S $) at 680 °C versus x for $\text{Sr}_{1-1.5x}\text{Y}_x\text{TiO}_3$ ($x = 0.02, 0.03, 0.04, 0.06, 0.08, 0.15$).	86
Figure 6-7 (a) Thermal conductivity (κ) and (b) lattice thermal conductivity (κ_L) versus temperature for $\text{Sr}_{1-1.5x}\text{Y}_x\text{TiO}_3$ ($x = 0.02, 0.03, 0.04, 0.06, 0.08, 0.15$). For a comparison, the data for $\text{Y}_2\text{Ti}_2\text{O}_7$ is also included in Figure 6-7.	87
Figure 6-8 Thermoelectric figure of merit (ZT) versus temperature for $\text{Sr}_{1-1.5x}\text{Y}_x\text{TiO}_3$ ($x = 0.02, 0.03, 0.04, 0.06, 0.08, 0.15$). The dash line ($\text{Sr}_{0.9}\text{Y}_{0.1}\text{TiO}_3$) is cited from work of others [162].	89
Figure 6-9 XRD patterns of $\text{Sr}_{1-1.5x}\text{La}_x\text{TiO}_3$ ($x = 0, 0.04, 0.08, 0.12, 0.25, 0.40$). Insert shows the XRD patterns over 46 ° to 47 ° and 76.5 ° to 78 °, respectively.	90
Figure 6-10 Molar cell volume (V_m) as a function of x for $\text{Sr}_{1-1.5x}\text{La}_x\text{TiO}_3$ ($x = 0, 0.04, 0.08, 0.12, 0.25, 0.40$).	91
Figure 6-11 Oxygen deficiency (δ) versus x for $\text{Sr}_{1-1.5x}\text{La}_x\text{TiO}_3$ ($x = 0, 0.04, 0.08, 0.12, 0.25, 0.40$).	92
Figure 6-12 Relative weight change of $\text{Sr}_{1-1.5x}\text{La}_x\text{TiO}_3$ ($x = 0, 0.04, 0.08, 0.12, 0.25, 0.40$) on heating in flowing oxygen as a function of (a) temperature and (b) time.	93
Figure 6-13 SEM micrographs of $\text{La}_x\text{Sr}_{1-1.5x}\text{TiO}_3$. (a) $x = 0.04$, (b) $x = 0.08$, (c) $x = 0.12$, (d) $x = 0.25$, and (e) $x = 0.40$	94
Figure 6-14 Electrical conductivity (σ) versus (a) temperature and (b) La content (x) for $\text{Sr}_{1-1.5x}\text{La}_x\text{TiO}_3$ ($x = 0.04, 0.08, 0.12, 0.25, 0.40$).	95

Figure 6-15 Concentration of Ti^{3+} , the electrical conductivity (σ) at 680 °C, and the absolute values of Seebeck coefficient ($ S $) at 680 °C versus x for $Sr_{1-1.5x}La_xTiO_3$ ($x = 0.04, 0.08, 0.12, 0.25, 0.40$).	96
Figure 6-16 Seebeck coefficient (S) versus (a) temperature and (b) La content (x) for $Sr_{1-1.5x}La_xTiO_3$ ($x = 0.04, 0.08, 0.12, 0.25, 0.40$).....	97
Figure 6-17 Temperature dependent of the thermal conductivity of $Sr_{1-1.5x}La_xTiO_3$ ($x = 0.04, 0.08, 0.12, 0.25, 0.40$).	98
Figure 6-18 Temperature dependence of the lattice thermal conductivity of $Sr_{1-1.5x}La_xTiO_3$ and $Sr_{1-1.5x}Y_xTiO_3$ ($x = 0.04$ and 0.08).....	99
Figure 6-19 Temperature dependent of ZT of $Sr_{1-1.5x}La_xTiO_3$ ($x = 0.04, 0.08, 0.12, 0.25, 0.40$).	99
Figure 7-1 XRD patterns of $Sr_xY_{0.04}TiO_3$ ($x = 0.92, 0.94, 0.95, 0.96, 0.98, 1$). Insert shows the XRD patterns (over 26 ° to 35 °) of $Sr_xY_{0.04}TiO_3$ with $x = 0.98$ and 1	104
Figure 7-2 SEM micrograph and elemental distribution of Sr, Y, and Ti from EDS mapping of $Sr_{0.92}Y_{0.04}TiO_3$	105
Figure 7-3 (a) Bright-field image and Sr, Ti, and Y distribution from EDS line scanning, (b) SAED pattern of Grain 1, and (c) SAED pattern of Grain 2 of $Sr_{0.92}Y_{0.04}TiO_3$	106
Figure 7-4 SEM micrographs of $Sr_xY_{0.04}TiO_3$. (a) $x = 0.92$, (b) $x = 0.94$, (c) $x = 0.95$, (d) $x = 0.96$, (e) $x = 0.98$, and (f) $x = 1$. Ti-rich grains in (a) are labeled by white arrows.	107
Figure 7-5 Electrical conductivity (σ) of $Sr_xY_{0.04}TiO_3$ ($x = 0.92, 0.94, 0.95, 0.96, 0.98, 1$) versus (a) temperature and (b) Sr content (x).....	108
Figure 7-6 Sr stoichiometry (x) dependence of the (a) oxygen deficiency (δ) and concentration of Ti^{3+} ($[Ti_{Ti}^{3+}]$) and (b) $[Ti_{Ti}^{4+}]$, electrical conductivity (σ) at 680 °C, and Seebeck coefficient (S) at 680 °C of $Sr_xY_{0.04}TiO_{3-\delta}$ ($x = 0.92, 0.94, 0.95, 0.96, 0.98, 1$).	109
Figure 7-7 Electrical conductivity (σ) of $Sr_xY_{0.04}TiO_3$ ($x = 0.92, 0.94$, and 0.95) versus temperature.....	111
Figure 7-8 Seebeck coefficient (S) of $Sr_xY_{0.04}TiO_3$ ($x = 0.92, 0.94, 0.95, 0.96, 0.98, 1$) versus (a) temperature and (b) x	112
Figure 7-9 Temperature dependence of the (a) thermal conductivity κ and (b) lattice thermal conductivity κ_L of $Sr_xY_{0.04}TiO_3$ ($x = 0.92, 0.94, 0.95, 0.96, 0.98, 1$).....	113
Figure 7-10 Temperature dependence of the thermoelectric figure-of-merit (ZT) of $Sr_xY_{0.04}TiO_3$ ($x = 0.92, 0.94, 0.95, 0.96, 0.98, 1$).....	114
Figure 7-11 XRD patterns of $Sr_xLa_{0.12}TiO_3$ ($x = 0.82, 0.86, 0.87, 0.88, 0.885, 0.9$) sintered at (a) 1400 °C and (b) 1600 °C. The inserts show the XRD patterns over 31.5 ° to 33.3 ° and 57 ° to 58.5 °.....	117
Figure 7-12 (a) Oxygen deficiency (δ) and (b) concentration of SrO ($[SrO]$) of $Sr_xLa_{0.12}TiO_{3-\delta}$ ($x = 0.82, 0.86, 0.87, 0.88, 0.9$) versus x sintered at 1400 and 1600 °C.	120
Figure 7-13 SEM micrographs of $Sr_xLa_{0.12}TiO_3$ sintered at 1400 °C. (a) $x = 0.82$, (b) $x = 0.86$, (c) $x = 0.87$, (d) $x = 0.88$, (e) $x = 0.885$, and (f) $x = 0.9$	121

Figure 7-14 SEM micrographs of $\text{Sr}_x\text{La}_{0.12}\text{TiO}_3$ sintered at 1600 °C. (a) $x = 0.82$, (b) $x = 0.86$, (c) $x = 0.87$, (d) $x = 0.88$, (e) $x = 0.885$, and (f) $x = 0.9$.	121
Figure 7-15 (a) Electrical conductivity (σ) versus temperature and (b) σ at 675 °C versus Sr content (x) for $\text{Sr}_x\text{La}_{0.12}\text{TiO}_3$ ($x = 0.82, 0.86, 0.87, 0.88, 0.885, 0.9$) sintered at 1400 and 1600 °C.	122
Figure 7-16 Electrical conductivity (σ) at 680 °C and Ti^{3+} concentration ($[\text{Ti}^{3+}]$) versus x for $\text{Sr}_x\text{La}_{0.12}\text{TiO}_3$ ($x = 0.82, 0.86, 0.87, 0.88, 0.885, 0.9$) sintered at (a) 1400 °C and (b) 1600 °C.	124
Figure 7-17 Temperature dependent of the electrical conductivity (σ) of $\text{Sr}_x\text{La}_{0.12}\text{TiO}_3$ ($x = 0.82, 0.86, 0.87$) sintered at 1400 °C and 1600 °C.	125
Figure 7-18 Seebeck coefficient (S) versus temperature for $\text{La}_{0.12}\text{Sr}_x\text{TiO}_3$ ($x = 0.82, 0.86, 0.87, 0.88, 0.885, 0.9$) sintered at (a) 1400 and (b) 1600 °C.	126
Figure 7-19 Absolute values of the Seebeck coefficient ($ S $) versus x for $\text{La}_{0.12}\text{Sr}_x\text{TiO}_3$ ($x = 0.82, 0.86, 0.87, 0.88, 0.885, 0.9$) sintered at 1400 and 1600 °C.	127
Figure 7-20 Thermal conductivity (κ) versus temperature for $\text{La}_{0.12}\text{Sr}_x\text{TiO}_3$ ($x = 0.82, 0.86, 0.87, 0.88, 0.885, 0.9$) sintered at 1400 and 1600 °C.	127
Figure 7-21 Thermoelectric figure-of-merit ZT versus temperature for $\text{La}_{0.12}\text{Sr}_x\text{TiO}_3$ ($x = 0.82, 0.86, 0.87, 0.88, 0.885, 0.9$) sintered at 1400 and 1600 °C.	128
Figure 8-1 (a) XRD patterns and (b) lattice parameter (a) versus x for $\text{Sr}_{0.96}\text{Y}_{0.04}\text{Ti}_{1+z-x}\text{Nb}_x\text{O}_3$ ($x = 0, x = 0.04, x = 0.1, x = 0.2; z = 0, 0.01$).	132
Figure 8-2 (a) Thermogravimetric curve in oxygen (50 ml/min) versus temperature and (b) oxygen deficiency (δ) versus x for $\text{Sr}_{0.96}\text{Y}_{0.04}\text{Ti}_{1+z-x}\text{Nb}_x\text{O}_{3-\delta}$ ($x = 0, x = 0.04, x = 0.1, x = 0.2; z = 0, 0.01$).	133
Figure 8-3 SEM micrographs of $\text{Sr}_{0.96}\text{Y}_{0.04}\text{Ti}_{1+z-x}\text{Nb}_x\text{O}_3$. (a) $x = 0, z = 0$, (b) $x = 0.1, z = 0$, (c) $x = 0, z = 0.01$, and (d) $x = 0.1, z = 0.01$.	134
Figure 8-4 The electrical conductivity (σ) of $\text{Sr}_{0.96}\text{Y}_{0.04}\text{Ti}_{1+z-x}\text{Nb}_x\text{O}_3$ ($x = 0, x = 0.04, x = 0.1, x = 0.2; z = 0, 0.01$) versus (a) temperature and (b) Nb content (x).	135
Figure 8-5 Concentration of Ti^{3+} versus x for $\text{Sr}_{0.96}\text{Y}_{0.04}\text{Ti}_{1+z-x}\text{Nb}_x\text{O}_3$ ($x = 0, x = 0.04, x = 0.1, x = 0.2; z = 0, 0.01$).	136
Figure 8-6 Temperature dependence of the Seebeck coefficient (S) of $\text{Sr}_{0.96}\text{Y}_{0.04}\text{Ti}_{1+z-x}\text{Nb}_x\text{O}_3$ ($x = 0, x = 0.04, x = 0.1, x = 0.2; z = 0, 0.01$).	137
Figure 8-7 Temperature dependence of the thermal conductivity (κ) of $\text{Sr}_{0.96}\text{Y}_{0.04}\text{Ti}_{1+z-x}\text{Nb}_x\text{O}_3$ ($x = 0, x = 0.04, x = 0.1, x = 0.2; z = 0, 0.01$).	138
Figure 8-8 Thermal conductivity κ_c of $\text{Sr}_{0.96}\text{Y}_{0.04}\text{Ti}_{1+z-x}\text{Nb}_x\text{O}_3$ ($x = 0, x = 0.04, x = 0.1, x = 0.2; z = 0, 0.01$) versus (a) temperature and (b) Nb content (x). Lattice thermal conductivity κ_{cL} versus (c) temperature and (d) Nb content (x). All values were corrected for porosity.	139
Figure 8-9 Temperature dependence of figure-of-merit ZT of $\text{Sr}_{0.96}\text{Y}_{0.04}\text{Ti}_{1+z-x}\text{Nb}_x\text{O}_3$ ($x = 0, x = 0.04, x = 0.1, x = 0.2; z = 0, 0.01$).	139

List of Tables

Table 5-1 Sintering methods and parameters, relative densities, lattice parameters of $\text{Na}_{0.77}\text{CoO}_2$, and goodness of fit (GOF) of $0.5\text{Na}_{0.77}\text{CoO}_2/0.5\text{Ca}_3\text{Co}_4\text{O}_9$	62
Table 5-2 Sintering methods, nominal compositions, sintering parameters, theoretical densities and relative densities of $(1-x)\text{Na}_{0.77}\text{CoO}_2/x\text{Ca}_3\text{Co}_4\text{O}_9$	67
Table 6-1 Structural parameters from Rietveld refinements of powder XRD data of $\text{Sr}_{1-1.5x}\text{La}_x\text{TiO}_3$ ($x = 0, 0.04, 0.08, 0.12, 0.25, 0.40$).	91
Table 7-1 Nominal composition, constituents in molar ratio, lattice parameter a , sintered densities, theoretical densities, and relative densities of $\text{Sr}_x\text{Y}_{0.04}\text{TiO}_3$ ($x = 0.92, 0.94, 0.95, 0.96, 0.98, 1$).	104
Table 7-2 Bulk densities of $\text{Sr}_x\text{La}_{0.12}\text{TiO}_3$ ($x = 0.82, 0.86, 0.87, 0.88, 0.885, 0.90$) sintered at $1400\text{ }^\circ\text{C}$ and $1600\text{ }^\circ\text{C}$. Theoretical density is assumed to be 5.12 g/cm^3 (JCPDS 73-0661).	120
Table 8-1 Lattice parameter a , theoretical density, bulk density, and relative density of $\text{Sr}_{0.96}\text{Y}_{0.04}\text{Ti}_{1+z-x}\text{Nb}_x\text{O}_{3-\delta}$ ($x = 0, x = 0.04, x = 0.1, x = 0.2; z = 0, 0.01$).	134

Chapter 1 Introduction

1.1 Background

Fossil fuels are the primary energy source for power generation and have an 82% share in the total energy consumption in 2012 [1]. They are natural resources containing hydrocarbon and include petroleum, coal, and natural gas. The emission of CO₂ from the combustion of fossil fuels has become the major source of greenhouse gases, resulting in a devastating effect on global warming and other environmental concerns. As a result, new energy generation technologies with low environmental impact are highly desirable, such as renewable energy and nuclear energy. One method to utilize the renewable energy is to generate electricity from solar thermal energy by the use of thermoelectric generators. The thermoelectric generators can also be used for waste heat recovery from industries and vehicles where only approximately 30% of the fuel energy is used for power generation and the rest is released as waste heat. The thermoelectric generators are highly reliable, scalable, and modular, indicating of little requirement for maintenance and low cost due to feasibility of mass production. Solid-state refrigeration can be achieved by thermoelectric coolers where electricity is converted to temperature difference.

Low energy conversion efficiency is detrimental to the extensive application of thermoelectric devices. The conversion efficiency of a state-of-practice radioisotope thermoelectric generator such as PbTe, AgSbTe₂-GeTe (TAGS), or SiGe alloys for deep-space missions and planetary surface operation is about 6.5% [2]. A high beginning-of-life efficiency of about 15% has been demonstrated in the segmented thermoelectric couples [2]. A flat-panel solar thermoelectric generator utilizing nanostructured Bi₂Te₃ alloys shows a peak efficiency of 4.6% under AM1.5G conditions [3]. However, these conversion efficiencies are still too low compared with other renewable energy, such as commercialized solar cells with an efficiency of about 15%. Therefore, more effort is required to improve the conversion efficiency of thermoelectric devices.

The conversion efficiency of a thermoelectric device is determined by the temperature difference between the heat source and sink and the figure-of-merit (ZT) of

the materials. High ZT is essential to achieve high conversion efficiency. ZT is defined as $ZT = \sigma S^2 T / \kappa = \sigma S^2 T / (\kappa_e + \kappa_L)$, where σ is the electrical conductivity, S is the Seebeck coefficient, T is the absolute temperature, and κ is the thermal conductivity consisting of the electronic contribution (κ_e) and the lattice or phonon contribution (κ_L). The highest ZT value of Bi_2Te_3 - Sb_2Te_3 alloys is about 1.56 at 25 °C [4]. PbTe and AgSbTe_2 - GeTe (TAGS) alloys operate in mid-temperature range with a ZT of 1.5 at about 450 °C [5-7]. ZT of p-type and n-type SiGe alloys is 0.95 and 1.3 at 900 °C, respectively [8,9]. Although ZT values of these alloys are relatively high, the mass production is limited by their high cost and toxicity. For example, the price of tellurium rose from US\$ 5 per kg in 2000 to US\$ 158 per kg in 2014 [10]. The price of germanium was US\$ 1875 per kg in 2013 [11]. The toxicity of Te, Sb, and Pb poses risks during manufacturing and handling. Furthermore, low stability of the materials including oxidation and decomposition at high temperatures is an issue for certain applications. In contrast, thermoelectric oxides have the advantages of low cost, nontoxicity, and high general stability. However, oxides generally show inferior ZT to the aforementioned materials. Therefore, it is necessary to develop thermoelectric oxides with high ZT .

Na_xCoO_2 is a promising p-type thermoelectric oxide with high Seebeck coefficient (100 $\mu\text{V/K}$ at 27 °C) and low electrical resistivity (in-plane: 200 $\mu\Omega\text{cm}$ at 27 °C) [12]. ZT of Na_xCoO_2 single crystals is as high as ~ 1 at 527 °C [13]. Na_xCoO_2 has a layered crystal structure with alternating Na^+ layers and two-dimensional edge-sharing CoO_6 octahedra. The low lattice thermal conductivity of Na_xCoO_2 is due to the highly vacant and randomly distributed Na^+ in Na^+ layers. The high Seebeck coefficient originates from the low-spin state of Co^{3+} [14]. One approach to improve the electrical properties of Na_xCoO_2 is substituting Co with other transition metal ions. Although Na_xCoO_2 is found to possess high ZT , it is unstable in air. It reacts with moisture and/or CO_2 from the ambient environment, forming insulating $\text{Co}(\text{OH})_2$ and/or CoCO_3 [15]. $\text{Co}(\text{OH})_2$ and CoCO_3 further decompose to insulating Co_3O_4 and CoO upon heating [16]. The poor stability remains an issue for the realistic application of Na_xCoO_2 .

In contrast to the instability of Na_xCoO_2 , $\text{Ca}_3\text{Co}_4\text{O}_9$ is less sensitive to compositional changes and is more stable in air. It is a p-type thermoelectric oxide with high Seebeck coefficient (125 $\mu\text{V/K}$ at 27 °C) and low electrical resistivity (in-place: 700 $\mu\Omega\text{cm}$ at 27 °C) [17]. Similarly, $\text{Ca}_3\text{Co}_4\text{O}_9$ has a layered crystal structure in which the rock-salt type Ca_2CoO_3 and edge-sharing CoO_2 are stacked alternately. $\text{Ca}_3\text{Co}_4\text{O}_9$

has a lower thermal conductivity than Na_xCoO_2 due to the complexity of the rock-salt layers [18]. The high Seebeck coefficient is caused by the strong electron-electron correlation due to the low-spin state of Co^{3+} sites [14]. The thermoelectric properties of $\text{Ca}_3\text{Co}_4\text{O}_9$ can be adjusted by doping strategy. Bi-doped $\text{Ca}_3\text{Co}_4\text{O}_9$ shows improved electrical conductivity and Seebeck coefficient due to increased mobility. The reduced thermal conductivity with Bi doping is due to the large ionic radius and atomic mass of Bi [19-21]. ZT is improved from 0.20 to 0.27 at 700 °C by doping Bi ($\text{Ca}_{3-x}\text{Bi}_x\text{Co}_4\text{O}_9$ with $x = 0.2$) [21]. A substantial increase in ZT is achieved in Lu-doped $\text{Ca}_3\text{Co}_4\text{O}_9$ with Ag nanoinclusions, from 0.20 to 0.46 at 700 °C [22].

The thermoelectric generators consist of both p-type and n-type thermoelectric legs. Therefore, it is also important to develop n-type oxide materials with compatible thermoelectric performance. Pure SrTiO_3 has a cubic perovskite crystal structure. It has a wide bandgap and is thus an insulator at room temperature. Donor-doped SrTiO_3 is an n-type thermoelectric oxide and shows high electrical conductivity after sintering in a reducing atmosphere. The Sr^{2+} sites are usually doped with lanthanide elements, while the Ti^{4+} sites could be doped with Nb^{5+} [23-25]. For example, La-doped SrTiO_3 ($\text{Sr}_{0.9}\text{La}_{0.1}\text{TiO}_3$) sintered at 1600 °C in argon exhibits a high electrical conductivity (190 S/cm) and Seebeck coefficient (-200 $\mu\text{V/K}$) at 600 °C [25]. ZT values of donor-doped bulk SrTiO_3 are in the range from 0.14 to 0.33 at 600 °C [26]. Enhanced thermoelectric properties have been demonstrated in $\text{SrTiO}_3/\text{SrTi}_{0.8}\text{Nb}_{0.2}\text{O}_3$ superlattices with a Seebeck coefficient of -480 $\mu\text{V/K}$ at room temperature [27]. It has been indicated that the electrical conductivity of donor-doped SrTiO_3 is highly sensitive to A-site stoichiometry [28-30]. However, the reports regarding the thermoelectric properties of Sr-deficient donor-doped SrTiO_3 are limited. Therefore, it is worthwhile to study the effects of donor concentration on the thermoelectric properties of Sr-deficient SrTiO_3 . Furthermore, it is necessary to study the effects of Sr content on the donor-doped SrTiO_3 with a certain amount of dopant.

1.2 Objectives and overview

The general objective of this thesis is to develop Na_xCoO_2 and donor-doped SrTiO_3 with compatible thermoelectric performance. The electrical resistivity and the Seebeck coefficient of Na_xCoO_2 are closely related to its $\text{Co}^{3+}/\text{Co}^{4+}$ ratio which can be altered by changing Na content or substituting Co with other transition metal ions. In

this study, Fe^{3+} was introduced to Co sites to manipulate the electrical properties and improve its thermoelectric performance. The stability of Na_xCoO_2 was improved by forming composites with $\text{Ca}_3\text{Co}_4\text{O}_9$ without deteriorating its thermoelectric properties.

The effects of Y and La doping on the structural and thermoelectric properties of Sr-deficient SrTiO_3 have been investigated. With the determined solubility of Y and La in SrTiO_3 , the effects of Sr content on the structural and thermoelectric properties of Y or La doped SrTiO_3 were examined. In order to further improve the thermoelectric performance of SrTiO_3 , the thermoelectric properties of Y and Nb co-doped stoichiometric and TiO_2 excess SrTiO_3 were compared.

The thesis is structured as follows:

- Chapter 2 gives the literature review about the thermoelectric theories, the properties of Na_xCoO_2 , $\text{Ca}_3\text{Co}_4\text{O}_9$, and SrTiO_3 in terms of crystal/electronic structure, defect structure, and thermoelectric properties.
- Chapter 3 introduces the experimental methods, including synthesis methods and characterization methods.
- Chapter 4 and Chapter 5 present the investigation of p-type thermoelectric materials. Chapter 4 focuses on the thermoelectric properties of $\text{Na}_{0.8}\text{Co}_{1-x}\text{Fe}_x\text{O}_2$ prepared by spark plasma sintering. Chapter 5 describes the effects of spark plasma sintering conditions (temperature and time) and compositions (x) on the thermoelectric properties and chemical stability of $(1-x)\text{Na}_{0.77}\text{CoO}_2/x\text{Ca}_3\text{Co}_4\text{O}_9$ composites.
- Chapter 6 to Chapter 8 present the SrTiO_3 -based n-type thermoelectric materials. Chapter 6 presents the effects of Y and La content on the crystal phase, microstructure, and thermoelectric properties of Sr-deficient $\text{Sr}_{1-1.5x}\text{M}_x\text{TiO}_3$ ($M = \text{Y}, \text{La}$). Chapter 7 further describes the influences of Sr content on the thermoelectric performance of $\text{Sr}_x\text{Y}_{0.04}\text{TiO}_3$ ($0.92 \leq x \leq 1$) and $\text{Sr}_x\text{La}_{0.12}\text{TiO}_3$ ($0.82 \leq x \leq 0.9$). Chapter 8 compares the effects of Y and Nb co-doping on SrTiO_3 and $\text{SrTi}_{1.01}\text{O}_3$.
- Chapter 9 concludes the new findings of this work and an outlook on future work is proposed.

Chapter 2 Literature review

2.1 Thermoelectric phenomena

2.1.1 Thermoelectric effects

The thermoelectric effects include the Seebeck effect, Peltier effect, and Thomson effect. Among these, the Seebeck effect is related to the conversion of thermal energy into electrical energy, while the Peltier effect and Thomson effect are associated with the change in heat content as a result of the flow of an electric current.

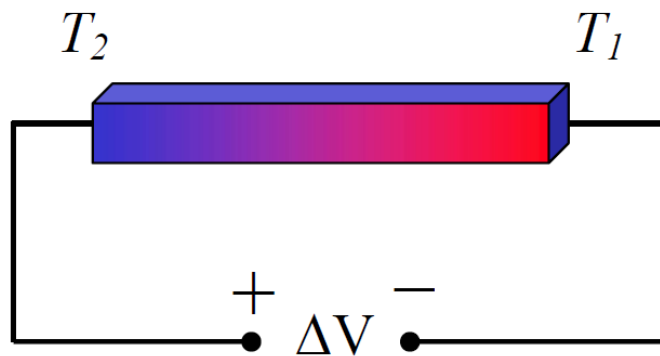


Figure 2-1 A metal subject to a temperature gradient.

The Seebeck effect was discovered by German Physicist Thomas Johann Seebeck in 1821. The Seebeck effect is a phenomenon in which a net source of electromotive force is induced due to a temperature gradient between pairs of points in any individual electrically conducting material. The schematic Seebeck effect is depicted in Figure 2-1. The absolute Seebeck coefficient S is introduced to gauge the magnitude of this effect and is defined as the potential difference developed per unit temperature difference, as indicated in Equation 2-1.

$$S(T) = \lim_{\Delta T \rightarrow 0} \frac{\Delta V}{\Delta T} = \frac{dV}{dT} \quad \text{Equation 2-1}$$

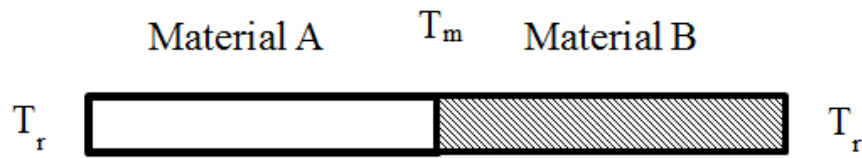


Figure 2-2 The Seebeck effect. A thermoelectric circuit composed of two different materials, A and B.

The relative Seebeck electromotive force is developed when two dissimilar electrical conductors are connected, with the shared junction at temperature T_m and both termini at temperature T_r as shown in Figure 2-2. The corresponding relative Seebeck coefficient is

$$S_{AB}(T_m, T_r) = S_A(T_m, T_r) - S_B(T_m, T_r) \quad \text{Equation 2-2}$$

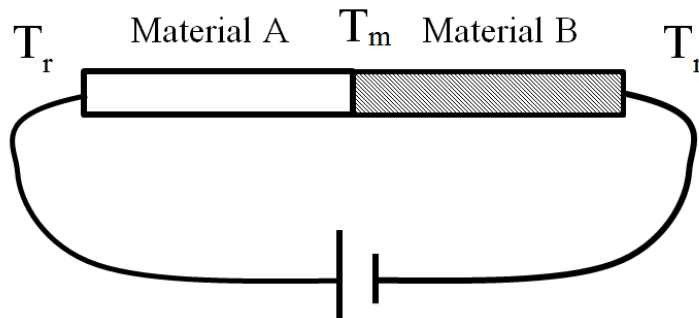


Figure 2-3 The Peltier effect. A thermoelectric circuit composed of two different materials, A and B.

The Peltier effect was discovered by J.C.A. Peltier in 1834. The Peltier effect suggests that when an electric current flows across a junction of two different conductors, as shown in Figure 2-3, heat is liberated or absorbed depending on the direction in which the current flows. The Peltier effect is defined as the change in reversible heat content when unit current flows across a junction of two dissimilar conductors. The Peltier heat is proportional to the magnitude and duration of the external current and is expressed as

$$dQ_p = \pi I dt \quad \text{Equation 2-3}$$

where π is the Peltier coefficient.

Thomson (1855) predicted and demonstrated a third thermoelectric effect. He concluded that when an electric current passes through a homogeneous conductor in which a temperature gradient exists, the reversible evolution or absorption of heat occurs. This Thomson heat is proportional to the current I passing for a time dt .

$$dQ_T = \tau I dt dT \quad \text{Equation 2-4}$$

where τ is referred to as Thomson coefficient. The three thermoelectric coefficients are related to each other according to the Kelvin relation, as shown in Equation 2-5 and Equation 2-6.

$$\pi = ST \quad \text{Equation 2-5}$$

$$\tau = T \frac{dS}{dT} \quad \text{Equation 2-6}$$

In real devices, apart from the reversible Peltier effect and Thomson effect, two irreversible effects take place, namely Joule heating and heat conduction. The rate of Joule heating is given by Equation 2-7, and moreover the rate of heat conduction at a unit cross section is depicted in Equation 2-8.

$$Q_J = \rho J^2 \quad \text{Equation 2-7}$$

$$Q_F = -\kappa \frac{dT}{dx} \quad \text{Equation 2-8}$$

where ρ is the electrical resistivity, J is the current density, and κ is the thermal conductivity.

2.1.2 Thermoelectric devices

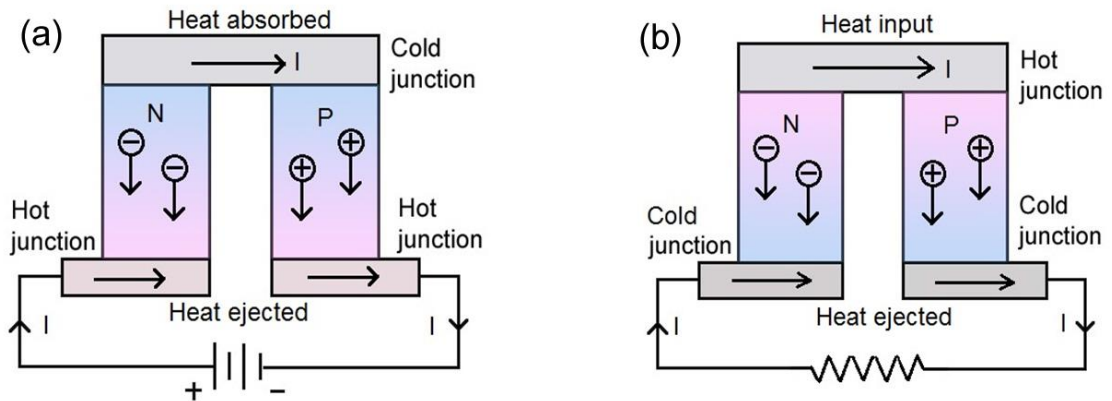


Figure 2-4 Illustration of thermoelectric devices. (a) A cooler and (b) a power generator.

There are two types of thermoelectric devices, i.e., coolers and power generators, both made from alternating n-type and p-type semiconductors connected by metallic conductors, as shown in Figure 2-4. When a power source is supplied (Figure 2-4a), a current flows from the n-type to the p-type semiconductor in series. The electrons in n-type and the holes in p-type semiconductor leave the cold side in parallel, and therefore the heat energy carried by the electrons and holes is moved away from the cold junction, acting as a cooler. It is illustrated in Figure 2-4b that the charge carriers are heated at the hot junction by a heat source, and thus they are driven to the cool side through diffusion, creating a current flowing in the external circuit to do useful work. This thermoelectric device acts as a power generator, converting thermal energy into electrical energy.

Many of the cooling or power generator units can be interconnected with conducting materials to compose a thermoelectric cooling or power generator module, as seen in Figure 2-5. The module is typically mounted between two ceramic substrates which provide both mechanical protection and electrical insulation. The thermocouples are connected electrically in series and thermally in parallel. When a voltage is applied across the device, a temperature difference could be developed between the two sides. When the two sides of the module are heated to different temperatures, a voltage will be built up and extracted from the device.

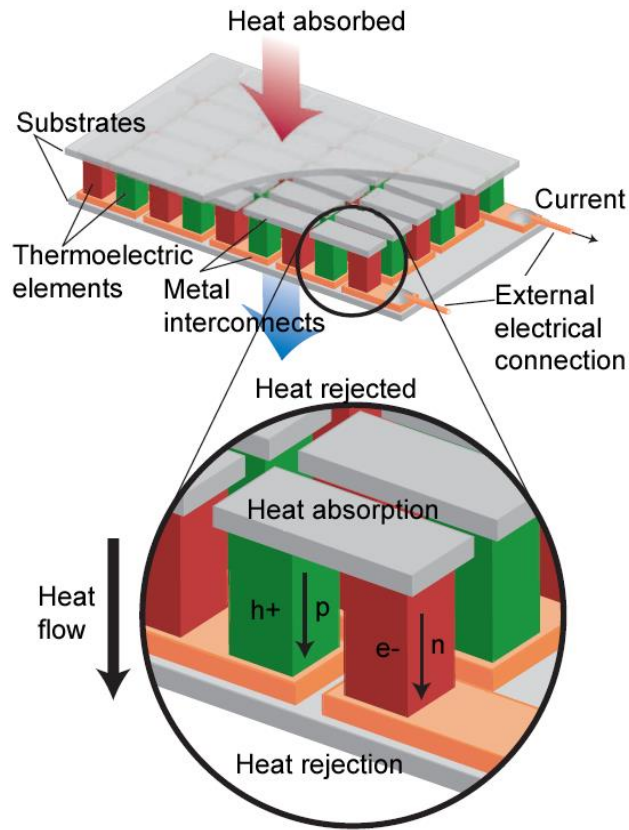


Figure 2-5 Schematic of a thermoelectric cooler or power generator [31].

The thermoelectric solid-state energy conversion has its unique advantages. For example, there are no moving parts inside the modules. Therefore, they have high reliability and little requirement for maintenance. A typical application is the radioisotope thermoelectric generators for spacecraft. Moreover, the modules could be made into a miniature with a flexible shape. Therefore, it could be used for spot cooling or heating for photon detectors or electronic devices. Silent operation can also be achieved in these devices. Most importantly, it is environmentally friendly since it can utilize solar thermal energy or waste heat from automobile engines and industries. For example, energy in the form of waste heat (0% efficiency) that would normally be lost may be converted into useful electrical energy ($\geq 7\%$ to 8% efficiency) using a thermoelectric power generation device [32]. The disadvantages of thermoelectric devices include relatively low conversion efficiency and high cost.

The efficiency of a thermoelectric power generator is defined as the energy supplied to the load divided by the heat energy absorbed at the hot junction. According

to Ioffe (1957) [33], the optimum efficiency of a thermoelectric power generator with respect to the load resistance and geometry is given by

$$\eta = \frac{T_h - T_c}{T_h} \cdot \frac{\sqrt{1 + Z\bar{T}} - 1}{\sqrt{1 + Z\bar{T}} + T_c/T_h} \quad \text{Equation 2-9}$$

where

$$\bar{T} = (T_h + T_c)/2 \quad \text{Equation 2-10}$$

and

$$ZT = \left[\frac{S_n - S_p}{\left[(\rho_n \kappa_n)^{\frac{1}{2}} + (\rho_p \kappa_p)^{\frac{1}{2}} \right]} \right]^2 T \quad \text{Equation 2-11}$$

where $S_{n,p}$ is the Seebeck coefficient, $\rho_{n,p}$ is the electrical resistivity, $\kappa_{n,p}$ is the thermal conductivity of the n and p arms, and ZT is the figure of merit of the couple. The optimized efficiency is achieved when $\gamma_n/\gamma_p = (\rho_n \kappa_p / \rho_p \kappa_n)^{1/2}$, where γ_n and γ_p are the ratio of area to length for the n and p arms. It is indicated in Equation 2-9 that the efficiency of a thermoelectric device is limited by the Carnot efficiency (the first term), since the Carnot efficiency is less than unity. The Carnot efficiency could only be approached by increasing the Z value.

The figure of merit is a function of material constants of both arms that form a thermoelectric power generator. However, in order to compare the thermoelectric properties of materials, the figure-of-merit (ZT) is defined for a single material as

$$ZT = \frac{S^2 \sigma T}{\kappa} \quad \text{Equation 2-12}$$

where σ ($\sigma = 1/\rho = ne\mu$) is the electrical conductivity, n is the carrier concentration, and μ is the carrier mobility. $S^2\sigma$ is referred to as power factor.

The performance of a thermoelectric cooler is described by the coefficient of performance (*COP*). *COP* is defined as the heat absorbed divided by the electric power input. The maximum *COP* can be calculated by [34]

$$COP_{max} = \frac{\sqrt{1 + Z\bar{T}} - T_h/T_c}{\sqrt{1 + Z\bar{T}} + 1} \quad \text{Equation 2-13}$$

The maximum temperature difference is given by

$$T_h - T_c = \frac{1}{2} Z T_c^2 \quad \text{Equation 2-14}$$

It is obvious that the maximum *COP* and temperature difference depend on the figure-of-merit *Z*. Therefore, thermoelectric materials with high *Z* are required for high energy conversion efficiency.

2.1.3 Requirements for thermoelectric materials

It is shown in Equation 2-12 that a high figure of merit can be achieved in a material with a high absolute value of Seebeck coefficient $|S|$ for a high voltage output, a high electrical conductivity σ for a low Joule heat, and a low thermal conductivity κ for maintaining a large temperature difference. Maximum *ZT* can be achieved by adjusting the carrier concentration in the range from 10^{19} cm^{-3} to 10^{21} cm^{-3} [31]. However, it is difficult to achieve a further improvement in *ZT*, since all these properties are strongly related to each other through the effective mass m^* , carrier mobility μ , and scattering factor r , etc.

2.1.3.1 Metals and degenerate semiconductors

The Seebeck coefficient is the entropy per mobile charge carrier [35]. It is assumed that the band has a parabolic density-of-state distribution and that the carriers obey classical statistics. The Seebeck coefficient for metals and degenerate semiconductors can be expressed as

$$S = \mp \frac{\pi^2 k_B}{3 e} \frac{(r + 3/2)}{\eta} \quad \text{Equation 2-15}$$

where k_B is the Boltzmann constant, e is the elementary charge, r is the scattering factor, η is the reduced Fermi energy $E_F/k_B T$. r equals $-1/2$ if the charge carriers are predominantly scattered by the acoustic-mode lattice vibration. r equals $3/2$ if the dominant scattering is due to ionized impurities. Equation 2-15 can be rewritten as

$$S = \mp \frac{8\pi^2 k_B^2}{3 e h^2} m^* \left(\frac{\pi}{3n} \right)^{\frac{2}{3}} (r + 3/2) \quad \text{Equation 2-16}$$

where m^* is the effective mass of the carrier, n is the carrier concentration, h is the Planck constant.

The electrical conductivity (σ) is given by

$$\sigma = ne\mu \quad \text{Equation 2-17}$$

in which

$$\mu = \frac{e\tau_0(E_F)^r}{m^*} \quad \text{Equation 2-18}$$

where τ_0 is a constant for a given scattering process.

Electrons are dominant heat carriers in a metal or a degenerate semiconductor, since the electrons carry both heat and electricity. The electrical conductivity (σ) and the electronic thermal conductivity (κ_e) are interrelated by the Wiedemann-Franz relationship

$$\kappa \approx \kappa_e = L\sigma T = \frac{\pi^2}{3} \left(\frac{k_B}{e} \right)^2 \sigma T \quad \text{Equation 2-19}$$

where L is the Lorenz number and $L = 2.44 \times 10^{-8} \text{ W}\Omega/\text{K}^2$ for the free electrons in a metal.

The figure-of-merit (ZT) is therefore expressed as

$$ZT = \frac{S^2 \sigma}{\kappa_e} T = \frac{S^2}{L} \quad \text{Equation 2-20}$$

ZT is determined mainly by the Seebeck coefficient as shown in Equation 2-20. The Seebeck coefficients of metals and degenerate semiconductors are usually smaller than k_B/e (86.2 $\mu\text{V/K}$) since E_F is much larger than $k_B T$. Therefore, metals and degenerate semiconductors are not suitable for thermoelectric power generation.

2.1.3.2 *Non-degenerate semiconductors and insulators*

2.1.3.2.1 *Broad-band semiconductors*

The Seebeck coefficient of semiconductors and insulators is larger than that for metals. The Seebeck coefficient of an extrinsic semiconductor with charge carriers of one sign is written as

$$S = \mp \frac{k_B}{e} \left[\eta - \left(r + \frac{5}{2} \right) \right] \quad \text{Equation 2-21}$$

Equation 2-21 can be rewritten as

$$S = \mp \frac{k_B}{e} \left\{ \ln \left[\frac{2(2\pi m^* k_B T)^{3/2}}{n h^3} \right] + \left(r + \frac{5}{2} \right) \right\} \quad \text{Equation 2-22}$$

The electrical conductivity of a non-degenerate semiconductor can be expressed as Equation 2-17. The carrier concentration and mobility are given by

$$n = 2 \left(\frac{2\pi m^* k_B T}{h^2} \right)^{3/2} \exp(\eta) \quad \text{Equation 2-23}$$

$$\mu = \frac{4}{3\pi^{\frac{1}{2}}} \Gamma\left(r + \frac{5}{2}\right) \frac{e\tau_o(k_B T)^r}{m^*} \quad \text{Equation 2-24}$$

where the gamma function is such that

$$\Gamma(n + 1) = n\Gamma(n) \quad \text{Equation 2-25}$$

Heat is carried by electrons and quantized vibrations of the lattice (phonons). The lattice thermal conductivity is higher than the electronic component in non-degenerate semiconductors. The thermal conductivity is

$$\kappa = \kappa_e + \kappa_L = L\sigma T + \kappa_L = \left(\frac{k_B}{e}\right)^2 \left(r + \frac{5}{2}\right) \sigma T + \kappa_L \quad \text{Equation 2-26}$$

where κ_L is the lattice thermal conductivity.

The figure-of-merit (ZT) can be described in terms of reduced Fermi energy

$$ZT = \frac{S^2 \sigma T}{\kappa_e + \kappa_L} = \frac{\left[\eta - \left(r + \frac{5}{2}\right)\right]^2}{(\beta \exp(\eta))^{-1} + \left(r + \frac{5}{2}\right)} \quad \text{Equation 2-27}$$

where β is a material parameter and is defined as

$$\beta = \left(\frac{k_B}{e}\right)^2 \frac{\sigma_o T}{\kappa_L} \quad \text{Equation 2-28}$$

in which

$$\sigma_o = 2e\mu \left(\frac{2\pi m^* k_B T}{h^2}\right)^{3/2} \quad \text{Equation 2-29}$$

ZT is a function of β , reduced Fermi energy, and scattering factor, as indicated in Equation 2-27. For certain Fermi energy and scattering mechanism, we can obtain the following expression

$$ZT \propto \beta \propto \frac{\mu(m^*)^{\frac{3}{2}}}{\kappa_L} \quad \text{Equation 2-30}$$

Equation 2-30 shows that a large effective mass, a high mobility, and a low lattice thermal conductivity are desirable for a high ZT value. The aforementioned effective mass m^* refers to the density-of-states effective mass. Several methods could be employed to increase m^* . For example, m^* could be increased by the quantum size effects in low-dimensional materials due to the creation of sharp features in density of states [27,36]. A local maximum density of state and a resonant level can be created by introducing nano-inclusions [37] or impurity energy levels into the conduction or valence band [5]. Moreover, high effective mass could be found in a multi-valley semiconductor with a low inertial mass [38]. Furthermore, energy filtering can improve the Seebeck coefficient by scattering low energy carriers [39].

A semiconductor with a large effective mass usually exhibits a small carrier mobility, thus imposing a limitation on the improvement in ZT . However, the exact relationship between mobility and effective mass depends on the carrier scattering mechanism which is governed by the electronic band structure and the chemical bonding of the material. If the charge carriers are scattered by ionized impurities, ZT increases with increasing m^* , since $\mu(m^*)^{1/2}$ is a constant. If the charge carriers are scattering by acoustic phonons, ZT decreases with increasing m^* , since $\mu(m^*)^{5/2}$ is a constant. Therefore, ZT could be improved if the carrier scattering is dominated by ionized impurities.

2.1.3.2.2 *Narrow-band semiconductors*

In ionic or highly polar crystals such as transition metal oxides, strong electron-phonon coupling exists due to the Coulomb interaction between charge carriers and lattice ions. The charge carrier together with its self-induced polarization is called a polaron. When the polarization is confined to a volume of the order of a unit cell, the polaron is called a small polaron. The small polarons are localised or self-trapped. The transport of small polarons thus includes moving of both the charge carriers and their polarization. The carrier mobility is low and increases with increasing temperature. The

motion of small polarons occurs via thermally-activated hopping. These materials have narrow bandgaps, thus called narrow-band semiconductors.

The electrical conductivity for a simple cubic lattice of lattice constant ‘ a ’ is [40]

$$\sigma = \frac{c(1-c)e^2}{ak_B T} \tau_0^{-1} \exp(-\Delta G/k_B T) \quad \text{Equation 2-31}$$

where c is the carrier concentration per site, ΔG is the activation (Gibbs free) energy and is equal to the work required for the lattice to adjust such that the site at which the charge is located and that to which it jumps are degenerate.

Each electron can only occupy one site in a system with strong on-site Coulomb repulsion. Each electron may have states of spin up or spin down. The Seebeck coefficient is expressed as

$$S = -\frac{k_B}{e} \left[\ln \frac{2(1-c)}{c} + \frac{\Delta S_R}{k_B} \right] \quad \text{Equation 2-32}$$

where ΔS_R is the entropy change due to the trapping of a charge carrier. Equation 2-32 is called the Heikes formula. At sufficiently high temperature, the Seebeck coefficient becomes temperature-independent due to the constant carrier concentration per site. The simplest form of the Heikes formula doesn’t take the spin degrees of freedom into account, and is expressed as [41]

$$S = -\frac{k_B}{e} \left[\ln \frac{(1-c)}{c} \right] \quad \text{Equation 2-33}$$

Since the electrons can have states of spin up and spin down, Equation 2-33 is modified as

$$S = -\frac{k_B}{e} \left[\ln \frac{(2-c)}{c} \right] \quad \text{Equation 2-34}$$

When the electron-electron repulsion is large, only one electron can occupy a single site. Equation 2-34 is modified as

$$S = -\frac{k_B}{e} \left[\ln \frac{2(1-c)}{c} \right] \quad \text{Equation 2-35}$$

The thermal conductivity of a narrow-band material is dominated by the lattice contribution. There is no net flow of charges, since they are localized. Equal and opposite amount of external work or heat is required to remove/add a change from/to its site. Therefore, the electronic thermal conductivity is zero.

The figure-of-merit (ZT) of a narrow-band or mixed-valency semiconductor is written as

$$ZT = \frac{k_B}{\kappa_L a} \left[\frac{\Delta S_R}{k_B} - \ln \frac{c}{2(1-c)} \right]^2 \tau_o^{-1} c(1-c) \exp(-\Delta G/k_B T)$$

$$\text{Equation 2-36}$$

By setting ΔG_R , ε , and ΔG to zero, ZT is a function of c . The optimum c value for the maximized ZT is approximately 0.12. In fact, ε is not zero. Moreover, a zero ΔG_R results in a large electrical conductivity but a low Seebeck coefficient. By setting $\Delta S_R/k_B$ to a certain value, maximum ZT can be achieved by optimizing the c value.

2.1.3.2.3 Bipolar Effects

Both electrons and holes appear in a broad-band semiconductor at high temperatures as it becomes more intrinsic. Moreover, both types of carriers could exist in narrow-band semiconductors as they can be excited from the valence band to conduction band. Bipolar effects occur when both types of carriers are present. The electrical conductivity is a sum of the respective conductivity ($\sigma = \sigma_n + \sigma_p$). The Seebeck coefficient is a weighted average of the respective Seebeck coefficient (S_n, S_p) as shown in Equation 2-37. Due to the opposite signs of S_n and S_p , the Seebeck coefficient is suppressed (Equation 2-37).

$$S = \frac{S_n \sigma_n + S_p \sigma_p}{\sigma_n + \sigma_p} \quad \text{Equation 2-37}$$

Both types of carriers transfer heat, although the net electrical current is zero. The total electronic thermal conductivity (κ_e) is

$$\kappa_e = \kappa_n + \kappa_p + \frac{\sigma_n \sigma_p}{\sigma_n + \sigma_p} (S_n - S_p)^2 T \quad \text{Equation 2-38}$$

It is clear that the total κ_e is the sum of the respective electronic thermal conductivity and a bipolar thermal conductivity. The bipolar contribution can be much larger than either κ_n or κ_p . Thus, it is important to reduce the bipolar effect in order to improve the Seebeck coefficient and reduce the thermal conductivity. This effect can be restrained in heavily doped thermoelectric materials or by introducing nanostructures to selectively scatter the minor carriers [42].

2.1.3.3 *Reduction of the thermal conductivity*

It is obvious that thermoelectric materials require low thermal conductivity to maintain the temperature difference between the hot and cold ends and thus reduce the heat loss. The thermal conductivity is composed of electronic and lattice contribution. In heavily doped semiconductors, the charge carriers inevitably contribute to the total thermal conductivity. Alternatively, we can minimize the lattice thermal conductivity to improve ZT , as indicated in Equation 2-30 and Equation 2-36.

Lattice thermal conductivity can be qualitatively understood employing the classical kinetic theory of gases formula

$$\kappa_L = \frac{1}{3} C_v l v \quad \text{Equation 2-39}$$

where C_v is the specific heat at constant volume, l is the mean free path, v is the velocity of sound in the material. At low temperatures C_v is proportional to T^3 , whereas at high temperatures C_v reaches $3R$ (R is the ideal gas constant). The mean free path is affected by the scattering events, including scattering with phonons, point defects, charge carriers, and grain boundaries. The sound velocity is independent of temperature. At low temperatures the phonon mean free path is usually long and independent of temperature at the presence of rough surface. The major scattering event is phonon-

boundary scattering. Therefore, at low temperatures the lattice thermal conductivity is proportional to T^3 . At high temperatures, the mean free path is decreased due to the increased phonon-phonon scattering. Therefore, the lattice thermal conductivity decreases as $1/T$.

2.1.3.3.1 Point defects

Equation 2-39 indicates that the lattice thermal conductivity could be decreased by reducing phonon mean free path. Phonons can be scattered by point defects present in the crystals caused by the local changes in density and elastic constants. More specifically, the local changes in density correspond to the mass fluctuation, i.e. atomic mass difference between isotopes, alloy elements, dopants and host atoms, lattice vacancies, etc. For example, a reduced thermal conductivity has been achieved in alloys such as SiGe and $\text{Pb}_{1-x}\text{Sn}_x\text{Te}$. On the other hand, the local changes in elastic constants could be caused by the difference in ionic radii or bond types between dopants and host atoms. According to Klemens [43,44], the ratio of the lattice thermal conductivity of a material that contains defects to that of a pure and perfect material is proportional to a disorder parameter, Γ . Γ is given by

$$\Gamma = \sum_i \Gamma_i = \sum_i x_i \left[\left(\frac{\Delta M_i}{M} \right)^2 + 2 \left(\left(\frac{\Delta G_i}{G} \right) - 6.4\gamma(\Delta\delta_i/\delta) \right)^2 \right] \quad \text{Equation 2-40}$$

where x_i is the fractional concentration of the impurity of mass M_i , G_i is the average stiffness constant of the nearest-neighbor bonds from the impurity to the host atom, δ_i is the cube root of the atomic volume for the i th impurity in its own lattice, γ is the average anharmonicity of the bonds, $\Delta M_i = M_i - M$, $\Delta G_i = G_i - G$, $\Delta\delta_i = \delta_i - \delta$. Furthermore, nanoinclusions or nano-precipitates act as phonon scattering centers if the size of the precipitates matches the wavelength of the primary phonon density of states. The short-wavelength phonons are preferentially scattered by the point defects.

2.1.3.3.2 Grain boundary/Interface scattering by nanostructuring approach

At low temperatures, phonons usually have long mean free path and low vibrational frequency. The phonons can be scattered by the interfaces or grain

boundaries of crystals under such condition. Even though the number of low-frequency phonons is small, the scattering of such phonons can effectively reduce the thermal conductivity. For instance, grain boundaries contribute a 9% increase in the thermal resistance of SiGe alloys with a grain size $\sim 40 \mu\text{m}$ [45]. Nanostructuring approaches have been implemented to obtain even lower lattice thermal conductivity. Such approaches include the synthesis of nanocomposites, superlattices, and nanowires. Due to the nano-size crystal grains, the mid- to long-wavelength phonons can be effectively scattered. For instance, SiGe nanocomposites have a reduced thermal conductivity (2.5 W/m/K at 50 °C) compared with that of a bulk sample (5 W/m/K at 50 °C), for the density of interfaces and grain boundaries are increased [8].

2.1.4 Thermoelectric materials

2.1.4.1 Alloys

Thermoelectric materials have been developed since the 1960s, for example, $\text{Bi}_2\text{Te}_3\text{-Sb}_2\text{Te}_3$ alloys, PbTe alloys, $(\text{AgSbTe}_2)_{100-x}(\text{GeTe})_x$ (TAGS- x) alloys, and SiGe alloys. Figure 2-6 shows the temperature dependent ZT of some conventional thermoelectric materials. The Bi_2Te_3 -type materials have mainly been used for the application of refrigeration, operating near room temperature. ZT of p-type BiSbTe alloys can be enhanced via high-energy ball milling followed by hot pressing, reaching 1.4 at 100 °C, due to the significant reduction in the thermal conductivity caused by the interface or grain boundary scattering [46]. By improving the synthesis technique (melt spinning combined with spark plasma sintering), ZT of BiSbTe is increased to 1.56 at room temperature [4]. CsBi_4Te_6 is another material that operates at low temperatures, peak ZT reaching 0.82 at -48 °C [47].

PbTe, TAGS, $(\text{AgSbTe}_2)\text{-}m(\text{PbTe})$ (LAST- m), CoSb_3 , and $\text{CeFe}_4\text{Sb}_{12}$ operate in the mid-temperature range (227 °C to 627 °C). ZT of bulk PbTe was approximately 0.6 at 400 °C in the 1960s. ZT of PbTe has been enhanced to ~ 1.5 at 400 °C via band structure engineering or nanostructuring approaches [5,6]. The nanostructured TAGS-75 has a maximum $ZT \sim 1.53$ at 447 °C as a result of the low lattice thermal conductivity due to the existence of nanoscale domains [7]. LAST has the same rock-salt crystal structure as TAGS, showing ZT values higher than 1 [48,49]. The lattice thermal conductivity of LAST is reduced due to the inhomogeneity in the nanoscale

microstructure. CoSb_3 and $\text{CeFe}_4\text{Sb}_{12}$ have skutterudite crystal structure. Enhanced thermoelectric performance of these materials can be reached by inserting “rattler” atoms in the voids provided by the cage-like crystal structure. The unfilled CoSb_3 has a high power factor but also a high lattice thermal conductivity. The crystal structure of CoSb_3 allows a void space in the body-centered position of the eight corner-shared XY_6 ($X = \text{Co, Rh, Ir}$; $Y = \text{P, As, Sb}$) octahedra. Partial void filling by small and heavy atoms results in a reduction in the lattice thermal conductivity and an improvement in ZT . A thermal conductivity as low as 2.6 W/m/K and a ZT as high as 1.7 at 577 °C have been reported in the CoSb_3 with multiple cofillers of Ba, La, and Yb [50].

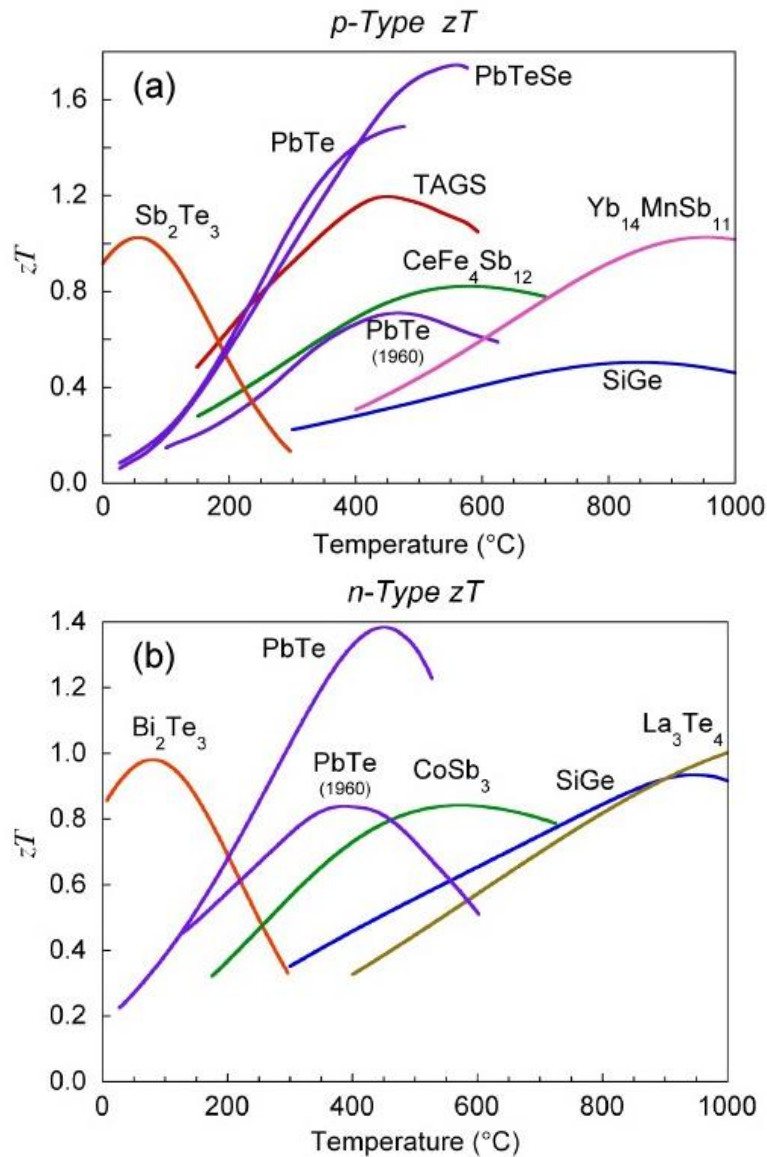


Figure 2-6 Temperature dependence of ZT for (a) n-type and (b) p-type thermoelectric materials [51].

SiGe alloys, $\text{Ba}_8\text{Ga}_{16}\text{Ge}_{30}$, $\text{Yb}_{14}\text{MnSb}_{11}$, and ZrNiSn-based half-Heusler compounds operate at high temperatures ($T > 627 \text{ }^\circ\text{C}$). Figure 2-6 shows the temperature dependent ZT of the bulk SiGe that was developed in the 1960s. By using the high-energy ball milling and hot pressing technique, SiGe nanocomposites have been prepared. The ZT values of p-type and n-type SiGe nanocomposites are 0.95 and 1.3 at $900 \text{ }^\circ\text{C}$, respectively [8,9]. $\text{Ba}_8\text{Ga}_{16}\text{Ge}_{30}$ is one of the n-type clathrates, showing a ZT value ~ 1.63 at $827 \text{ }^\circ\text{C}$ [52]. In clathrates, the guest atoms are filled into the voids provided by the frameworks consisting of tetrahedrally coordinated Ga, Si, Ge, or Sn. $\text{Yb}_{14}\text{MnSb}_{11}$ is a high-performance Zintl compound with $ZT \sim 1$ at $950 \text{ }^\circ\text{C}$ [53]. It has a very low thermal conductivity, $\sim 0.8 \text{ W/m/K}$ in the temperature range $27 \text{ }^\circ\text{C} \leq T \leq 1000 \text{ }^\circ\text{C}$, resulting from its complex crystal structure and heavy atomic mass. Materials with half-Heusler structure show large Seebeck coefficient and electrical conductivity. However, their thermal conductivity is relatively large ($\kappa \approx 5 \text{ W/m/K}$ at $500 \text{ }^\circ\text{C}$) [54]. By applying nanostructuring strategies, n-type $\text{Hf}_{0.75}\text{Zr}_{0.25}\text{NiSn}_{0.99}\text{Sb}_{0.01}$ half-Heusler nanocomposites show maximum $ZT \sim 1$ at $600 \text{ }^\circ\text{C}$ - $700 \text{ }^\circ\text{C}$ [55], while ZT of p-type $\text{Zr}_{0.5}\text{Hf}_{0.5}\text{CoSb}_{0.8}\text{Sn}_{0.2}$ nanocomposites reach 0.8 at $700 \text{ }^\circ\text{C}$ [56]. La_3Te_4 is another n-type thermoelectric material for high-temperature operation. La-deficient $\text{La}_{2.74}\text{Te}_4$ has a peak $ZT \sim 1.05$ at $927 \text{ }^\circ\text{C}$ [57].

Although the thermoelectric performance of conventional thermoelectric materials is relatively high, most of them contain rare metals such as Te and Ge, and toxic elements like Sb and Pb. The scarcity and toxicity limit the mass production and operation of the thermoelectric modules. Furthermore, sublimation and oxidation of these materials at high temperatures have deleterious effects on the long-term operation of thermoelectric modules. On the contrary, oxide thermoelectric materials possess the advantages of high general stability, nontoxicity, and low cost. Therefore, oxides have been intensively studied as substitutes for the conventional thermoelectric materials.

2.1.4.2 Oxides

Cobalt-based layered oxides including Na_xCoO_2 , $\text{Ca}_3\text{Co}_4\text{O}_9$, and their derivative compounds are typical p-type thermoelectric materials with high power factor and low thermal conductivity. Polycrystalline Na_xCoO_2 could reach a ZT of 0.8 at $682 \text{ }^\circ\text{C}$ [58]. Similarly, a ZT of 0.61 has been achieved in polycrystalline $\text{Ca}_3\text{Co}_4\text{O}_9$ at $845 \text{ }^\circ\text{C}$ [22]. In contrast, n-type oxide materials demonstrate inferior thermoelectric properties to those

of the p-type oxide materials. $(\text{Zn}_{1-x}\text{Al}_x)\text{O}$ obtained by solid-state reaction between ZnO and Al_2O_3 exhibits a peak ZT of 0.3 at 1000 °C [59]. CaMnO_3 doped with Yb on Ca site or Nb on Mn site exhibit $ZT \sim 0.2$ at 700 °C [26,60]. Donor-doped SrTiO_3 is a promising n-type oxide with maximum $ZT \sim 0.37$ at 727 °C [61]. Although the power factor of donor-doped SrTiO_3 is high, their thermal conductivity is high due to the simplicity of crystal structure and light atomic mass. Therefore, recently the efforts have been made on nanostructured SrTiO_3 to achieve reduced thermal conductivity [62].

2.2 Na_xCoO_2 and $\text{Ca}_3\text{Co}_4\text{O}_9$

2.2.1 Crystal structure

Na_xCoO_2 exhibits several interesting properties depending on the Na content, x . Superconductivity has been found in the hydrated form of $\text{Na}_{0.35}\text{CoO}_2$ ($T_c = 4.5$ K) [63]. Although Na_xCoO_2 has low electrical resistivity over a wide range of x , $\text{Na}_{0.5}\text{CoO}_2$ is an insulating phase at low temperatures possibly due to the charge ordering of holes with Na^+ [64]. A large Seebeck coefficient and a low electrical resistivity have been obtained in Na_xCoO_2 with $x \sim 0.7$ due to the transport of spin entropy by strongly correlated electron hopping [12]. Furthermore, magnetic ordering has been observed in $\text{Na}_{0.75}\text{CoO}_2$ [65]. These various properties are closely related to the crystal structure of Na_xCoO_2 .

Na_xCoO_2 has a layered structure where the Na ions are intercalated between sheets of two-dimensional (2D) edge-sharing CoO_6 octahedra (Figure 2-7a). The degree of filling of the Na layers determines the number of charge supplied to the CoO_2 layers. There are four crystallographic phases for Na_xCoO_2 according to the sodium content (x), including α - Na_xCoO_2 ($0.90 \leq x \leq 1.0$), α' - Na_xCoO_2 ($x = 0.75$), β - Na_xCoO_2 ($0.55 \leq x \leq 0.60$), and γ - Na_xCoO_2 ($0.3 \leq x \leq 1$) [66]. Depending on the stacking sequence of the oxygen layers, α , α' , and β phase Na_xCoO_2 possess three CoO_2 layers per unit cell, while γ phase Na_xCoO_2 possesses two CoO_2 layers per unit cell. The crystal structure is strongly related to both Na content and Na^+ coordination especially for the three-layer systems.

Pure γ -phase Na_xCoO_2 can only be prepared by conventional thermodynamic methods with $0.60-0.65 \leq x \leq 0.75-0.80$ [67]. It indicates that the stoichiometric $\text{Na}_{0.5}\text{CoO}_2$ doesn't exist, even though Na evaporation is completely prevented. Additionally, it was proved by Sakurai et al.(2004) that γ - Na_xCoO_2 is formed only in the

narrow range of $0.70 \leq x \leq 0.78$ [68]. Furthermore, it is suggested that $x = 0.75$ or $x = 2/3$ turns out not to be the most stable phase among $x > 1/2$, and that $x = 0.71$ exhibits a clear superstructure formed by Na^+ /vacancy ordering of special stability [69]. It was also proposed by Shu et al.(2010) that oxygen vacancies are important in stabilizing the superlattice structure, and that $\text{Na}_{2/3}\text{CoO}_{1.98}$ has nearly identical Na superstructure and magnetic properties as $\text{Na}_{0.71}\text{CoO}_2$ due to the generation of oxygen defects [70]. γ -phase Na_xCoO_2 with $x < 0.60$ or $x > 0.80$ can be synthesized by chemical deintercalation or intercalation method [66,71].

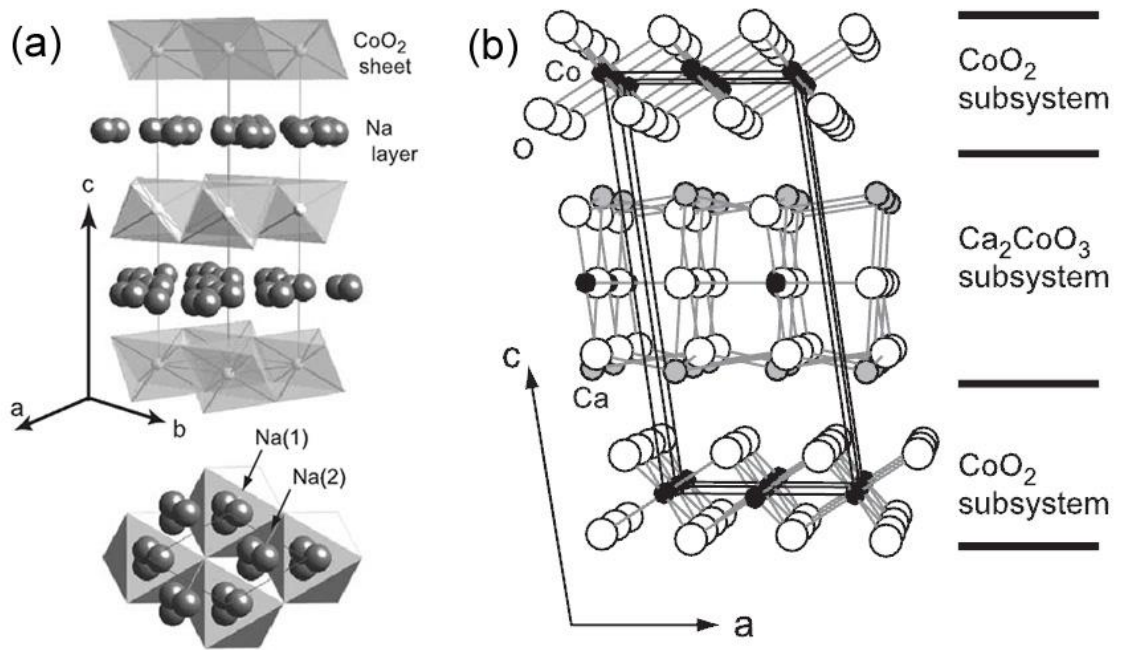


Figure 2-7 Schematic illustration of crystal structure of (a) γ -phase Na_xCoO_2 and (b) $\text{Ca}_3\text{Co}_4\text{O}_9$ [72].

The schematic illustration of γ -phase Na_xCoO_2 is shown in Figure 2-7a. The compound consists of alternating CdI_2 -type CoO_2 triangular layers and Na layers. Na site splits into Na(1) and Na(2) with each of them containing three equivalent positions. Both Na sites form trigonal prisms with oxygen atoms. Na(1) prisms share faces with CoO_6 octahedral while Na(2) prisms share edges with CoO_6 octahedral. Na(1) and Na(2) sites have occupancies approximately 0.21 and 0.49, respectively [72]. Na(2) is more energetically stable than Na(1) due to the longer Co-Na(2) distance than Co-Na(1). The Na ions and vacancies are statistically located in Na(1) and Na(2) sites. The disordering of Na vacancies reduces the thermal conductivity by enhancing phonon scattering. $\text{Ca}_3\text{Co}_4\text{O}_9$ is also a promising p-type thermoelectric material with similar crystal

structure (Figure 2-7b). The Na layers are substituted with layers of three-layered rock-salt type CaO-CoO-CaO structure. The lattice parameters of rock-salt layers and CoO₂ layers are incommensurate along *b*-axis, resulting in a misfit layered structure. Therefore, Ca₃Co₄O₉ is better to be written as [Ca₂CoO₃]_{*p*}[CoO₂] where *p* equals *b*-axis length of CoO₂ divided by *b*-axis length of Ca₂CoO₃ and *p* ~ 0.62.

2.2.2 Electronic structure

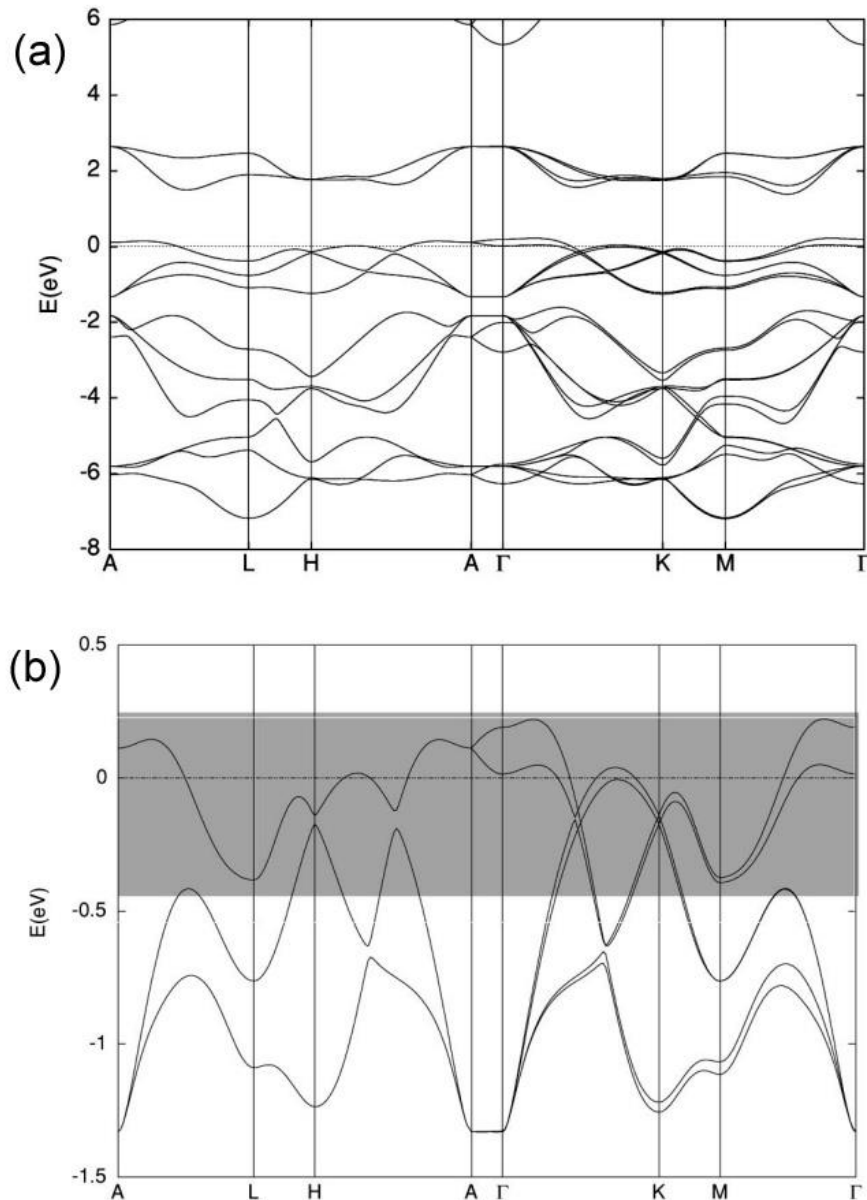


Figure 2-8 (a) Local density approximation (LDA) paramagnetic band structure and (b) the magnification of T_{2g} manifold of Na_{0.5}CoO₂ [73].

Figure 2-8 shows the band structure of $\text{Na}_{0.5}\text{CoO}_2$ predicted by local density approximation (LDA). The Co 3d band splits into a doubly degenerated upper e_g and triply degenerated lower t_{2g} levels in the octahedral O environment. The O 2p band is located between approximately -7 ~ -2 eV. The t_{2g} manifold extends across the Fermi energy (0 eV). The e_g orbitals extend above the Fermi energy, ~2.5 eV above the t_{2g} manifold [73]. The t_{2g} manifold further splits into a single-degenerate a_{1g} level and a doubly degenerated e_g' levels, since the octahedral CoO_6 is distorted rhombohedrally. The a_{1g} band forms large cylindrical hole (less electron occupation) Fermi surfaces around the Γ point, while the e_g' band forms small hole pockets along the Γ -K direction. It is suggested that the large Seebeck coefficient is owing to the a_{1g} band with localized carriers, while superconductivity and susceptibility are owing to the e_g' band [73]. The small hole pockets have been obtained from the LDA calculation; however, it is not observed experimentally by angle-resolved photoemission spectroscopy (ARPES) [74], possibly due to the presence of Na disorder or strong correlation in real samples. The Seebeck coefficient of $\text{Na}_{0.5}\text{CoO}_2$ can be calculated by Mott formula using values from the LDA prediction, and is 110 $\mu\text{V/K}$ at 27 $^\circ\text{C}$. It agrees well with the Seebeck coefficient of the single-crystalline $\text{Na}_{0.5}\text{CoO}_2$ (γ phase) measured experimentally which is 100 $\mu\text{V/K}$ at 27 $^\circ\text{C}$ [12].

The rock-salt type Ca_2CoO_3 and CdI_2 type CoO_2 layers are incommensurate along the b direction of $\text{Ca}_3\text{Co}_4\text{O}_9$, or $(\text{Ca}_2\text{CoO}_3)(\text{CoO}_2)_{1.62}$, leading to difficulties in modelling and the theoretical calculation of its electronic structure [75,76]. However, according to its ARPES spectra, $\text{Ca}_3\text{Co}_4\text{O}_9$ has similar electronic structure to Na_xCoO_2 in the vicinity of the Fermi level, i.e., consisting of a_{1g} and e_g' bands from the CoO_2 layers [77]. Moreover, the Ca_2CoO_3 layers provide holes to the CoO_2 layers, and the holes are conducted along the CoO_2 layers [78].

2.2.3 Thermoelectric properties of single-crystalline Na_xCoO_2 and $\text{Ca}_3\text{Co}_4\text{O}_9$

The in-plane (ab direction) and out-of-plane (c direction) electrical resistivity of single-crystalline Na_xCoO_2 ($x = 0.5$) versus temperature are shown in Figure 2-9a. The resistivity of Na_xCoO_2 is anisotropic. A lower in-plane electrical resistivity (200 $\mu\Omega\text{cm}$ at 27 $^\circ\text{C}$) compared with the out-of-plane resistivity is observed in single-crystalline $\text{Na}_{0.5}\text{CoO}_2$ [12]. Furthermore, the in-place resistivity shows metallic behavior, while the out-of-plane resistivity shows a mixed metallic-semiconducting behavior. $\text{Ca}_3\text{Co}_4\text{O}_9$

with similar crystal structure possesses much higher electrical resistivity than Na_xCoO_2 , which is probably due to the random potential scattering of the conduction electrons by the misfit structure [79]. Similarly, the electrical resistivity of $\text{Ca}_3\text{Co}_4\text{O}_9$ is highly anisotropic ($\rho_{ab} \ll \rho_c$) [17].

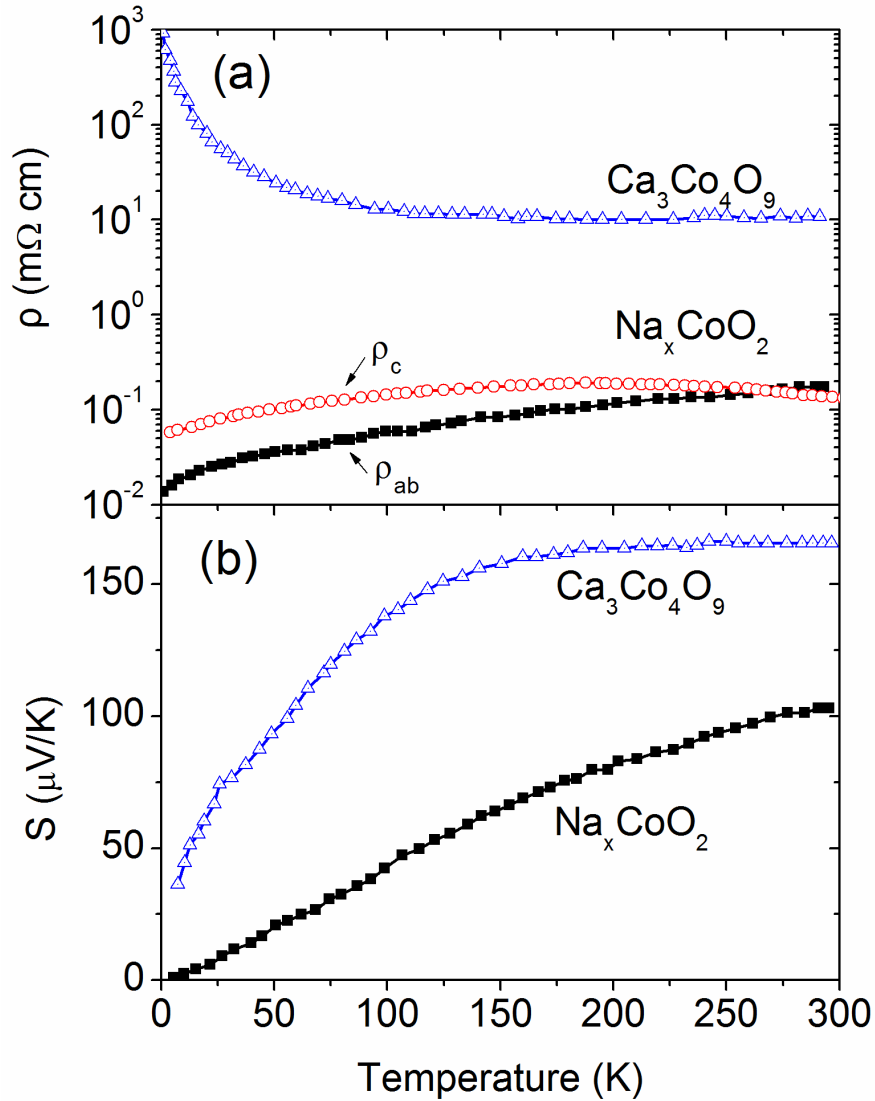


Figure 2-9 Temperature dependence of the (a) electrical resistivity (ρ) of Na_xCoO_2 along in-plane (ab) and out-of-plane (c) direction, ρ of $\text{Ca}_3\text{Co}_4\text{O}_9$ along ab direction and (b) Seebeck coefficient (S) of Na_xCoO_2 and $\text{Ca}_3\text{Co}_4\text{O}_9$ along ab direction [12,18].

Both Na_xCoO_2 and $\text{Ca}_3\text{Co}_4\text{O}_9$ exhibit high Seebeck coefficient at room temperature (Figure 2-9b). It is suggested that the origin of the large Seebeck coefficient is due to the strong electron-electron correlation in this material [14]. The Seebeck

coefficient can be expressed by the generalized Heikes formula which could be generated from the Hubbard model. The Seebeck coefficient of a cobalt oxide is

$$S = -\frac{k_B}{e} \ln\left(\frac{g_3}{g_4} \frac{x}{1-x}\right) \quad \text{Equation 2-41}$$

where g_3 and g_4 are the numbers of the configuration of Co^{3+} and Co^{4+} , respectively, x is the concentration of Co^{4+} ions. The valence state of Co in $\text{Na}_{0.5}\text{CoO}_2$ is +3.5, thus the concentration of Co^{4+} is 0.5. Both Co^{3+} and Co^{4+} are in low spin state according to the magnetic measurement, and therefore g_3/g_4 equals 1/6 [14]. According to Equation 2-41, the Seebeck coefficient is 154 $\mu\text{V/K}$. It has been indicated that in a strongly correlated electron system the Seebeck coefficient is not obviously varied with temperature as the temperature is larger than the nearest-neighbor hopping integral [80]. Although the value (154 $\mu\text{V/K}$) calculated by the Heikes formula is the value at the high temperature limit, it can be viewed as the Seebeck coefficient at room temperature. It is in good agreement with the LDA prediction and the measured value [12,73]. Furthermore, it implies that Seebeck coefficient is not only affected by carrier concentration, but also spin and orbital degeneracies. The Seebeck coefficient of $\text{Ca}_3\text{Co}_4\text{O}_9$ is higher than that of Na_xCoO_2 (Figure 2-9b).

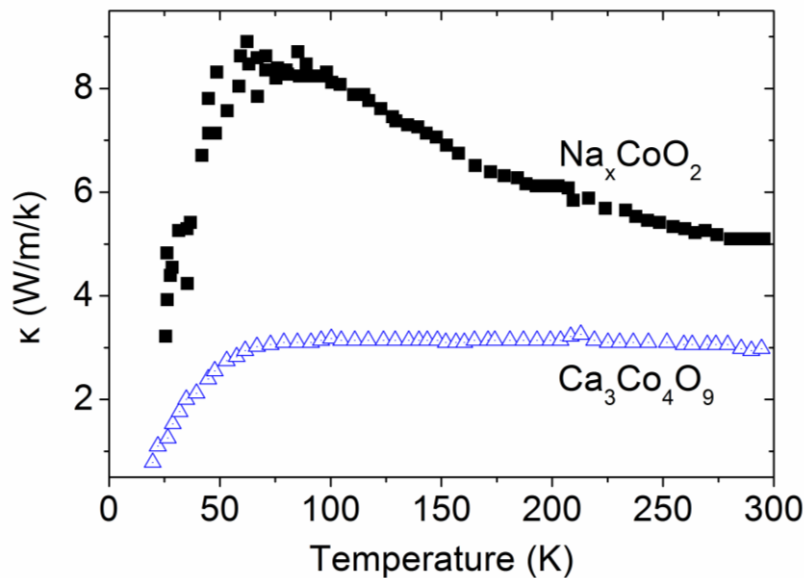


Figure 2-10 Thermal conductivity of Na_xCoO_2 and $\text{Ca}_3\text{Co}_4\text{O}_9$ along the in-plane direction measured by the Harman method [81].

Na_xCoO_2 and $\text{Ca}_3\text{Co}_4\text{O}_9$ show rather low thermal conductivity with respect to other oxides. The in-plane thermal conductivity of the layered cobaltates is determined by the block layers, i.e., Na^+ layers or Ca_2CoO_3 layers, and the more complex block layer shows the lower thermal conductivity [18]. In Na_xCoO_2 , the highly vacant and disordered Na layers are responsible for the low thermal conductivity owing to the increased phonon scattering. On the other hand, the nonperiodicity and the associated modulated potential arise from the misfit structure of $\text{Ca}_3\text{Co}_4\text{O}_9$, leading to a partial localization of the phonons dispersion and thus a reduction in the thermal conductivity [82]. Therefore, $\text{Ca}_3\text{Co}_4\text{O}_9$ possesses lower thermal conductivity than Na_xCoO_2 (Figure 2-10). ZT of Na_xCoO_2 single crystals has reached ~ 1 at 527 °C [13]. ZT of single-crystalline $\text{Ca}_3\text{Co}_4\text{O}_9$ is about 0.87 at 700 °C [83].

2.2.4 Thermoelectric properties of polycrystalline Na_xCoO_2 and $\text{Ca}_3\text{Co}_4\text{O}_9$

Na_xCoO_2 is highly anisotropic in electrical resistivity ($\rho_{ab} < \rho_c$), as indicated in Figure 2-9a. Therefore, polycrystalline Na_xCoO_2 possesses a much higher electrical resistivity than the single-crystalline Na_xCoO_2 due to the anisotropy and the increased grain boundary resistivity (Figure 2-11a). The resistivity of single crystalline Na_xCoO_2 at room temperature is a little higher than the value in Figure 2-9a. It is likely due to the fact that the electrical resistivity is affected by both Na content and oxygen nonstoichiometry. Furthermore, the electrical resistivity of polycrystalline $\text{Ca}_3\text{Co}_4\text{O}_9$ is higher than that of Na_xCoO_2 . The Seebeck coefficient is less anisotropic than the electrical resistivity, as shown in Figure 2-11b. The difference between the Seebeck coefficient of single-crystalline and polycrystalline Na_xCoO_2 may be caused by the variation in Na content, structural change and anisotropy [13]. Polycrystalline $\text{Ca}_3\text{Co}_4\text{O}_9$ shows higher Seebeck coefficient compared to Na_xCoO_2 .

The thermal conductivity of single-crystalline and polycrystalline Na_xCoO_2 at room temperature is ~ 5 and ~ 1.8 W/m/K, respectively (Figure 2-10 and Figure 2-11c). The polycrystalline sample shows lower thermal conductivity due to the grain boundary scattering and the anisotropy effect [13]. Polycrystalline $\text{Ca}_3\text{Co}_4\text{O}_9$ has similar thermal conductivity as polycrystalline Na_xCoO_2 . The polycrystalline Na_xCoO_2 shows lower ZT values than the single crystalline sample. It is mainly due to the relatively high electrical resistivity in polycrystalline Na_xCoO_2 as a result of the high anisotropy in conductivity, microstructure and stoichiometric variations of the materials. The highest ZT of

polycrystalline Na_xCoO_2 is 0.8 at 682 °C according to Ito et al. (2003) using polymerized complex method followed by pressureless sintering [58]. The highest ZT of polycrystalline $\text{Ca}_3\text{Co}_4\text{O}_9$ is 0.61 at 845 °C after doping with Lu and Ag nano-inclusions prepared by spark plasma sintering [22].

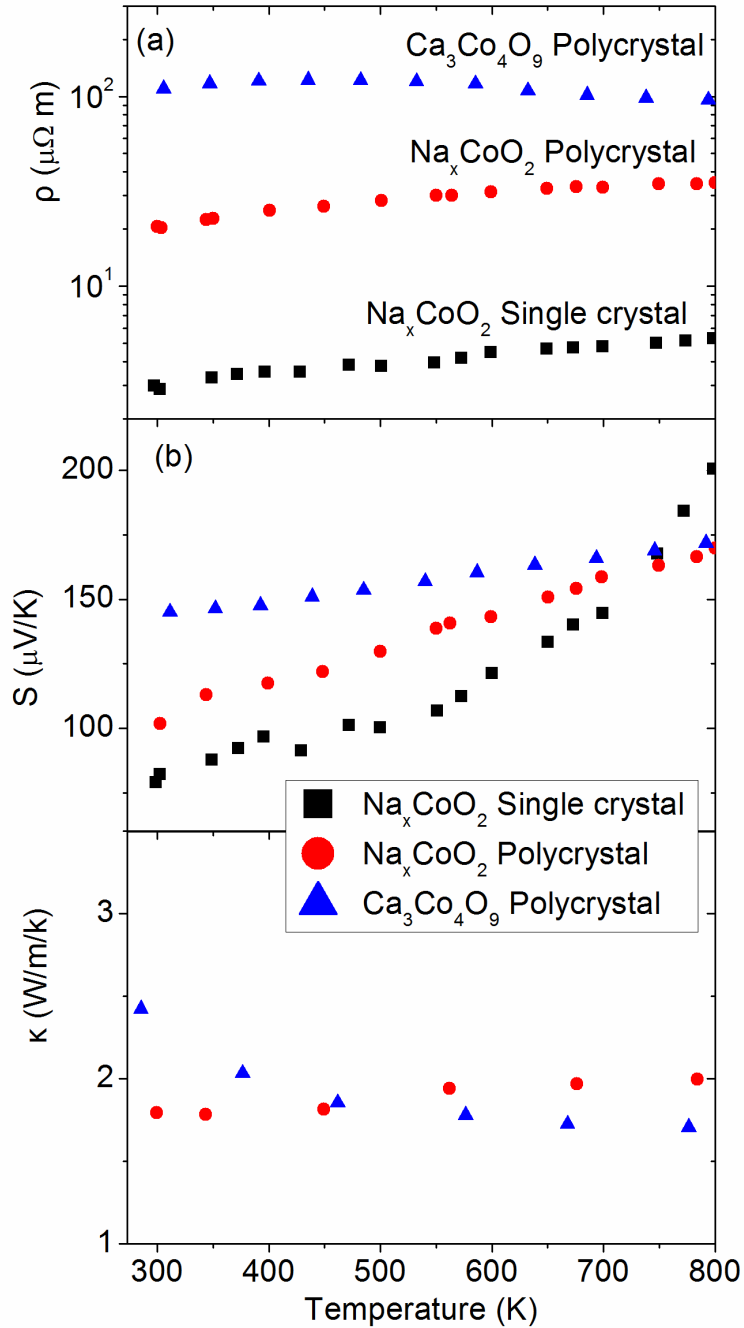


Figure 2-11 Temperature dependence of the (a) electrical resistivity (ρ), (b) Seebeck coefficient (S) of single-crystalline (in-plane) Na_xCoO_2 , and polycrystalline Na_xCoO_2 and $\text{Ca}_3\text{Co}_4\text{O}_9$ [13,22], and (c) thermal conductivity (κ) of polycrystalline Na_xCoO_2 and $\text{Ca}_3\text{Co}_4\text{O}_9$ [13,22].

Various doping elements have been introduced into Na_xCoO_2 in order to enhance the thermoelectric properties of this material. The thermoelectric properties of Na-site doped Na_xCoO_2 have been studied, for example, K, Ca, Sr, Y, Nd, Sm, and Yb-doped Na_xCoO_2 [84,85]. Moreover, the thermoelectric performance of Co-site doped Na_xCoO_2 has been investigated with dopants including Cu [86,87], Zn [88,89], Ni [88], Ga [90], Mn [90], Ti [91], Ag [92,93], Fe [94], etc. However, most of the experiments have indicated that the improvement in ZT of Na_xCoO_2 by doping technique is negligible [85,88,93]. Only one exceptions is found in Cu-doped Na_xCoO_2 in which ZT is twice as high as the undoped sample [86]. In addition, there are some doping studies with incomplete measurement of the thermoelectric properties [84,87,89,92,94-96].

Although the thermoelectric performance of Na_xCoO_2 is promising, it has the disadvantage of poor chemical stability. Na_xCoO_2 reacts with moisture and CO_2 in air and becomes insulating upon heating [15]. This problem has to be solved for realistic application. On the contrary to the high volatility of Na and instability against humidity, $\text{Ca}_3\text{Co}_4\text{O}_9$ has much higher stability. However, $\text{Ca}_3\text{Co}_4\text{O}_9$ possesses higher electrical resistivity than Na_xCoO_2 . It is interesting to know whether the thermoelectric performance and chemical stability could be improved in the $\text{Na}_x\text{CoO}_2/\text{Ca}_3\text{Co}_4\text{O}_9$ composites.

2.3 SrTiO_3

2.3.1 Crystal structure

SrTiO_3 belongs to the transition metal oxides with ABO_3 stoichiometry and has a cubic perovskite crystal structure at room temperature (Figure 2-12). The A-site cations usually have larger ionic radii than the B-site cations. A-site cations could be Na^+ , Sr^{2+} , Ca^{2+} , Ba^{2+} , etc, while B-site cations could be Mn^{4+} , Cr^{3+} , Ti^{4+} , Ga^{3+} , etc. In SrTiO_3 , each Ti^{4+} ion is coordinated by 6 O^{2-} ions, forming one TiO_6 octahedron. Each TiO_6 octahedron shares corners with other TiO_6 units, forming a network of TiO_6 octahedra, with Sr atoms sit at the center of a cube formed by eight corner-shared TiO_6 octahedra. Alternatively, the center of the cubic unit cell can be a Ti^{4+} ion, forming an octahedron with 6 O^{2-} ions located at the face-center positions, and 8 Sr^{2+} ions in the corners of the cube. The perovskite structure is capable of tolerating structural distortions and thus allows substitution and defects. A Goldschmidt tolerance factor t is

introduced to estimate the degree of distortion under an assumption of ionic bonding and is expressed as

$$t = \frac{r_A + r_O}{\sqrt{2}(r_B + r_O)} \quad \text{Equation 2-42}$$

where r_A , r_B , and r_O are the ionic radii of A, B, and O ions, respectively. SrTiO₃ has the ideal cubic crystal structure, since its tolerance factor equals 1. Deformed crystal structure and lower symmetry appear as t deviates from 1. Illmenite structure occurs as $t < \sim 0.81$, e.g. MgTiO₃ and FeTiO₃. Orthorhombic structure has been proved in GdFeO₃ ($t = 0.81$), SrZrO₃ ($t = 0.94$), CaTiO₃ ($t = 0.97$), etc. With $t > 1$ BaNiO₃ possesses hexagonal structure. Note that the factors affecting the distortion of crystal structure are complex, and t is just an estimate.

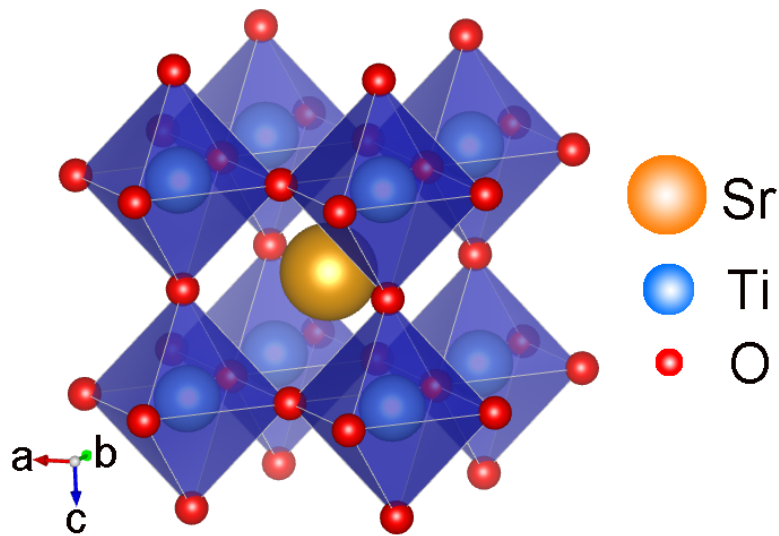


Figure 2-12 Schematic crystal structure of SrTiO₃.

Apart from the lowered symmetry, a distortion could be accompanied by the formation of layered derivatives of the perovskite structure, e.g. the Ruddlesden-Popper (RP) phases. The RP phases of Sr-Ti-O is a natural superlattice and can be written as SrO(SrTiO₃)_{*n*} ($1 \leq n \leq \infty$). SrTiO₃ corresponds to SrO(SrTiO₃)_{*n*} where $n = \infty$. The crystal structure of SrO(SrTiO₃)_{*n*} consists of intergrowth of perovskite layers (SrTiO₃)_{*n*} and rock salt layers SrO along the c -axis (Figure 2-13). The value n could be integer or noninteger depending on the disorder in the stacks. Two different Ti-O bonds are found in SrO(SrTiO₃), whereas three different Ti-O bonds are found in SrO(SrTiO₃)₂.

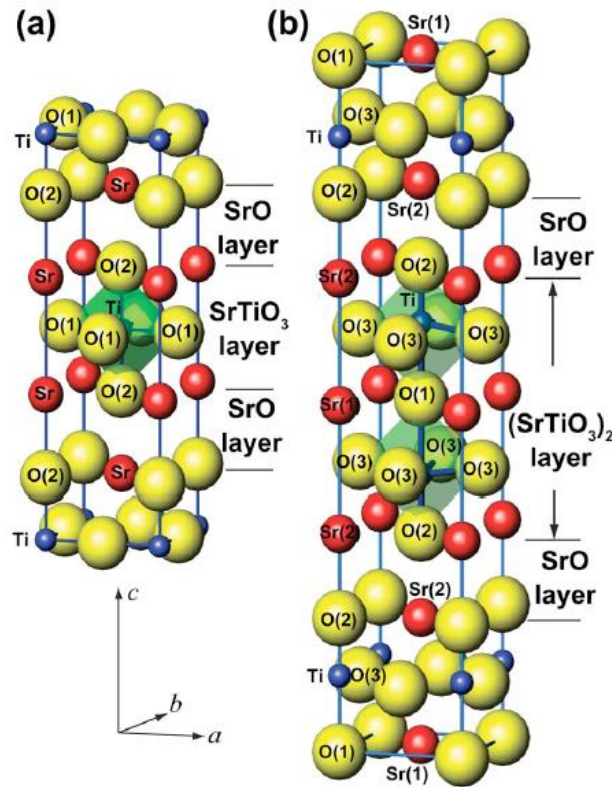


Figure 2-13 Schematic crystal structures of $\text{SrO}(\text{SrTiO}_3)_n$ [97]. (a) $n = 1$, Sr_2TiO_4 and (b) $n = 2$, $\text{Sr}_3\text{Ti}_2\text{O}_7$.

2.3.2 Electronic structure

Experiments and theoretical calculations have been carried out to study the electronic structure of SrTiO_3 [98-101]. It has been confirmed experimentally by vacuum ultraviolet spectroscopy that the direct and indirect bandgap of SrTiO_3 are 3.75 and 3.25 eV, respectively [99]. Ab initio band structure calculation has been employed to describe the electronic band structure of undoped and electron-doped SrTiO_3 . Figure 2-14 shows the density of states of stoichiometric SrTiO_3 (a), oxygen-deficient SrTiO_3 (b), and La-doped SrTiO_3 (c), respectively, by ab initio calculation [98]. The bandgap of the stoichiometric SrTiO_3 is ~ 2.5 eV and is lower than the experimental values due to the limitation of the local-density approximation. The upper valence bands from $-7 \sim -2.5$ eV are dominated by the O $2p$ states and hybridized with Ti and Sr states. The conduction bands are primarily Ti $3d t_{2g}$ and e_g bands. Therefore, the undoped SrTiO_3 is an insulator (Figure 2-14a).

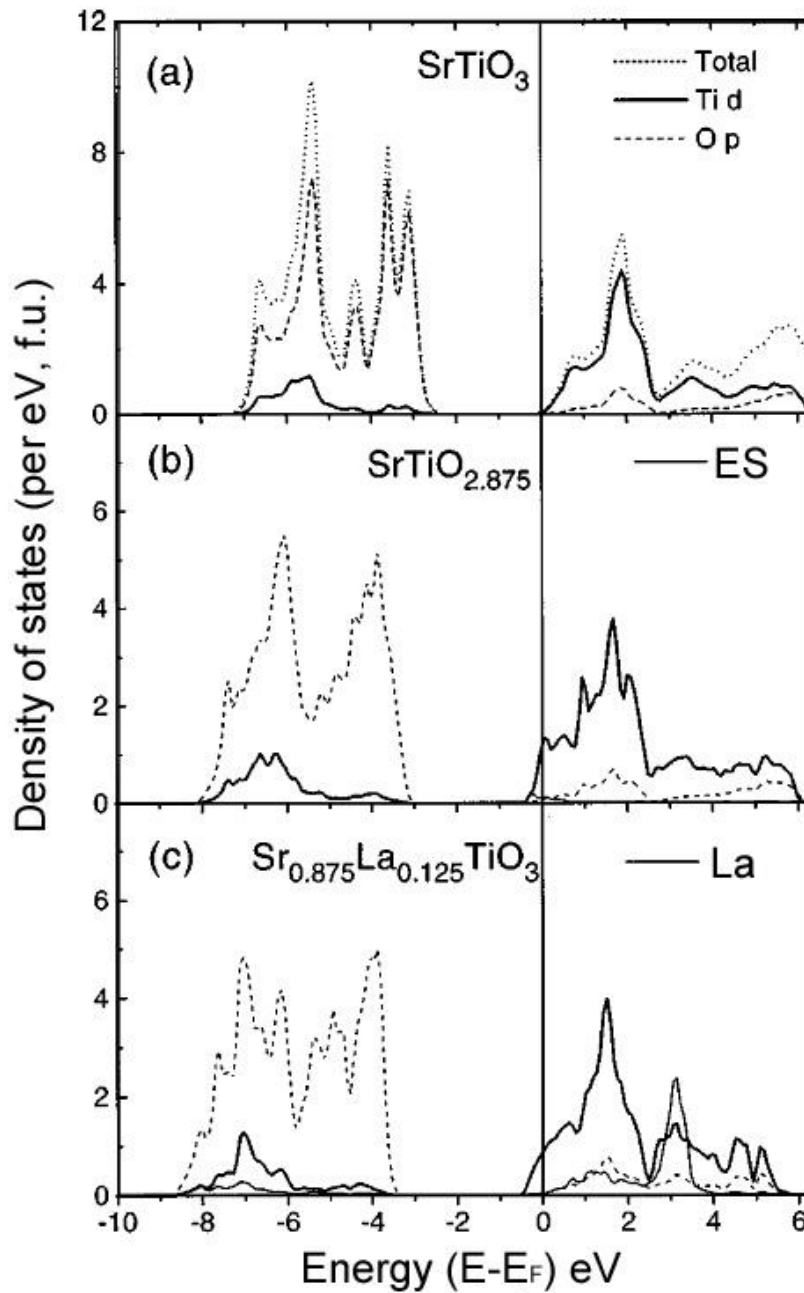


Figure 2-14 (a) Total density of states (DOS), Partial DOS (PDOS) of Ti *d* and O *p* in SrTiO₃. (b) PDOS of Ti *d*, O *p*, and empty sphere (ES) in SrTiO_{2.875}. (c) PDOS of Ti *d*, O *p*, and La in Sr_{0.875}La_{0.125}TiO₃. [98]

Extra electrons can be doped into SrTiO₃ by introducing oxygen vacancies or dopants. Two electrons are generated by each oxygen vacancy (SrTiO_{3-δ}), while one extra electron is generated by substituting Sr²⁺ with La³⁺. With the addition of extra electrons, the Fermi level shifts into the conduction band progressively (Figure 2-14b and c). Therefore, the electron-doped SrTiO₃ exhibits metallic conduction. The

conduction band of La-doped SrTiO_3 can be described by the rigid-band model; however, it becomes different in oxygen deficient SrTiO_3 . The rigid-band model is applicable for the small concentration of oxygen vacancies (Figure 2-14b). If the concentration of oxygen vacancies is large, i.e., $\delta \geq 0.25$, a localized midgap forms at the bottom of the conduction band due to the vacancy clusters [98]. It indicates that the number of electrons contributed by each δ could be lower than 2δ .

2.3.3 Defect chemistry of donor doped SrTiO_3

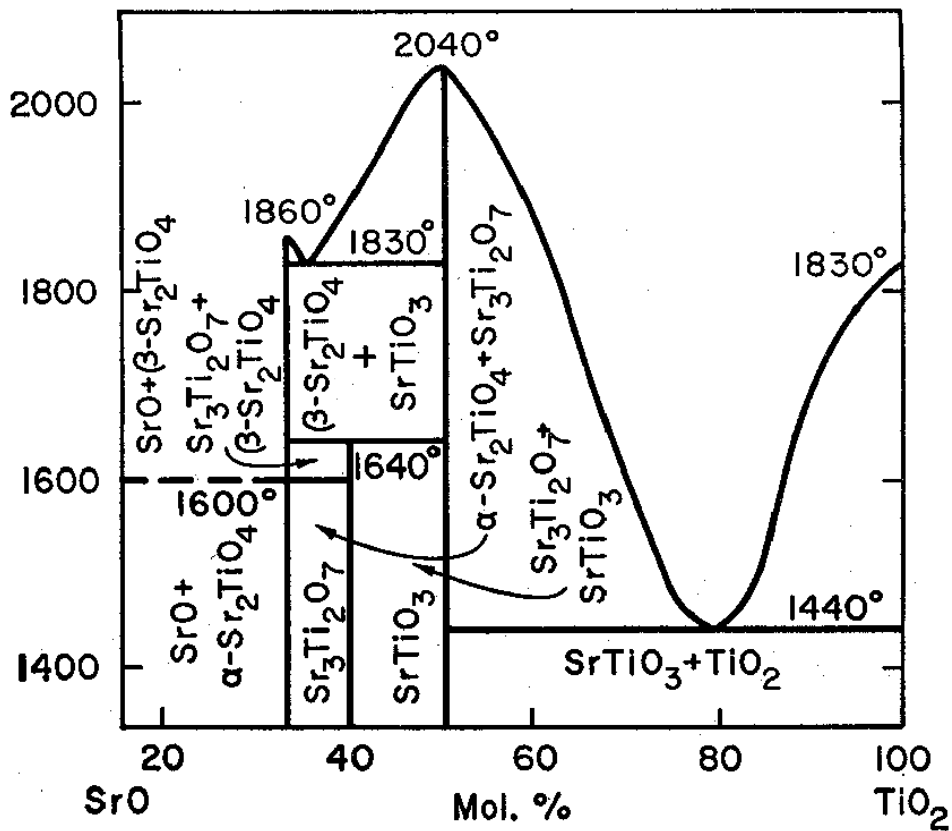
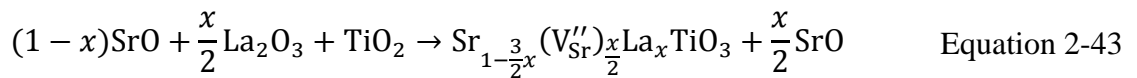


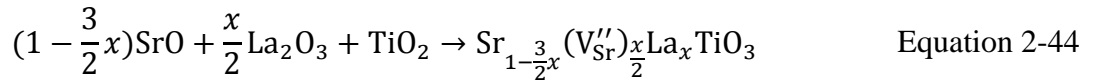
Figure 2-15 Phase diagram of SrO-TiO₂ binary system [102].

According to the phase diagram of SrO-TiO₂ (Figure 2-15), pure SrTiO₃ can only be obtained with the stoichiometric composition. Excess SrO or TiO₂ results in the formation of secondary phases. Although a dispute exists about the solubility of excess SrO or TiO₂ in SrTiO₃, it is generally accepted that the solubility of excess SrO and TiO₂ are less than 0.2 and 0.5 mol%, respectively [103]. Ruddlesden-popper phases appear with the addition of excess SrO, while Rutile or Magnéti phase TiO₂ appears in the TiO₂ excess compositions.

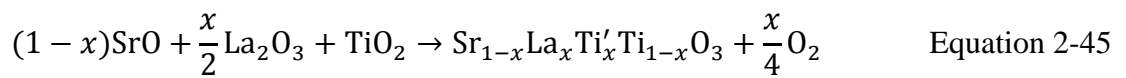
An n-type dopant has more cationic charges than the host cation in SrTiO₃. Common dopants for SrTiO₃ include lanthanide elements for Sr sites [25,104-106], Nb or Ta for Ti sites [24,61,101,107,108], and oxygen vacancies for O sites. Charge neutralization has to be achieved by either the uptake of excess oxygen in an oxidizing atmosphere or the formation of mixed Ti^{3+/4+} couples in a reducing atmosphere. Under oxidizing condition, the excess oxygen could be accommodated into the crystal structure with the formation of Sr vacancies. For example, in a La-doped SrTiO₃ (Sr_{1-x}La_xTiO₃),



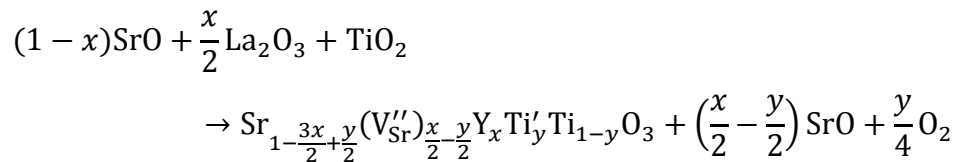
The produced ordered SrO layers together with SrTiO₃ form the RP phases. The starting composition could be adjusted to avoid the formation of RP phases



In a strongly reducing atmosphere, the extra electrons are neutralized by the formation of Ti³⁺ ions,



However, it has been indicated that the completion of reduction is hard even in a strongly reducing atmosphere for the stoichiometric composition [28,109]. The reaction could be written as



Equation 2-46

Therefore, in order to avoid the formation of RP phases in this case, excess TiO_2 has to be added to the starting composition. However, the amount of TiO_2 depends on both the doping concentration and the oxygen deficiency of this material. TiO_2 in its various forms of Magnéli phases could be easily formed under this condition.

2.3.4 Thermoelectric properties of SrTiO_3

Pure SrTiO_3 possesses a wide bandgap and is an insulator. Donor doped SrTiO_3 sintered under a reducing atmosphere exhibits promising thermoelectric properties [25,109-111]. The common dopants for SrTiO_3 are lanthanide ions for Sr^{2+} sites, Nb^{5+} for Ti^{4+} sites, and oxygen vacancies for O^{2-} sites. The oxygen deficiency is sensitive to the sintering conditions, including temperatures, duration, and atmosphere. Therefore, it is hard to compare the thermoelectric properties across different studies due to the difference in the sintering conditions. The electrical conductivity of lanthanide ions doped SrTiO_3 are shown in Figure 2-16a [25]. The electron concentration is contributed by both donors and oxygen vacancies. Due to similarity in electron concentration, the electrical conductivity and the Seebeck coefficient of these materials are almost the same (Figure 2-16a and b).

In contrast, obvious difference in thermal conductivity has been observed with various dopants (Figure 2-16c). Phonon-phonon scattering dominates the thermal conductivity for all the samples. The single-crystalline stoichiometric SrTiO_3 exhibits a high thermal conductivity due to the simplicity in crystal structure and light atomic weight. After introducing dopants, the thermal conductivity of single-crystalline $\text{Sr}_{0.95}\text{La}_{0.05}\text{TiO}_3$ is reduced. It is caused by the reduced phonon mean free path due to lattice defects. The thermal conductivity is further reduced in the polycrystalline samples. The thermal conductivity of $\text{Sr}_{0.9}\text{M}_{0.1}\text{TiO}_3$ decreases with decreasing ionic radii of M ions except Y ions due to its smaller atomic weight than Yb ions. It indicates the strain field scattering is important for the reduction of the thermal conductivity of SrTiO_3 .

Moreover, nanostructuring approaches have been applied to SrTiO_3 . The Seebeck coefficient can be enhanced in the $\text{SrTi}_{0.8}\text{Nb}_{0.2}\text{TiO}_3/\text{SrTiO}_3$ superlattices (-480 $\mu\text{V}/\text{K}$) compared with the value of bulk $\text{SrTi}_{0.8}\text{Nb}_{0.2}\text{TiO}_3$ (-108 $\mu\text{V}/\text{K}$) at 300 K [27]. In addition, the nanocomposites consisting of $\text{Sr}_{0.95}\text{La}_{0.05}\text{TiO}_3$ grains and Nb-doped

$\text{Sr}_{0.95}\text{La}_{0.05}\text{TiO}_3$ grain boundaries show improved Seebeck coefficient due to the energy filtering effect [112]. The thermal conductivity could be reduced in the SrTiO_3 with grain size in nano-range [62,113].

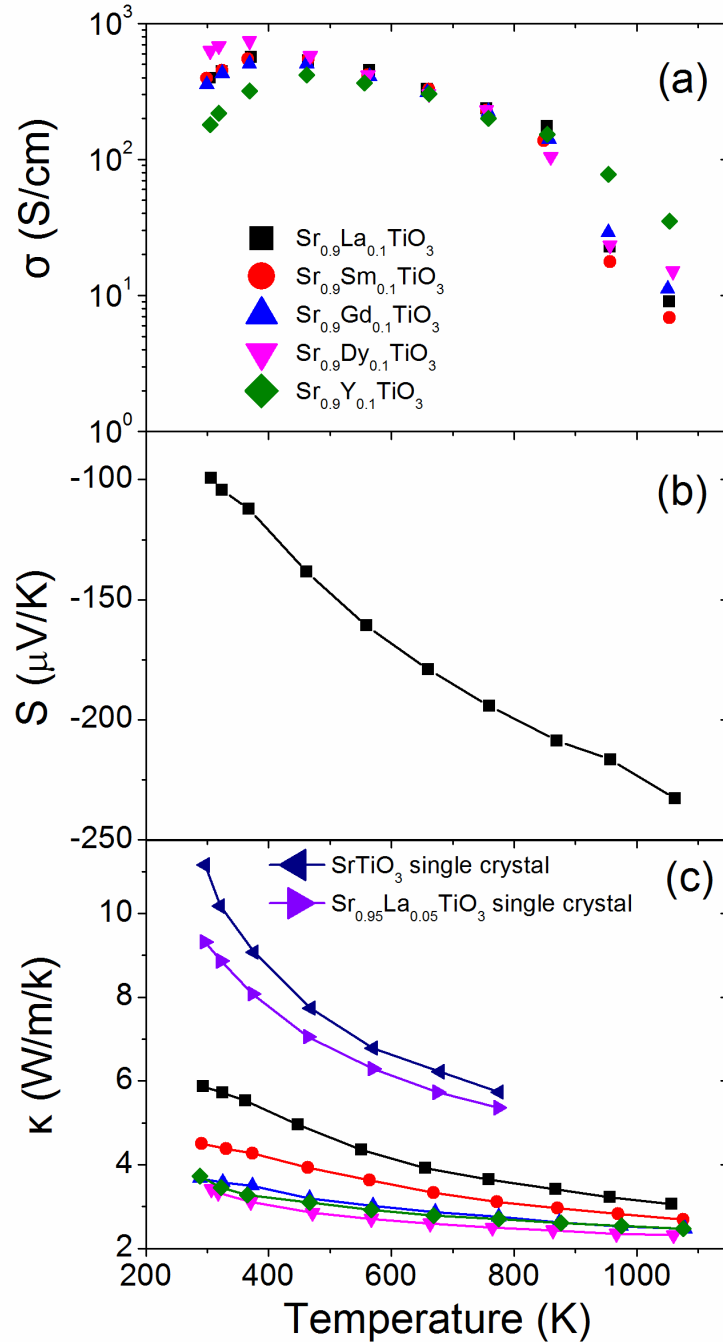


Figure 2-16 Temperature dependence of the (a) electrical conductivity (σ), (b) Seebeck coefficient (S), and (c) thermal conductivity (κ) of polycrystalline $\text{Sr}_{0.9}M_{0.1}\text{TiO}_3$ ($M = \text{La}, \text{Sm}, \text{Gd}, \text{Dy}, \text{Y}$) [25]. Two extra lines in (b) are κ of single-crystalline SrTiO_3 and $\text{Sr}_{0.95}\text{La}_{0.05}\text{TiO}_3$ [110]. Only one curve is present in (b) due to the similarity between different dopants.

Chapter 3 Experimental methods

3.1 Sample preparation

3.1.1 $\text{Na}_{0.77}\text{CoO}_2$

$\text{Na}_{0.77}\text{CoO}_2$ was synthesized by conventional solid-state reaction combined with spark plasma sintering (SPS) technique. The starting materials, Na_2CO_3 (99.8%, Ajax Finechem) and Co_3O_4 (99.7%, Alfa Aesar), were baked in oven at 150 °C for 3 h to eliminate moisture. The powders were mixed according to a molar ratio of Na:Co = 0.77:1. The precursor powders were mixed using parallel ball milling in ethanol with zirconia balls in a glass jar for 12 h at a rotation rate of 90 rpm. The slurry was dried at 120 °C for 3 h followed by hydraulic uniaxial pressing into pellets. The pellets were then directly put into a tube furnace preheated at 800 °C and sintered for 16 h in air. It has been reported that the decarbonation and Na evaporation of Na_2CO_3 and Co_3O_4 mixture occur over the temperature range from 500 to 750 °C [114]. Therefore, a sintering temperature of 800 °C and “rapid heat-up” technique were chosen in order to obtain the single-phase $\text{Na}_{0.77}\text{CoO}_2$ with accurate control of Na content. The sintered pellets were ground into powder, ball milled, and dried. The $\text{Na}_{0.77}\text{CoO}_2$ powder was subsequently consolidated into 20 mm-diameter pellets using spark plasma sintering (Dr. Sinter SPS-825, Syntex, Inc., Japan). All sintering was carried out under a uniaxial pressure of 50 MPa in vacuum. After SPS, the sintered pellets were polished to eliminate the graphite foil. The schematic illustration of the experimental procedure of $\text{Na}_{0.77}\text{CoO}_2$ and SrTiO_3 is shown in Figure 3-1.

3.1.2 SrTiO_3

The donor-doped SrTiO_3 was synthesized by conventional solid-state reaction method. The starting powders included SrCO_3 (99.9%, Sigma Aldrich), TiO_2 (Puriss grade, Sigma Aldrich), Y_2O_3 (99.99%, Sigma Aldrich), La_2O_3 (99.99%, Prochem Inc), and Nb_2O_5 (99.9%, Sigma Aldrich). La_2O_3 was dried in furnace at 900 °C for 2 h before use, while the other powders were all baked in oven at 150 °C for 3 h. The powders were mixed by ball milling in a planetary ball mill machine (Retsch, PM400) at 150 rpm for 6 h in ethanol with zirconia balls. After drying, the powder was calcined at 1300 °C for 6 h in 5% H_2/Ar . The powder was then ground and subjected to ball milling again.

After drying, the powder was compacted into 20 mm pellets with cold pressing machine under a pressure of 200 MPa with the aid of PVA binder. The pellets were annealed at 500 °C for 0.5 h in air to eliminate the binder. Finally, the pellets were sintered at temperatures between 1400 °C and 1600 °C for 5-11 h in 5% H₂/Ar.

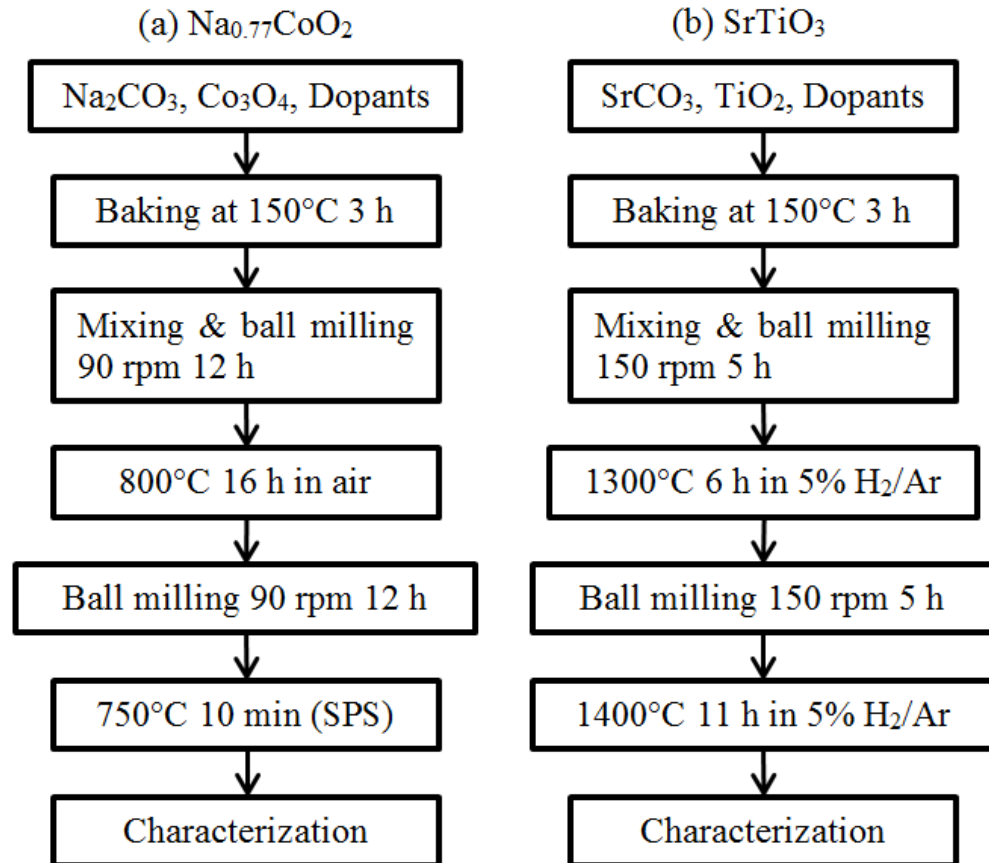


Figure 3-1 Schematic illustration of experimental procedure for (a) Na_{0.77}CoO₂ and (b) SrTiO₃.

3.1.3 Spark plasma sintering

The spark plasma sintering (SPS) system employs the punch/die concept, as shown in Figure 3-2. The powder is placed in the graphite die which is wrapped by the graphite foil. A thermocouple is inserted into the hole at the surface of the die to measure the temperature. During sintering, the punches simultaneously supply pulsed direct current and pressure to the graphite spacers/die/powder. Apart from the Joule heat provided by the pulsed direct current, spark plasma, spark impact pressure, and an electrical field diffusion effect in the gap between the two electrodes are also present during sintering process [115]. It is proposed that the plasma has a cleansing effect on

the surface of the particles and therefore promotes sintering process [116]. Moreover, a local temperature increase could be induced by the plasma, and thus necks are formed around the contact area of the powder particles due to the vaporization and melting of the particles. The heating rate of SPS can approach 1000 °C/min [116]. The use of SPS enables the enhanced densification of powder at a lower temperature and in a shorter duration. The parameters of pulsed direct current and sintering conditions can be adjusted to control the SPS. The most important parameters for SPS include the sintering temperature, dwell time, and pressure. The sintering temperature and time are directly related to the final microstructure and grain size. The pressure-assisted sintering is necessary for the densification of nanopowders due to its ability of rearrangement and destruction of agglomerates. The pulsing and heating rate have little influence on the densification and grain growth of the sintered powder [117].

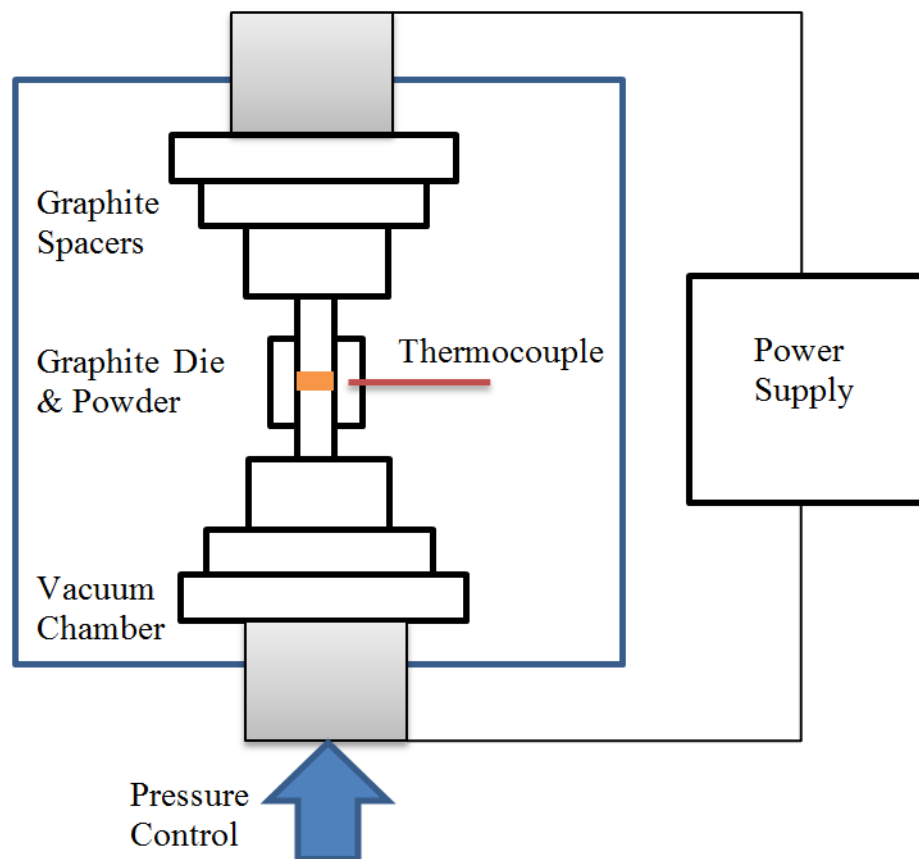


Figure 3-2 Schematic of spark plasma sintering (SPS).

3.2 Structural characterization

3.2.1 X-ray diffraction

Powder X-ray diffraction (XRD) (Panalytical X'pert MPD) was carried out at a voltage of 45 kV and a current of 40 mA, using Cu K α radiation ($\lambda = 1.54 \text{ \AA}$). Powder XRD of Na_{0.77}CoO₂ and SrTiO₃ were collected with a step size of 0.013 ° in a 2θ range from 12 ° to 70 ° and from 20 ° to 130 °, respectively. Besides, the chemical stability of Na_{0.77}CoO₂/Ca₃Co₄O₉ composites was examined by XRD of the pellet samples. The lattice parameters were calculated by Rietveld refinements using PANalytical-HighScore Plus software or Jana 2006 [118]. The refinement parameters included zero shift, lattice parameters, and peak profile. The pseudo-Voigt function was chosen as the peak profile function. The refinement of Na_{0.77}CoO₂ was based on Na_{0.77}CoO₂ with space group P6₃/mmc [71]. The refinement of cubic and tetragonal donor-doped SrTiO₃ was performed using SrTiO₃ with space group Pm $\bar{3}$ m and I4/mcm, respectively [119,120].

3.2.2 Scanning electron microscopy

The microstructure was examined by scanning electron microscopy (SEM) and energy-dispersive X-ray spectroscopy (EDS) with FEI Nova NanoSEM 230 field-emission scanning electron microscope. Prior to SEM, the samples were polished and thermal etched at a temperature lower than the sintering temperature for 0.5 h. The samples were coated with chromium for SEM micrographs and graphite for EDS analysis. The SEM images were obtained under an accelerating voltage of 5 kV using Through the Lens Detector (TLD) detector or under an accelerating voltage of 10 kV using Everhart-Thornley detector. EDS analysis was taken at lower magnifications and higher voltages (10 kV to 15 kV).

3.2.3 Transmission electron microscopy

The TEM images and selected area electron diffraction (SAED) patterns were taken by transmission electron microscopy (TEM) (Phillips CM200) operated at 200 kV. The samples for TEM analysis were prepared by focused ion beam (FIB) (XT Nova Nanolab 200).

3.3 Electrical resistivity and thermopower measurement

Temperature dependence of the electrical resistivity and the Seebeck coefficient were simultaneously measured with a bar sample using the ULVAC-ZEM3 system. The schematic illustration of the measurement is shown in Figure 3-3. The measurement is carried out in a temperature-controlled furnace under a low-pressure helium atmosphere. The bar sample is placed between two Pt electrodes. The electrical resistivity is measured by the direct current four-point method. The thermocouples are pressed against the side of the sample. The voltage drop dV between two contact points with a distance L is therefore measured by the two thermocouples. A constant current I is supplied to the Pt electrodes from the upper one to the lower one and vice versa in order to cancel out the thermo-electromotive force. The electrical resistivity (ρ) is calculated by

$$\rho = \frac{1}{\sigma} = \frac{dV A}{I L} \quad \text{Equation 3-1}$$

where A is the cross-sectional area of the sample and σ is the electrical conductivity.

When measuring the Seebeck coefficient, a temperature difference is introduced by heating the bottom end of the sample through the heater inside the lower block. The thermocouples measure the temperatures at the two contact points and the voltage or thermo-electromotive force between the two points. The Seebeck coefficient (S) is expressed as

$$S = \frac{dV}{dT} \quad \text{Equation 3-2}$$

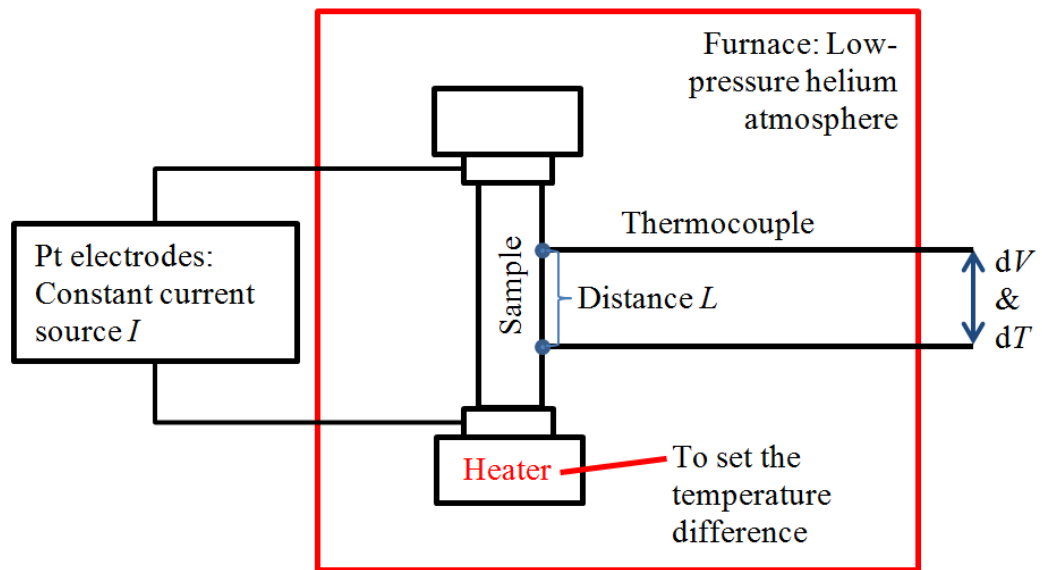


Figure 3-3 Schematic of ULVAC-ZEM3 system.

3.4 Thermal conductivity characterization

Thermal conductivity describes the ability of a material to conduct heat. It is defined as the heat flux density (heat energy flow per unit area per unit time) divided by the temperature gradient. The thermal conductivity can be measured using steady-state and non-steady state techniques. The steady-state measurement is performed when the sample is in complete equilibrium. The steady-state methods include unguarded or guarded hot plate/cylinder, hot wire, heat flow meter, comparative method, and direct heating. However, the steady-state methods have the disadvantages including the complexity of the experimental set-up and the long time required to achieve equilibrium, for example, the guarded hot/plate/cylinder method. Moreover, high uncertainty exists with the heat flow meter and comparative methods. Direct heating is used for materials with high thermal conductivity, e.g., metals. Therefore, non-steady state methods are widely used for the measurement of thermal conductivity due to the straightforward experimental set-up and short measurement duration. Transient hot wire method is useful for thermal conductivity measurement of liquid, foam, gases, and powders. Modified hot wire method can be used to measure solids, whereas the mathematical simulation is insufficient for the calculation.

In our study, the laser flash method has been employed for the determination of thermal conductivity. It is a widely used non-steady state method due to its high

accuracy and capability of measurement of a variety of materials over a broad temperature range. Temperature dependence of the thermal conductivity (κ) is obtained from the product of the temperature dependent density (d), the specific heat capacity (C_p), and the thermal diffusivity (a) as shown in Equation 3-3. Thermal diffusivity (with the unit mm^2/s) measures the speed of heat conduction in a material when the temperature changes with time.

$$\kappa(T) = d(T) \times C_p(T) \times a(T) \quad \text{Equation 3-3}$$

The principles of measurements of temperature dependent density, specific heat capacity, and thermal diffusivity are introduced in 3.4.1, 3.4.2, and 3.4.3, respectively.

3.4.1 Dilatometry

The temperature dependent density $d(T)$ of a specimen is expressed as

$$d(T) = \frac{d_o}{\left(1 + \frac{\Delta L(T)}{L_o}\right)^3} \quad \text{Equation 3-4}$$

where d_o is the density of the specimen at 20 °C, ΔL is the change of the length of the specimen as a function of temperature, and L_o is the original length of the specimen at 20 °C. The linear thermal expansion, $\Delta L(T)/L_o$, was measured by a push rod dilatometry method using NETZSCH DIL402C in this study (Figure 3-4).

Dilatometry is a technique for measurement of thermal expansion or shrinkage of materials as a function of temperature or time by the use of a push rod with a negligible load. During measurement, both the sample (with a dimension of 3 mm × 3 mm × 16 mm) and the push rod are along the central axis of the tube. The sample is clamped between the push rod and the close end of the tube in a controlled atmosphere. The temperature is controlled by the thermocouple near the sample. As the temperature increases, the displacement of the push rod and the sample is transmitted to a linear variable displacement transducer (LVDT). A standard specimen, i.e. Al_2O_3 with the same dimensions as the sample, is used for the correction of the thermal expansion of

the push rod. Furthermore, the coefficient of the linear thermal expansion (α) can be obtained by

$$\alpha = \frac{1}{L_0} \frac{dL}{dT} \quad \text{Equation 3-5}$$

where dL/dT is the temperature derivative of the change in length of the specimen. Apart from the thermal expansion coefficient, the dilatometry could be applied to examine the glass transition temperatures and the change in dimensions caused by sintering or chemical reaction.

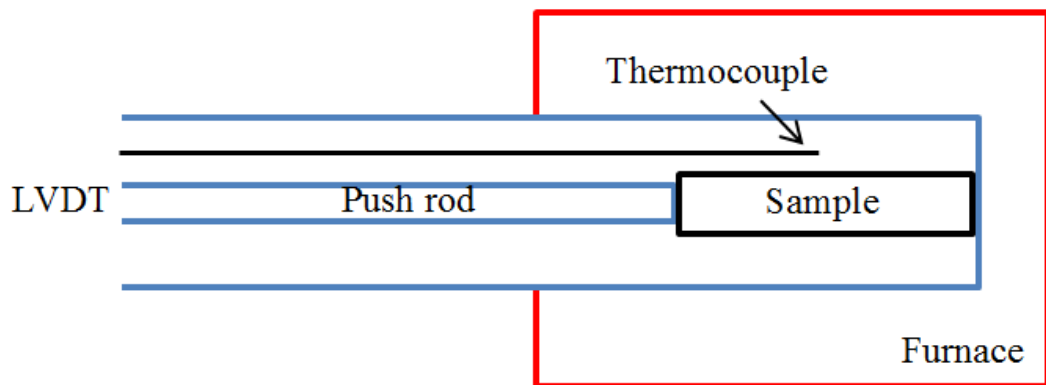


Figure 3-4 Schematic of NETZSCH DIL402C.

3.4.2 Differential scanning calorimetry

The specific heat capacity is measured by heat flux differential scanning calorimetry (DSC) using NETZSCH DSC 404C. DSC can also be used for determination of glass transition, melting, crystallization, and other phase transitions. As shown in Figure 3-5, the sample and reference pans are placed symmetrically in the same atmosphere controlled furnace. Platinum pans are used for measurement in order to achieve high accuracy. Three measurements with the same temperature/time program and atmosphere are required to obtain the specific heat of a specimen. The heating rate used for all measurements was 5 °C/min, and the temperature range was from 30 °C to 750 °C. The measurement of p-type thermoelectric materials like Na_xCoO_2 was carried out under an oxygen atmosphere, while that of donor-doped SrTiO_3 was conducted under Ar. The measurements include measurement of empty pans, calibration sample

(sapphire), and the specimen. During measurement, the furnace exchanges heat with the reference side and the sample side. The temperatures of both sides are measured under the respective pans with respect to time and temperature. The temperature difference between the two sides corresponding to the heat flow rates (DSC signal) is also recorded.

After obtaining the DSC signals of the three measurements, the specific heat of a sample ($C_{p,s}$) can be calculated by

$$C_{p,s} = \frac{m_c}{m_s} \frac{DSC_s - DSC_o}{DSC_c - DSC_o} C_{p,c} \quad \text{Equation 3-6}$$

where m_c and m_s are the respective mass of the calibration sample (sapphire) and sample, DSC_o , DSC_c , and DSC_s are the respective DSC signals of the baseline (empty pans), calibration sample, and the sample, $C_{p,c}$ and $C_{p,s}$ are the respective specific heat of the calibration sample and the sample.

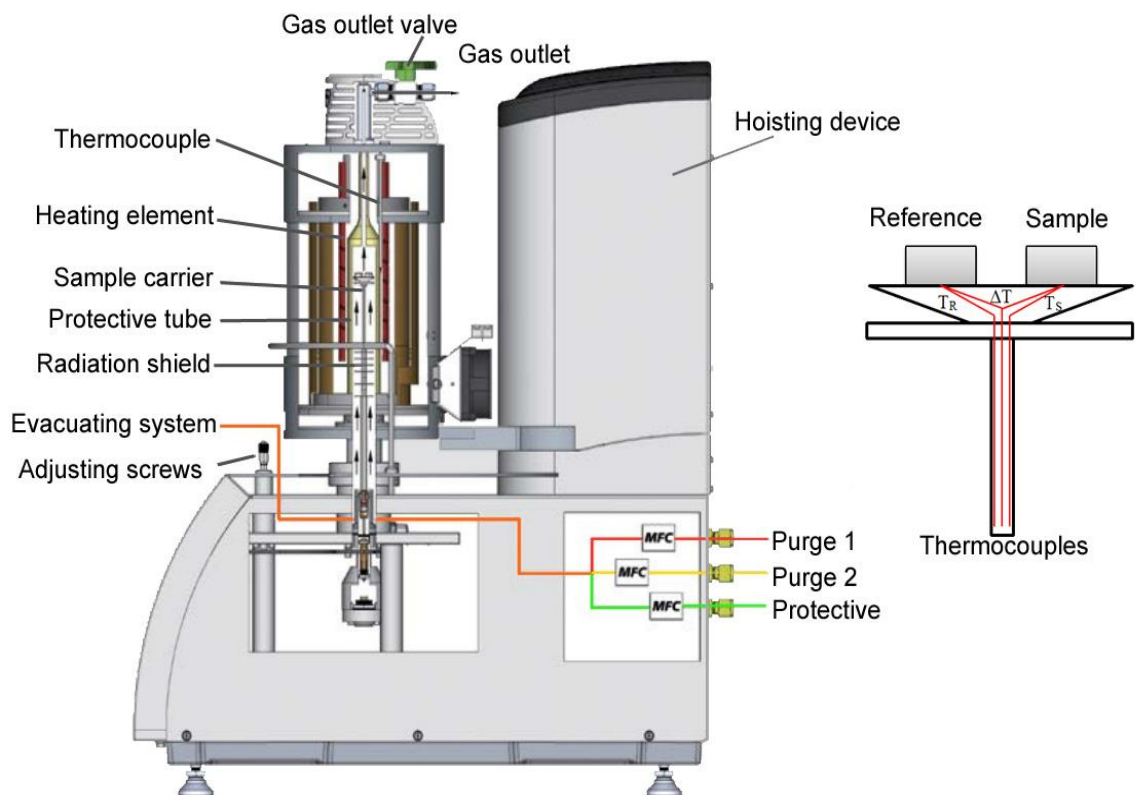


Figure 3-5 Schematic of NETZSCH DSC 404C [121].

3.4.3 Thermal diffusivity measured by laser flash method

The laser flash method is intensively used for the measurement of thermal diffusivity. In this study, NETZSCH LFA427 was applied for the measurement. The schematic of the experiment set-up is shown in Figure 3-6. The square sample with a dimension of 10 mm × 10 mm × 3 mm is placed on the top of the sample carrier inside a furnace. The sample is coated with graphite to improve the absorption and emissivity. The temperature of the sample is measured by the thermocouple at the same height. After stabilizing at a measurement temperature, the pulsed laser irradiates the bottom of the sample. The heat is conducted to the top of the sample, and the temperature rise is detected by the infrared (IR) sensor as a function of time. The thermal diffusivity is then calculated by a mathematical model. In this study, the Cape-Lehmen and pulse correction were employed for the calculation. If the heat is conducted in one direction under adiabatic condition, the thermal diffusivity (a) is determined by

$$a = 0.1388 \frac{l^2}{t_{0.5}} \quad \text{Equation 3-7}$$

where l is the thickness of the sample, $t_{0.5}$ is the time to the half of the maximum of the temperature rise.

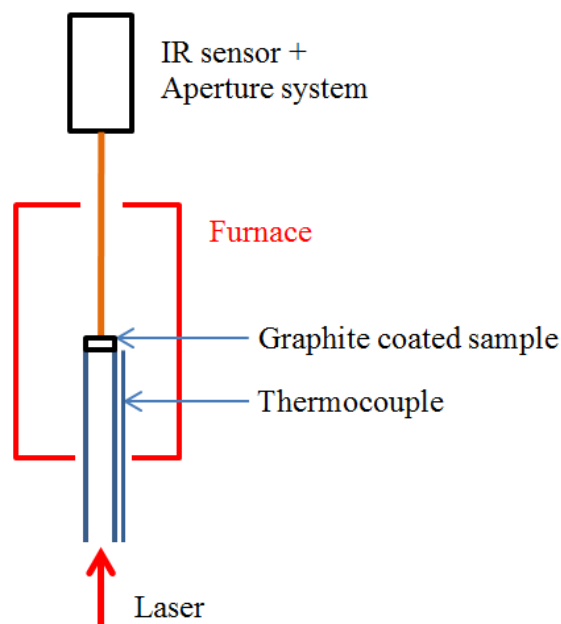


Figure 3-6 Schematic of NETZSCH LFA427.

3.5 Thermogravimetric analysis

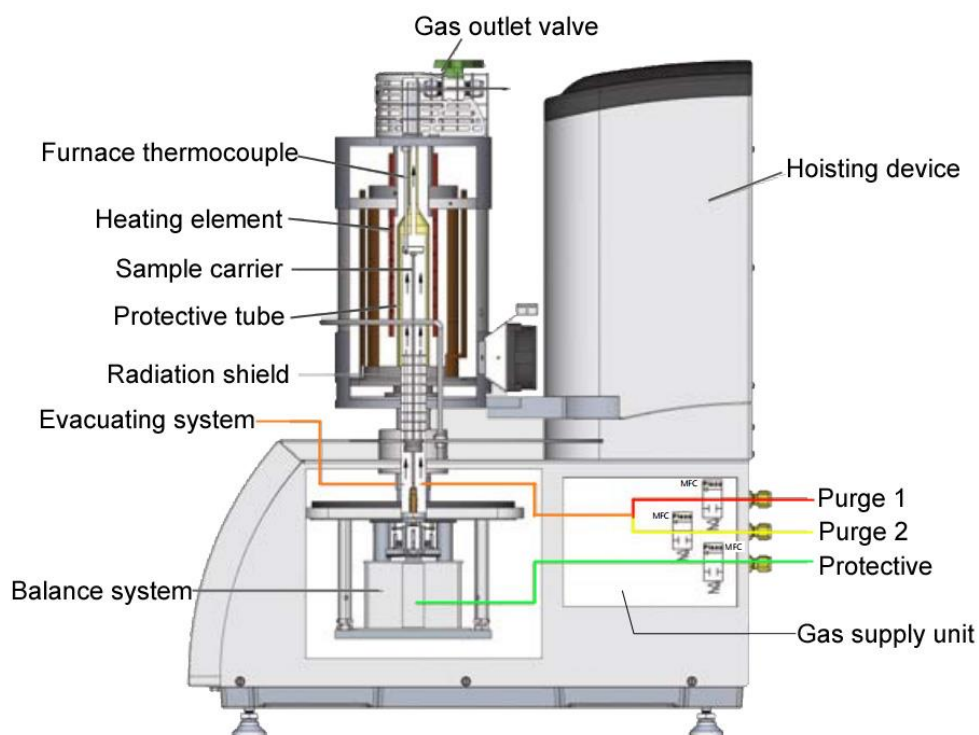


Figure 3-7 Schematic of NETZSCH STA 449 [122].

Thermogravimetric analysis (TGA) is a method in which the mass of a material is measured as a function of temperature or time in a controlled atmosphere. It is widely used to determine the mass gain or loss due to decomposition reactions, reactions with atmospheric gases, second-order phase transitions, or Curie temperatures of magnetic transitions. To imply the basic function, a TGA requires a sample pan supported by a thermocouple and precision balance, and a programmable furnace. The mass gain or loss during experiment is recorded as a function of time and temperature.

NETZSCH STA 449 (Figure 3-7) was employed to carry out the TGA. The weight increase of donor-doped SrTiO_3 was determined at elevated temperatures in flowing oxygen (50 ml/min). The powder sample was heated from 40 °C to 1000 °C at a heating rate of 5 °C/min and kept at 1000 °C for 20 h until equilibrium was reached. The oxygen deficiency of $\text{SrTiO}_{3-\delta}$ was determined by Equation 3-8.

$$\delta = \frac{\Delta m / A_o}{m_{ox} / A_{STO}} \quad \text{Equation 3-8}$$

where δ is the oxygen deficiency per formula unit, m_{ox} is the weight of the oxidized sample after annealing, Δm is the weight gain after annealing the sample in oxygen, A_o is the atomic weight of oxygen, and A_{STO} is the atomic weight of the SrTiO₃. NETZSCH STA 449 can also be used for simultaneous TG/DSC by changing the sample carrier.

Chapter 4 Thermoelectric properties of $\text{Na}_{0.8}\text{Co}_{1-x}\text{Fe}_x\text{O}_2$ prepared by spark plasma sintering

4.1 Introduction

Na_xCoO_2 is a promising p-type thermoelectric material due to its high Seebeck coefficient and low electrical resistivity [12]. A figure-of-merit (ZT) ~ 1 at 527 °C has been achieved for Na_xCoO_2 single crystals [13]. Na_xCoO_2 has a layered crystal structure with alternating stacks of Na ions and two-dimensional CoO_2 . A CoO_2 layer is a network of edge-sharing CoO_6 octahedra and a conduction path for holes. The electron transport properties of Na_xCoO_2 are determined by the $\text{Co}^{3+}/\text{Co}^{4+}$ ratio [123]. The $\text{Co}^{3+}/\text{Co}^{4+}$ ratio could be altered by varying Na content or by substituting Co with other transition metal ions. The electrical properties could be adjusted by doping transition metal ions to the Co sites of the CoO_2 layers. For example, Cu substituted $\text{Na}_{0.5}\text{CoO}_2$ shows enhanced coupling between the conduction-electron and the magnetic fluctuation [124].

$\text{Ca}_3\text{Co}_4\text{O}_9$ is also a p-type thermoelectric oxide, in which the low thermal conductive layer of $[\text{Ca}_2\text{CoO}_3]$ is sandwiched between the electrically conductive $[\text{CoO}_2]$ layers. Such a complex incommensurate monoclinic misfit structure consists of two subsystems, which share the common lattice parameters of a , c and β with different b . Therefore, it can also be written as $[\text{Ca}_2\text{CoO}_3]_{0.62}[\text{CoO}_2]$. In order to enhance the electrical conductivity and the Seebeck coefficient of $[\text{Ca}_2\text{CoO}_3]_{0.62}[\text{CoO}_2]$, small amount of Fe was strategically introduced into $[\text{CoO}_2]$ layer to improve its electronic conductivity [125,126]. In this case, the chemical formula of the Fe doped $[\text{Ca}_2\text{CoO}_3]_{0.62}[\text{CoO}_2]$ can be rewritten as $[\text{Ca}_2\text{CoO}_3]_{0.62}[\text{Co}_{1-y}\text{Fe}_y\text{O}_2]$. However, the thermoelectric properties deteriorate when higher amount of Fe is doped into $[\text{Ca}_2\text{CoO}_3]_{0.62}[\text{Co}_{1-y}\text{Fe}_y\text{O}_2]$, for the electron conduction path is disturbed and the activation energy is increased [125,127]. Although studies regarding Fe-doped Na_xCoO_2 have been reported, the study about high-temperature thermoelectric properties of Na_xCoO_2 with Fe content lower than 5% has been limited. Considering the similarity in the crystal structure between Na_xCoO_2 and $\text{Ca}_3\text{Co}_4\text{O}_9$, it is intriguing to know whether minor amount of Fe doping has positive effects on the thermoelectric properties of Na_xCoO_2 .

The objective of the study is to investigate the effects of minor amount of Fe doping on the thermoelectric properties of $\text{Na}_{0.8}\text{CoO}_2$. In this work, $\text{Na}_{0.8}\text{Co}_{1-x}\text{Fe}_x\text{O}_2$ ($x = 0, 0.25\%, 0.5\%, 1\%, 3\%$) were prepared by solid-state reaction followed by spark plasma sintering (SPS). Thermoelectric properties of $\text{Na}_{0.8}\text{Co}_{1-x}\text{Fe}_x\text{O}_2$ were investigated. The results showed, with moderate Fe doping, that the electrical resistivity and the Seebeck coefficient were improved, and that the thermal conductivity was reduced. The overall values of ZT were increased in the Fe-doped $\text{Na}_{0.8}\text{CoO}_2$.

4.2 Experimental procedure

$\text{Na}_{0.8}\text{Co}_{1-x}\text{Fe}_x\text{O}_2$ ($x = 0, 0.25\%, 0.5\%, 1\%, 3\%$) was synthesized by conventional solid-state reaction. Stoichiometric amount of Na_2CO_3 (99.8%, Ajax Finechem), Co_3O_4 (99.7%, Alfa Aesar), and Fe_2O_3 (99%, Sigma Aldrich) were mixed in a planetary ball mill machine (Retsch, PM400) at 150 rpm for 6 h in ethanol with zirconia balls. After drying, the mixtures were pelletized and directly put into a tube furnace at 850 °C for 24 h with intermittent grinding. Subsequently, the samples were ground into powder and ball milled at 150 rpm for 5 h in ethanol with zirconia balls. After drying, the powder was subjected to spark plasma sintering at 760 °C under a uniaxial pressure of 50 MPa for 5 min in vacuum. In order to eliminate the graphite, the samples were annealed in air at 800 °C for 2 h. The densities of the samples were measured by the Archimedes' principle. X-ray diffraction (XRD) measurement (Panalytical X'pert X-ray diffractometer) was carried out to determine the crystalline phase of the pellets. Scans were conducted using $\text{Cu } K\alpha$ radiation over the range of $12^\circ \leq 2\theta \leq 90^\circ$.

The sintered pellets had a diameter of 20 mm and thickness ~3 mm. The pellets were cut into a square of 10 mm × 10 mm × 3 mm and a rectangular bar of about 15 mm × 3 mm × 3 mm. The electrical resistivity and the Seebeck coefficient were simultaneously measured with the rectangular bar using the ULVAC-ZEM3 system. Thermal conductivity κ was obtained from the product of the measured density (NETZSCH DIL 402C for the thermal expansion, bar samples), the specific heat capacity (NETZSCH DSC 404C), and the thermal diffusivity (NETZSCH LFA427, square samples). In addition, scanning electron microscopy (SEM) characterization was performed on sintered pellets with Nova NanoSEM 230. Prior to SEM characterization, the cross-sections of the samples were polished and annealed at 700 °C for 15 min.

4.3 Results and discussion

The powder XRD pattern shown in Figure 4-1 verified the formation of pure $\text{Na}_{0.8}\text{CoO}_2$, which was synthesized with solid state reaction in a tube furnace. All pellets sintered by SPS showed the existence of impurity phases as justified by the diffraction peaks at $\sim 14.8^\circ$, 35.1° , and 35.7° . Furthermore, an additional diffraction peak at $2\theta \sim 33.178^\circ$ in the XRD spectra of the sample with $x = 3\%$ prepared by SPS indicates a tiny trace of impurity phase, which may be resulted by the excess Fe in $\text{Na}_{0.8}\text{Co}_{1-x}\text{Fe}_x\text{O}_2$. The lattice parameters remain unchanged after doping Fe due to the similarity of the ionic radii between Fe and Co. The relative density is improved with increasing Fe content.

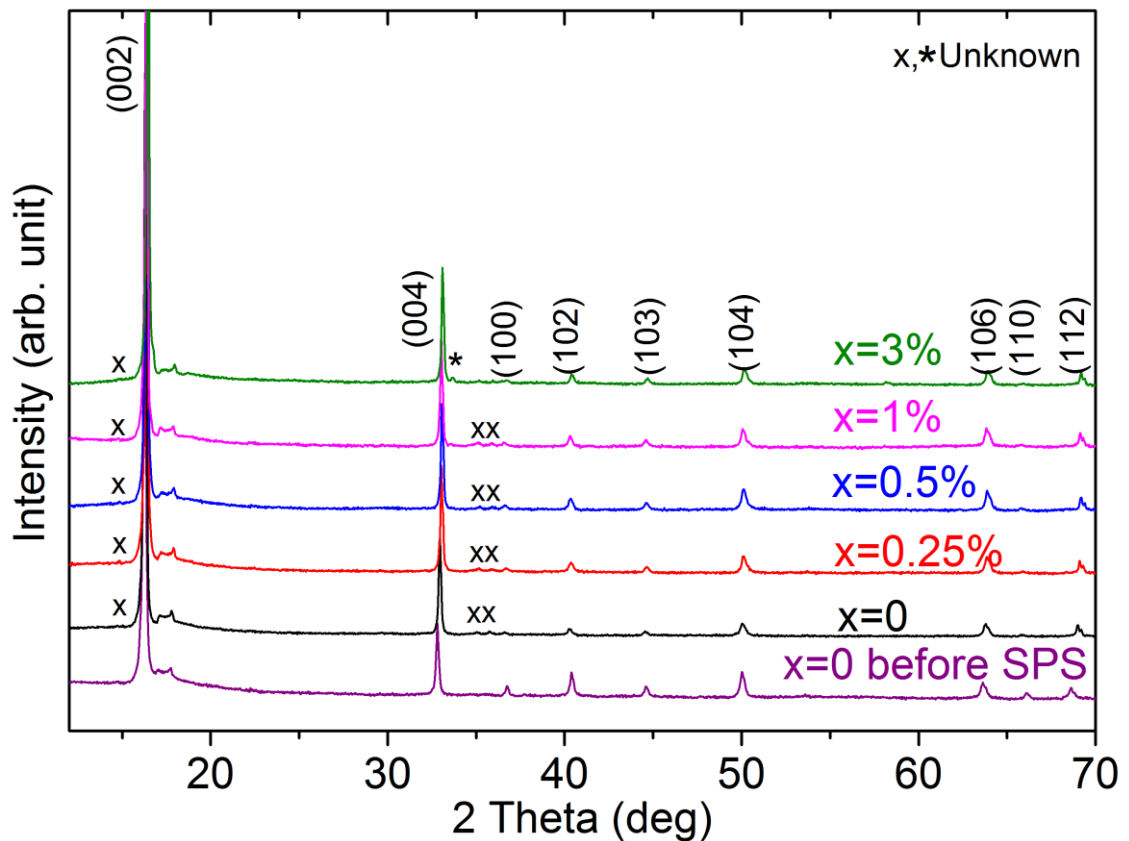


Figure 4-1 XRD patterns of $\text{Na}_{0.8}\text{Co}_{1-x}\text{Fe}_x\text{O}_2$ ($x = 0, 0.25\%, 0.5\%, 1\%, 3\%$). The star (*) and cross (x) indicate unknown peaks.

The SEM micrographs (Figure 4-2) of the cross-sections of the samples confirmed that the samples were almost fully densified. It is also noted that the average grain size was significantly increased with increasing Fe content. However, the mechanism behind it is not clear at this stage. The Scherrer equation which could be

used to calculate the crystallite size is $B(2\theta) = K\lambda / (L \cos\theta)$, where B is peak width, K is a dimensionless shape factor, λ is the X-ray wavelength, L is the crystallite size, and θ is the Bragg angle, respectively. The Scherrer equation is suitable to calculate the size of nanocrystallites using the XRD data. However, the grain sizes in this study are in the range from 1 μm to 10 μm . Hence, the Scherrer equation cannot be used for this study.

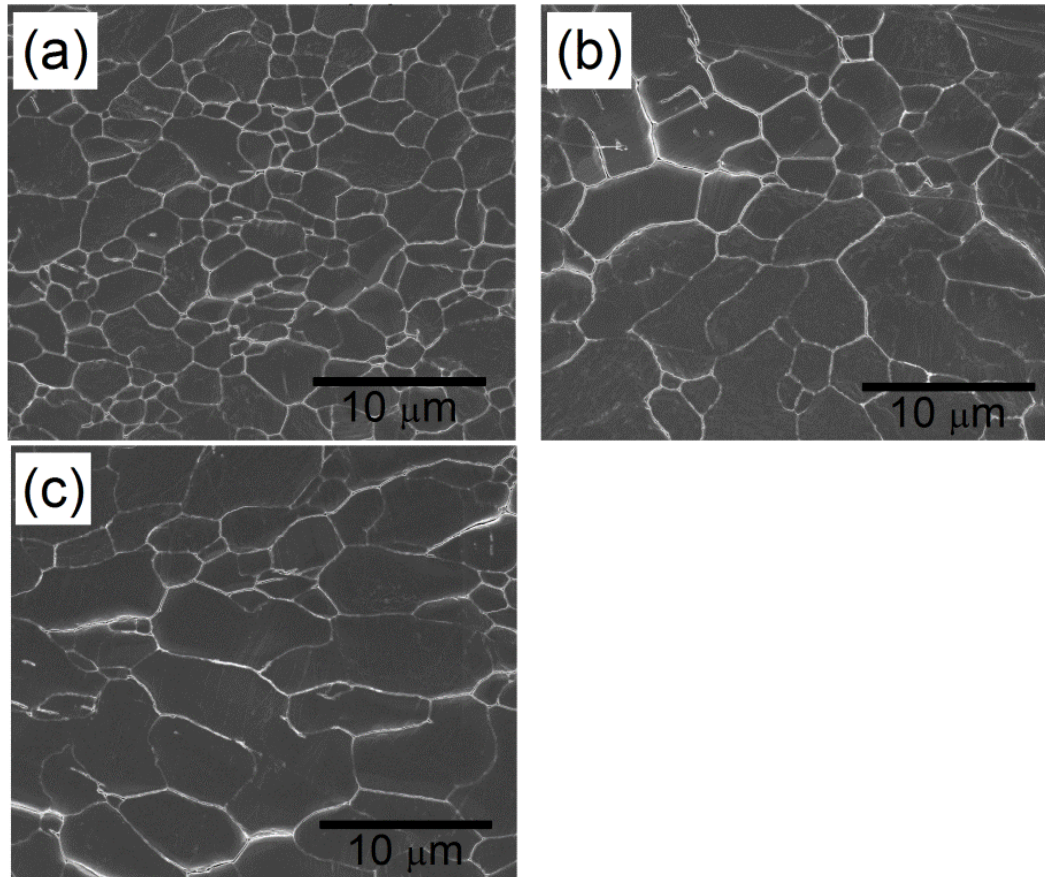


Figure 4-2 SEM micrographs of $\text{Na}_{0.8}\text{Co}_{1-x}\text{Fe}_x\text{O}_2$. (a) $x = 0$, (b) $x = 0.25\%$, and (c) $x = 1\%$.

Figure 4-3a shows the temperature dependence of the electrical resistivity (ρ) of $\text{Na}_{0.8}\text{Co}_{1-x}\text{Fe}_x\text{O}_2$. For all of the samples, ρ increases with increasing temperature, exhibiting metallic conduction. Below 500 $^\circ\text{C}$, ρ increases with increasing Fe content. However, above 500 $^\circ\text{C}$, this relation is reversed and the undoped sample shows the highest ρ .

Figure 4-3b shows the Seebeck coefficient (S) of $\text{Na}_{0.8}\text{Co}_{1-x}\text{Fe}_x\text{O}_2$ versus temperature. The positive S indicates $\text{Na}_{0.8}\text{Co}_{1-x}\text{Fe}_x\text{O}_2$ is a p-type thermoelectric oxide.

In addition, S goes up with increasing temperature. S increases with increasing Fe content until $x = 1\%$, and is slightly decreased in the sample with $x = 3\%$.

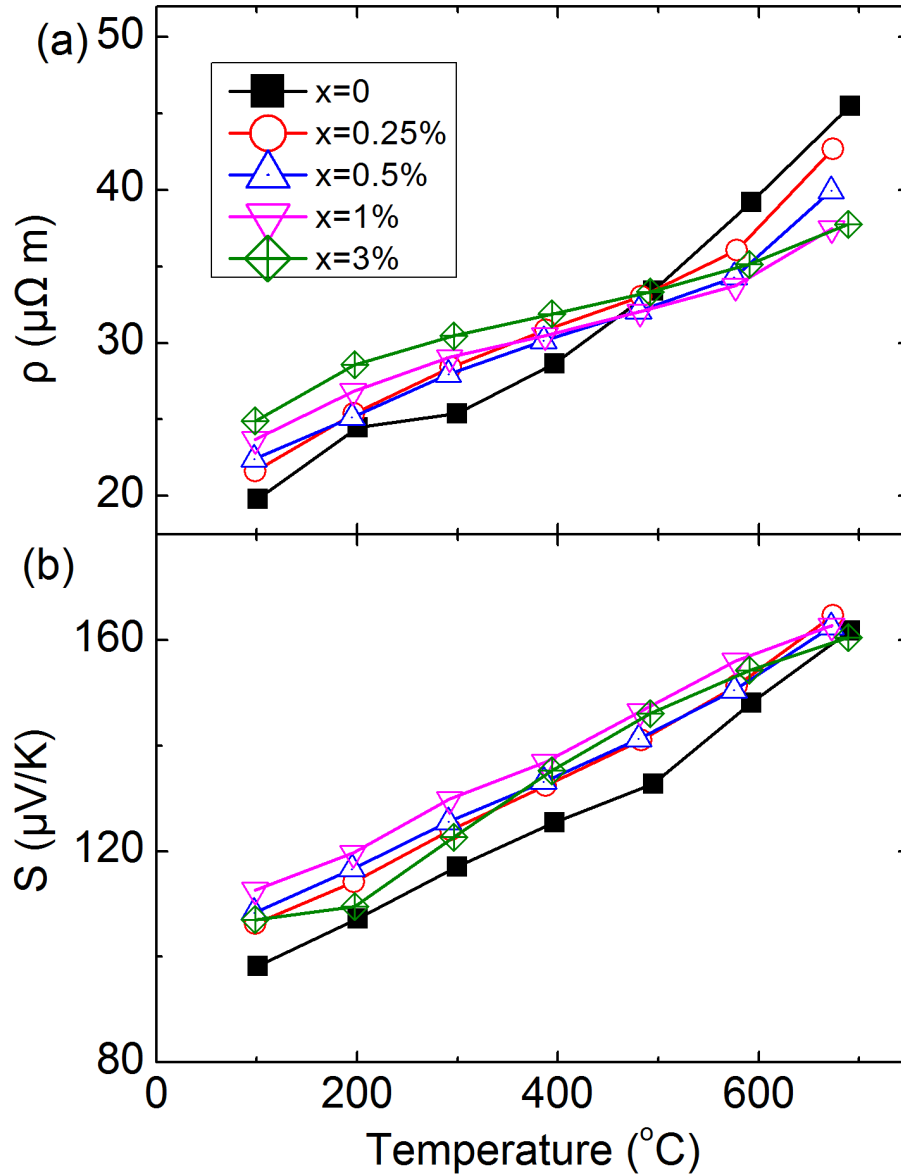


Figure 4-3 Temperature dependence of the (a) electrical resistivity (ρ) and (b) Seebeck coefficient (S) of $\text{Na}_{0.8}\text{Co}_{1-x}\text{Fe}_x\text{O}_2$ ($x = 0, 0.25\%, 0.5\%, 1\%, 3\%$).

Doping Fe into $\text{Na}_{0.8}\text{Co}_{1-x}\text{Fe}_x\text{O}_2$ increases both the electrical resistivity and the Seebeck coefficient. ρ and S for a two-dimensional metal are given by Equation 4-1 and Equation 4-2

$$\rho = \frac{1}{en\mu} = \frac{1}{e^2} \frac{1}{\tau} \frac{m^*}{n} \quad \text{Equation 4-1}$$

$$S = \frac{\pi k_B^2 T}{2e\hbar^2 d_c} \frac{m^*}{n} \quad \text{Equation 4-2}$$

where e is the elemental charge, τ is the average scattering time, m^* is the effective mass, n is the carrier concentration, and d_c is the interlayer spacing. From Equation 4-1 and Equation 4-2, it is speculated that m^*/n goes up with increasing Fe content, that is, an increase in m^* and/or a decrease in n . Moreover, a decrease in τ or an increase in scattering rate may also increase ρ . However, S starts to decrease with Fe doping level $> 1\%$. It is likely that the improvement of m^*/n is suppressed at higher doping level [124].

Above 500 °C, ρ decreases with increasing Fe substitution, which is attributed to the improved relative density of $\text{Na}_{0.8}\text{Co}_{1-x}\text{Fe}_x\text{O}_2$ with increasing x . In this study, the measurement of ρ and S were carried out in a low-pressure helium atmosphere at elevated temperatures. The lattice oxygen of cobaltates could be removed with increased temperature and decreased oxygen partial pressure [70,128-130]. It has been found that Na_xCoO_2 tends to lose oxygen at ~ 500 °C in inert atmosphere [130]. Furthermore, the lattice oxygen is easier to be removed from porous structure under the same condition due to the large surface area that exposes to environment. Consequently, the samples with higher Fe content tend to lose less lattice oxygen due to their higher relative densities. ρ increases with increasing oxygen vacancies, since the hole concentration is reduced by the free electrons introduced by the oxygen vacancies.

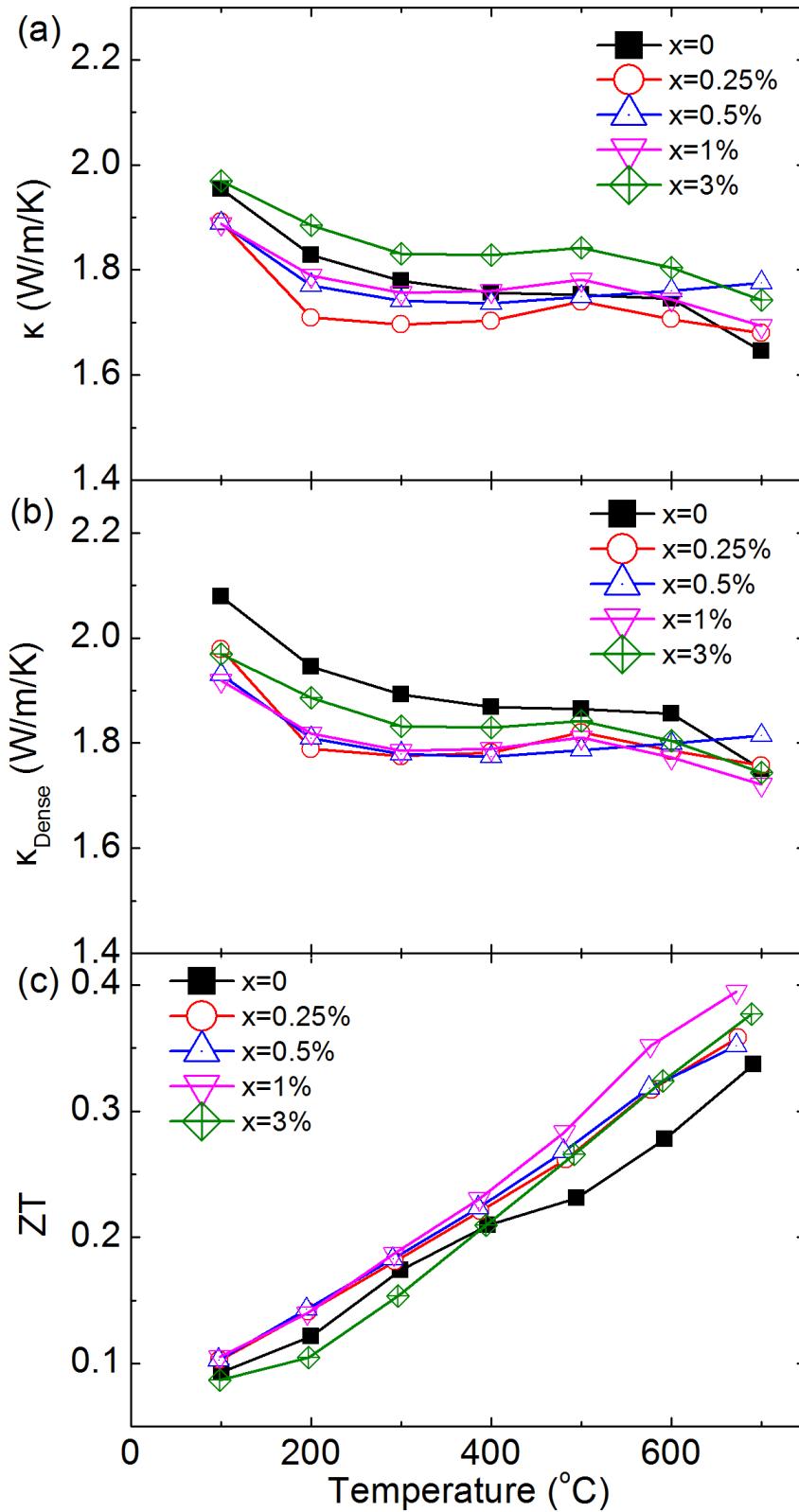


Figure 4-4 Temperature dependence of the (a) measured thermal conductivity (κ), (b) calculated thermal conductivity for dense $\text{Na}_{0.8}\text{Co}_{1-x}\text{Fe}_x\text{O}_2$ (κ_{Dense}), and (c) ZT of $\text{Na}_{0.8}\text{Co}_{1-x}\text{Fe}_x\text{O}_2$ ($x = 0, 0.25\%, 0.5\%, 1\%, 3\%$).

The thermal conductivity (κ) of $\text{Na}_{0.8}\text{Co}_{1-x}\text{Fe}_x\text{O}_2$ versus temperature is plotted in Figure 4-4a. Accounting for the difference in relative density, the thermal conductivity of the fully densified samples are calculated by Equation 4-3 [131]

$$\kappa_{Dense} = \kappa / (1 - \frac{3}{2}\phi) \quad \text{Equation 4-3}$$

where κ_{Dense} is the thermal conductivity of the fully densified sample, κ is the measured thermal conductivity, and Φ is the relative porosity ($\Phi = 1 - \text{Relative density}$). κ_{Dense} versus temperature is shown in Figure 4-4b. κ_{Dense} of the undoped sample is higher than the Fe doped samples. The samples with $0.25\% \leq x \leq 1\%$ exhibit similar κ_{Dense} , while the sample with $x = 3\%$ shows increased κ_{Dense} . This result suggests doping Fe is effective in reducing the thermal conductivity of $\text{Na}_{0.8}\text{CoO}_2$. Substituting Co with Fe is likely to induce disorder in the Na layers and thus increases the phonon scattering. Similar observation has been reported in 5% Fe doped $\text{Na}_{0.5}\text{CoO}_2$ at temperature range of 75 – 300 K [132].

Figure 4-4c illustrates ZT of $\text{Na}_{0.8}\text{Co}_{1-x}\text{Fe}_x\text{O}_2$ as a function of temperature. ZT is calculated from equation $ZT = (S^2T)/(\rho\kappa)$. ZT is increased with increasing temperature. ZT is improved with increasing Fe content until $x = 1\%$ and starts to decrease with $x > 1\%$. The highest ZT ($ZT \sim 0.4$) is achieved at 680 °C with $x = 1\%$.

4.4 Summary

The thermoelectric properties of $\text{Na}_{0.8}\text{CoO}_2$ with moderate Fe doping prepared by solid-state reaction and spark plasma sintering were studied. The resistivity and the Seebeck coefficient of $\text{Na}_{0.8}\text{Co}_{1-x}\text{Fe}_x\text{O}_2$ increased with increasing Fe content. It might be due to an increase in the effective mass and/or a decrease in the carrier concentration induced by Fe doping on the Co sites. The thermal conductivity of $\text{Na}_{0.8}\text{Co}_{1-x}\text{Fe}_x\text{O}_2$ was effectively reduced in the range of $0.25\% \leq x \leq 1\%$. ZT of Fe-doped samples were improved over the un-doped sample. The maximum ZT , ~ 0.40 at 680 °C, was obtained in the $\text{Na}_{0.8}\text{Co}_{1-x}\text{Fe}_x\text{O}_2$ with $x = 1\%$.

Chapter 5 Thermopower and chemical stability of $\text{Na}_{0.77}\text{CoO}_2/\text{Ca}_3\text{Co}_4\text{O}_9$ composites

5.1 Introduction

Composite structures have been widely used to optimize the properties of materials for structural, thermal and electrochemical applications. For example, the micromechanics and mechanical behavior of structural materials can be improved by making ceramic matrix composites, such as SiC enforced Al_2O_3 and Si_3N_4 [133,134]. Moreover, electroceramic composites have been intensively investigated and have been used in a wide range of applications as resistors [135], sensors [136], and transducers [137]. By simply manipulating the mixing ratio and the microstructures, many properties of a two-phase mixture can be tailored. For instance, Ni/ ZrO_2 - Y_2O_3 mixtures exhibit mixed ionic-electronic conduction, depending on the volume ratio of each component [138].

The composite concept has recently been applied to thermoelectric systems, especially in alloy matrix, such as $\text{CoSb}_3/\text{C}_{60}$ [139], $\text{CoSb}_3/\text{ZrO}_2$ [140], and $\text{Yb}_x\text{Co}_4\text{Sb}_{12}/\text{Yb}_2\text{O}_3$ [141]. It has been found that both charge carrier scattering and phonon scattering are increased by incorporating ZrO_2 or Yb_2O_3 into the host materials, leading to the reduction of both electrical and thermal conductivity. On the other hand, the Seebeck coefficient can be enhanced by the carrier filtering effect caused by the interfacial energy barrier in nanocomposites or even bulk polycrystalline composite systems [142]. Furthermore, the Cu/Bi/Ni composites, which consist of the materials with extremely different thermal conductivities, have demonstrated enhancement of the Seebeck coefficient [143].

Na_xCoO_2 and $\text{Ca}_3\text{Co}_4\text{O}_9$ are p-type layered cobaltate thermoelectric materials with promising figure-of-merit (ZT) values, e.g. $ZT \sim 1$ at 527 °C for Na_xCoO_2 single crystals [13] and $ZT \sim 0.87$ at 700 °C for $\text{Ca}_3\text{Co}_4\text{O}_9$ single crystals [83]. The crystal structures of the two materials are similar and both contain CoO_2 planes. To the best of our knowledge, no systematic research has yet been carried out on the transport properties of bulk $\text{Na}_x\text{CoO}_2/\text{Ca}_3\text{Co}_4\text{O}_9$ composites. In the present work, $\text{Na}_{0.77}\text{CoO}_2/\text{Ca}_3\text{Co}_4\text{O}_9$ composites were fabricated by spark plasma sintering (SPS). The

effects of sintering temperature, dwell time, and composition on the structural and thermoelectric properties of these composites were investigated.

Although Na_xCoO_2 possesses superior thermoelectric performance to other oxide-based materials, its application has been limited caused by the degradation due to the existence of moisture in air. It decomposes into the insulating $\text{Co}(\text{OH})_2$ and/or CoCO_3 by absorbing moisture and/or CO_2 from the ambient environment [15]. Upon heating, both $\text{Co}(\text{OH})_2$ and CoCO_3 decompose further into insulating Co_3O_4 and CoO [16]. Therefore, it is important to explore the chemical stability of Na_xCoO_2 by using the “composite effect”, i.e., adding certain amount of $\text{Ca}_3\text{Co}_4\text{O}_9$. In this study, we demonstrated the improved chemical stability of Na_xCoO_2 by adding up to a 30 vol.% fraction of $\text{Ca}_3\text{Co}_4\text{O}_9$ without impairing its thermoelectric properties.

5.2 Experimental procedure

Both $\text{Na}_{0.77}\text{CoO}_2$ and $\text{Ca}_3\text{Co}_4\text{O}_9$ powder were synthesized by conventional solid-state reaction method. The starting materials for $\text{Na}_{0.77}\text{CoO}_2$ were Na_2CO_3 (99.8%, Ajax Finechem) and Co_3O_4 (99.7%, Alfa Aesar), at a molar ratio of 0.77:1 (Na:Co). The precursors were mixed by parallel ball milling in ethanol using zirconia balls in a glass jar for 12 h at a rotation rate of 90 rpm. The slurry was dried at 120 °C for 3 h, followed by hydraulic uniaxial pressing into pellets. The pellets were then put directly into a tube furnace preheated at 800 °C and sintered for 16 h in air. $\text{Ca}_3\text{Co}_4\text{O}_9$ was similarly prepared from CaCO_3 (99.0%, Sigma-Aldrich) and Co_3O_4 (99.7%, Alfa Aesar). The precursors were mixed and ball milled in ethanol with zirconia balls for 12 h. After drying the slurry, the mixture was calcined at 900 °C for 40 h in air with intermittent regrinding. X-ray diffraction (XRD) (Panalytical X’pert MPD) was carried out on the sintered powders of $\text{Na}_{0.77}\text{CoO}_2$ and $\text{Ca}_3\text{Co}_4\text{O}_9$. They were verified as the individual pure phases without any impurity.

Subsequently, different ratios of $(1-x)\text{Na}_{0.77}\text{CoO}_2$ and $x\text{Ca}_3\text{Co}_4\text{O}_9$ powders were mixed (volume ratio $x = 0, 0.3, 0.5, 0.7, 1$), again by ball milling. The powders were then consolidated into 20 mm diameter pellets using the SPS technique. All sintering was carried out under a uniaxial pressure of 50 MPa in vacuum. For the composition with $x = 0.5$, two parameters of SPS were studied: sintering temperature (500, 600, 700 °C), and dwell time (10, 30, 60 min). From our preliminary results, a sintering

temperature of 700 °C and a dwell time of 10 min were chosen to sinter the $(1-x)\text{Na}_{0.77}\text{CoO}_2/x\text{Ca}_3\text{Co}_4\text{O}_9$ powders. The phase formation of the as-sintered materials was characterized by XRD analysis of powders from ground pellets. Rietveld refinements were performed on the $0.5\text{Na}_{0.77}\text{CoO}_2/0.5\text{Ca}_3\text{Co}_4\text{O}_9$ samples using Jana 2006 [118]. The lattice parameters of $\text{Na}_{0.77}\text{CoO}_2$ within the $0.5\text{Na}_{0.77}\text{CoO}_2/0.5\text{Ca}_3\text{Co}_4\text{O}_9$ samples were thus estimated from the Rietveld refinement (space group $P6_3/mmc$). For a reference, the composite with a nominal composition of $0.5\text{Na}_{0.77}\text{CoO}_2/0.5\text{Ca}_3\text{Co}_4\text{O}_9$ was also prepared by pressureless sintering. The sample was cold pressed under 160 MPa followed by conventional sintering (CS) at 700 °C for 12 h in air. To evaluate the chemical stability, $\text{Na}_{0.77}\text{CoO}_2$ and $0.7\text{Na}_{0.77}\text{CoO}_2/0.3\text{Ca}_3\text{Co}_4\text{O}_9$ pellets were put in ambient atmosphere for 14 days. XRD was applied to characterize the samples during the stability testing.

The bulk densities of the as-prepared materials with a diameter of ~20 mm and thickness of ~3 mm were evaluated with Archimedes' principle. Theoretical densities of $\text{Na}_{0.77}\text{CoO}_2$ and $\text{Ca}_3\text{Co}_4\text{O}_9$ were 4.61 g/cm³ from JCPDS 30-1182 and 4.68 g/cm³ [17], respectively. The $\text{Na}_{0.77}\text{CoO}_2/\text{Ca}_3\text{Co}_4\text{O}_9$ composites can be viewed as binary oxide mixtures, since no inter-diffusion was evidenced from the XRD analysis and Rietveld refinements. Therefore the theoretical densities of $(1-x)\text{Na}_{0.77}\text{CoO}_2/x\text{Ca}_3\text{Co}_4\text{O}_9$ composites were given by the sum of the products of the theoretical densities of each phase and their respective volume fractions. Each pellet was cut into a square of 10 mm × 10 mm × 3 mm and a rectangular bar of about 15 mm × 3 mm × 3 mm. Electrical resistivity ρ and Seebeck coefficient S were simultaneously measured with the bar samples using the ULVAC-ZEM3 system. Thermal conductivity κ was obtained from the product of the measured density (NETZSCH DIL402C for the thermal expansion, bar samples), the specific heat capacity (NETZSCH DSC 404C), and the thermal diffusivity (NETZSCH LFA427, square samples). In addition, scanning electron microscopy (SEM) characterization was performed on $\text{Na}_{0.77}\text{CoO}_2$, $0.5\text{Na}_{0.77}\text{CoO}_2/0.5\text{Ca}_3\text{Co}_4\text{O}_9$, and $\text{Ca}_3\text{Co}_4\text{O}_9$ sintered by SPS at 700 °C for 10 min with an FEI Nova NanoSEM 230 field-emission scanning electron microscope.

5.3 Results and discussion

5.3.1 Phase and Structural characterization

Table 5-1 shows the relative densities of $0.5\text{Na}_{0.77}\text{CoO}_2/0.5\text{Ca}_3\text{Co}_4\text{O}_9$ and the lattice parameters of $\text{Na}_{0.77}\text{CoO}_2$ within the composites sintered by SPS at various temperatures and durations. The relative density of the samples was improved by increasing the sintering temperature and the dwell time. All composites sintered by SPS at $700\text{ }^\circ\text{C}$ exhibited $> 92\%$ of the theoretical density, and nearly full densification was achieved by extending the sintering duration. In these $0.5\text{Na}_{0.77}\text{CoO}_2/0.5\text{Ca}_3\text{Co}_4\text{O}_9$ composites, the lattice parameters of $\text{Na}_{0.77}\text{CoO}_2$ remains similar by changing the SPS sintering parameters, implying limited reaction between $\text{Na}_{0.77}\text{CoO}_2$ and $\text{Ca}_3\text{Co}_4\text{O}_9$ during the sintering.

Table 5-1 Sintering methods and parameters, relative densities, lattice parameters of $\text{Na}_{0.77}\text{CoO}_2$, and goodness of fit (GOF) of $0.5\text{Na}_{0.77}\text{CoO}_2/0.5\text{Ca}_3\text{Co}_4\text{O}_9$.

Sintering method	Sintering temperature ($^\circ\text{C}$)	Dwell time (min)	Relative density	a of $\text{Na}_{0.77}\text{CoO}_2$ (\AA)	c of $\text{Na}_{0.77}\text{CoO}_2$ (\AA)	GOF
SPS	500	10	0.79	2.8239(3)	10.893(3)	2.62
	600	10	0.83	2.8263(5)	10.896(1)	2.48
	700	10	0.95	2.8267(8)	10.884(4)	2.13
	700	30	0.97	2.8271(5)	10.890(3)	2.15
	700	60	0.99	2.8276(4)	10.889(3)	2.60

Single-phase $\text{Na}_{0.77}\text{CoO}_2$ and $\text{Ca}_3\text{Co}_4\text{O}_9$ were successfully fabricated with solid-state reaction as shown in Figure 5-1. $(1-x)\text{Na}_{0.77}\text{CoO}_2$ and $x\text{Ca}_3\text{Co}_4\text{O}_9$ powders were mixed by low-energy parallel ball milling with different volume ratios of $x = 0, 0.3, 0.5, 0.7,$ and 1 . The XRD pattern of the mixture with $x = 0.5$ is shown in Figure 5-1, in which the peaks can be assigned to $\text{Na}_{0.77}\text{CoO}_2$ and $\text{Ca}_3\text{Co}_4\text{O}_9$, respectively. The subsequent SPS processes have very limited influence on the structure of the $0.5\text{Na}_{0.77}\text{CoO}_2/0.5\text{Ca}_3\text{Co}_4\text{O}_9$ composites. This has been demonstrated by the minimal change of the XRD spectra for the SPS processed samples.

However, an additional peak at $2\theta \sim 16.4^\circ$ appeared in the XRD patterns of $0.5\text{Na}_{0.77}\text{CoO}_2/0.5\text{Ca}_3\text{Co}_4\text{O}_9$ sintered by SPS at $700\text{ }^\circ\text{C}$, as shown in Figure 5-1. It has been reported that this additional peak is found in XRD patterns of Na_xCoO_2 with lower x values due to the volatility of sodium [144]. The SPS temperature was controlled by a

thermocouple which was inserted into the graphite die. The temperature of the powder compact was higher than that measured by the thermocouple in the case of conducting powder [145]. Therefore, the peak was not present in the samples sintered by SPS at lower temperatures (i.e. 500, 600 °C) and by the CS method at 700 °C. However, it is very difficult to achieve a relative density of more than 70% using the CS method. Therefore, the main advantage of using the SPS technique in this research was to improve the relative density of the composites, thus enhancing both the mechanical and electrical properties of the materials.

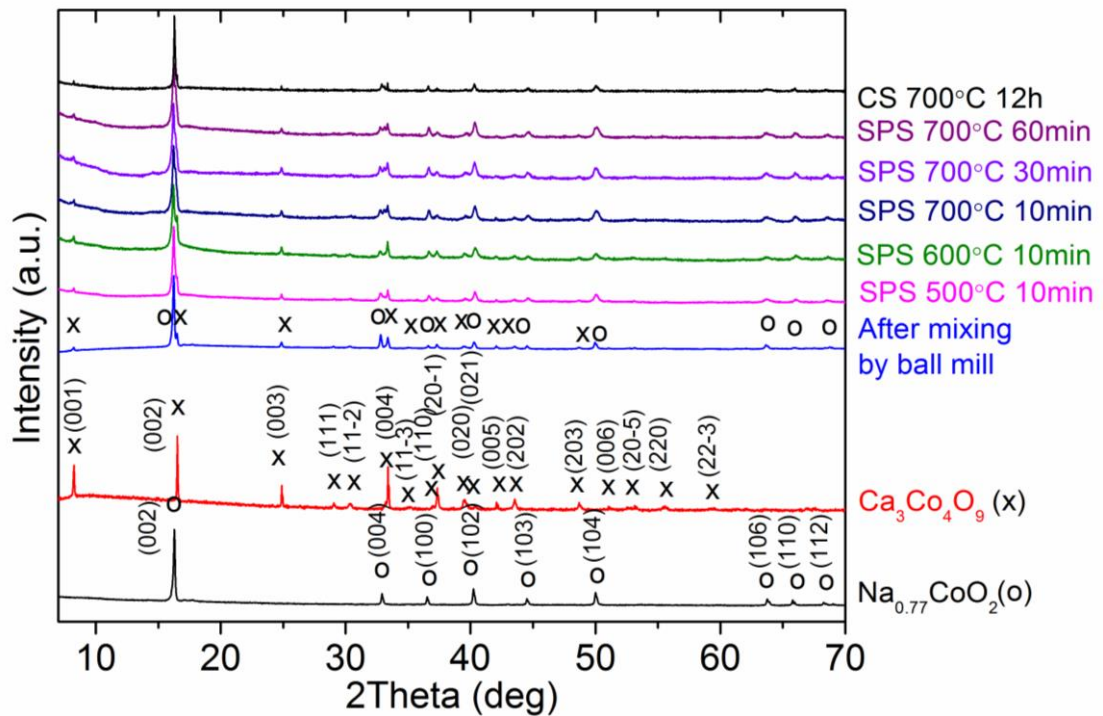


Figure 5-1 XRD patterns of Na_{0.77}CoO₂ and Ca₃Co₄O₉ after solid-state reaction, the mixture of 0.5Na_{0.77}CoO₂/0.5Ca₃Co₄O₉ after mixing by ball milling, 0.5Na_{0.77}CoO₂/0.5Ca₃Co₄O₉ sintered by SPS at various temperatures for different durations, 0.5Na_{0.77}CoO₂/0.5Ca₃Co₄O₉ sintered by the CS method at 700 °C for 12 h in air.

The XRD patterns of (1-x)Na_{0.77}CoO₂/xCa₃Co₄O₉ with various x processed by SPS are shown in Figure 5-2. Since Na_{0.77}CoO₂ and Ca₃Co₄O₉ share similar crystal structure, the XRD patterns are very difficult to be separated.

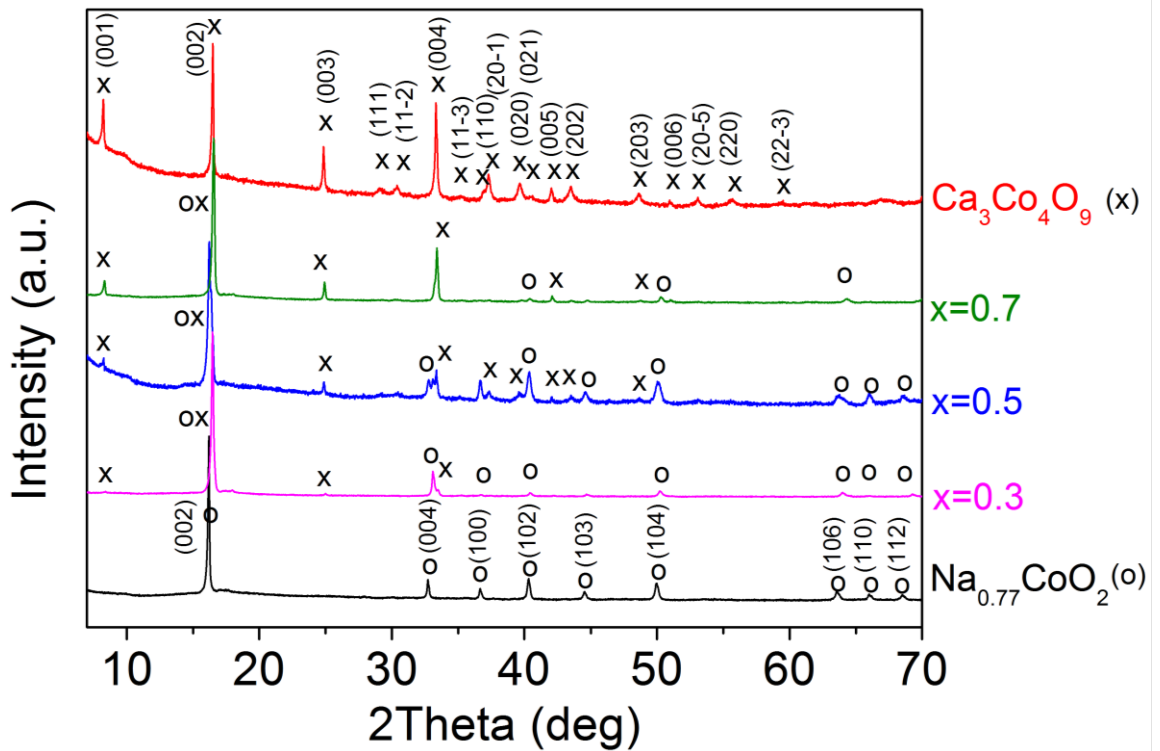
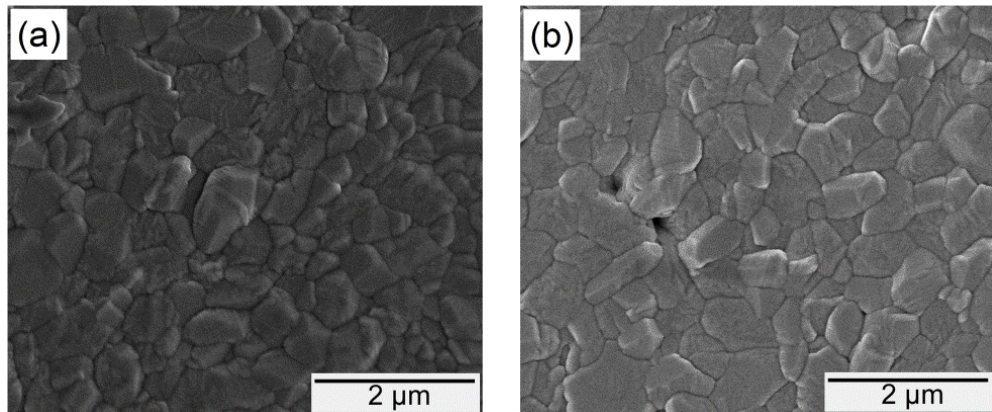


Figure 5-2 XRD patterns of $(1-x)\text{Na}_{0.77}\text{CoO}_2/x\text{Ca}_3\text{Co}_4\text{O}_9$ ($x = 0, 0.3, 0.5, 0.7, 1$) sintered by SPS at $700\text{ }^\circ\text{C}$ for 10 min.

The microstructures of $\text{Na}_{0.77}\text{CoO}_2$, $0.5\text{Na}_{0.77}\text{CoO}_2/0.5\text{Ca}_3\text{Co}_4\text{O}_9$ and $\text{Ca}_3\text{Co}_4\text{O}_9$ sintered at $700\text{ }^\circ\text{C}$ for 10 min were characterized by SEM, as shown in Figure 5-3. The samples are all densely compacted, and exhibit a fine microstructure with a similar grain size of between 0.5 and $1\text{ }\mu\text{m}$. Therefore, it is beneficial to use SPS technique to prepare a highly densified sample with a fine microstructure. Moreover, the grain sizes of the composite are increased by extending the sintering duration to 60 min.



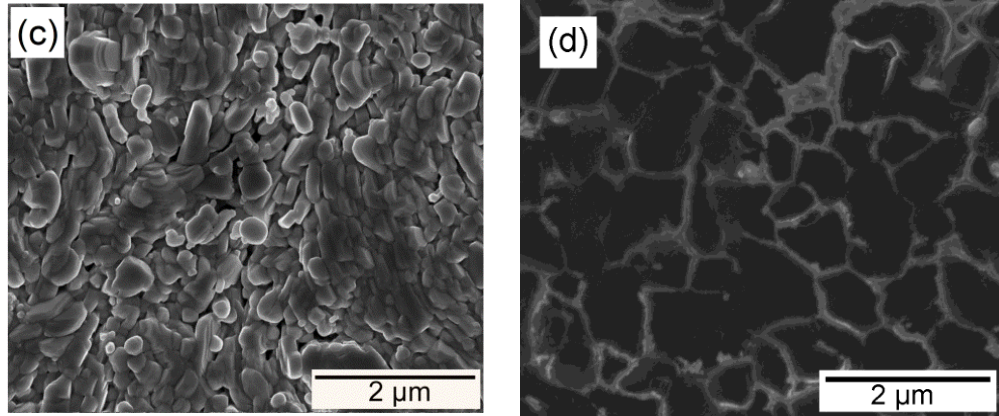


Figure 5-3 SEM micrographs of (a) $\text{Na}_{0.77}\text{CoO}_2$, (b) $0.5\text{Na}_{0.77}\text{CoO}_2/0.5\text{Ca}_3\text{Co}_4\text{O}_9$ composite, (c) $\text{Ca}_3\text{Co}_4\text{O}_9$, sintered by SPS at 700 °C for 10 min, and (d) $0.5\text{Na}_{0.77}\text{CoO}_2/0.5\text{Ca}_3\text{Co}_4\text{O}_9$ sintered by SPS at 700 °C for 60 min.

5.3.2 Effects of sintering temperature and dwell time on $0.5\text{Na}_{0.77}\text{CoO}_2/0.5\text{Ca}_3\text{Co}_4\text{O}_9$

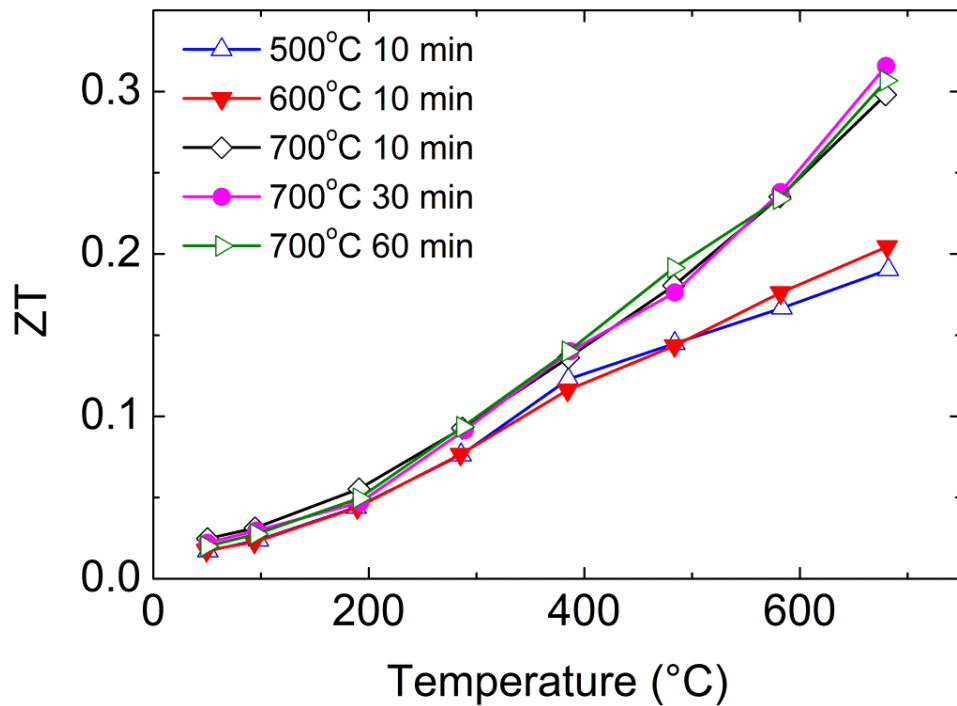


Figure 5-4 Temperature dependence of figure-of-merit (ZT) for $0.5\text{Na}_{0.77}\text{CoO}_2/0.5\text{Ca}_3\text{Co}_4\text{O}_9$ sintered at 500, 600, 700 °C for 10 min and at 700 °C for 30 and 60 min.

The samples listed in Table 5-1 were used to evaluate the effects of sintering temperature and dwell time on the transport properties of $0.5\text{Na}_{0.77}\text{CoO}_2/0.5\text{Ca}_3\text{Co}_4\text{O}_9$ composites. It is noted that all the samples possess similar ZT values below $400\text{ }^\circ\text{C}$. However, ZT as a function of temperature presents a different trend when the temperature is over $400\text{ }^\circ\text{C}$, as shown in Figure 5-4. The ZT values of the composites sintered at $700\text{ }^\circ\text{C}$ for 10, 30 and 60 min increase significantly with increasing temperature; however, this trend is less pronounced for the samples sintered at 500 and $600\text{ }^\circ\text{C}$. This difference is most likely associated with the change in resistivity ρ with increasing temperature (Figure 5-5) because ZT is inversely proportional to ρ .

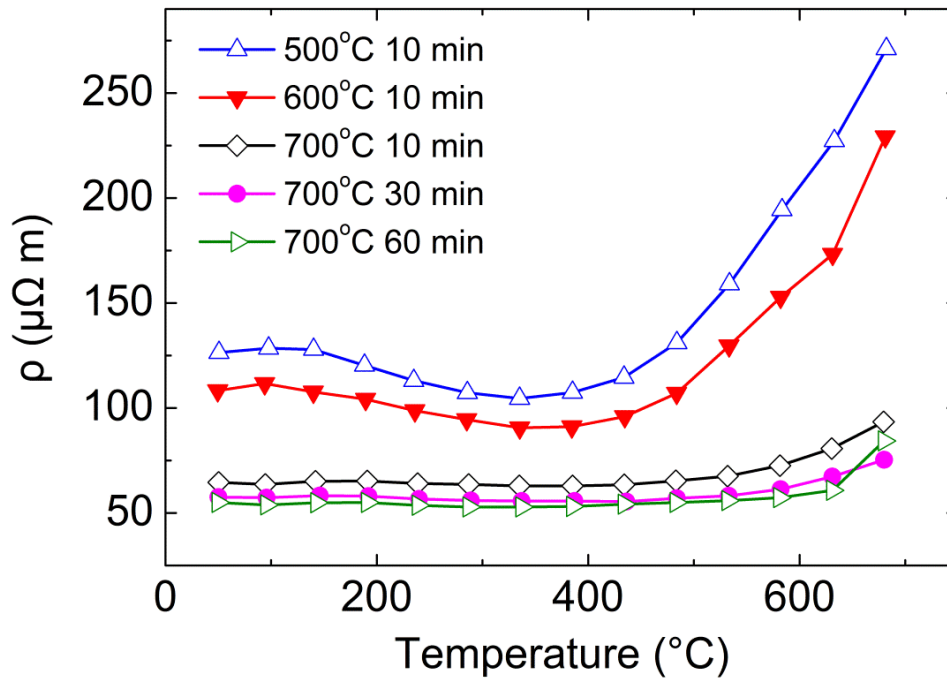


Figure 5-5 Temperature dependence of electrical resistivity (ρ) for $0.5\text{Na}_{0.77}\text{CoO}_2/0.5\text{Ca}_3\text{Co}_4\text{O}_9$ sintered at 500, 600, $700\text{ }^\circ\text{C}$ for 10 min and at $700\text{ }^\circ\text{C}$ for 30 and 60 min.

Both $\text{Na}_{0.77}\text{CoO}_2$ and $\text{Ca}_3\text{Co}_4\text{O}_9$ are prone to losing oxygen at high temperatures. For instance, it has been reported that $\text{Ca}_3\text{Co}_4\text{O}_9$ tends to lose oxygen at $\sim 447\text{--}457\text{ }^\circ\text{C}$ in air [146] and at $\sim 347\text{--}357\text{ }^\circ\text{C}$ in an inert atmosphere [147]. Consequently, $400\text{ }^\circ\text{C}$ appears to be a critical temperature for both the ZT and ρ of the composites in the present study. With the loss of oxygen, free electrons are introduced, thus decreasing the main charge carrier (hole) concentration through their recombination. Oxygen can be removed more easily from porous samples than from dense samples in an inert

atmosphere due to the larger surface area that is exposed to the environment. This explains the rapid upsurge in ρ (above 400 °C) of low-density samples (i.e., sintered at \leq 600 °C) compared with the composites sintered at 700 °C (Figure 5-5). This observation is instructive to the practical application because the dense samples with high relative density (\geq 92% in this case) possess not only superior ZT values but also good stability. Therefore, it is of interest to investigate the behaviors of composites sintered at a temperature of 700 °C.

5.3.3 Effects of different compositions on $(1-x)\text{Na}_{0.77}\text{CoO}_2/x\text{Ca}_3\text{Co}_4\text{O}_9$

$(1-x)\text{Na}_{0.77}\text{CoO}_2/x\text{Ca}_3\text{Co}_4\text{O}_9$ ($x = 0, 0.3, 0.5, 0.7, 1$) samples were sintered at 700°C for 10 min. All samples exhibit a relative density of \geq 92% (Table 2). In particular, the sample with a composition of $0.3\text{Na}_{0.77}\text{CoO}_2/0.7\text{Ca}_3\text{Co}_4\text{O}_9$ was almost fully densified.

Table 5-2 Sintering methods, nominal compositions, sintering parameters, theoretical densities and relative densities of $(1-x)\text{Na}_{0.77}\text{CoO}_2/x\text{Ca}_3\text{Co}_4\text{O}_9$.

Sintering method	x	Sintering temperature (°C)	Dwell time (min)	Theoretical density (g/cm^3)	Relative density
CS	0.5	700	720	4.65	0.61
SPS	0	700	10	4.61	0.92
	0.3	700	10	4.63	0.92
	0.5	700	10	4.65	0.95
	0.7	700	10	4.66	0.99
	1	700	10	4.68	0.92

Electrical resistivity of $(1-x)\text{Na}_{0.77}\text{CoO}_2/x\text{Ca}_3\text{Co}_4\text{O}_9$

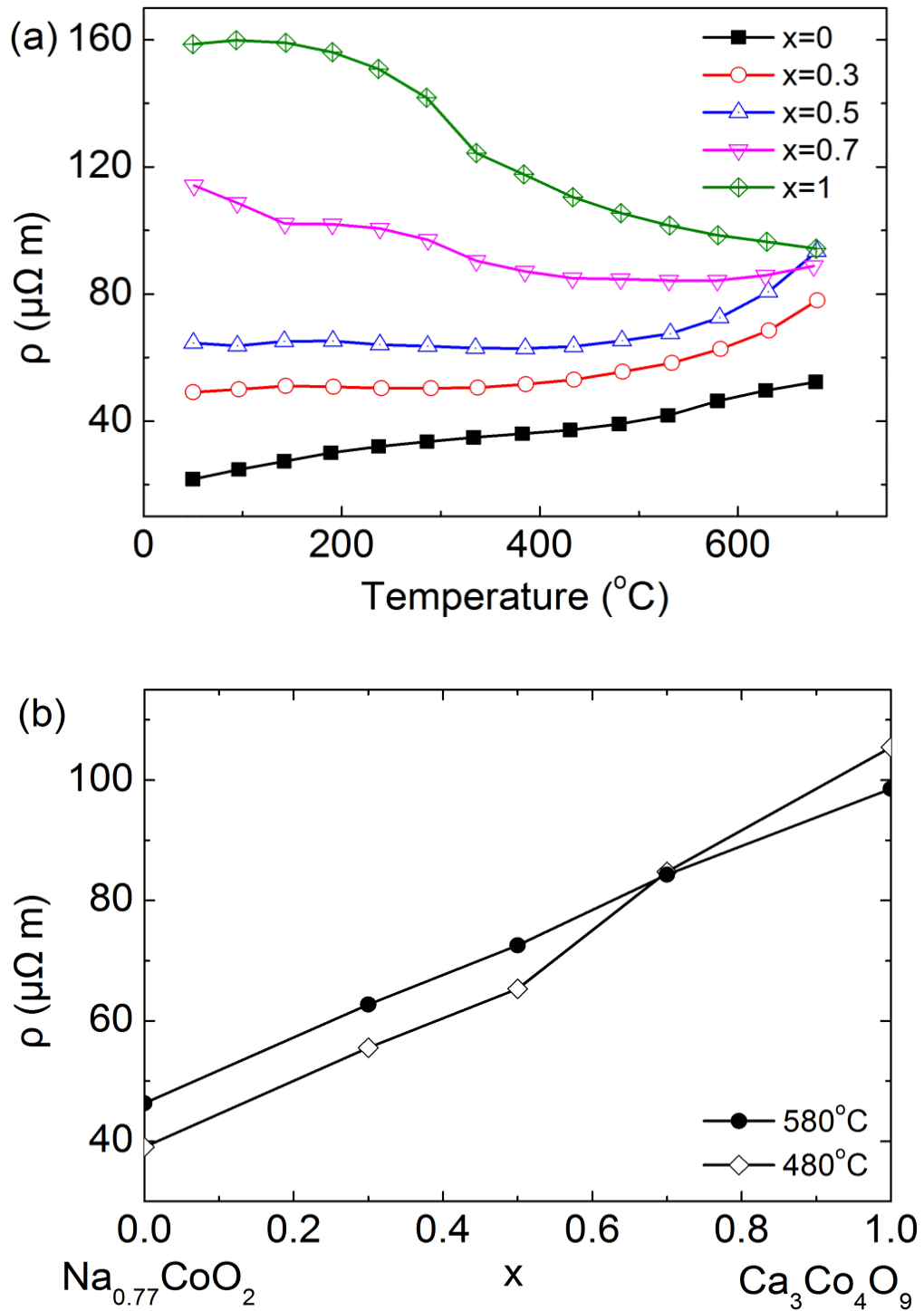


Figure 5-6 (a) Electrical resistivity (ρ) of $(1-x)\text{Na}_{0.77}\text{CoO}_2/x\text{Ca}_3\text{Co}_4\text{O}_9$ ($x = 0, 0.3, 0.5, 0.7, 1$) versus temperature, and (b) ρ of $(1-x)\text{Na}_{0.77}\text{CoO}_2/x\text{Ca}_3\text{Co}_4\text{O}_9$ versus nominal composition x at 480 $^{\circ}\text{C}$ and 580 $^{\circ}\text{C}$, respectively.

The electrical resistivity (ρ) of $(1-x)\text{Na}_{0.77}\text{CoO}_2/x\text{Ca}_3\text{Co}_4\text{O}_9$ versus temperature and ρ versus volume fraction (x) of $\text{Ca}_3\text{Co}_4\text{O}_9$ are shown in Figure 5-6a and b, respectively. ρ increases linearly with increasing x . The boundary between the metallic and semiconducting conduction is found in the composite with $x = 0.5$. At temperatures lower than 450 °C, the resistivity of $0.5\text{Na}_{0.77}\text{CoO}_2/0.5\text{Ca}_3\text{Co}_4\text{O}_9$ is nearly independent of temperature. The increased resistivity with increasing temperature over 450 °C is due to the oxygen loss during measurement in vacuum.

In 1952, Landauer [148] proposed a model for the calculation of electrical resistivity of a random binary metallic mixture. It is assumed in this model that two phases in the mixture are randomly distributed and completely fill the space. In addition, the voltage drop across the grain boundaries is ignored, assuming good contact between the grains. In this case, the composites that we prepared are in good agreement with these assumptions, even though our composites are not fully densified. Based on this model, a modified equation for the calculation of the theoretical electrical resistivity of $(1-x)\text{Na}_{0.77}\text{CoO}_2/x\text{Ca}_3\text{Co}_4\text{O}_9$ considering the relative density (voids existing in the composites) is proposed as:

$$\frac{(\rho_m - \rho_2)x_2}{2\rho_2 + \rho_m} + \frac{(\rho_m - \rho_1)x_1}{2\rho_1 + \rho_m} = \frac{1 - (x_1 + x_2)}{2} \quad \text{Equation 5-1}$$

where x_1 and x_2 are the product of the relative density and the respective molar ratio of $\text{Na}_{0.77}\text{CoO}_2$ and $\text{Ca}_3\text{Co}_4\text{O}_9$. ρ_1 and ρ_2 are the respective resistivity of $\text{Na}_{0.77}\text{CoO}_2$ and $\text{Ca}_3\text{Co}_4\text{O}_9$. ρ_m is the resistivity of the mixture. By solving Equation 5-1, the resistivity of the mixture can be determined by:

$$\rho_m = \frac{\sqrt{(3\rho_1x_2 + 3\rho_2x_1)^2 + (\rho_1 - \rho_2)^2 + 6(\rho_1x_2 - \rho_2x_1)(\rho_2 - \rho_1)} - 3(\rho_1x_2 + \rho_2x_1) + \rho_1 + \rho_2}{3x_2 + 3x_1 - 1}$$

$$\text{Equation 5-2}$$

As shown in Figure 5-7b, the theoretical values derived from Landauer's model are lower than the experimental results.

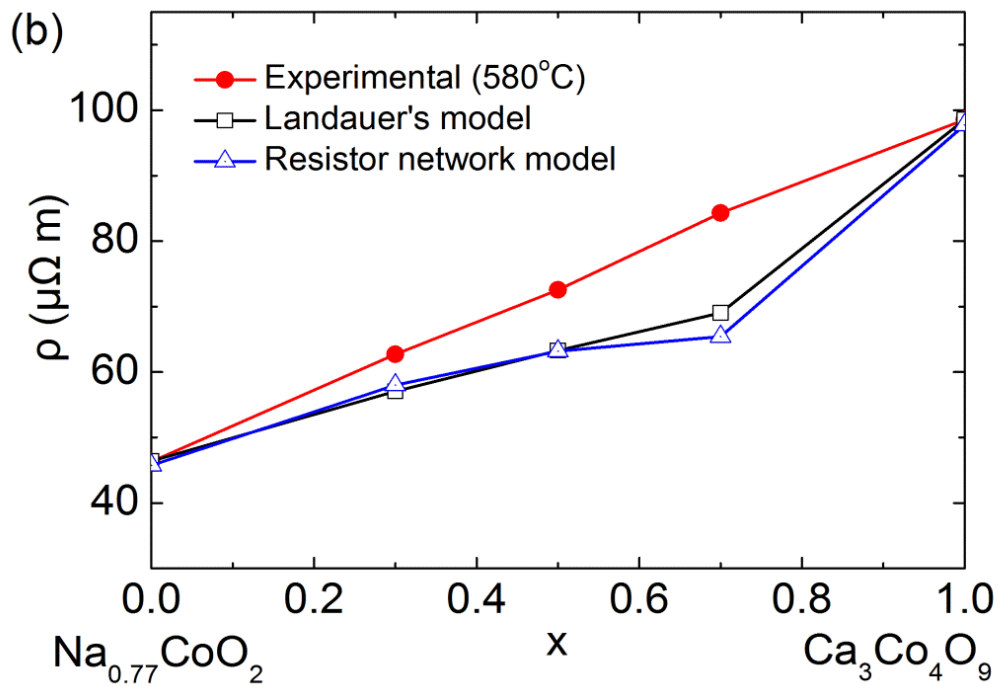
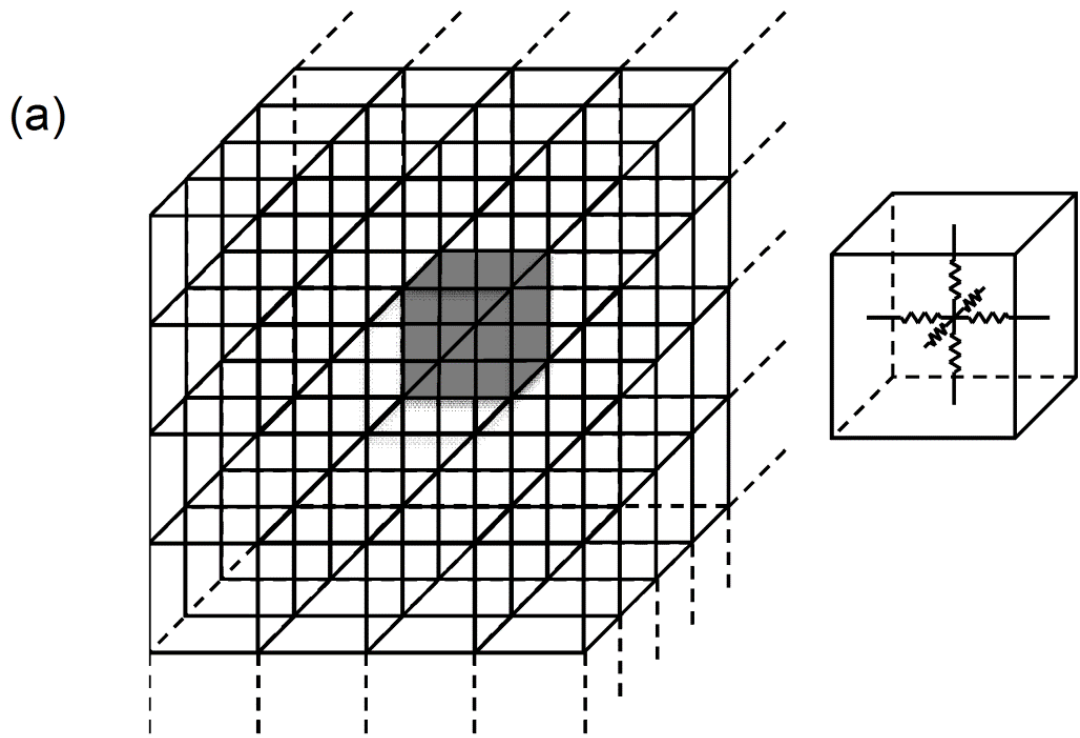


Figure 5-7 (a) Schematic diagram of a resistor network representing $(1-x)\text{Na}_{0.77}\text{CoO}_2/x\text{Ca}_3\text{Co}_4\text{O}_9$ samples and (b) the experimental and calculated electrical resistivity (ρ) of $(1-x)\text{Na}_{0.77}\text{CoO}_2/x\text{Ca}_3\text{Co}_4\text{O}_9$ versus nominal composition (x) at 580 °C.

Moreover, a 3-D resistor network model (Figure 5-7a) is constructed by considering the compositions of $(1-x)\text{Na}_{0.77}\text{CoO}_2/x\text{Ca}_3\text{Co}_4\text{O}_9$ and the relative density to

verify the ideal electrical resistivity of the composites. The assumptions used to derive this model are similar to those in Landauer's work. To simplify the calculation, we further assume that the composites have the same size of cubic grains of $\text{Na}_{0.77}\text{CoO}_2$ and $\text{Ca}_3\text{Co}_4\text{O}_9$ and voids with a cubic unit. In each unit there are six resistors, each of which is connected to the one in the adjacent unit sharing the same facet. The resistance of each resistor is set to be half the value of the resistivity of the material. The 3-D matrix consists of N^3 cubic units. The resistance of the matrix from one side to the opposite side times N yields the resistivity of the composite material. SPICE is used to calculate the total resistance of the network. Furthermore, MATLAB is applied to generate the input file for SPICE, which contains over 10^4 resistors. The calculated resistivity is also lower than the experimental results, as shown in Figure 5-7b. In summary, resistivity values calculated from both Landauer's model and the resistor network model deviate from the experimental results, implying the existence of other factors that influence the resistivity. Moreover, the insufficiency of both models should also contribute to the deviation. Equation 5-1 is derived based on the assumption of spherical grains and uniform electrical field within the composites. Similarly, the resistor network model oversimplified the shapes of the grains and voids. These assumptions about grain shapes may partially cause the deviation, since the electrical resistivities of $\text{Na}_{0.77}\text{CoO}_2$ and $\text{Ca}_3\text{Co}_4\text{O}_9$ is highly anisotropic between in- and out-of-plane directions [12]. However, as will be shown in the next section, both of the abnormal increase of the electrical resistivity and the Seebeck coefficient appeared in the composites implies that the interface effect is most likely to be the main influence factor.

Strain induced enhancement of Seebeck coefficient

The Seebeck coefficient (S) of $(1-x)\text{Na}_{0.77}\text{CoO}_2/x\text{Ca}_3\text{Co}_4\text{O}_9$ as a function of temperature and S versus volume fraction of $\text{Ca}_3\text{Co}_4\text{O}_9$ (x) are shown in Figure 5-8a and b, respectively. The composites, especially $0.3\text{Na}_{0.77}\text{CoO}_2/0.7\text{Ca}_3\text{Co}_4\text{O}_9$, exhibit a larger S than the individual $\text{Na}_{0.77}\text{CoO}_2$ and $\text{Ca}_3\text{Co}_4\text{O}_9$ at ~ 400 °C and above. Figure 5-9a shows the experimental and theoretical predictions of S as a function of temperature for $0.3\text{Na}_{0.77}\text{CoO}_2/0.7\text{Ca}_3\text{Co}_4\text{O}_9$. The theoretical values of S of the composite are calculated based on the equation proposed by Bergmann and Levy [149]. The experimental results show larger S , and there is a monotonic increase in the difference between the experimental and theoretical S with increasing temperature.

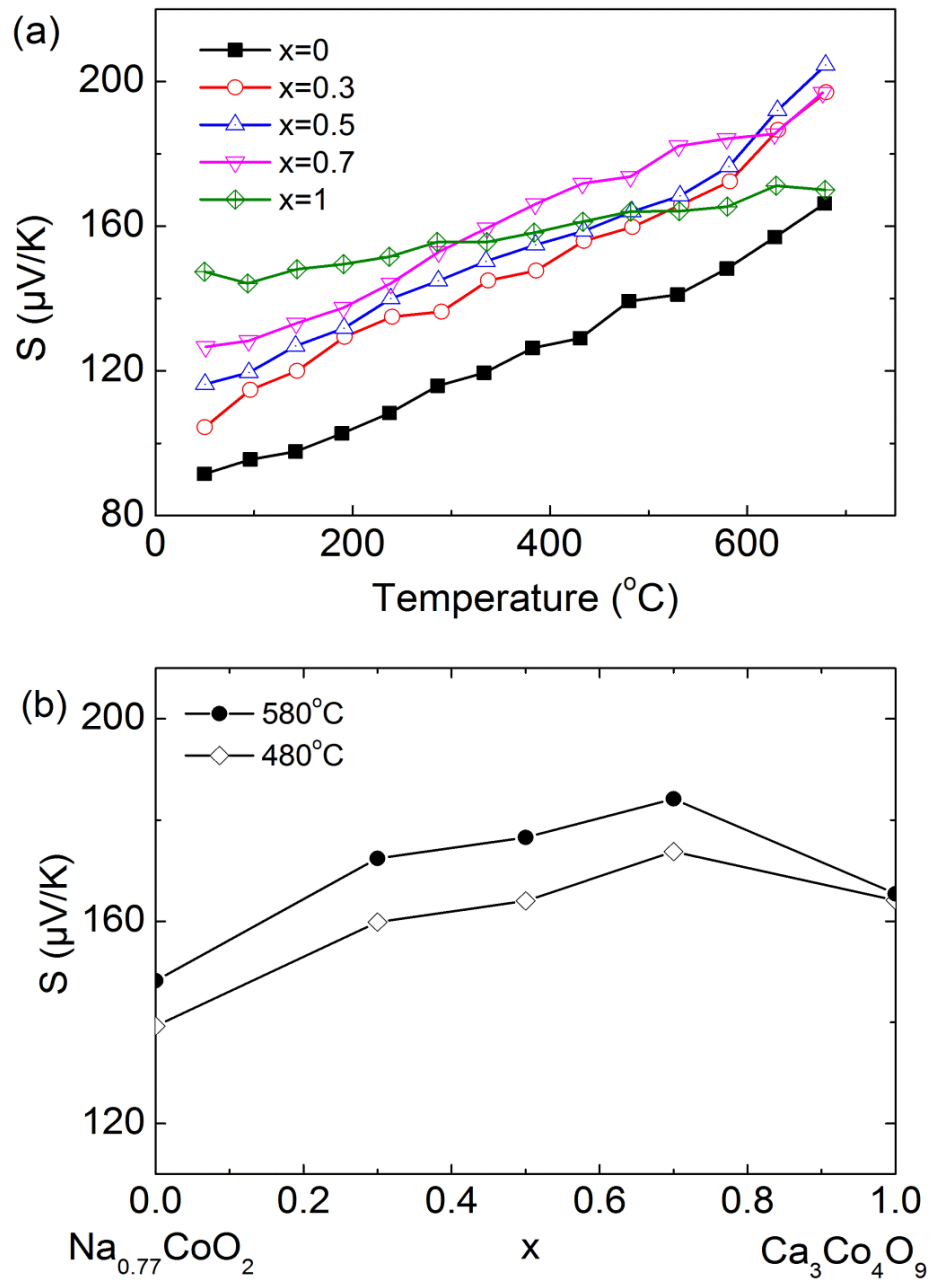


Figure 5-8 (a) Seebeck coefficient (S) of $(1-x)\text{Na}_{0.77}\text{CoO}_2/x\text{Ca}_3\text{Co}_4\text{O}_9$ ($x = 0, 0.3, 0.5, 0.7, 1$) versus temperature (b) S of $(1-x)\text{Na}_{0.77}\text{CoO}_2/x\text{Ca}_3\text{Co}_4\text{O}_9$ versus nominal composition x measured at 480°C and 580°C , respectively.

The enhancement of the Seebeck coefficient mainly originates from the unique properties of the composites. A similar enhancement of S (13% increase over that of single-phase $\text{Ca}_3\text{Co}_4\text{O}_9$) was also observed in the superlattice structure $\text{Na}_{0.66}\text{CoO}_2/\text{Ca}_3\text{Co}_4\text{O}_9$ ($0.25\text{Na}_{0.77}\text{CoO}_2/0.75\text{Ca}_3\text{Co}_4\text{O}_9$) [150]. As reported by Odahara et al. [143], the large variation in the thermal conductivity of two components in a composite leads to an uneven thermal gradient and hence the enhancement of the

Seebeck coefficient. However, this mechanism is ruled out here as $\text{Na}_{0.77}\text{CoO}_2$ and $\text{Ca}_3\text{Co}_4\text{O}_9$ possess similar thermal conductivity (Figure 5-10). Additionally, both experimental and theoretical studies indicate that the Seebeck coefficient can be affected by the strain present in the materials, which can be induced by lattice mismatch [151] or external pressure [152].

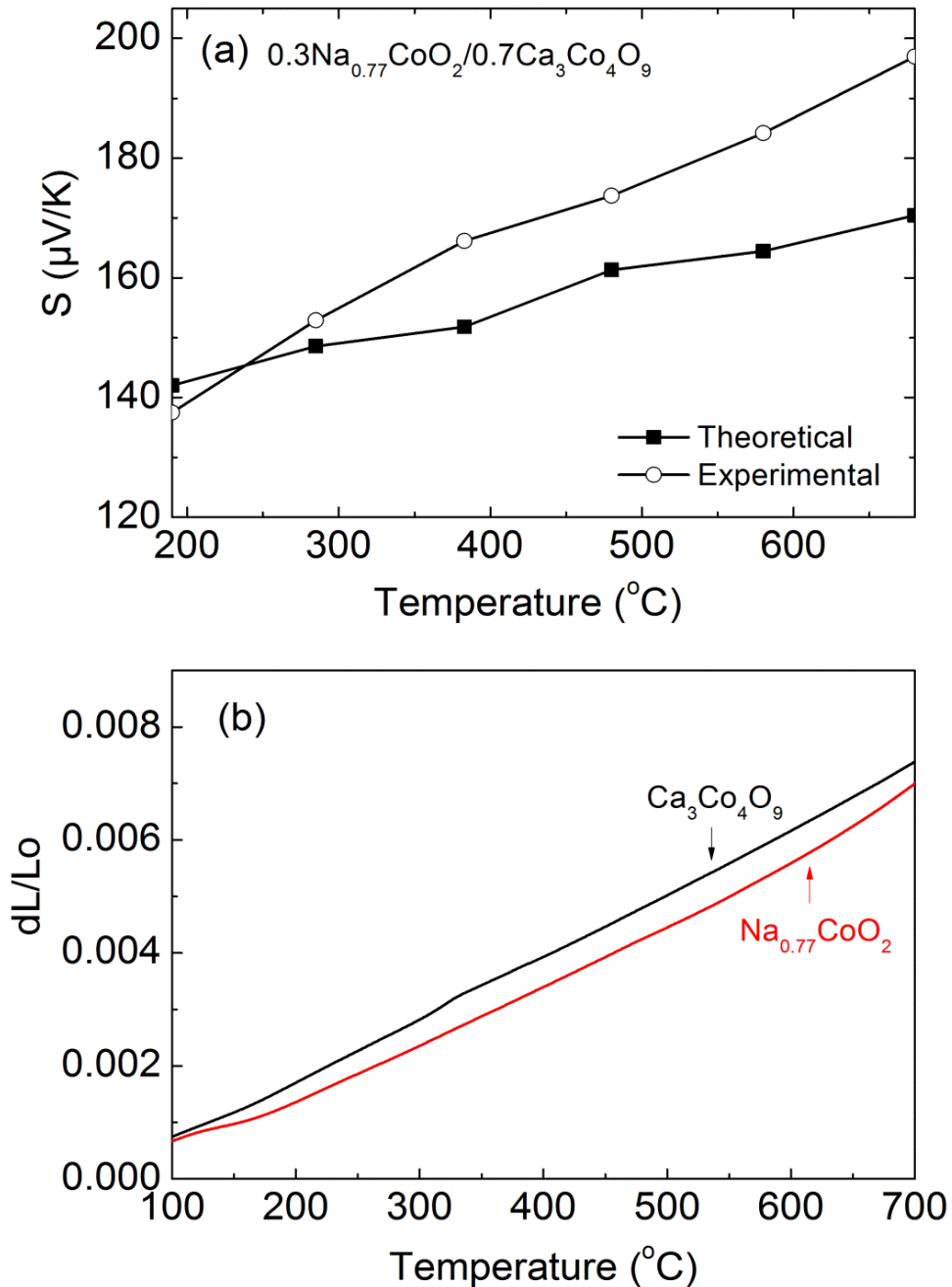


Figure 5-9 (a) Theoretical and experimental Seebeck coefficient (S) versus temperature for $0.3\text{Na}_{0.77}\text{CoO}_2/0.7\text{Ca}_3\text{Co}_4\text{O}_9$. (b) Thermal expansion dL/L_0 of single-phase $\text{Na}_{0.77}\text{CoO}_2$ and $\text{Ca}_3\text{Co}_4\text{O}_9$ versus temperature.

A previous study by Matsubara et al. [151] on $(\text{Ca}_2\text{CoO}_3)_x\text{CoO}_2$ thin films demonstrated a 9% improvement on S due to compressive strain within the crystal structure induced by misfit lattice parameters. Figure 5-9b shows that the thermal expansion coefficient (dL/L_0) of $\text{Ca}_3\text{Co}_4\text{O}_9$ is higher than that of $\text{Na}_{0.77}\text{CoO}_2$ from 100 to 700 °C. Therefore, the $\text{Ca}_3\text{Co}_4\text{O}_9$ grains are subjected to the compressive strain exerted by the neighboring $\text{Na}_{0.77}\text{CoO}_2$ grains with a smaller thermal expansion at elevated temperatures. Moreover, such an effect would become more pronounced as the temperature increases, which is in good agreement with Figure 5-9a. In addition, it is reported that the compressive strain leads to an increase in ρ [151]. This is also consistent with the observation of ρ behavior in our study, showing that the experimental resistivity is higher than the calculated and modeling ρ_m values. Therefore, the interfacial effect, specifically the compressive strain, should be mainly responsible for the enhancement of the Seebeck coefficient.

Thermoelectric properties

With the calculation, we find that power factor ($PF = S^2/\rho$) deteriorates with increasing amount of $\text{Ca}_3\text{Co}_4\text{O}_9$. Moreover, the PF of $\text{Na}_{0.77}\text{CoO}_2$ is similar to that of $0.7\text{Na}_{0.77}\text{CoO}_2/0.3\text{Ca}_3\text{Co}_4\text{O}_9$ at temperatures higher than 200 °C. Figure 5-10a and b show that thermal conductivity (κ) does not change significantly with different compositions. Basically, the trend of κ is the same as that of the relative densities of the samples. The thermal conductivity of $0.3\text{Na}_{0.77}\text{CoO}_2/0.7\text{Ca}_3\text{Co}_4\text{O}_9$ exhibits the highest κ because of its highest relative density.

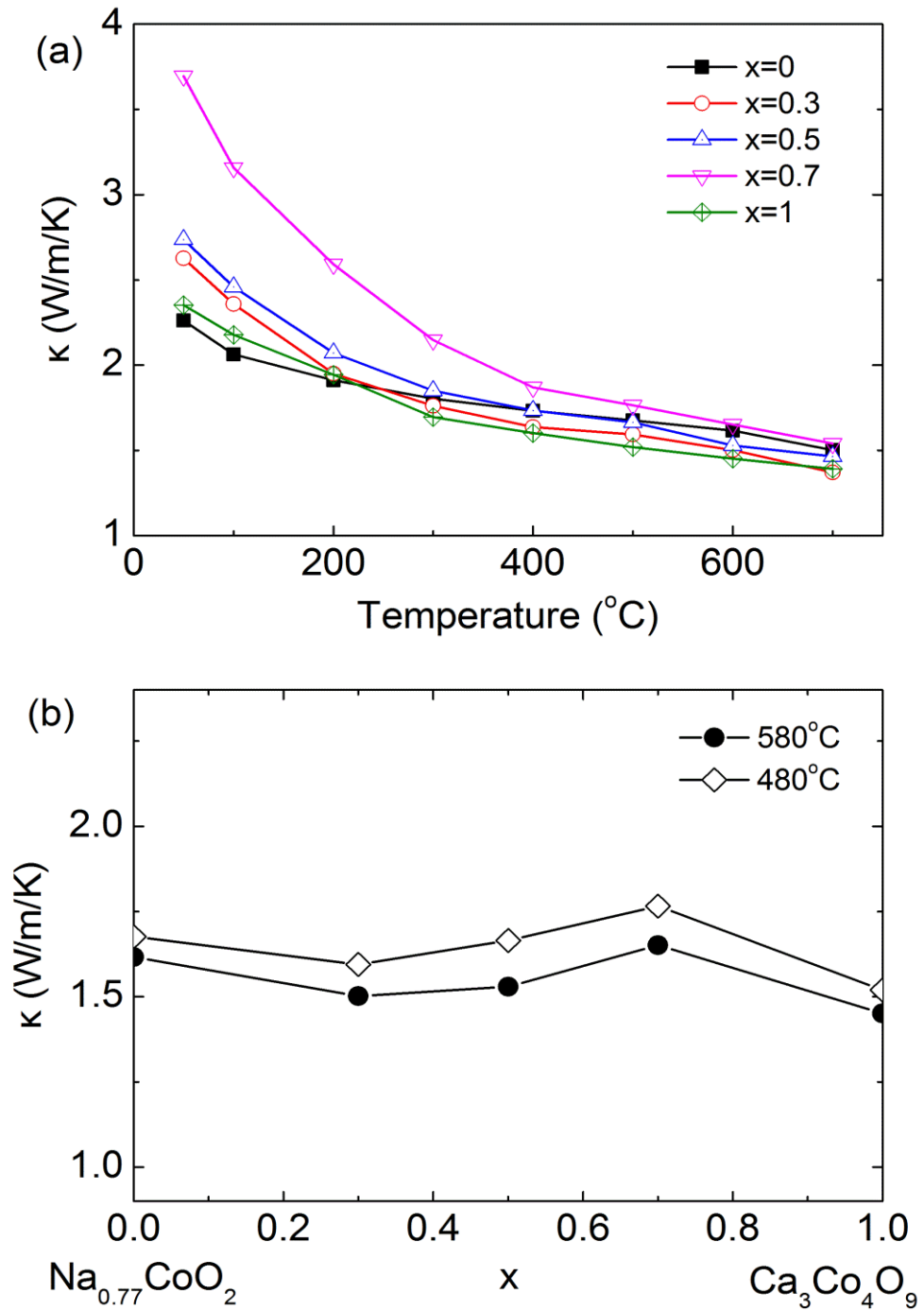


Figure 5-10 (a) Thermal conductivity κ of $(1-x)\text{Na}_{0.77}\text{CoO}_2/x\text{Ca}_3\text{Co}_4\text{O}_9$ ($x = 0, 0.3, 0.5, 0.7, 1$) versus temperature and (b) κ of $(1-x)\text{Na}_{0.77}\text{CoO}_2/x\text{Ca}_3\text{Co}_4\text{O}_9$ versus nominal composition x measured at 480 $^{\circ}\text{C}$ and 580 $^{\circ}\text{C}$, respectively.

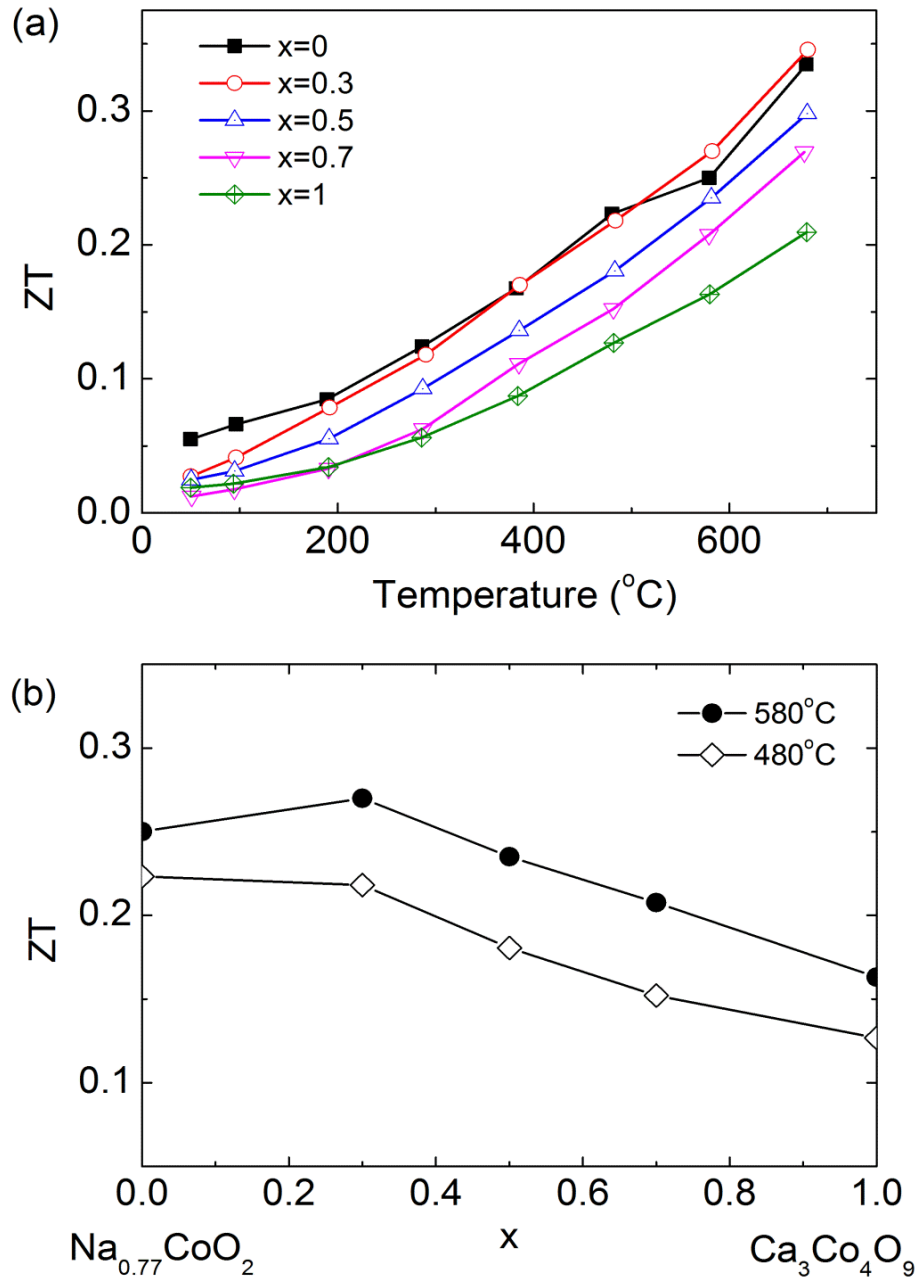


Figure 5-11 (a) ZT of $(1-x)\text{Na}_{0.77}\text{CoO}_2/x\text{Ca}_3\text{Co}_4\text{O}_9$ ($x = 0, 0.3, 0.5, 0.7, 1$) versus temperature, and (b) ZT of $(1-x)\text{Na}_{0.77}\text{CoO}_2/x\text{Ca}_3\text{Co}_4\text{O}_9$ versus nominal composition x at 480 $^{\circ}\text{C}$ and 580 $^{\circ}\text{C}$, respectively.

$\text{Na}_{0.77}\text{CoO}_2$ and $0.7\text{Na}_{0.77}\text{CoO}_2/0.3\text{Ca}_3\text{Co}_4\text{O}_9$ samples exhibit similar ZT [$ZT = S^2T/(\rho\kappa)$] values, both achieving 0.35 at 680 $^{\circ}\text{C}$ (Figure 5-11a and b). The overall value of ZT decreases with increasing volume fraction of $\text{Ca}_3\text{Co}_4\text{O}_9$ when x exceeds 0.3.

5.3.4 Chemical stability

As the moisture absorption would be limited at temperatures above 100 °C, therefore, it is of interest to investigate the chemical stability of $\text{Na}_{0.77}\text{CoO}_2$ and $0.7\text{Na}_{0.77}\text{CoO}_2/0.3\text{Ca}_3\text{Co}_4\text{O}_9$ samples in air. Figure 5-12a shows that the $\text{Na}_{0.77}\text{CoO}_2$ sample starts to decompose after 7 days. The impurities were most likely to be Na_2CO_3 (JCPDS 86-0289) and $\text{Co}(\text{OH})_2$ (JCPDS 45-0031). After 14 days testing, the diffraction peaks corresponding to $\text{Na}_{0.77}\text{CoO}_2$ phase had almost disappeared, indicating the degradation as a result of the moisture. The major phases existing in the composites were Co_3O_4 (JCPDS 80-1542), Na_2CO_3 (JCPDS 86-0289), and $\text{Co}(\text{OH})_2$ (JCPDS 45-0031). In contrast, only a trace amount of impurity phase presented in the XRD patterns of $0.7\text{Na}_{0.77}\text{CoO}_2/0.3\text{Ca}_3\text{Co}_4\text{O}_9$ after 7 days of testing (Figure 5-12b). Even after 14 days, the major phase was still $\text{Na}_{0.77}\text{CoO}_2$, with limited amounts of Na_2CO_3 (JCPDS 86-0289) and $\text{Co}(\text{OH})_2$ (JCPDS 45-0031). Therefore the chemical stability of $\text{Na}_{0.77}\text{CoO}_2$ can be improved significantly by compositing it with $\text{Ca}_3\text{Co}_4\text{O}_9$.

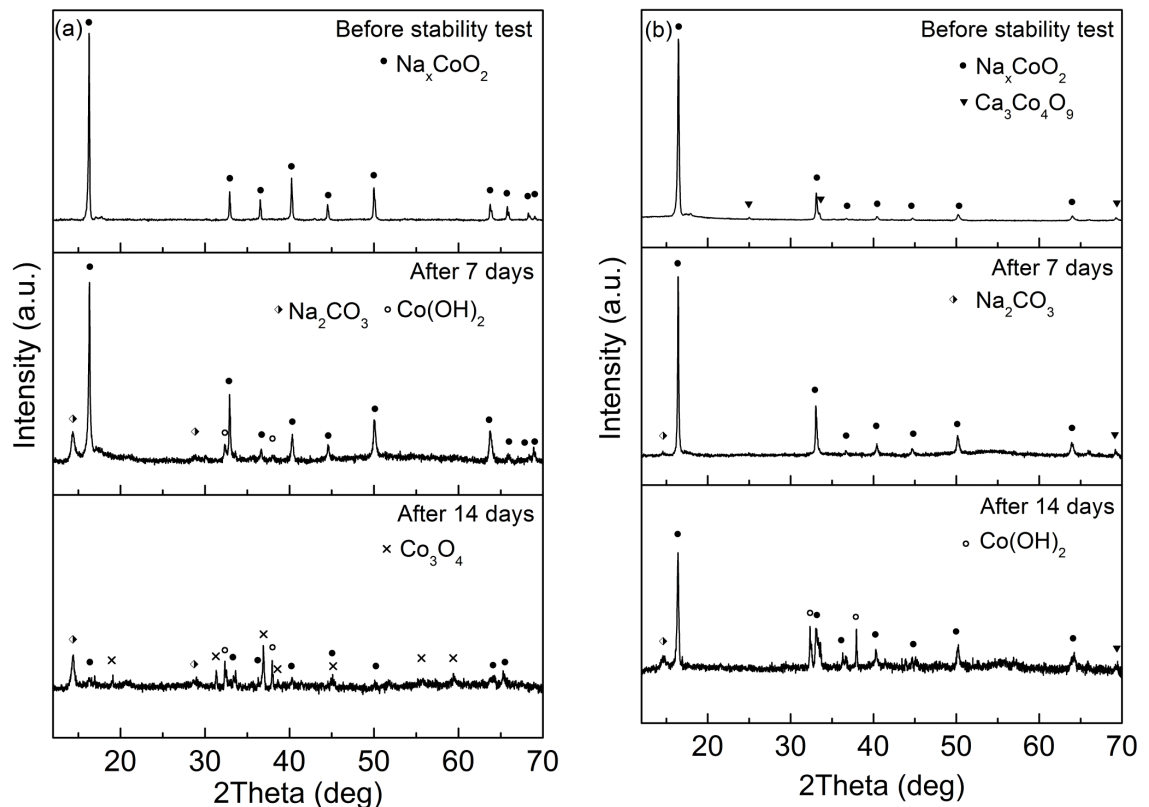


Figure 5-12 XRD patterns of pellets of (a) $\text{Na}_{0.77}\text{CoO}_2$ and (b) $0.7\text{Na}_{0.77}\text{CoO}_2/0.3\text{Ca}_3\text{Co}_4\text{O}_9$ before stability test, after testing for 7 days and after testing for 14 days, respectively.

$\text{Na}_{0.77}\text{CoO}_2$ is highlighted for its good thermoelectric properties. However, due to its moisture-sensitive nature, the application of $\text{Na}_{0.77}\text{CoO}_2$ is limited. This observation is promising for the development of $\text{Na}_{0.77}\text{CoO}_2$ thermoelectric materials for practical applications, because the chemical stability of $\text{Na}_{0.77}\text{CoO}_2$ could be significantly improved by compositing with $\text{Ca}_3\text{Co}_4\text{O}_9$ (up to 30 vol.% fraction) while retaining its thermoelectric performance.

5.4 Summary

$\text{Na}_{0.77}\text{CoO}_2/\text{Ca}_3\text{Co}_4\text{O}_9$ composites have been successfully synthesized by SPS and their thermoelectric properties have been studied. No solid-state reaction between $\text{Na}_{0.77}\text{CoO}_2$ and $\text{Ca}_3\text{Co}_4\text{O}_9$ has been observed with increasing sintering temperature up to 700 °C and sintering duration up to 1 h. With increasing relative density up to ~92%, ZT of the composites could be improved. We applied a modified Landauer's model and a resistor network model to calculate the theoretical electrical resistivity of the composites. The experimental resistivity is larger than the calculated data. Furthermore, the Seebeck coefficient of the composites is enhanced by 17% at 680 °C compared with that of single-phase $\text{Ca}_3\text{Co}_4\text{O}_9$. Both phenomena are attributed to the compressive strain on $\text{Ca}_3\text{Co}_4\text{O}_9$ originating from the mismatch of thermal expansion coefficients between $\text{Ca}_3\text{Co}_4\text{O}_9$ and $\text{Na}_{0.77}\text{CoO}_2$. Above all, the chemical stability of $\text{Na}_{0.77}\text{CoO}_2$ could be improved by adding up to a 30 vol.% fraction of $\text{Ca}_3\text{Co}_4\text{O}_9$ to form composites without affecting the thermoelectric performance. The present study is promising as it opens the way for the practical application of such thermoelectric materials.

Chapter 6 Effects of Y and La content on the crystal phase, microstructure, and thermoelectric properties of Sr-deficient $\text{Sr}_{1-1.5x}\text{M}_x\text{TiO}_3$ ($M = \text{Y, La}$)

6.1 Introduction

Donor-doped SrTiO_3 appears to be a promising n-type thermoelectric oxide due to its unusually high power factor [27], low cost, low toxicity, and high thermal and chemical stability at high temperatures. The thermoelectric properties of SrTiO_3 can be adjusted by introducing cationic doping and oxygen vacancies. A common doping strategy is to substitute Sr with lanthanide ions or to substitute Ti with Nb^{5+} ions [23-25]. Additionally, stoichiometric $\text{Sr}_{1-x}\text{Y}_x\text{TiO}_3$ and $\text{Sr}_{1-x}\text{La}_x\text{TiO}_3$ sintered under a reducing atmosphere exhibits high Seebeck coefficient and low thermal conductivity [25,153]. It has also been reported that the Sr-deficient compositions have higher electrical conductivity than the stoichiometric compositions [28-30]. However, the reports in the thermoelectric properties of Sr-deficient $\text{Sr}_{1-1.5x}\text{M}_x\text{TiO}_3$ ($M = \text{Y, La}$) are limited.

The thermal properties of materials may also be tailored by introducing dopants or a secondary phase. The secondary phase can act as phonon-scattering centers to reduce the lattice thermal conductivity when it is embedded inside the grains [154]. For example, the thermal conductivity of Nb-doped SrTiO_3 has been reduced by introducing nanosized yttria stabilized zirconia into grains and triple junctions [155]. Moreover, the secondary phase that locates at grain boundaries plays an important role in the mechanical properties, electrical properties, and thermal stability of ceramics [156]. It has been found that excessive doping of Y into SrTiO_3 results in the formation of a secondary phase, $\text{Y}_2\text{Ti}_2\text{O}_7$. Since $\text{Y}_2\text{Ti}_2\text{O}_7$ is grown in-situ during sintering, it is expected that its distribution is uniform within the composites. Therefore it is worthwhile to study the distribution and effects of $\text{Y}_2\text{Ti}_2\text{O}_7$ on the thermoelectric properties of Y-doped SrTiO_3 .

In contrast to the limited solubility of Y in SrTiO_3 ($x \approx 0.08$), up to 40 at.% ($x \approx 0.4$) of La can be doped into SrTiO_3 [157]. It is necessary to study the thermoelectric properties of $\text{Sr}_{1-1.5x}\text{M}_x\text{TiO}_3$ within and beyond the solubility of dopants. Therefore, in this study, we have examined the structural and thermoelectric properties of Y and La

substituted strontium titanates with nominal compositions of $\text{Sr}_{1-1.5x}\text{M}_x\text{TiO}_3$ ($M = \text{Y, La}$; $x = 0, 0.02, 0.03, 0.04, 0.06, 0.08, \text{ and } 0.15$ for Y; $x = 0, 0.04, 0.08, 0.12, 0.25, \text{ and } 0.40$ for La).

6.2 Experimental procedure

$\text{Sr}_{1-1.5x}\text{Y}_x\text{TiO}_3$ ($x = 0, 0.02, 0.03, 0.04, 0.06, 0.08, \text{ and } 0.15$), $\text{Y}_2\text{Ti}_2\text{O}_7$, and $\text{Sr}_{1-1.5x}\text{La}_x\text{TiO}_3$ ($x = 0, 0.04, 0.08, 0.12, 0.25, \text{ and } 0.40$) were synthesized by conventional solid-state reaction method. The starting powders were SrCO_3 (99.9%, Sigma Aldrich), TiO_2 (Puriss grade, Sigma Aldrich), Y_2O_3 (99.99%, Sigma Aldrich), and La_2O_3 (99.99%, Prochem Inc). Except for La_2O_3 dried in furnace at $900\text{ }^\circ\text{C}$ for 2 h, the other powders were all baked in oven at $150\text{ }^\circ\text{C}$ for 3 h before use. The powders were then mixed according to the aforementioned nominal compositions. The mixture was ball milled in a planetary ball mill machine (Retsch, PM400) at 150 rpm for 6 h in ethanol with zirconia balls. After drying, the powder was calcined at $1300\text{ }^\circ\text{C}$ for 6 h in 5% H_2/Ar . The powder was then ground and subjected to ball milling again. After drying, the powder was compacted into 20 mm pellets with cold pressing machine under a pressure of 200 MPa with the aid of PVA binder. The pellets were annealed at $500\text{ }^\circ\text{C}$ for 0.5 h in air to eliminate the binder. Finally, the pellets were sintered at $1400\text{ }^\circ\text{C}$ for 11 h in 5% H_2/Ar .

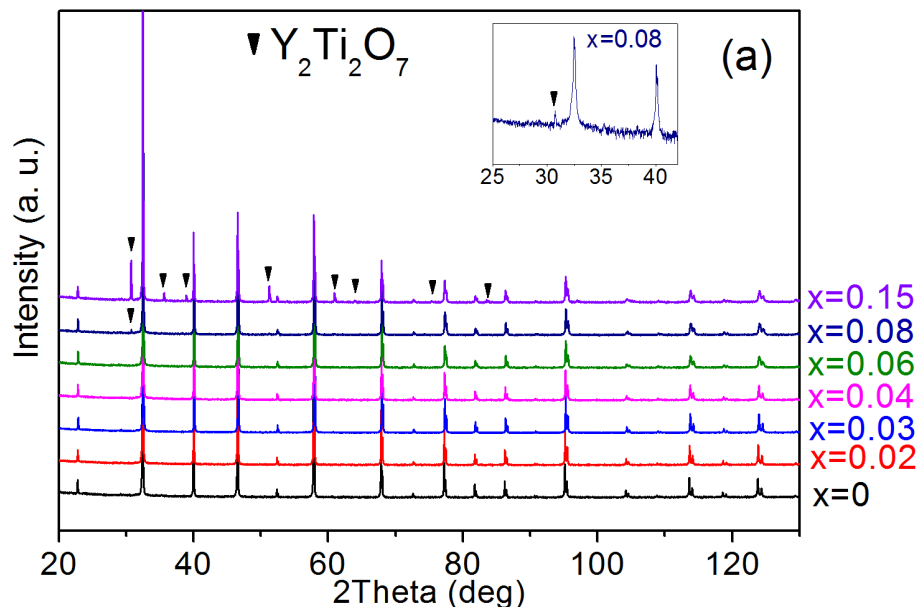
Powder X-ray diffraction (XRD) measurement was carried out employing Panalytical X'pert MPD scanning 2θ from 20° to 130° . Rietveld refinements were performed using PANalytical-HighScore Plus software. Density of the pellets was evaluated by Archimedes' principle. The microstructural analysis was conducted using scanning electron microscopy (SEM) and energy-dispersive X-ray spectroscopy (EDS) (FEI Nova NanoSEM 230 FESEM). Prior to SEM, the samples were polished and thermal etched at $1300\text{ }^\circ\text{C}$ for 0.5 h in 5% H_2/Ar . The bright-field images and selected area electron diffraction (SAED) patterns were taken by transmission electron microscopy (TEM) (Phillips CM200). The samples for TEM analysis were prepared by focused ion beam (FIB) (XT Nova Nanolab 200). Electrical conductivity σ and Seebeck coefficient S were simultaneously measured by the ULVAC-ZEM3 system. Thermal conductivity κ was obtained from the product of the measured density (NETZSCH DIL402PC for the thermal expansion), the specific heat capacity (NETZSCH DSC404C), and the thermal diffusivity (NETZSCH LFA427). Thermogravimetric

measurement was carried out employing thermogravimetric analysis (NETZSCH STA449). The oxygen deficiency was determined by the weight increase upon annealing samples at 1000 °C for 20 h in oxygen atmosphere (50 ml/min). Both physical and chemical properties of Ti^{3+} and Ti^{4+} are similar, and therefore, it is hard to determine the Ti^{3+} concentration via experiments. In the donor-doped SrTiO_3 system, defect chemistry method with the charge neutrality is the common method for the determination of Ti^{3+} concentration. Therefore, this method is applied in the thesis.

6.3 Results and discussion

6.3.1 Effects of Y content and Sr deficiency on the crystal phase, microstructure, and thermoelectric properties of $\text{Sr}_{1-1.5x}\text{Y}_x\text{TiO}_3$ ($0 \leq x \leq 0.15$)

The XRD patterns shown in Figure 6-1 indicate that the samples of composition $0 \leq x \leq 0.06$ were single-phase perovskite structure with space group $\text{Pm}\bar{3}\text{m}$. Diffraction peaks corresponding to the $\text{Y}_2\text{Ti}_2\text{O}_7$ phase appeared in the XRD patterns with $x \geq 0.08$ (insert in Figure 6-1a), indicating the solubility limit of Y in $\text{Sr}_{1-1.5x}\text{Y}_x\text{TiO}_3$ between 6-8%. Rietveld analysis of the XRD patterns shows a linear decrease of lattice parameter (a) with increasing Y content up to $x = 0.08$ (Figure 6-1b). It indicates a successful substitution of Sr^{2+} with Y^{3+} due to the smaller ionic radius of Y^{3+} compared to Sr^{2+} . The lattice parameter remains unchanged above the solubility limit of Y^{3+} in SrTiO_3 ($0.08 \leq x \leq 0.15$). All samples showed > 94% of the theoretical density.



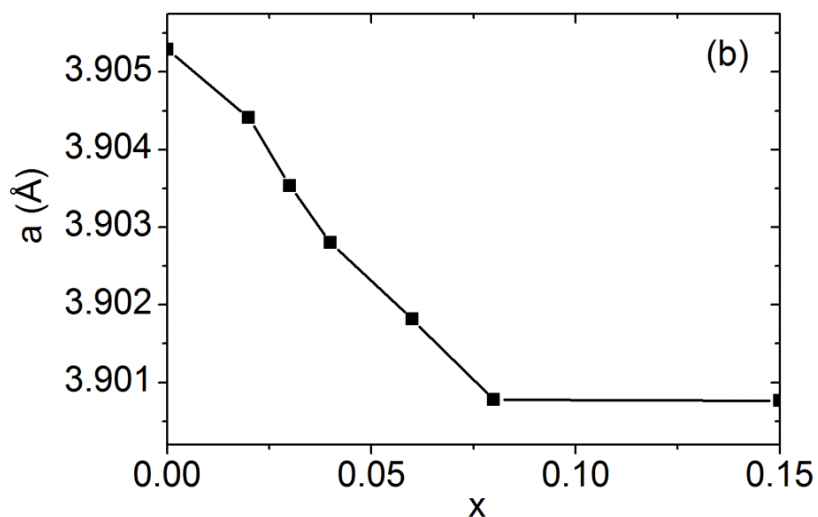


Figure 6-1 (a) XRD patterns and (b) lattice parameter a versus x , for $\text{Sr}_{1-1.5x}\text{Y}_x\text{TiO}_3$ ($x = 0, 0.02, 0.03, 0.04, 0.06, 0.08, 0.15$). Insert in Figure 6-1a shows the XRD pattern over 25° to 45° for the composition with $x = 0.08$.

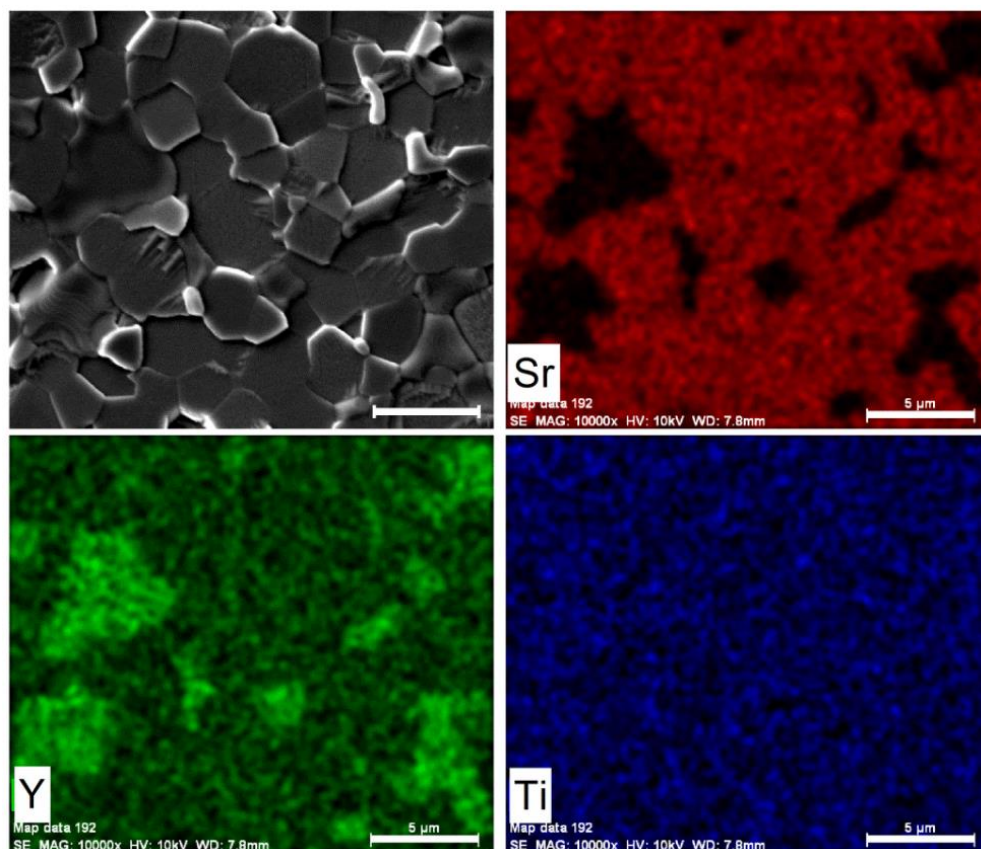


Figure 6-2 SEM micrograph and elemental distribution of Sr, Y, and Ti from EDS mapping of $\text{Sr}_{1-1.5x}\text{Y}_x\text{TiO}_3$ with $x = 0.15$. The scale bar indicates $5\ \mu\text{m}$.

Detailed SEM and EDS analysis have been carried out to examine the microstructure of $\text{Sr}_{1-1.5x}\text{Y}_x\text{TiO}_3$. The samples with $0 \leq x \leq 0.06$ show the well-defined polygonal grains with homogeneous grain sizes, while the samples with $x \geq 0.08$ contain both polygonal grains and liquid-like grains. Figure 6-2 shows the microstructure and EDS mapping of the sample with $x = 0.15$. It is noticed that Sr and Y elements are not uniformly distributed, while Ti element is homogeneously distributed in the micrograph. The grains with uneven distribution of Y and Sr elements appear to be impurity phase and have been further examined by TEM analysis. The bright-field image and selected area electron diffraction patterns of this sample confirm the impurity phase as $\text{Y}_2\text{Ti}_2\text{O}_7$ (Figure 6-3). Grain 1 in Figure 6-3a is indexed based on $\text{Y}_2\text{Ti}_2\text{O}_7$ with $a = 0.915 \pm 0.003$ nm, while grain 2 is indexed based on SrTiO_3 with $a = 0.320 \pm 0.001$ nm. The lattice parameter a of a cubic structure is calculated by

$$a = d_{hkl} \times \sqrt{h^2 + k^2 + l^2} \quad \text{Equation 6-1}$$

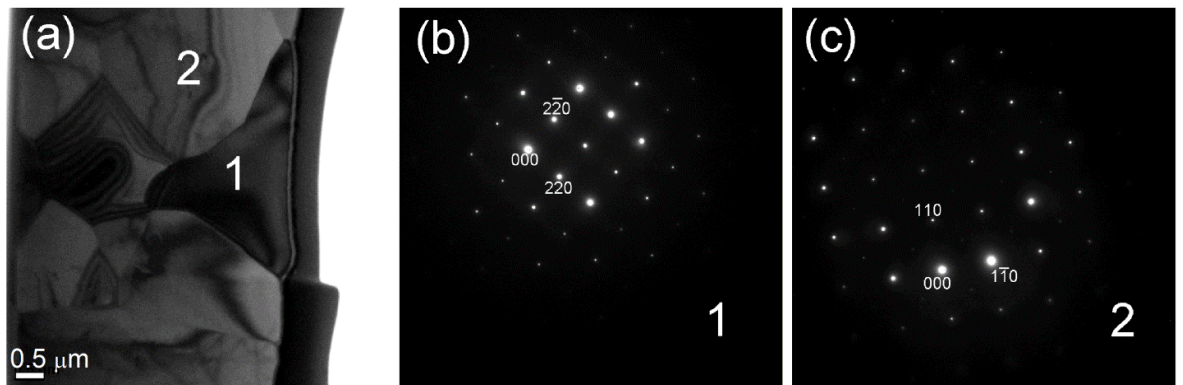


Figure 6-3 (a) Bright-field image, (b) SAED pattern of grain 1, and (c) SAED pattern of grain 2 of $\text{Sr}_{1-1.5x}\text{Y}_x\text{TiO}_3$ with $x = 0.15$.

The temperature dependence of the electrical conductivity of $\text{Sr}_{1-1.5x}\text{Y}_x\text{TiO}_3$ is shown in Figure 6-4a. The samples appear semiconducting below 150 °C and metallic above 200 °C. Below 150 °C, the electrical conduction of $\text{Sr}_{1-1.5x}\text{Y}_x\text{TiO}_3$ is contributed by the electron hopping between Ti^{3+} and Ti^{4+} via an oxygen ion. The mobility of electron-hopping process is thermally-activated; therefore, the electrical conductivity increases with increasing temperature. Above 200 °C, the electrons become delocalized and act as free electrons, leading to the metallic conduction. The electrical resistivity is also plotted as a function of the square of the absolute temperature as shown in Figure

6-4b. Above 200 °C, the resistivity versus temperature is well-characterized by a linear relationship, $\rho = \rho_0 + AT^2$. The quadratic temperature dependence indicates that the electron-electron scattering dominates the electron-phonon scattering process [158].

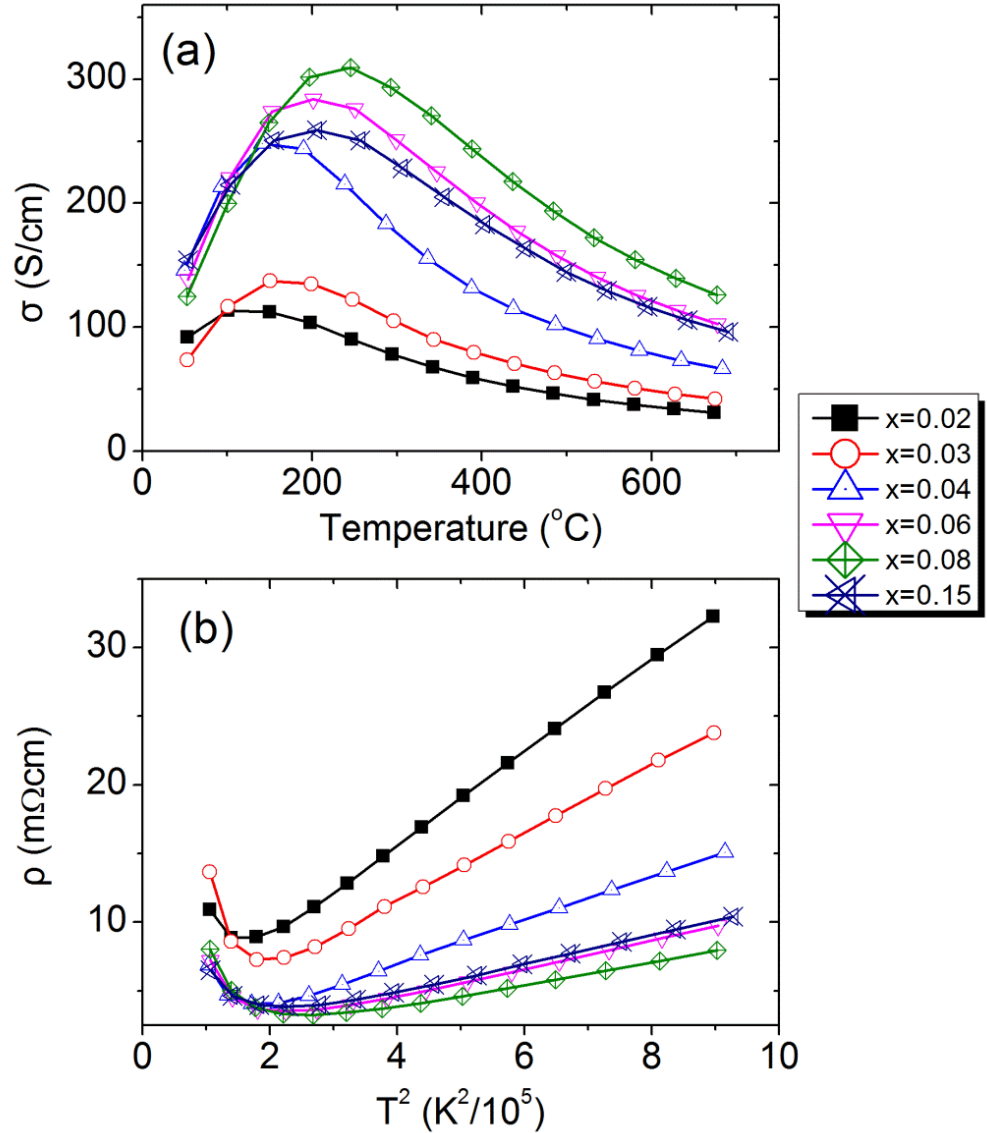


Figure 6-4 (a) Electrical conductivity (σ) versus temperature and (b) electrical resistivity (ρ) versus the square of the temperature (T) for Sr_{1-1.5x}Y_xTiO₃ ($x = 0.02, 0.03, 0.04, 0.06, 0.08, 0.15$).

The increasing electrical conductivity with increasing Y content above 200 °C is attributed to the increase in carrier concentration. The charge carriers for the electrical conduction are contributed by both Y substitution and oxygen vacancies in Sr_{1-1.5x}Y_xTiO₃ sintered in a reducing atmosphere. Each Y_{Sr}[•] generates one electron, while each oxygen vacancy (V_O^{••}) generates two electrons. In order to maintain charge

neutrality, the released electrons are transferred to Ti^{4+} ions, forming mixed $\text{Ti}^{3+}/\text{Ti}^{4+}$ ions. Therefore, the charge carrier concentration should be equal to the concentration of Ti^{3+} , which could be expressed as $n = [\text{Ti}^{3+}] = [\text{Y}_{\text{Sr}}^{\bullet}] + 2[\text{V}_{\text{O}}^{\bullet\bullet}]$. The concentration of oxygen vacancies could be calculated based on Equation 6-2.

$$[\text{V}_{\text{O}}^{\bullet\bullet}] = \delta = \frac{\Delta m/A_{\text{O}}}{m_{\text{ox}}/A_{\text{YSTO}}} \quad \text{Equation 6-2}$$

where δ is the oxygen deficiency per formula unit, m_{ox} is the weight of the oxidized sample after annealing, Δm is the weight gain after annealing the sample in oxygen, A_{O} is the atomic weight of oxygen, and A_{YSTO} is the atomic weight of the $\text{Sr}_{1-1.5x}\text{Y}_x\text{TiO}_3$. For a clear comparison, oxygen deficiency, charge carrier concentration (i.e., $[\text{Ti}^{3+}]$), and electrical conductivity as a function of Y content are plotted in Figure 6-5. It is clear that in the range $0.02 \leq x \leq 0.08$ the electrical conductivity increases proportionally to $[\text{Ti}^{3+}]$. Although a further increase in x leads to an increase in $[\text{Ti}^{3+}]$, the electrical conductivity decreases. It is due to the presence of $\text{Y}_2\text{Ti}_2\text{O}_7$ which blocks the conduction path as it possesses a much lower electrical conductivity [159].

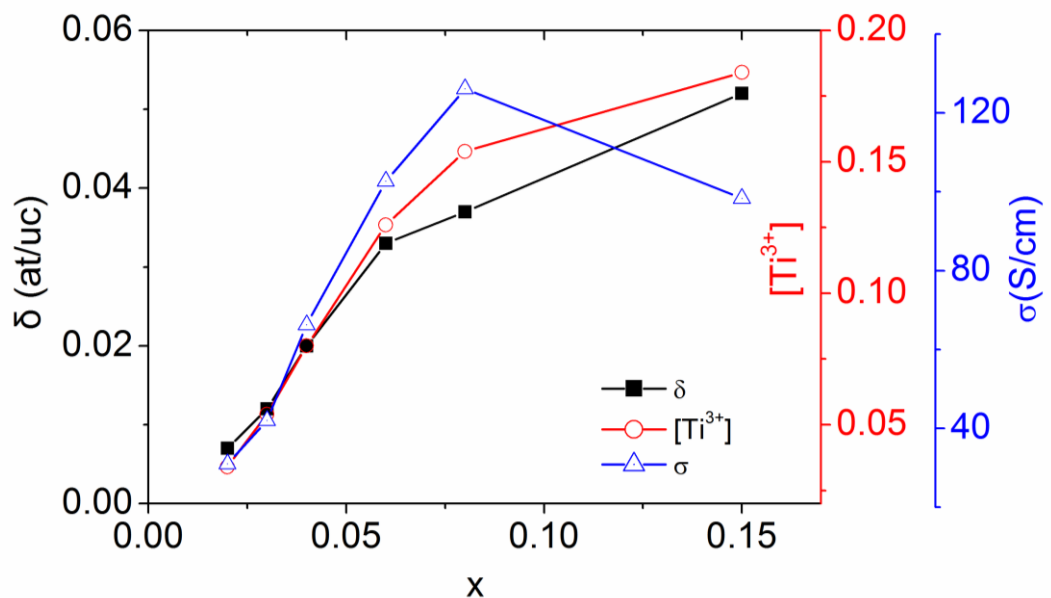


Figure 6-5 Oxygen deficiency δ , concentration of Ti^{3+} , and the electrical conductivity (σ) at 680 °C of $\text{Sr}_{1-1.5x}\text{Y}_x\text{TiO}_3$ ($x = 0.02, 0.03, 0.04, 0.06, 0.08, 0.15$).

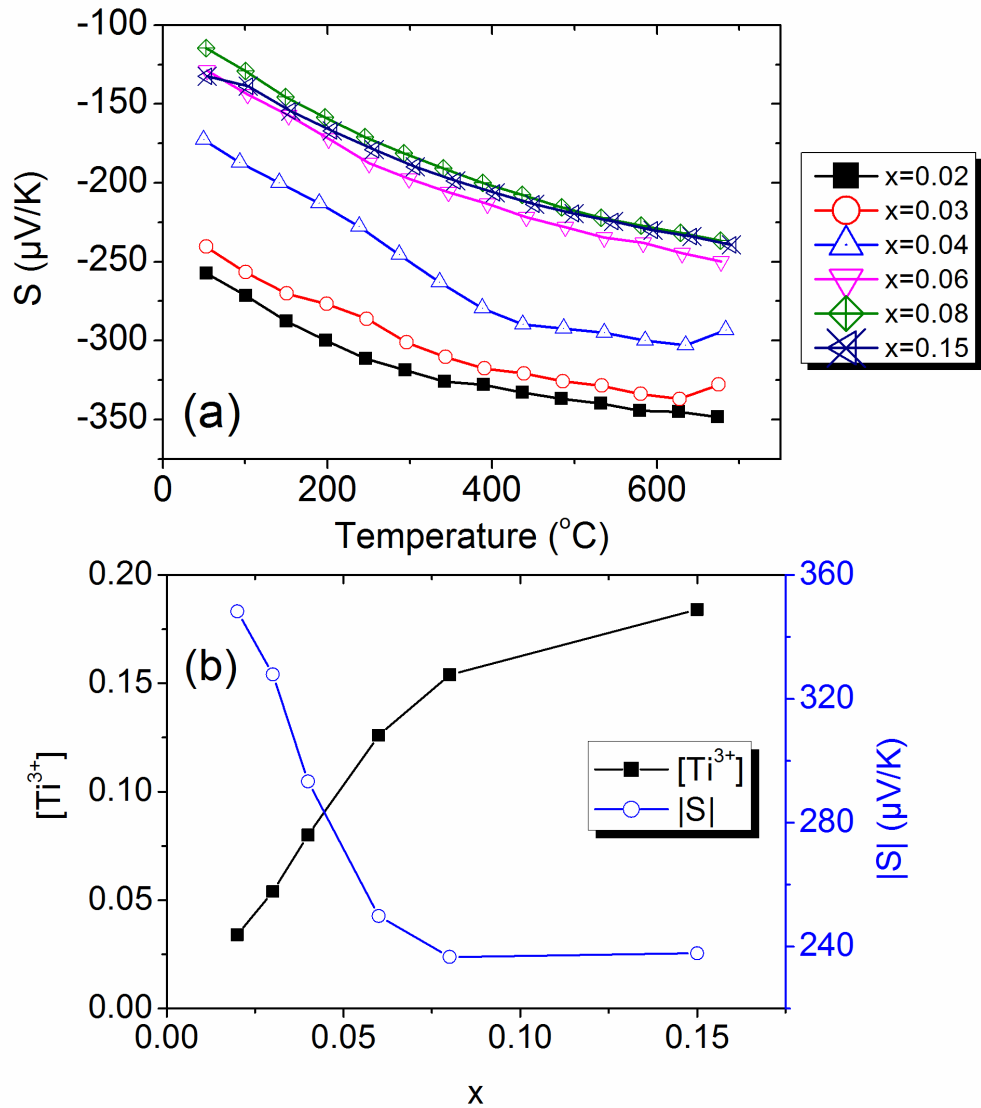


Figure 6-6 (a) Seebeck coefficient (S) versus temperature and (b) concentration of Ti^{3+} and the absolute values of S ($|S|$) at 680 $^{\circ}\text{C}$ versus x for $\text{Sr}_{1-1.5x}\text{Y}_x\text{TiO}_3$ ($x = 0.02, 0.03, 0.04, 0.06, 0.08, 0.15$).

The values of the Seebeck coefficient are negative over the entire temperature range (Figure 6-6a), indicating of n-type conduction. The absolute value of the Seebeck coefficient ($|S|$) initially decreases with increasing x up to $x = 0.08$ due to the increased carrier concentration, as shown in Figure 6-6b. A further increase in x has no effect on the Seebeck coefficient. This is due to the fact that the main conducting phase in the compositions with $0.08 \leq x \leq 0.15$ is almost the same, which has been evidenced by the XRD analysis.

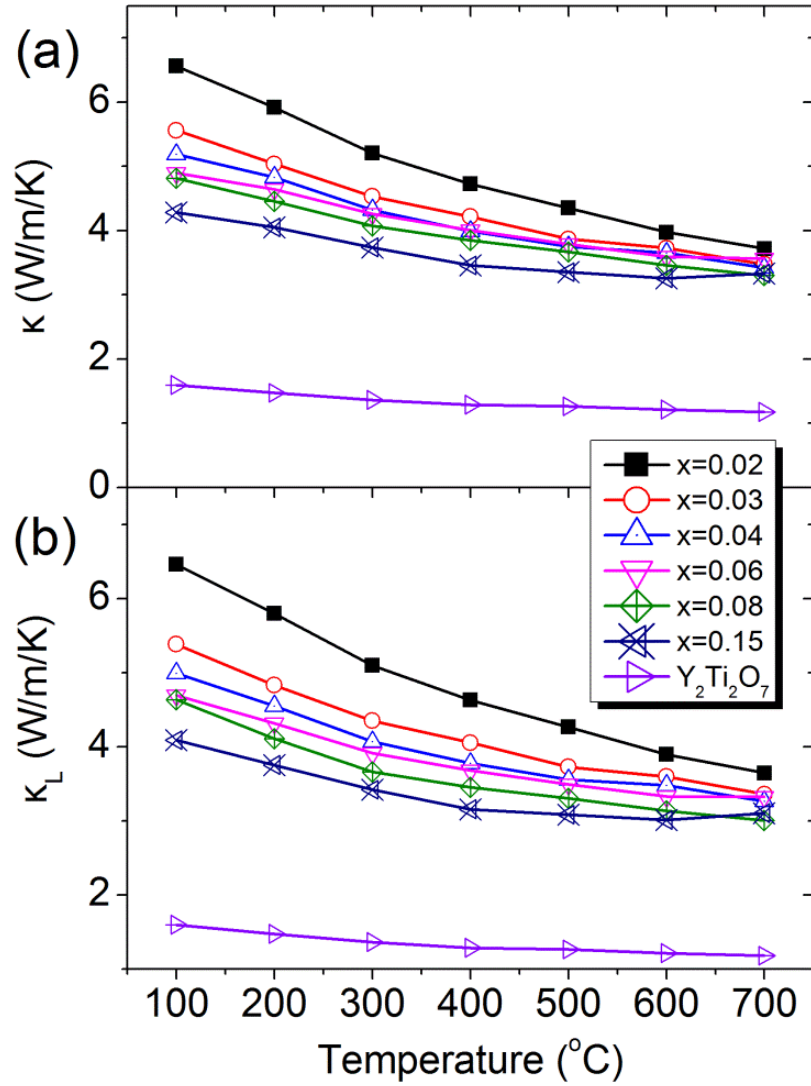


Figure 6-7 (a) Thermal conductivity (κ) and (b) lattice thermal conductivity (κ_L) versus temperature for $\text{Sr}_{1-1.5x}\text{Y}_x\text{TiO}_3$ ($x = 0.02, 0.03, 0.04, 0.06, 0.08, 0.15$). For a comparison, the data for $\text{Y}_2\text{Ti}_2\text{O}_7$ is also included in Figure 6-7.

Temperature dependence of the thermal conductivity (κ) and lattice thermal conductivity (κ_L) of $\text{Sr}_{1-1.5x}\text{Y}_x\text{TiO}_3$ are shown in Figure 6-7a and b, respectively. The thermal conductivity decreases with increasing temperature, indicating of lattice scattering dominated thermal conductivity. The electronic thermal conductivity can be calculated from the Wiedemann-Franz law, $\kappa_e = \sigma LT$, where L is the Lorenz number ($L = 2.44 \times 10^{-8} \text{ W}\Omega\text{K}^{-2}$). The lattice thermal conductivity (κ_L) can be obtained by $\kappa_L = \kappa - \kappa_e$. Since the electrical conductivity of $\text{Y}_2\text{Ti}_2\text{O}_7$ is very low, the electronic thermal conductivity of it could be neglected in the calculation, i.e. $\kappa_L = \kappa$. The lattice thermal conductivity is reduced with increasing x , as shown in Figure 6-7b.

Within the solubility limit of Y^{3+} in $SrTiO_3$, the decreased lattice thermal conductivity with increasing Y content is attributed to the increase of lattice straining due to Y doping and oxygen vacancies. The decreased lattice thermal conductivity with increasing Y content is associated with the increased lattice straining. Lattice distortion is introduced into $SrTiO_3$ by doping Y due to their different ionic radii, as verified by the change in lattice parameter (Figure 6-1b). Disorder parameter (Γ) is used to depict the effect of lattice distortion on the lattice thermal conductivity as shown in Equation 6-3.

$$\frac{\kappa_L}{\kappa_{OL}} \propto \frac{1}{\Gamma} \quad \text{Equation 6-3}$$

where κ_L is the disordered lattice thermal conductivity due to point defects, and κ_{OL} is the ordered lattice thermal conductivity without defects. The disorder parameter Γ is affected by the mass scattering parameter and the strain scattering parameter, as shown in Equation 6-4 [44].

$$\Gamma = \sum_i \Gamma_i \text{ where } \Gamma_i = x_i \left[\left(\frac{\Delta M}{M} \right)^2 + \varepsilon \left(\frac{\Delta \delta}{\delta} \right)^2 \right] \quad \text{Equation 6-4}$$

where Γ is the disorder parameter, x_i is the fractional concentration of the component i (Y) of the material, M and ΔM are the atomic weight and atomic weight difference between the dopant and original lattice atom, δ and $\Delta \delta$ are the ionic radii and ionic radii difference between the dopant and original lattice atom, ε is an adjustable parameter. It is evident that the strain scattering parameter is increased with increasing Y content, resulting in a reduced lattice thermal conductivity.

On the other hand, the reduction in lattice thermal conductivity with increasing Y content could also be attributed to the enhanced phonon scattering with oxygen vacancies. It has been demonstrated that oxygen vacancies can effectively scatter phonons in La-doped $SrTiO_3$ due to the comparable size of oxygen vacancies and wavelength of the phonons [160,161]. As indicated in Figure 6-5, the oxygen deficiency increases with increasing x . Therefore a decrease in lattice thermal conductivity with increasing Y content is expected.

It is interesting to note that even though the concentration of dopants and oxygen vacancies remain almost unchanged in the compositions with $0.08 \leq x \leq 0.15$, the lattice

thermal conductivity is further decreased. It is due to the formation of $Y_2Ti_2O_7$ in Y-doped $SrTiO_3$ above the solubility limit. $Y_2Ti_2O_7$ possesses significantly low thermal conductivity (Figure 6-7) and therefore results in a decrease in the lattice thermal conductivity.

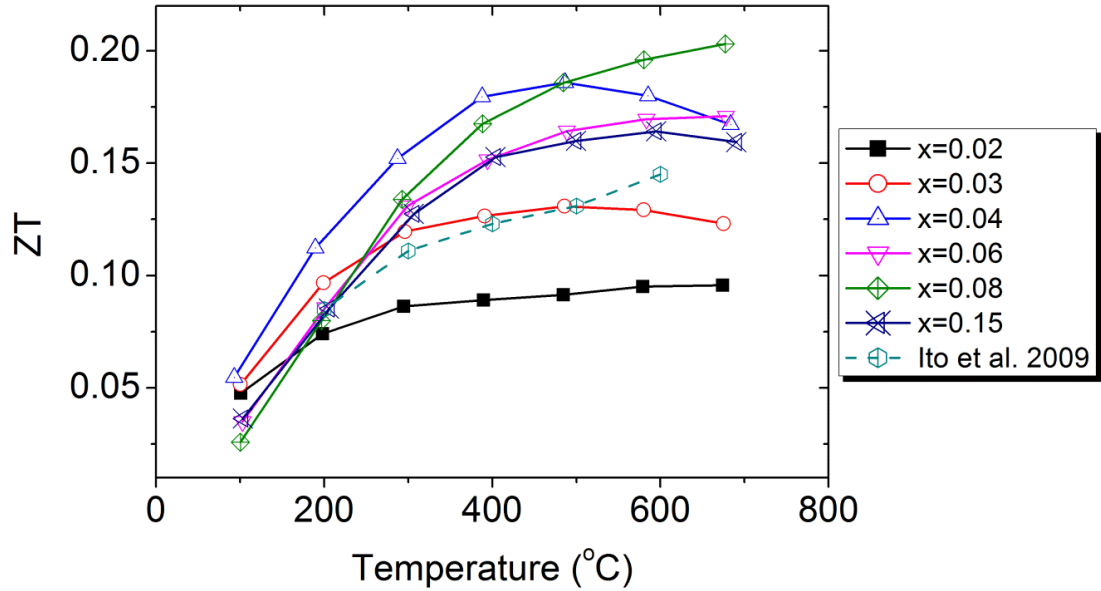


Figure 6-8 Thermoelectric figure of merit (ZT) versus temperature for $Sr_{1-1.5x}Y_xTiO_3$ ($x = 0.02, 0.03, 0.04, 0.06, 0.08, 0.15$). The dash line ($Sr_{0.9}Y_{0.1}TiO_3$) is cited from work of others [162].

ZT values of $Sr_{1-1.5x}Y_xTiO_3$ were calculated by $ZT = \sigma S^2 T / \kappa$. Temperature dependence of ZT is shown in Figure 6-8. ZT increases with increasing x up to $x = 0.08$, and decreases with a further increase of x above 300 °C. Although $Y_2Ti_2O_7$ is effective in reducing the thermal conductivity, it deteriorates the electrical conductivity and therefore results in a decrease in ZT . The sample with the nominal composition $Sr_{0.88}Y_{0.08}TiO_3$ exhibits the highest ZT , ~ 0.20 at 680 °C. At 600 °C, ZT of $Sr_{0.88}Y_{0.08}TiO_3$ is increased by 35% over that of $Sr_{0.9}Y_{0.1}TiO_3$ prepared by polymerized complex method combined with hot pressing [162].

6.3.2 Effects of La content and Sr deficiency on the crystal phase, microstructure, and thermoelectric properties of $\text{Sr}_{1-1.5x}\text{La}_x\text{TiO}_3$ ($0 \leq x \leq 0.4$)

$\text{Sr}_{1-1.5x}\text{La}_x\text{TiO}_3$ with $0 \leq x \leq 0.12$ are found to be single-phase cubic perovskites with space group $\text{Pm}\bar{3}\text{m}$, as shown in Figure 6-9. Peak splitting at $2\theta \sim 46.5^\circ$ and $\sim 77.2^\circ$ appears in the compositions with higher La content ($0.25 \leq x \leq 0.40$), indicating of a decreased lattice symmetry from cubic to tetragonal due to distorted TiO_6 octahedral [109,163]. It has been reported that $\text{La}_2\text{Ti}_2\text{O}_7$ -like lamellar impurities with chemical composition $\text{La}_4\text{Sr}_{n-4}\text{Ti}_n\text{O}_{3n+2}$ appear in $\text{Sr}_{1-x}\text{La}_x\text{TiO}_3$ with $0.15 < x \leq 0.4$ due to the segregation of overstoichiometric La and oxygen atoms.

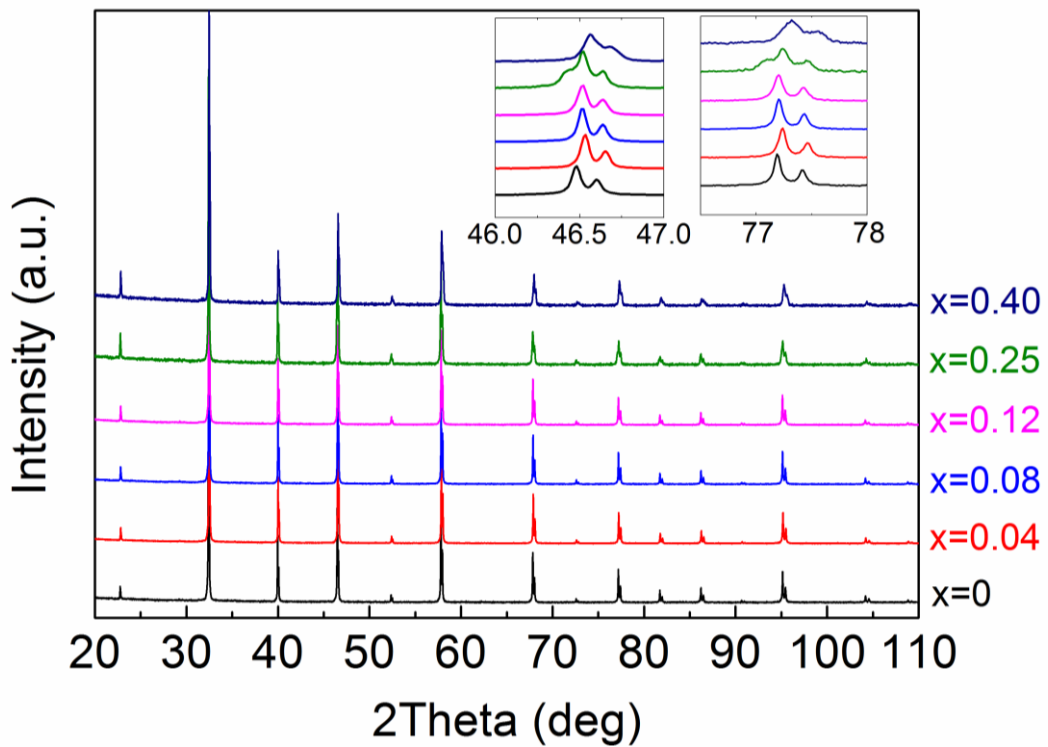


Figure 6-9 XRD patterns of $\text{Sr}_{1-1.5x}\text{La}_x\text{TiO}_3$ ($x = 0, 0.04, 0.08, 0.12, 0.25, 0.40$). Insert shows the XRD patterns over 46° to 47° and 76.5° to 78° , respectively.

The lattice parameters of the samples were calculated by Rietveld refinement. The refinement of compositions with $0 \leq x \leq 0.12$ and $0.25 \leq x \leq 0.40$ were performed with space group $\text{Pm}\bar{3}\text{m}$ and I4/mcm , respectively. The structural parameters from the refinement are shown in Table 6-1.

Table 6-1 Structural parameters from Rietveld refinements of powder XRD data of $\text{Sr}_{1-1.5x}\text{La}_x\text{TiO}_3$ ($x = 0, 0.04, 0.08, 0.12, 0.25, 0.40$).

Sample	$x = 0$	$x = 0.04$	$x = 0.08$	$x = 0.12$	$x = 0.25$	$x = 0.40$
Symmetry	$\text{Pm}\bar{3}\text{m}$	$\text{Pm}\bar{3}\text{m}$	$\text{Pm}\bar{3}\text{m}$	$\text{Pm}\bar{3}\text{m}$	I4/mcm	I4/mcm
z	1	1	1	1	4	4
a (Å)	3.90511(1)	3.90588(1)	3.90712(1)	3.90770(1)	5.52082(5)	5.5185(1)
b (Å)	-	-	-	-	-	-
c (Å)	-	-	-	-	7.8222(1)	7.8006(2)
V (Å ³)	59.5525(3)	59.5877(3)	59.6445(3)	59.6710(3)	238.417(4)	237.56(1)
$R_p/\%$	2.48	2.47	2.56	2.44	4.51	5.62
$R_{wp}/\%$	3.51	3.56	3.73	3.35	5.66	7.13
g.o.f	1.61	1.84	1.86	1.62	1.18	1.26

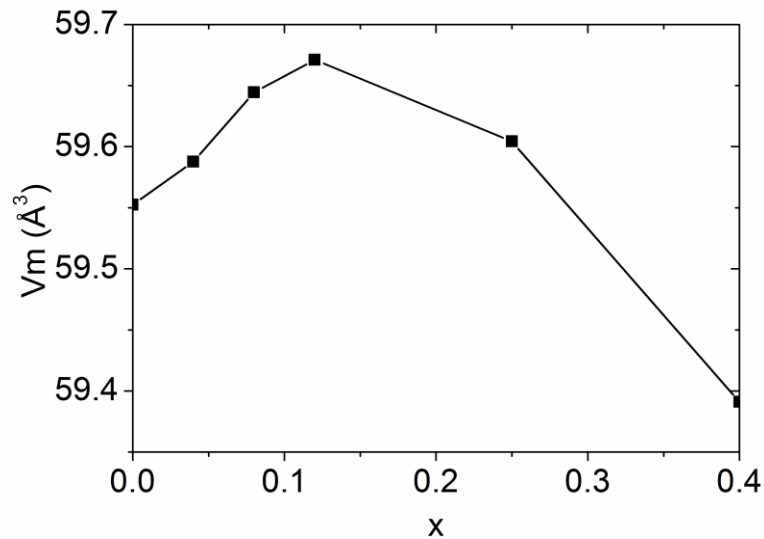


Figure 6-10 Molar cell volume (V_m) as a function of x for $\text{Sr}_{1-1.5x}\text{La}_x\text{TiO}_3$ ($x = 0, 0.04, 0.08, 0.12, 0.25, 0.40$).

Although La^{3+} possesses a smaller ionic radius than Sr^{2+} , the lattice parameter (a) increases systematically with increasing La content up to $x = 0.12$ (Table 6-1). For the simplicity of comparison between different crystal symmetries, the molar cell volume is defined as $V_m = V_{\text{cell}}/z$, where V_{cell} is the unit cell volume and z the number of formula units in the unit cell. It is interesting to note that the molar cell volume increases with La content up to $x = 0.25$ and then decreases with a further increase in La content (Figure 6-10). The mechanisms are discussed in the following.

The charge neutrality in La-doped SrTiO_3 sintered in reducing atmosphere is achieved by the formation of mixed $\text{Ti}^{3+}/\text{Ti}^{4+}$ ions. Ti^{3+} has a larger ionic radius than

Ti⁴⁺; therefore, the unit cell volume is influenced by the concentration of both La³⁺ and Ti³⁺. The formation of Ti³⁺ is promoted by both the La substitution (La_{Sr}[•]) and the oxygen vacancies (V_O^{••}). The Ti³⁺ concentration can therefore be written as

$$[\text{Ti}^{3+}] = [\text{La}_{\text{Sr}}^{\bullet}] + 2[\text{V}_{\text{O}}^{\bullet\bullet}] \quad \text{Equation 6-5}$$

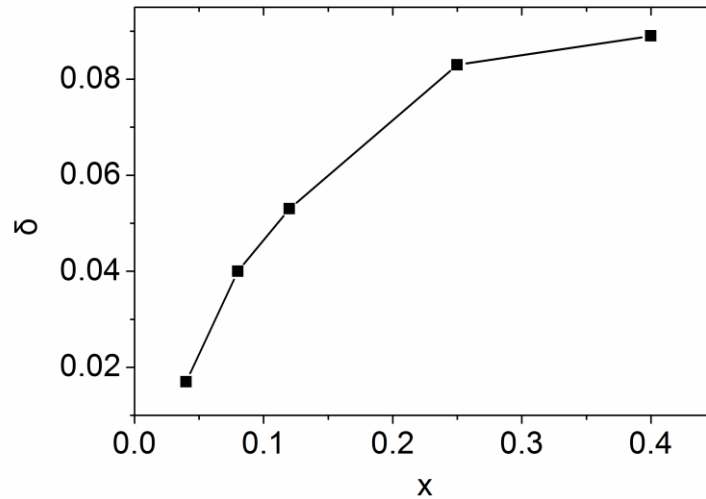


Figure 6-11 Oxygen deficiency (δ) versus x for $\text{Sr}_{1-1.5x}\text{La}_x\text{TiO}_3$ ($x = 0, 0.04, 0.08, 0.12, 0.25, 0.40$).

The ionic radii of 12-fold coordinated La³⁺ and Sr²⁺ are 1.36 and 1.44 Å, respectively, while the ionic radii of 6-fold coordinated Ti³⁺ and Ti⁴⁺ are 0.67 and 0.605 Å, respectively. It is obvious that the molar cell volume increases with increasing oxygen deficiency, since the Ti³⁺ produced by La substitution almost cancels out each other. Besides, the SrTiO₃ with more oxygen deficiency tends to have a larger unit cell volume due to the reduced Coulombic force [164]. The oxygen deficiency can be calculated from the weight increase of samples annealed in oxygen by Equation 6-6.

$$[\text{V}_{\text{O}}^{\bullet\bullet}] = \delta = \frac{\Delta m / A_{\text{O}}}{m_{\text{ox}} / A_{\text{LaSTO}}} \quad \text{Equation 6-6}$$

where δ is the oxygen deficiency per formula unit, m_{ox} is the weight of the oxidized sample after annealing, Δm is the weight gain after annealing the sample in oxygen, A_{O} is the atomic weight of oxygen, and A_{LaSTO} is the atomic weight of the $\text{Sr}_{1-1.5x}\text{La}_x\text{TiO}_3$. As shown in Figure 6-11, the oxygen deficiency increases with La content up to $x =$

0.25, and remains almost unchanged at higher La content. Therefore, in the range $0.04 \leq x \leq 0.12$ the oxygen deficiency is the major influencing factor dominating the molar cell volume, whereas in the range $0.25 \leq x \leq 0.40$ the La substitution is the major factor. Consequently, the molar cell volumes increases with x up to $x = 0.25$, and then decreases with a further increase in x .

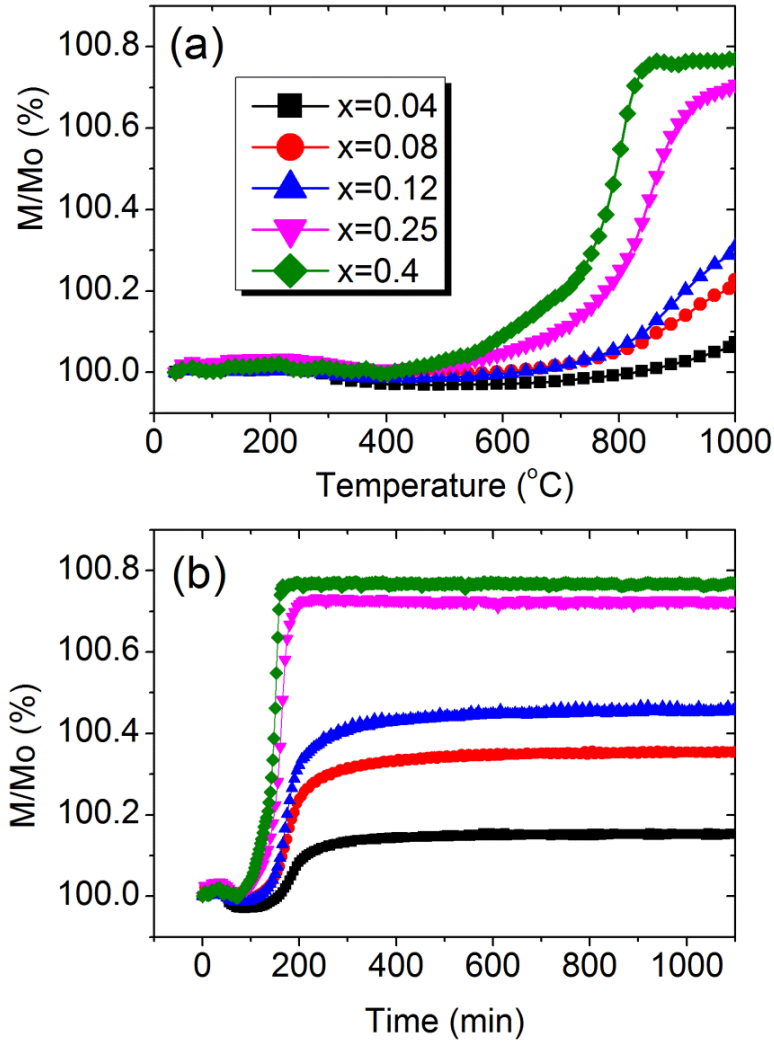


Figure 6-12 Relative weight change of $\text{Sr}_{1-1.5x}\text{La}_x\text{TiO}_3$ ($x = 0, 0.04, 0.08, 0.12, 0.25, 0.40$) on heating in flowing oxygen as a function of (a) temperature and (b) time.

The thermogravimetric results for the calculation of oxygen deficiency are plotted as a function of temperature and time in Figure 6-12a and b, respectively. It is obvious that the oxidation starts at a lower temperature for samples with a higher x , i.e. ~ 700 °C for sample with $x = 0.04$ to ~ 400 °C for sample with $x = 0.40$ (Figure 6-12a). Moreover, the thermodynamic equilibrium of samples with $0.25 \leq x \leq 0.40$ is achieved at

a lower temperature for a shorter duration than the samples with lower x values (Figure 6-12b). Different oxidation behaviors were observed in the samples with $0.04 \leq x \leq 0.12$ and $0.25 \leq x \leq 0.40$, which confirmed the presence of $\text{La}_2\text{Ti}_2\text{O}_7$ -like lamellar compounds in SrTiO_3 with $0.25 \leq x \leq 0.40$ [163]. The generation of lamellar compounds is promoted by increasing La concentration, from point defects at low La concentration to short-range planar defects at high La concentration.

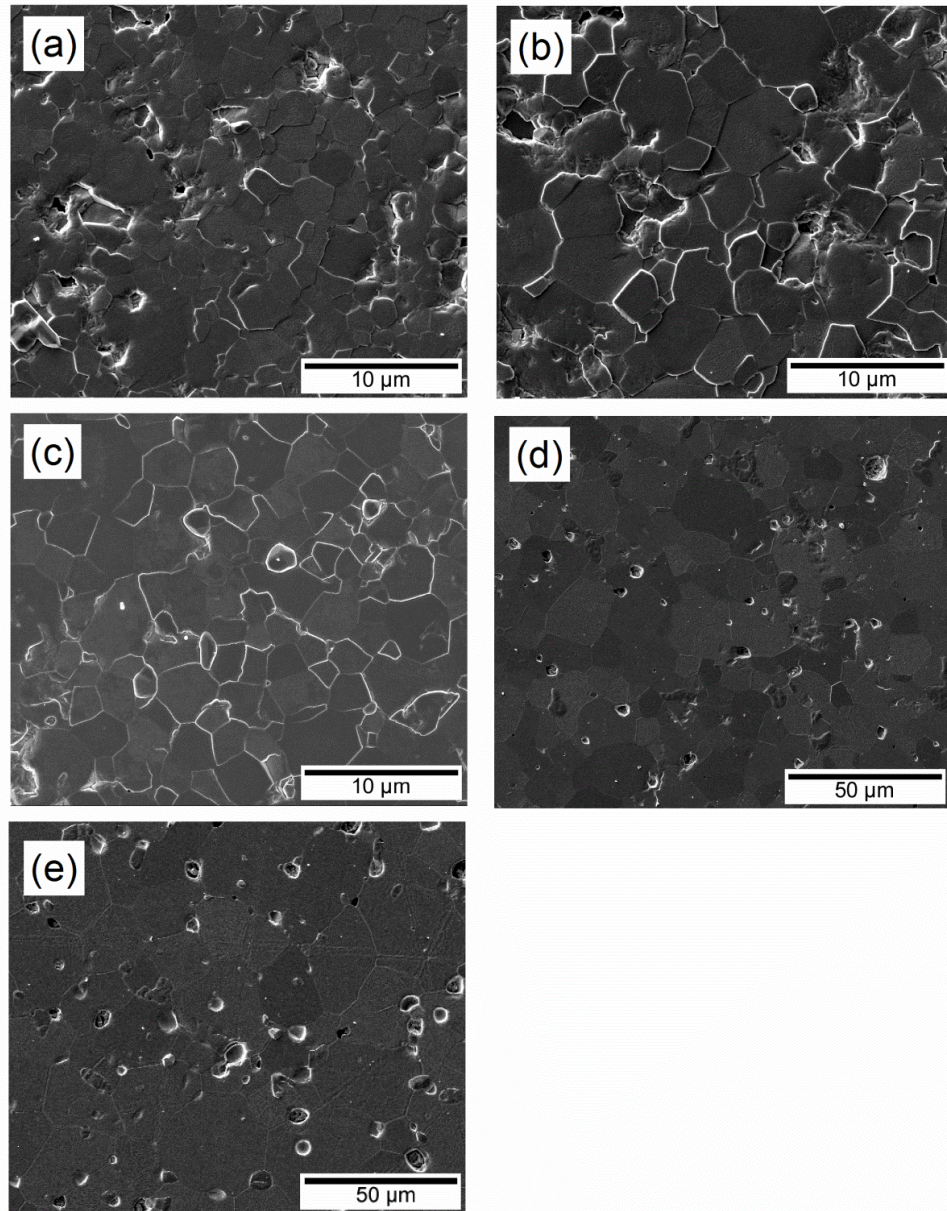


Figure 6-13 SEM micrographs of $\text{La}_x\text{Sr}_{1-1.5x}\text{TiO}_3$. (a) $x = 0.04$, (b) $x = 0.08$, (c) $x = 0.12$, (d) $x = 0.25$, and (e) $x = 0.40$.

SEM micrographs in Figure 6-13 show that all compositions show high relative density. Moreover, the average grain size for the samples with $0 < x \leq 0.12$ are similar, while it becomes much larger for the samples with $0.25 \leq x \leq 0.40$.

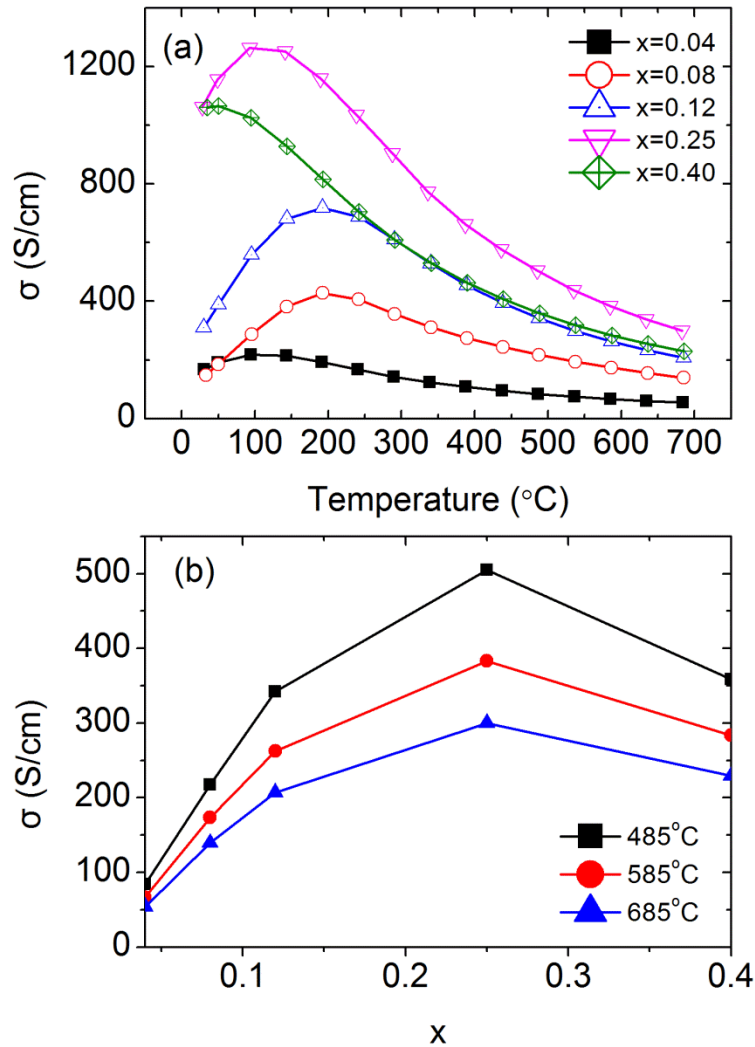


Figure 6-14 Electrical conductivity (σ) versus (a) temperature and (b) La content (x) for $\text{Sr}_{1-1.5x}\text{La}_x\text{TiO}_3$ ($x = 0.04, 0.08, 0.12, 0.25, 0.40$).

Temperature and La content dependence of electrical conductivity are shown in Figure 6-14a and b, respectively. The compositions with $0.04 \leq x \leq 0.25$ show semiconducting-metallic transition in the electrical conduction, while the composition with $x = 0.4$ show metallic conduction over the whole temperature range. The semiconducting conduction is induced by the thermally-activated electron hopping between Ti^{3+} and Ti^{4+} ions. Above a certain temperature, the electrons become delocalized and act as free charge carriers, thus exhibiting metallic conduction.

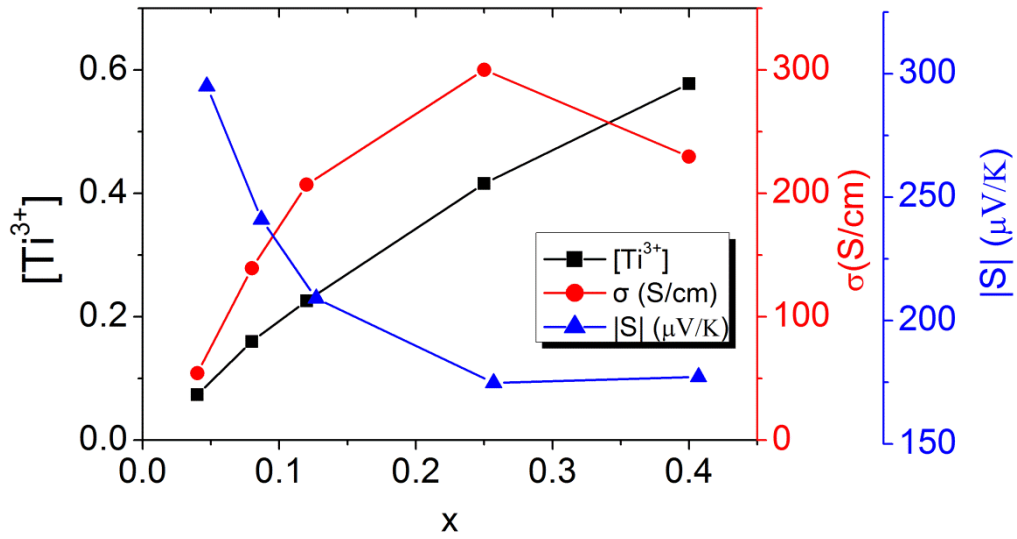


Figure 6-15 Concentration of Ti^{3+} , the electrical conductivity (σ) at 680 °C, and the absolute values of Seebeck coefficient ($|S|$) at 680 °C versus x for $\text{Sr}_{1-1.5x}\text{La}_x\text{TiO}_3$ ($x = 0.04, 0.08, 0.12, 0.25, 0.40$).

The electrical conductivity of $\text{Sr}_{1-1.5x}\text{La}_x\text{TiO}_3$ increases with x up to $x = 0.25$ and decreases at higher x values as shown in Figure 6-14b. The electrons in $\text{Sr}_{1-1.5x}\text{La}_x\text{TiO}_3$ are contributed by both La substitution and oxygen vacancies. The Ti^{3+} concentration estimated by Equation 6-5 increases with increasing x as shown in Figure 6-15, leading to an increase in the electrical conductivity. However, discrepancy appears in the composition with $x = 0.4$. It is likely due to the formation of the highly resistive lamellar compounds [163]. Therefore the actual Ti^{3+} concentration of compositions with $0.25 \leq x \leq 0.40$ might be lower than the values plotted in Figure 6-15, which is due to the presence of La-rich lamellar phases.

Temperature and La content dependence of the Seebeck coefficient of $\text{Sr}_{1-1.5x}\text{La}_x\text{TiO}_3$ is shown in Figure 6-16a and b, respectively. The negative values of the Seebeck coefficient indicate the major charge carriers are electrons. The absolute value of the Seebeck coefficient ($|S|$) decreases with increasing x up to $x = 0.25$ due to the increased Ti^{3+} concentration, as shown in Figure 6-15. $|S|$ becomes almost unchanged with x above $x = 0.25$. It is likely due to the saturation of La in SrTiO_3 above $x = 0.25$. The secondary lamellar phase is highly resistive and thus doesn't contribute to the Seebeck coefficient.

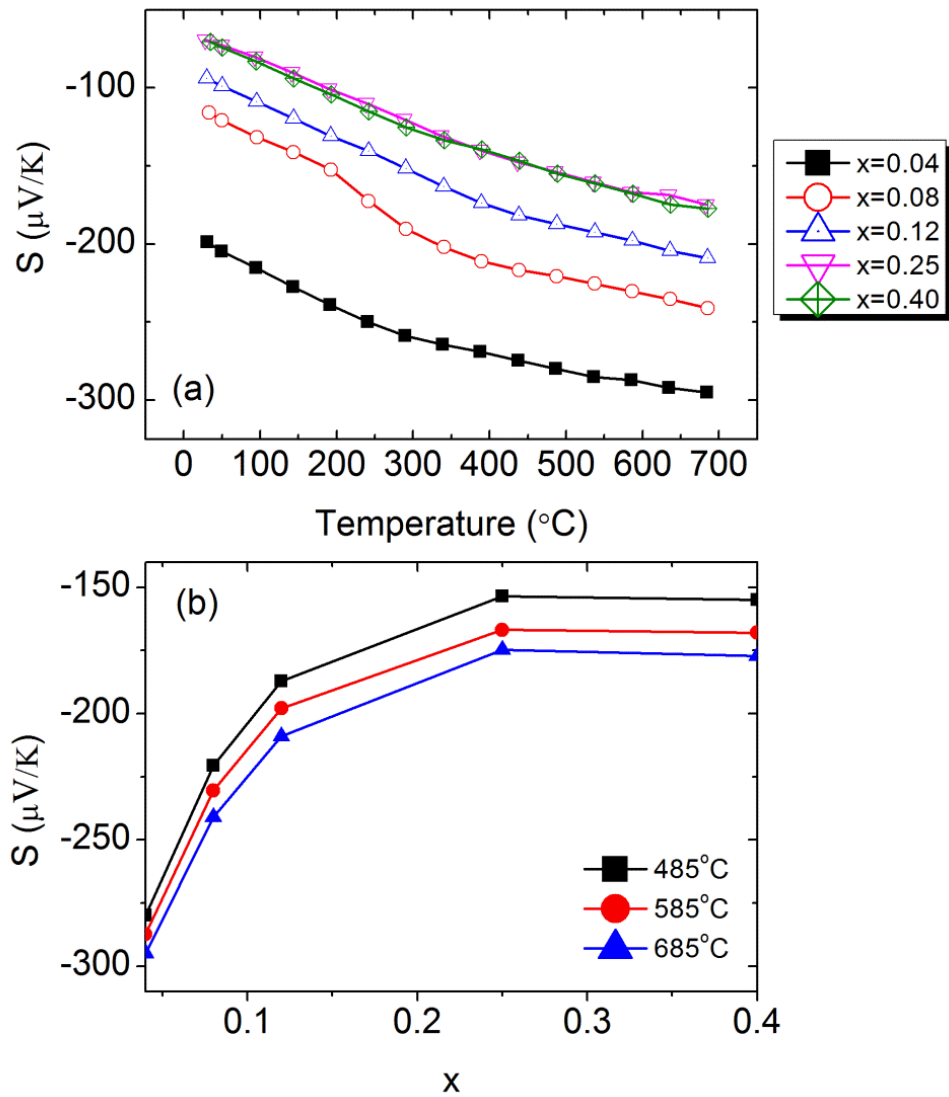


Figure 6-16 Seebeck coefficient (S) versus (a) temperature and (b) La content (x) for $\text{Sr}_{1-1.5x}\text{La}_x\text{TiO}_3$ ($x = 0.04, 0.08, 0.12, 0.25, 0.40$).

Temperature dependence of the thermal conductivity and lattice thermal conductivity of $\text{Sr}_{1-1.5x}\text{La}_x\text{TiO}_3$ is shown in Figure 6-17a and b, respectively. The thermal conductivity decreases with increasing temperature for the compositions with $0.04 \leq x \leq 0.25$, indicating of phonon scattering dominated behavior. However, the composition with $x = 0.4$ remains almost unchanged with temperature. Introducing La into SrTiO_3 with $0.04 \leq x \leq 0.25$ is effective in reducing the thermal conductivity over the temperature range $100 \text{ }^{\circ}\text{C} \leq T \leq 400 \text{ }^{\circ}\text{C}$. The lowest thermal conductivity is achieved in the composition with $x = 0.4$, possibly due to the presence of lamellar compounds. It implies that the La-rich lamellar compounds exhibit both low electrical and thermal conductivity. The lattice thermal conductivity has been calculated by

Wiedemann-Franz law and is shown in Figure 6-17b. The lattice thermal conductivity decreases with increasing La content.

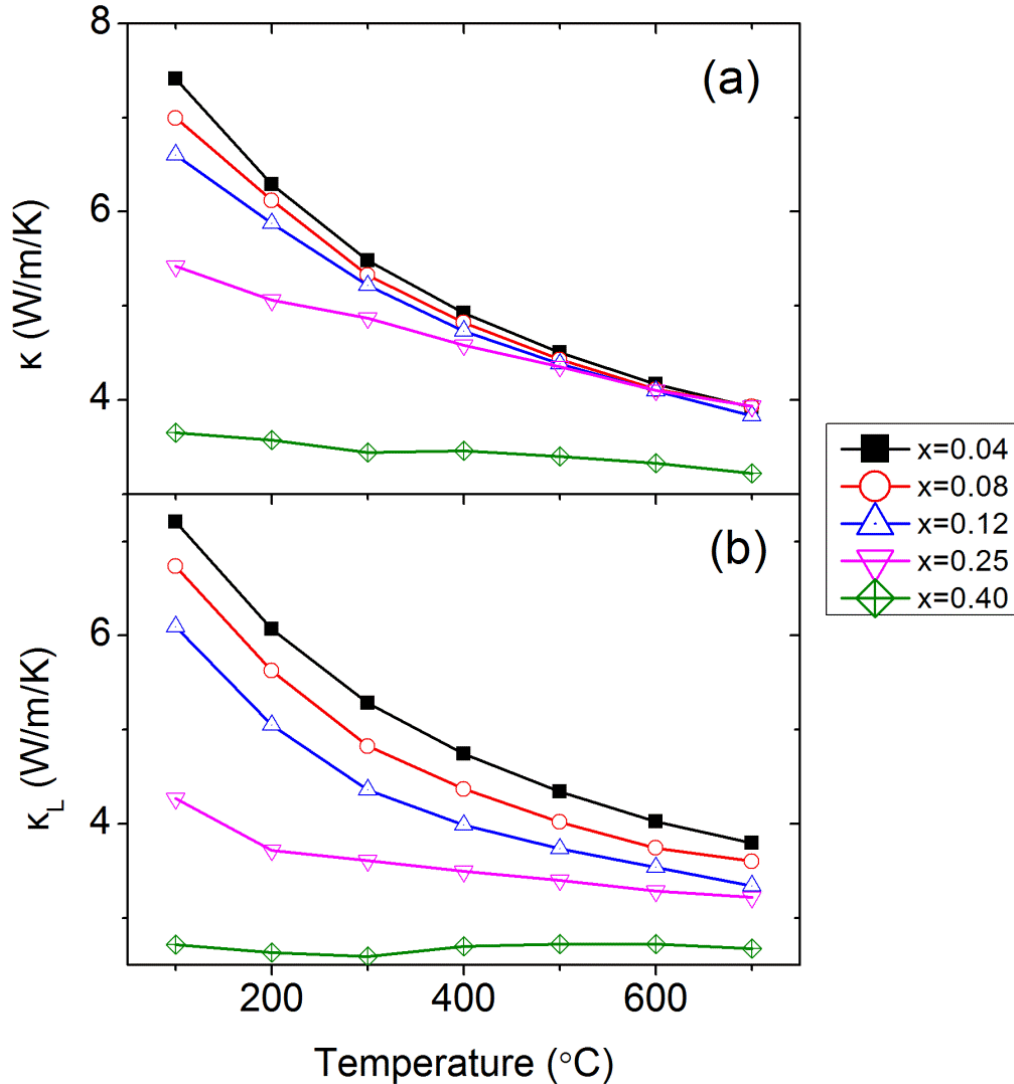


Figure 6-17 Temperature dependent of the thermal conductivity of $\text{Sr}_{1-1.5x}\text{La}_x\text{TiO}_3$ ($x = 0.04, 0.08, 0.12, 0.25, 0.40$).

Comparison has been made between the lattice thermal conductivity of $\text{Sr}_{1-1.5x}\text{La}_x\text{TiO}_3$ and $\text{Sr}_{1-1.5x}\text{Y}_x\text{TiO}_3$ as shown in Figure 6-18. The lattice thermal conductivity is more effectively reduced in the Y-doped SrTiO_3 compared with La-doped SrTiO_3 of the same doping concentration. According to Equation 6-3 and Equation 6-4, it is due to the larger strain scattering parameter of Y-doped SrTiO_3 caused by the larger ionic radii difference between Y and Sr.

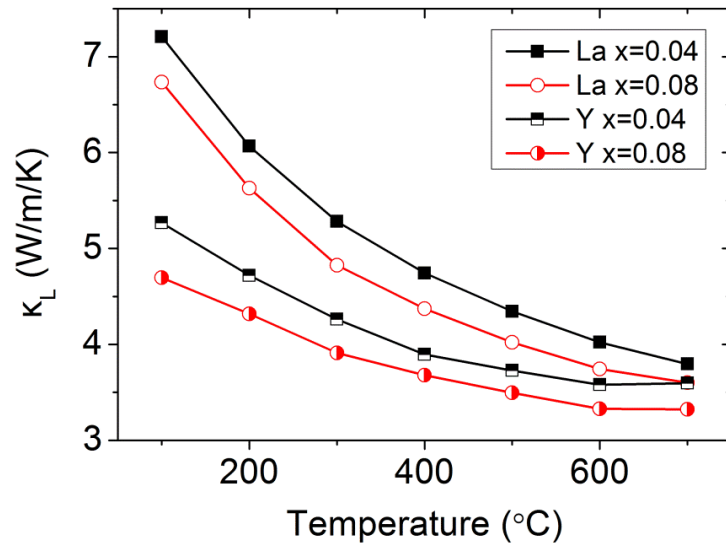


Figure 6-18 Temperature dependence of the lattice thermal conductivity of $\text{Sr}_{1-1.5x}\text{La}_x\text{TiO}_3$ and $\text{Sr}_{1-1.5x}\text{Y}_x\text{TiO}_3$ ($x = 0.04$ and 0.08).

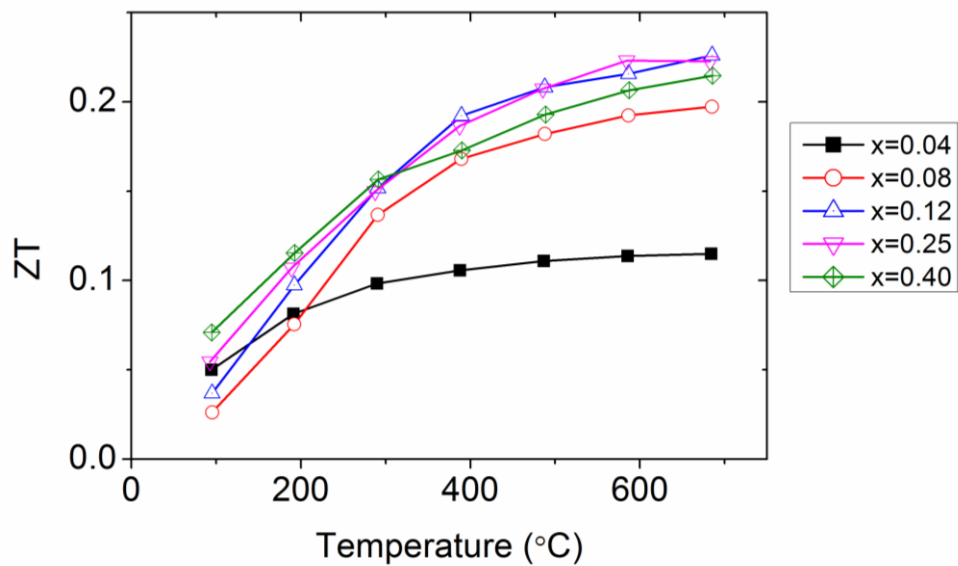


Figure 6-19 Temperature dependent of ZT of $\text{Sr}_{1-1.5x}\text{La}_x\text{TiO}_3$ ($x = 0.04, 0.08, 0.12, 0.25, 0.40$).

Temperature dependence of ZT of $\text{Sr}_{1-1.5x}\text{La}_x\text{TiO}_3$ is shown in Figure 6-19. ZT increases with increasing temperature for all compositions. Above $200\text{ }^\circ\text{C}$, ZT increases with increasing La content in the range $0.04 \leq x \leq 0.12$. Highest $ZT \sim 0.23$ at $684\text{ }^\circ\text{C}$ is obtained in the composition with $x = 0.12$. ZT remains unchanged with $x = 0.25$ and is reduced in the composition with $x = 0.4$. It indicates that although the existence of lamellar phases has no effect on the Seebeck coefficient, it results in a more substantial

decrease in the electrical conductivity than the thermal conductivity. Therefore a deteriorated ZT is observed in the composition with $x = 0.4$.

6.4 Summary

$\text{Sr}_{1-1.5x}\text{Y}_x\text{TiO}_3$ ($x = 0, 0.02, 0.03, 0.04, 0.06, 0.08, 0.15$) were systematically investigated with respect to the crystal phase, microstructure, and thermoelectric performance. Up to $x \sim 0.08$ of Y could be doped into SrTiO_3 as justified by the XRD analysis. The formation of $\text{Y}_2\text{Ti}_2\text{O}_7$ in $\text{Sr}_{1-1.5x}\text{Y}_x\text{TiO}_3$ with $x \geq 0.08$ was verified by SAED. The concentration of Ti^{3+} increases with increasing x up to $x = 0.08$, leading to the increase in both the electrical conductivity and the Seebeck coefficient. The lattice thermal conductivity was reduced with increasing Y content due to the increased strain scattering parameter and oxygen deficiency. The deteriorated thermoelectric performance of the compositions with $x > 0.08$ is attributed to the existence of $\text{Y}_2\text{Ti}_2\text{O}_7$, which possesses very poor electrical conductivity. The highest ZT value of 0.20 was achieved at 680 °C for $\text{Sr}_{0.88}\text{Y}_{0.08}\text{TiO}_3$.

The structural and thermoelectric properties of $\text{Sr}_{1-1.5x}\text{La}_x\text{TiO}_3$ ($x = 0, 0.04, 0.08, 0.12, 0.25, 0.4$) were also studied. The compositions with $0 < x \leq 0.12$ exhibited cubic structure, while the symmetry was reduced to tetragonal for the compositions with higher x possibly due to the appearance of $\text{La}_2\text{Ti}_2\text{O}_7$ -like lamellar compounds. The molar cell volume was closely associated with the oxygen deficiency. The difference in oxidation behavior in the composition with $0 < x \leq 0.12$ and $0.25 \leq x \leq 0.4$ verified the presence of lamellar compounds. Both the electrical conductivity and the Seebeck coefficient increased with increasing La content due to the increase in Ti^{3+} concentration. The composition with $x = 0.4$ exhibited low electrical and thermal conductivity due to the lamellar compounds. Maximum ZT of ~ 0.23 at 684 °C was obtained in the composition with $x = 0.12$.

Chapter 7 Thermoelectric properties of $\text{Sr}_x\text{Y}_{0.04}\text{TiO}_3$ ($0.92 \leq x \leq 1$) and $\text{Sr}_x\text{La}_{0.12}\text{TiO}_3$ ($0.82 \leq x \leq 0.9$)

7.1 Introduction

The general stability and doping flexibility of SrTiO_3 facilitate its investigation in fields of capacitors, photocatalysts, solid oxide fuel cells, and thermoelectricity. SrTiO_3 belongs to the transition metal oxides with ABO_3 stoichiometry and perovskite-type crystal structure. Pure SrTiO_3 possesses a wide bandgap and is an insulating material at room temperature. After introducing donor atoms and oxygen vacancies, SrTiO_3 becomes a promising n-type thermoelectric material. Superior thermoelectric performance has been demonstrated in lanthanide or niobium doped SrTiO_3 [25,104,107].

SrTiO_3 is known to be influenced by the cation nonstoichiometry (Sr/Ti ratio) in terms of microstructures [139,165,166], defect chemistry [103,167,168], dielectric properties [169], electrical conductivity [28,30,170], etc. It is generally accepted that the solubility of excess TiO_2 in SrTiO_3 is less than 0.5 mol% [103,165]. TiO_2 is incorporated into SrTiO_3 by the formation of Sr vacancies and O vacancies. Rutile or Magnéli TiO_2 retains in SrTiO_3 as a secondary phase above the solubility limit. Excess Sr in SrTiO_3 results in the formation of Ruddlesden-Popper phases in which the SrTiO_3 layers are interleaved with SrO layers [171]. Moreover, the electrical conductivity of SrTiO_3 depends on both A/B ratio and sintering atmosphere. High electrical conductivity could be achieved in the Sr-deficient ($A/B < 1$) donor-doped SrTiO_3 sintered in a reducing atmosphere [30].

To the best of our knowledge, there has been no systematic study regarding the effects of Sr/Ti ratio on the structural and thermoelectric properties of donor-doped SrTiO_3 . Therefore, the objective of the study is to investigate the influences of Sr content on the thermoelectric properties of Y- and La-doped SrTiO_3 . The solubility of Y in SrTiO_3 sintered at 1400 °C in a reducing atmosphere is ~ 4 at.% [29]. Hence, $\text{Sr}_x\text{Y}_{0.04}\text{TiO}_3$ ($x = 0.92, 0.94, 0.95, 0.96, 0.98, 1$) were prepared for the current study. According to our previous study, 12 at.% La in SrTiO_3 exhibits a high power factor. Therefore, $\text{Sr}_x\text{La}_{0.12}\text{TiO}_3$ ($x = 0.82, 0.86, 0.87, 0.88, 0.885, 0.9$) were synthesized. Oxygen vacancies have been reported to influence the electrical and thermal properties

of oxides [160,172]. Here, we adjusted the oxygen deficiency by sintering $\text{Sr}_x\text{La}_{0.12}\text{TiO}_3$ under a reducing atmosphere at different sintering temperatures. The oxygen deficiency was found to increase with increasing sintering temperature. We have demonstrated how Sr content affects the microstructure, phase constituents, and thermoelectric properties of $\text{Sr}_x\text{Y}_{0.04}\text{TiO}_3$ and $\text{Sr}_x\text{La}_{0.12}\text{TiO}_3$. A significant enhancement in ZT has been achieved in Sr-deficient compositions ($0.92 \leq x \leq 0.95$ for Y; $0.82 \leq x \leq 0.87$ for La).

7.2 Experimental procedure

$\text{Sr}_x\text{Y}_{0.04}\text{TiO}_3$ ($x = 0.92, 0.94, 0.95, 0.96, 0.98, 1$) were synthesized by conventional solid-state reaction method. The Sr-deficient or TiO_2 excess compositions are $\text{Sr}_x\text{Y}_{0.04}\text{TiO}_3$ with $0.92 \leq x \leq 0.95$, while the Sr-excess compositions are $\text{Sr}_x\text{Y}_{0.04}\text{TiO}_3$ with $0.98 \leq x \leq 1$. The starting powders were SrCO_3 (99.9%, Sigma Aldrich), TiO_2 (puriss grade, Sigma Aldrich), Y_2O_3 (99.99%, Sigma Aldrich), and La_2O_3 (99.99%, Prochem Inc). The powders were dried and mixed according to the nominal compositions. The mixture was ball milled in a planetary ball mill machine (Retsch, PM400) at 150 rpm for 5 h in ethanol with zirconia balls. After drying, the powder was calcined at 1300 °C for 6 h in 5% H_2/Ar . The calcined powder was ball milled at 150 rpm for 5 h in ethanol with zirconia balls. After drying, the powder was compacted into 20 mm pellets under a uniaxial pressure of 250 MPa with the aid of PVA binder. The pellets were annealed at 500 °C for 0.5 h in air to remove the binder, and then sintered at 1400 °C for 11 h in 5% H_2/Ar .

$\text{Sr}_x\text{La}_{0.12}\text{TiO}_3$ ($x = 0.82, 0.86, 0.87, 0.88, 0.885, 0.9$) were prepared with similar methods. The Sr-deficient or TiO_2 excess compositions are $\text{Sr}_x\text{La}_{0.12}\text{TiO}_3$ with $0.82 \leq x \leq 0.87$, while the Sr-excess compositions are $\text{Sr}_x\text{La}_{0.12}\text{TiO}_3$ with $0.885 \leq x \leq 0.9$. Except for La_2O_3 dried in furnace at 900 °C for 2 h, the other powders were all baked in oven at 150 °C for 3 h before use. After the same calcination, ball milling, and pressing process, the pellets were sintered at 1400 °C or 1600 °C for 6 h in 5% H_2/Ar .

Powder X-ray diffraction (XRD) (Panalytical X'pert MPD) was carried out to verify the phase composition. Lattice parameters of Y-doped SrTiO_3 were obtained from Rietveld refinements using PANalytical-HighScore Plus software. Density of the pellets was evaluated by Archimedes' principle. The microstructure was examined by scanning electron microscopy (SEM) and energy-dispersive X-ray spectroscopy (EDS)

(FEI Nova NanoSEM 230 FESEM). The samples were polished and thermal etched at 100 °C lower than the sintering temperature for 0.5 h in 5% H₂/Ar. The microstructure, EDS, and selected area electron diffraction (SAED) patterns were taken by transmission electron microscopy (TEM) (Phillips CM200). The samples for TEM analysis were prepared by focused ion beam (FIB) (XT Nova Nanolab 200). Electrical conductivity σ and Seebeck coefficient S were simultaneously measured by the ULVAC-ZEM3 system. Thermal conductivity κ was obtained from the product of the temperature dependent density (NETZSCH DIL 402C), specific heat capacity (NETZSCH DSC 404C), and thermal diffusivity (NETZSCH LFA 427). Thermogravimetric measurement was carried out employing thermogravimetric analysis (NETZSCH STA 449). The oxygen deficiency was determined by the weight increase upon annealing samples at 1000 °C for 20 h in oxygen atmosphere (50 ml/min).

7.3 Results and Discussion

7.3.1 Thermoelectric properties of Sr_xY_{0.04}TiO₃ (0.92 ≤ x ≤ 1)

The XRD analysis indicates that the compositions with 0.92 ≤ x ≤ 0.96 show a single-phase perovskite structure (Figure 7-1). A weak diffraction peak at 2 θ ~29.2° is observed in Sr-excess compositions, which is likely to be Y₂O₃ (JCPDS 43-0661). The values of lattice parameter a were calculated by Rietveld refinements of the XRD patterns using space group Pm $\bar{3}$ m and are listed in Table 7-1. It is clear that introducing Y³⁺ into SrTiO₃ leads to a decrease in the lattice parameter a due to the smaller ionic radii of Y³⁺ compared with that of Sr²⁺. However, it is noteworthy that the Sr-deficient compositions (0.92 ≤ x ≤ 0.95) show little difference in the lattice parameter, which is very close to that of Sr_{0.96}Y_{0.04}TiO₃. On the other hand, for the Sr-excess compositions, the lattice parameter a increases with increasing Sr content due to the progressive decrease in Y substitution concentration (Table 7-1). It is difficult to determine the concentration of Y₂O₃ in the Sr-excess compositions by carrying out Rietveld refinements on the XRD patterns, since the amount of Y₂O₃ is too small and falls within the margin of the error of XRD ($\pm 5\%$). In general, the radius of Y³⁺ is smaller than Sr²⁺. Therefore, the increase of lattice parameter a with increasing x ($x \geq 0.96$) indicates that more Sr²⁺ ions replace Y³⁺ ions in SrTiO₃, thus facilitating the formation of Y₂O₃. It

implies that Sr^{2+} rather than Y^{3+} has the preference to occupy A-sites when there are less available A-sites in SrTiO_3 .

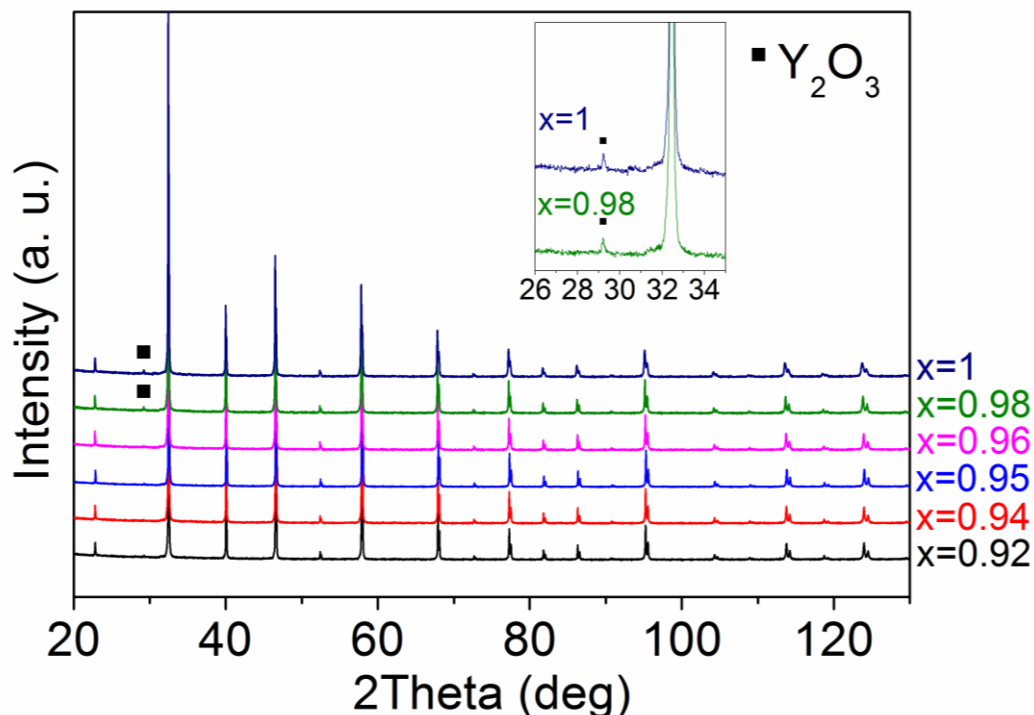


Figure 7-1 XRD patterns of $\text{Sr}_x\text{Y}_{0.04}\text{TiO}_3$ ($x = 0.92, 0.94, 0.95, 0.96, 0.98, 1$). Insert shows the XRD patterns (over 26° to 35°) of $\text{Sr}_x\text{Y}_{0.04}\text{TiO}_3$ with $x = 0.98$ and 1 .

Table 7-1 Nominal composition, constituents in molar ratio, lattice parameter a , sintered densities, theoretical densities, and relative densities of $\text{Sr}_x\text{Y}_{0.04}\text{TiO}_3$ ($x = 0.92, 0.94, 0.95, 0.96, 0.98, 1$).

x	Constituents in molar ratio	a (Å)	Sintered density (g/cm^3)	Theoretical density (g/cm^3)	Relative density
0.92	0.96 $\text{Sr}_{0.96}\text{Y}_{0.04}\text{TiO}_3/0.04 \text{TiO}_2$	3.90292(1)	4.82	5.106	0.94
0.94	0.98 $\text{Sr}_{0.96}\text{Y}_{0.04}\text{TiO}_3/0.02 \text{TiO}_2$	3.90292(1)	4.90	5.116	0.96
0.95	0.99 $\text{Sr}_{0.96}\text{Y}_{0.04}\text{TiO}_3/0.01 \text{TiO}_2$	3.90276(2)	4.94	5.121	0.97
0.96	$\text{Sr}_{0.96}\text{Y}_{0.04}\text{TiO}_3$	3.90325(1)	4.45	5.125	0.87
0.98	0.99 $\text{Sr}_{0.98}\text{Y}_{0.02}\text{TiO}_3/0.01 \text{Y}_2\text{O}_3$	3.90501(1)	4.49	5.117	0.88
1	0.98 $\text{SrTiO}_3/0.02 \text{Y}_2\text{O}_3$	3.90697(2)	4.70	5.110	0.92

Appearance of a Ti-rich phase in the SEM and EDS micrographs (Figure 7-2) of the Sr-deficient compositions indicates the existence of an impurity phase, although the Sr-deficient compositions are of single-phase, as shown in the XRD patterns. The Ti-rich phase has been clearly observed in the composition with $x = 0.92$ by SEM (Figure

7-2 and Figure 7-4a). Further examination by bright-field image (Figure 7-3a) confirmed that Grain 1 has a uniform distribution of Sr and Ti elements, while Grain 2 is deficient in Sr and rich in Ti. The SAED pattern of Grain 1 was indexed based on cubic SrTiO₃ and its $a = 0.364 \pm 0.003$ nm. The SAED pattern of Grain 2 is best fitted with anorthic Ti₄O₇ and therefore is indexed based on Ti₄O₇ with $a = 0.5593$ nm, $b = 0.7125$ nm, $c = 1.2456$ nm, and $\alpha = 95.02^\circ$, $\beta = 95.21^\circ$, $\gamma = 108.73^\circ$ (JCPDS 72-1722). Ti₄O₇ is a reduced form of TiO₂ and one of the Magnéli compounds. It is reasonable since all samples were sintered at 1400 °C in a strongly reducing atmosphere.

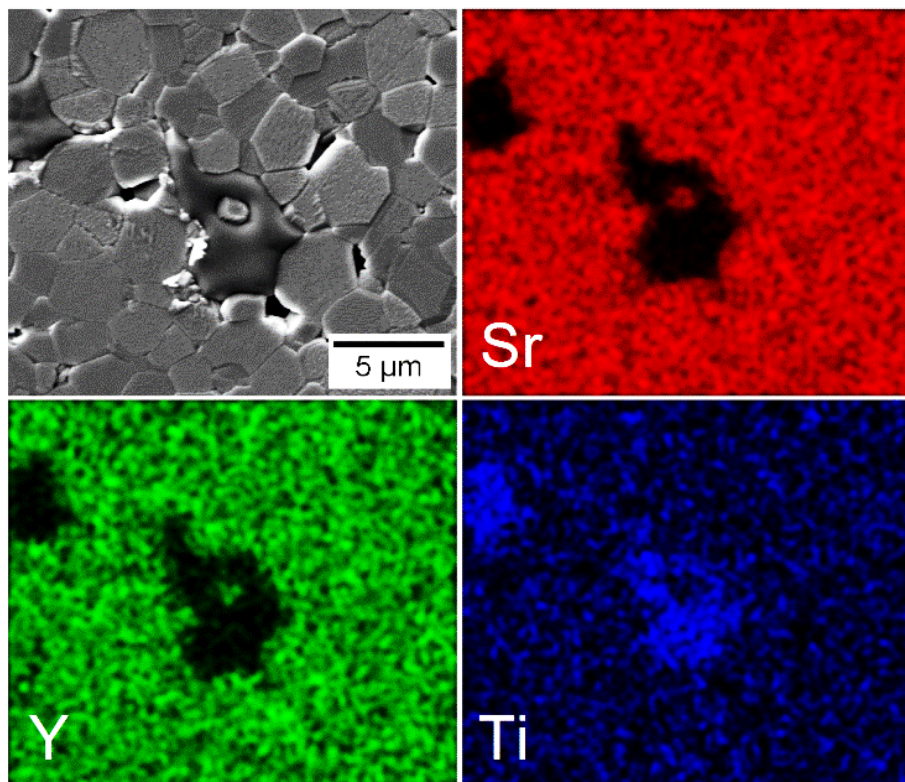


Figure 7-2 SEM micrograph and elemental distribution of Sr, Y, and Ti from EDS mapping of Sr_{0.92}Y_{0.04}TiO₃.

Based on the XRD and microstructural analyses above, all the samples studied could be treated as composites except the stoichiometric composition, Sr_{0.96}Y_{0.04}TiO₃. Their constituents are listed in the second column of Table 7-1. The theoretical densities were calculated from the total mass per mole of composites divided by the total volume per mole of composites. Theoretical densities of TiO₂ and Y₂O₃ are 4.23 g/cm³ from JCPDS 01-1292, and 5.14 g/cm³ from JCPDS 43-0661, respectively. High relative densities are achieved in the Sr-deficient and Sr-excess samples, in good agreement

with the SEM observation (Figure 7-4). This is due to the fact that excess TiO_2 or SrO promotes densification of SrTiO_3 during sintering [166,173].

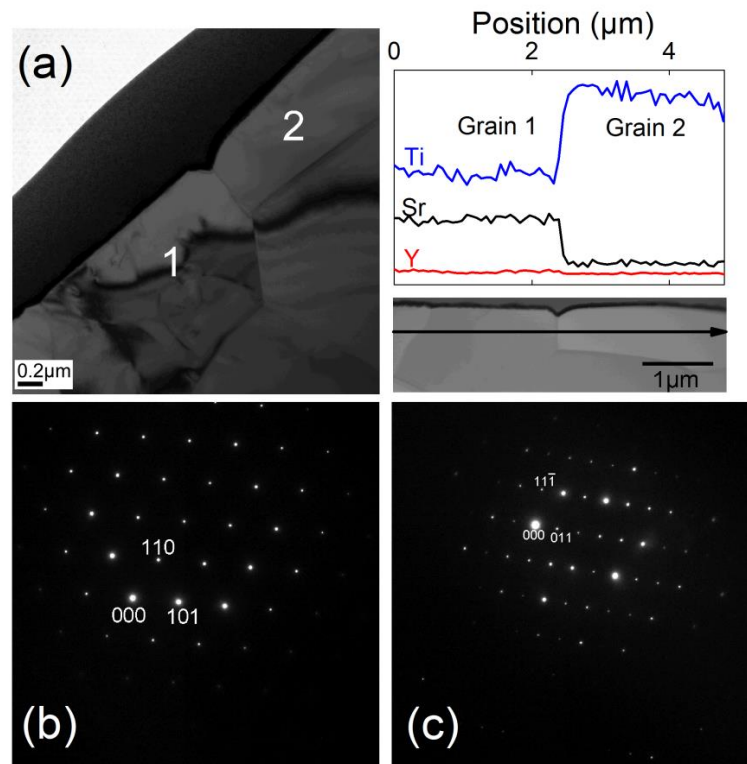


Figure 7-3 (a) Bright-field image and Sr, Ti, and Y distribution from EDS line scanning, (b) SAED pattern of Grain 1, and (c) SAED pattern of Grain 2 of $\text{Sr}_{0.92}\text{Y}_{0.04}\text{TiO}_3$.

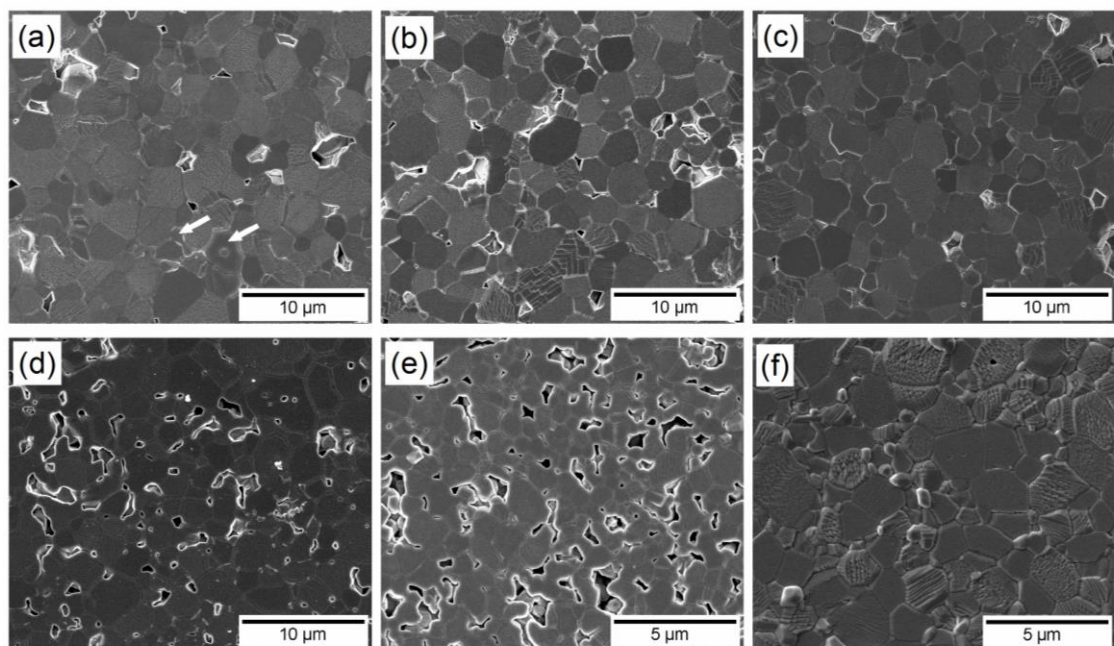


Figure 7-4 SEM micrographs of $\text{Sr}_x\text{Y}_{0.04}\text{TiO}_3$. (a) $x = 0.92$, (b) $x = 0.94$, (c) $x = 0.95$, (d) $x = 0.96$, (e) $x = 0.98$, and (f) $x = 1$. Ti-rich grains in (a) are labeled by white arrows.

Temperature and Sr content dependence of the electrical conductivity (σ) of $\text{Sr}_x\text{Y}_{0.04}\text{TiO}_3$ are shown in Figure 7-5a and b, respectively. The Sr-deficient compositions exhibit similar high conductivity ($\sigma = 65 \text{ S/cm}$ at 680°C) and show a transition from semiconducting to metallic conduction at 150°C . The stoichiometric composition has an intermediate conductivity ($\sigma = 6 \text{ S/cm}$ at 680°C) and show a semiconductor-metal transition at 500°C . However, the Sr-excess compositions possess low conductivity ($\sigma = 0.17 \text{ S/cm}$ at 680°C for $x = 1$) and show semiconducting conduction over the whole temperature range from 50 to 680°C . The conduction behavior of these samples is discussed in the following.

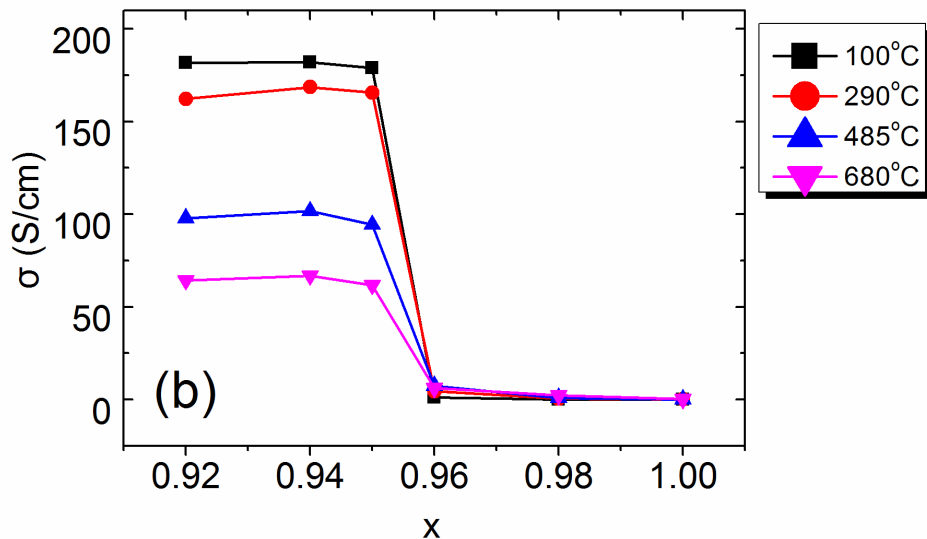
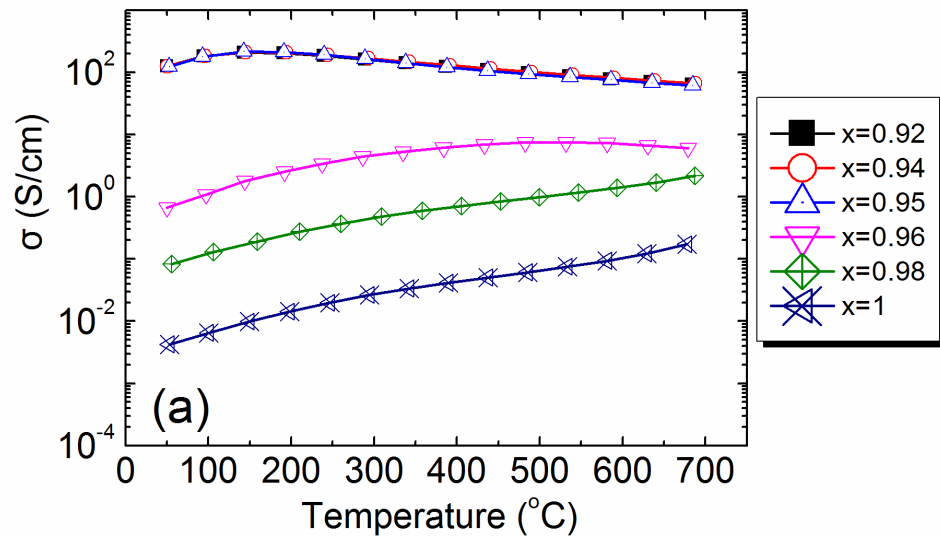


Figure 7-5 Electrical conductivity (σ) of $\text{Sr}_x\text{Y}_{0.04}\text{TiO}_3$ ($x = 0.92, 0.94, 0.95, 0.96, 0.98, 1$) versus (a) temperature and (b) Sr content (x).

For Y-doped SrTiO_3 sintered in a reduced atmosphere, the electrical conduction is contributed by electrons which are generated from (1) substituting Sr^{2+} with Y^{3+} (Equation 7-1), and (2) oxygen vacancies (Equation 7-2).



In order to maintain charge neutrality, it is generally accepted that the electrons are transferred to Ti^{4+} , forming intermediate values of $\text{Ti}^{3+/4+}$ [174]. Therefore, the concentration of Ti^{3+} ($[\text{Ti}'_{\text{Ti}}]$) equals the electron concentration (n) and could be expressed as

$$[\text{Ti}'_{\text{Ti}}] = n = [\text{Y}_{\text{Sr}}^{\bullet}] + 2[\text{V}_0^{\bullet\bullet}] \quad \text{Equation 7-3}$$

The oxygen deficiency can be determined by the thermogravimetric analysis and can be calculated by

$$[\text{V}_0^{\bullet\bullet}] = \delta = \frac{\Delta m/A_o}{m_{\text{ox}}/A_{\text{YSTO}}} \quad \text{Equation 7-4}$$

where δ is the oxygen deficiency per formula unit, m_{ox} is the weight of the oxidized sample after annealing, Δm is the weight gain after annealing the sample in oxygen, A_o is the atomic weight of oxygen, and A_{YSTO} is the atomic weight of the $\text{Sr}_x\text{Y}_{0.04}\text{TiO}_3$. It should be noted that the calculated oxygen deficiency corresponds to the difference in oxygen content between the as-sintered samples and the samples in equilibrium under oxygen atmosphere at 1000 °C. The calculated oxygen deficiency is probably higher than the real oxygen deficiency, since the donor-doped SrTiO_3 tends to uptake excess oxygen in oxidizing atmosphere.

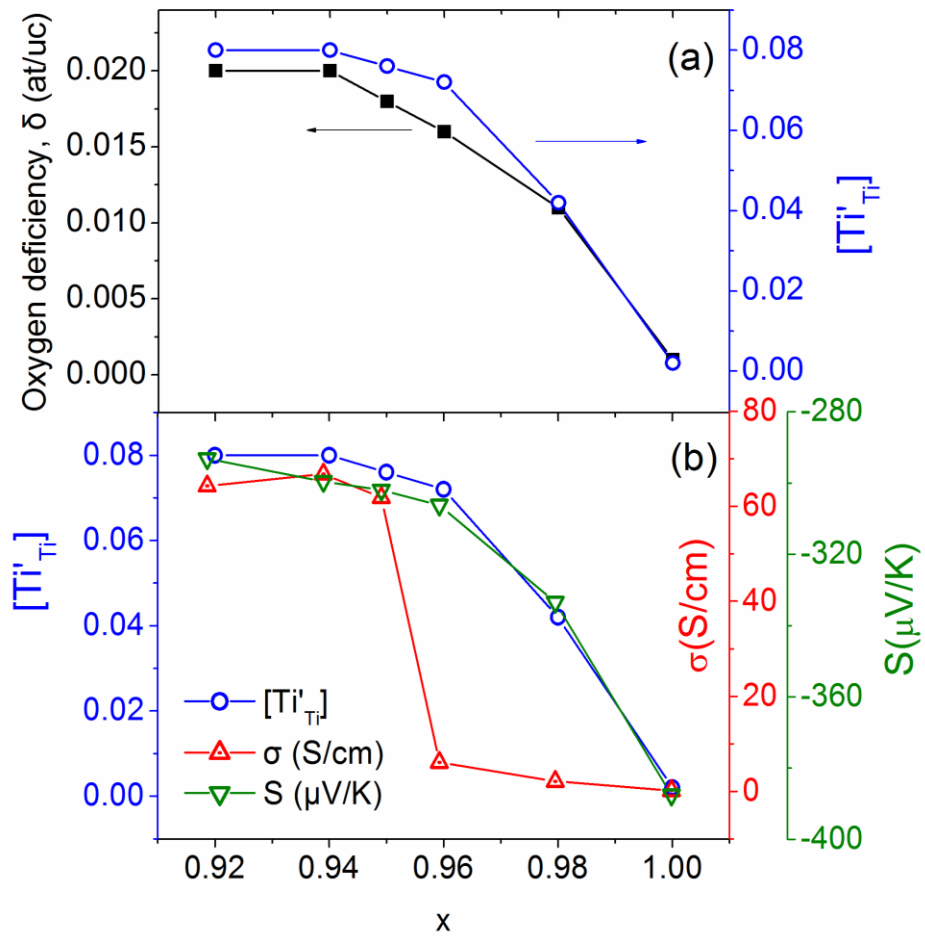


Figure 7-6 Sr stoichiometry (x) dependence of the (a) oxygen deficiency (δ) and concentration of Ti^{3+} ($[Ti_{Ti}^{3+}]$) and (b) $[Ti_{Ti}^{3+}]$, electrical conductivity (σ) at 680 °C, and Seebeck coefficient (S) at 680 °C of $Sr_xY_{0.04}TiO_{3-\delta}$ ($x = 0.92, 0.94, 0.95, 0.96, 0.98, 1$).

Based on the measured values of the oxygen deficiency and Y doping content, Ti^{3+} concentration was calculated and plotted in Figure 7-6a against Sr content (x). It is obvious that the Sr-deficient compositions possess higher electrical conductivity due to the increased Ti^{3+} concentration. Moreover, the charge carrier concentration, $[Ti^{3+}]$, has a significant influence on the conduction behavior (Figure 7-5a). The electronic energy level of perovskite $SrTiO_3$ is related to the covalent interaction between Ti 3d and O 2p orbitals [175,176]. The overlap of the wave functions or p - d -orbital mixing is small when the carrier concentration is low. Consequently, the orbitals are localized and exhibit semiconducting conduction. Therefore the semiconducting conduction is observed in the Sr-excess samples over the whole temperature range (Figure 7-5a). However, when the carrier concentration is beyond a certain level, the Fermi level shifts

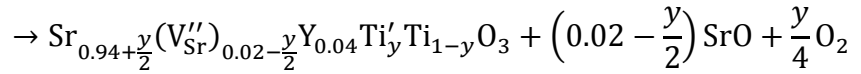
into the conduction bands, resulting in the metallic conduction [176]. This is the case for the compositions with $0.92 \leq x \leq 0.96$ (Figure 7-5a).

It is noted that the electrical conductivity exhibits a sudden decrease as the composition changes from Sr-deficient to stoichiometric value, as shown in Figure 7-5b. This is partially due to the decrease of Ti^{3+} concentration as mentioned before. More importantly, it is closely related to the defect structure of $\text{Sr}_{0.96}\text{Y}_{0.04}\text{TiO}_3$. Under an oxidizing atmosphere, the extra charge introduced by Y substitution will be neutralized by uptaking more oxygen atoms. The extra oxygen is accommodated into the crystal lattice sites by the formation of Sr vacancies and SrO layers between the SrTiO_3 layers according to Equation 7-5 [177]. The resultant alternate layers of SrO/ SrTiO_3 belong to the Ruddlesden-Popper phases [178].



Equation 7-5

Under a reducing atmosphere, the electrons could be electronically compensated by the formation of mixed $\text{Ti}^{3+/4+}$ ions. However, previous studies [28,109,177] confirmed that SrO could not be depleted completely in the stoichiometric composition even under strongly reducing atmosphere. The reaction can be expressed as Equation 7-6. It has been reported that the effective conduction band offset could be increased after introducing SrO layers into SrTiO_3 [179]. Therefore, the stoichiometric composition shows lower electrical conductivity with respect to the Sr-deficient compositions due to the increased number of potential barrier layers, which is resulted from the presence of SrO layers. It is discernable that the composition with $x = 0.98$ and 1 should have the same defect structure (i.e., the existence of SrO layers) as the stoichiometric composition. This is the main reason that the three compositions ($x = 0.96, 0.98,$ and 1) possess similar values of the electrical conductivity (Figure 7-5b), although there is a big difference in the charge carrier concentrations (Figure 7-6).



Equation 7-6

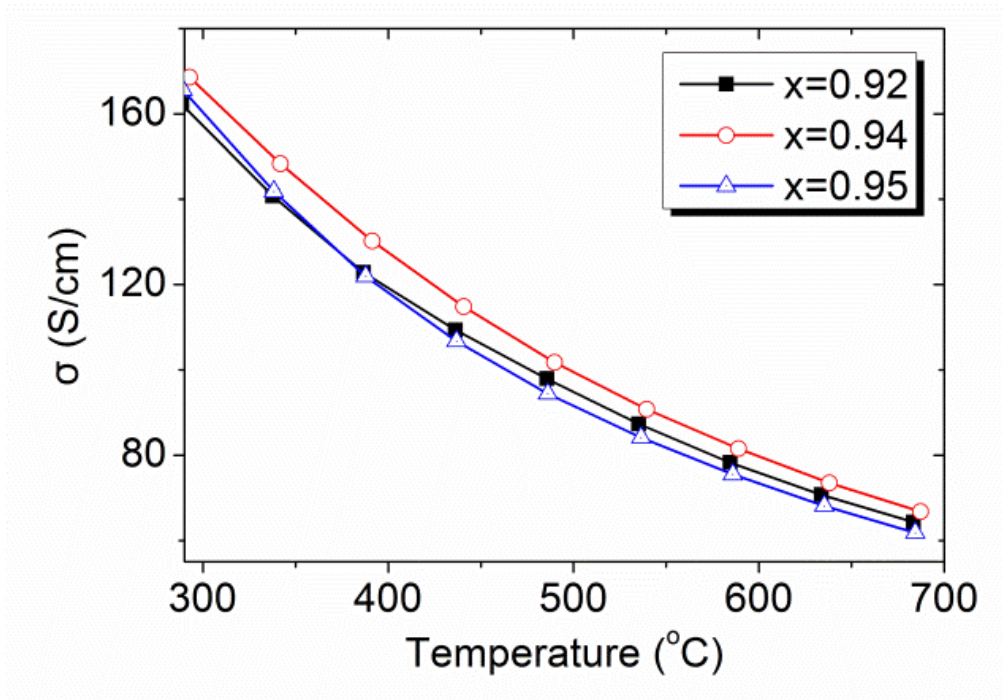
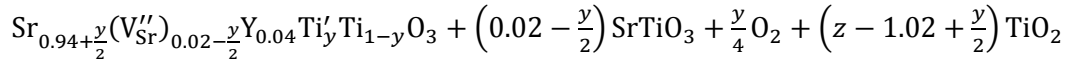
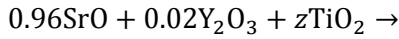


Figure 7-7 Electrical conductivity (σ) of $\text{Sr}_x\text{Y}_{0.04}\text{TiO}_3$ ($x = 0.92, 0.94,$ and 0.95) versus temperature.

In the Sr-deficient compositions, it is assumed that $(\text{Sr} + \text{Y}) / \text{Ti} = 1 / z$, where $z > 1$. The excess TiO_2 reacts with SrO , as written in Equation 7-7. It demonstrates the absence of the SrO potential barriers due to the complete depletion of SrO layers by the excess TiO_2 as a result of the formation of SrTiO_3 , thus leading to a significantly higher electrical conductivity for the Sr-deficient samples (i.e., $x = 0.92, 0.94,$ and 0.95). The remaining TiO_2 resides in the samples as Magnđi compounds. As indicated in Table 7-1, the Sr-deficient compositions could be viewed as $\text{Sr}_{0.96}\text{Y}_{0.04}\text{TiO}_3/\text{TiO}_2$ composites. It is noted that limited amount of TiO_2 secondary phase are beneficial for the electrical conductivity (Figure 7-7). However, a little bit more TiO_2 will block the conduction path [170], leading to a reduction in the electrical conductivity.



Equation 7-7

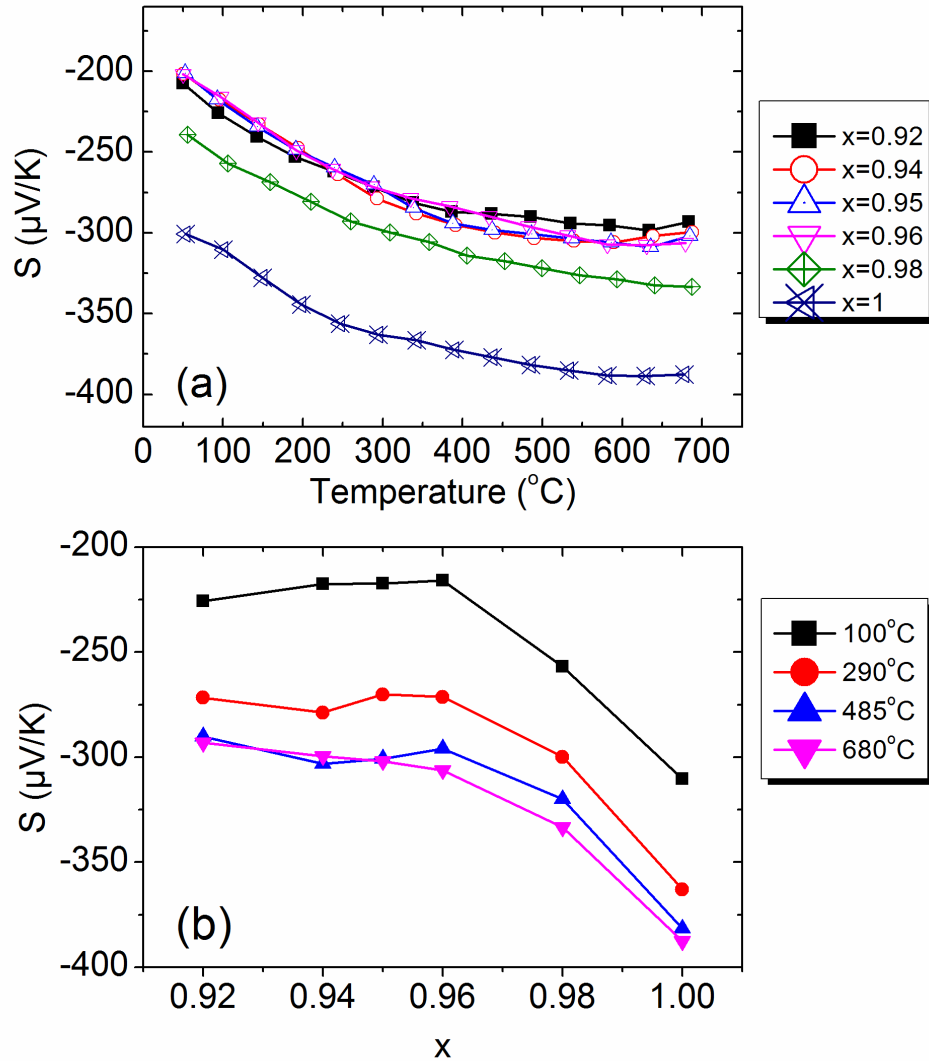


Figure 7-8 Seebeck coefficient (S) of $\text{Sr}_x\text{Y}_{0.04}\text{TiO}_3$ ($x = 0.92, 0.94, 0.95, 0.96, 0.98, 1$) versus (a) temperature and (b) x .

The negative values of the Seebeck coefficient (Figure 7-8) indicate that the major charge carriers are electrons in all the compositions. It is interesting to note that the Sr-deficient and stoichiometric compositions possess almost the same values of the Seebeck coefficient due to the same major phase ($\text{Sr}_{0.96}\text{Y}_{0.04}\text{TiO}_3$) in these samples, as

listed in Table 7-1. For the Sr-excess compositions, the absolute value of the Seebeck coefficient increases with increasing x (Figure 7-8). This is attributed to the decrease in the charge carrier concentration with increasing x (Figure 7-6).

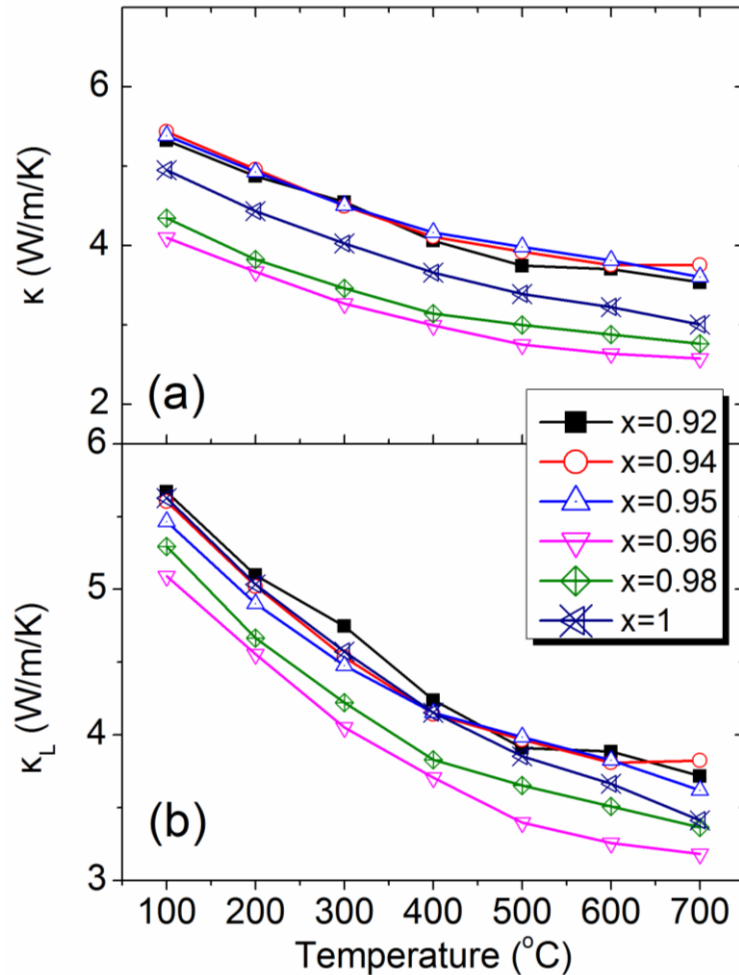


Figure 7-9 Temperature dependence of the (a) thermal conductivity κ and (b) lattice thermal conductivity κ_L of $\text{Sr}_x\text{Y}_{0.04}\text{TiO}_3$ ($x = 0.92, 0.94, 0.95, 0.96, 0.98, 1$).

The thermal conductivity (κ) (Figure 7-9a) decreases with increasing temperature, indicating that the lattice contribution is dominant in all the compositions. The lowest thermal conductivity is obtained in the stoichiometric composition. The Sr-deficient compositions exhibit similar thermal conductivity which is higher than the other samples. For the Sr-excess compositions, the thermal conductivity increases with increasing x . Due to the huge difference in the electrical conductivity between the samples, the lattice thermal conductivity was calculated and plotted in Figure 7-9b. The lattice thermal conductivity (κ_L) can be calculated by subtracting the electronic contribution (κ_e) from the total thermal conductivity (κ). According to the Wiedemann-

Franz law, the electronic thermal conductivity $\kappa_e = \sigma LT$, where L is the Lorenz number and is assumed to be $2.44 \times 10^{-8} \text{ W}\Omega\text{K}^{-2}$. Moreover the lattice thermal conductivity is corrected for porosity according to Equation 7-8 [131].

$$\kappa_L = \frac{\kappa'_L}{1 - \frac{3}{2}(1 - RD)} \quad \text{Equation 7-8}$$

where RD is relative density. It is clear from Figure 7-9b that $\text{Sr}_{0.96}\text{Y}_{0.04}\text{TiO}_3$ possesses the lowest lattice thermal conductivity. This is attributed to the existence of SrO layers and point defects. It has been reported that phonons could be effectively scattered by SrO/SrTiO₃ interfaces [180,181]. Furthermore, point defects including Sr and O vacancies scatter phonons and thus reduce the lattice thermal conductivity [160,182]. Therefore, due to the elimination of SrO, the Sr-deficient samples show higher lattice thermal conductivity than the stoichiometric sample. For the Sr-excess compositions, the lattice thermal conductivity increases with increasing x . It is associated with the reduced phonon scattering due to the decreased concentration of Y content and oxygen vacancies. Substitution of Sr with Y induces a lattice strain due to their difference in ionic radii. The Y doping concentration is reduced with increasing x , thus decreasing the phonon scattering associated with the lattice strain. Therefore, it is reasonable that an increase in the lattice thermal conductivity is observed in the Sr-excess samples.

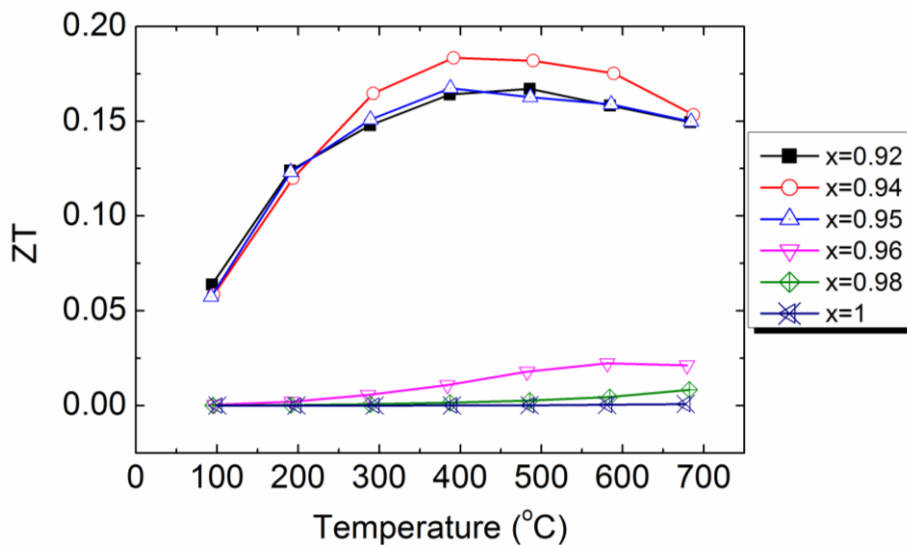


Figure 7-10 Temperature dependence of the thermoelectric figure-of-merit (ZT) of $\text{Sr}_x\text{Y}_{0.04}\text{TiO}_3$ ($x = 0.92, 0.94, 0.95, 0.96, 0.98, 1$).

All Sr-deficient samples possess much higher ZT values compared with the stoichiometric and Sr-excess compositions (Figure 7-10). Among these samples, $\text{Sr}_{0.94}\text{Y}_{0.04}\text{TiO}_3$ has the highest ZT value (0.183 at 390 °C), which is nearly 8 times as high as that of the stoichiometric composition, $\text{Sr}_{0.96}\text{Y}_{0.04}\text{TiO}_3$. This observation reveals an effective way to improve the thermoelectric properties of donor-doped SrTiO_3 system by incorporating an optimal amount of excess TiO_2 .

7.3.2 Thermoelectric properties of $\text{Sr}_x\text{La}_{0.12}\text{TiO}_3$ ($0.82 \leq x \leq 0.9$)

Figure 7-11a and b show the XRD patterns of $\text{Sr}_x\text{La}_{0.12}\text{TiO}_3$ sintered at 1400 °C and 1600 °C, respectively. The Sr-deficient compositions sintered at both temperatures are found to be single-phase and have cubic crystal structure with space group $\text{Pm}\bar{3}\text{m}$.

Appearance of the additional reflection peaks in the Sr-excess compositions sintered at both temperatures is likely due to the formation of $\text{SrO}(\text{SrTiO}_3)_2$, corresponding to JCPDS 11-0663. Ruddlesden-Popper (RP) phases ($n\text{SrTiO}_3 \cdot \text{SrO}$) have been reported to exist in the Sr-excess SrTiO_3 or the donor-doped stoichiometric SrTiO_3 prepared in high oxygen partial pressure conditions [171,178,183]. Therefore, it is expected that the formation of RP phases is promoted with increasing amount of excess Sr in $\text{Sr}_x\text{La}_{0.12}\text{TiO}_3$. In addition to the RP phases, another impurity phase is observed in the compositions with $x = 0.9$ sintered at 1400 °C and $x = 0.885$ sintered at 1600 °C, possibly corresponding to La_2O_3 according to JCPDS 24-0554. The exclusion of La_2O_3 in the samples is possibly associated with the fact that Sr has the preference of occupying both A-sites of SrTiO_3 and SrO layers. It is also difficult to determine the concentration of La_2O_3 in the aforementioned samples using the XRD technique since the samples are the composites composed of SrTiO_3 and $\text{SrO}(\text{SrTiO}_3)_2$ with diffraction peaks overlapping each other.

It is also interesting to note that the stoichiometric samples show different phase compositions under different sintering temperatures. Cubic SrTiO_3 together with tetragonal RP phases are formed in the sample sintered at 1400 °C as justified by the additional peaks, whereas single-phase cubic SrTiO_3 is obtained for the same composition sintered at 1600 °C. It is associated with the variation in the oxygen deficiencies of samples sintered at different temperatures. The oxygen content in $\text{Sr}_x\text{La}_{0.12}\text{TiO}_3$ determines the crystal structure and phase composition. The mechanism is explained in the following.

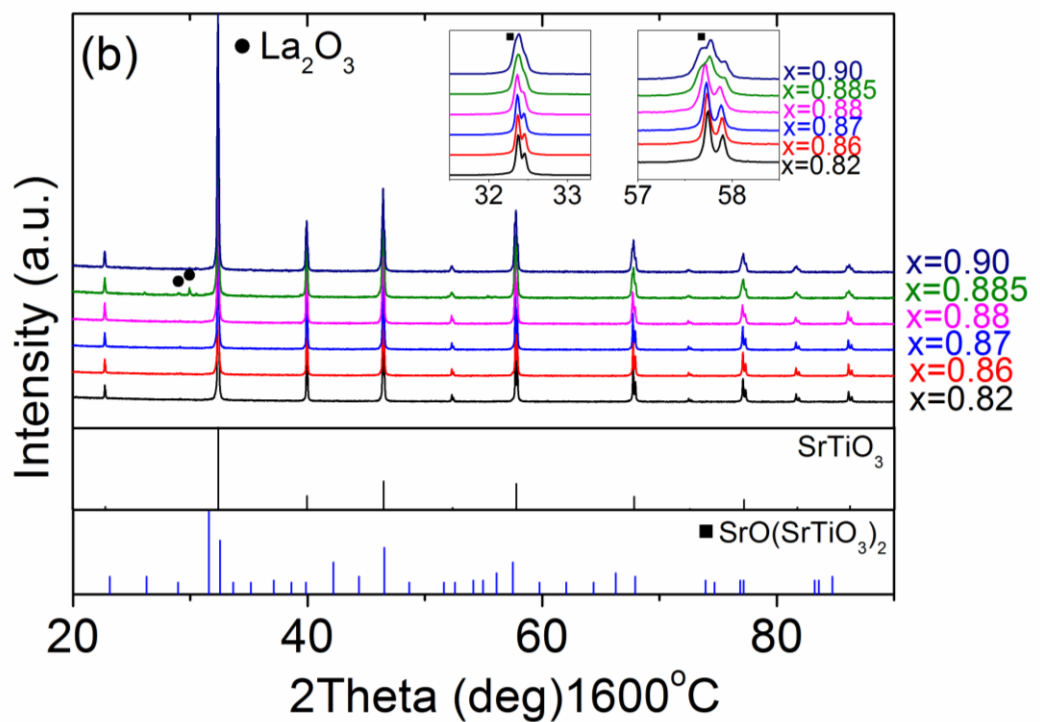
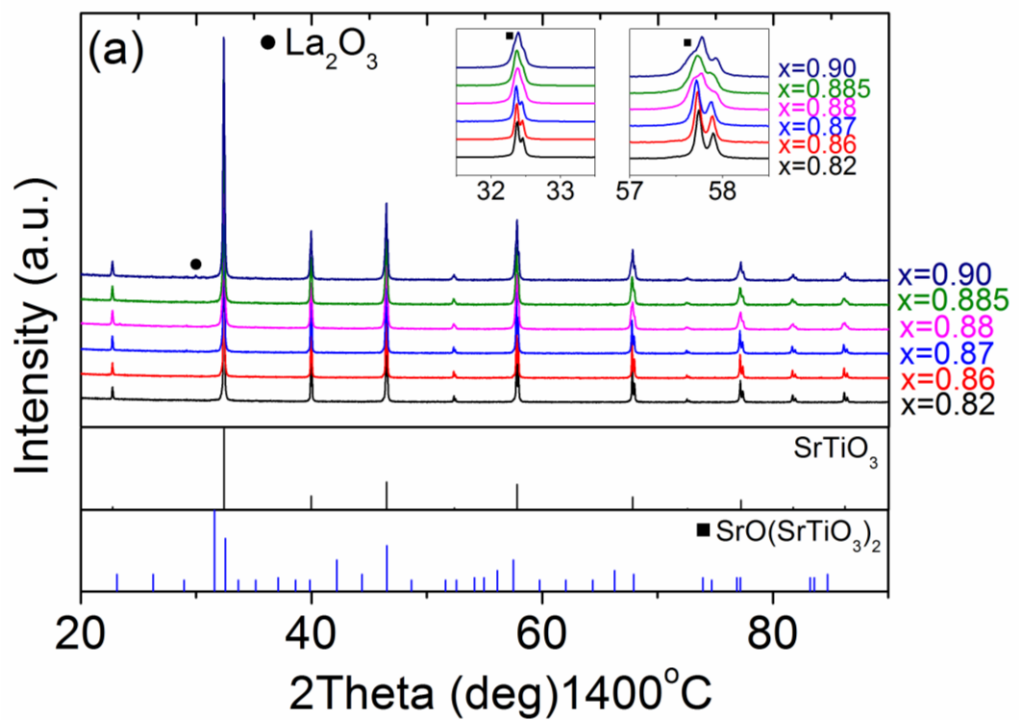
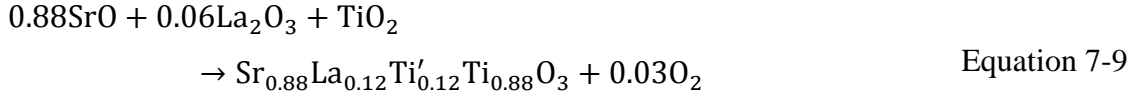
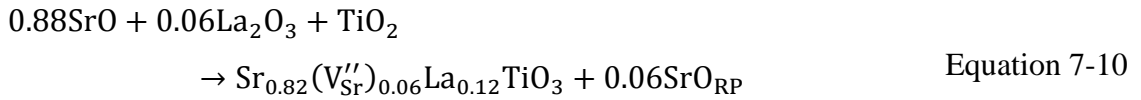


Figure 7-11 XRD patterns of $\text{Sr}_x\text{La}_{0.12}\text{TiO}_3$ ($x = 0.82, 0.86, 0.87, 0.88, 0.885, 0.9$) sintered at (a) 1400 °C and (b) 1600 °C. The inserts show the XRD patterns over 31.5 ° to 33.3 ° and 57 ° to 58.5 °.

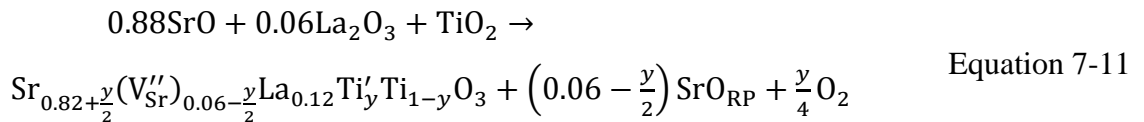
For $\text{Sr}_{0.92}\text{La}_{0.12}\text{TiO}_3$ sintered in a strongly reducing atmosphere, the extra charge introduced by substituting Sr^{2+} with La^{3+} is neutralized by controlled valency, i.e., the formation of mixed $\text{Ti}^{3+}/\text{Ti}^{4+}$ ions (Equation 7-9)



However, it has been suggested that both controlled valency and self-compensation mechanism are present in stoichiometric donor-doped SrTiO_3 sintered in a strongly reducing atmosphere [28,177]. Usually, the self-compensation mechanism occurs in donor-doped SrTiO_3 prepared in an oxidizing atmosphere. In this case, the extra charges are compensated by the uptake of excess oxygen. The excess oxygen atoms are accommodated into the crystal structure by the formation of Sr vacancies and RP phases in the form of alternating stacks of SrO and SrTiO_3 (Equation 7-10)



Since both compensation mechanisms present in the composition sintered in a reducing atmosphere as mentioned above, electrons are compensated by both the formation of Ti^{3+} and the Sr vacancy model (Equation 7-11). In this case, RP phases appear as a result of incomplete reduction.



It is clear from Equation 7-11 that the crystal structure and phase composition of $\text{Sr}_{0.88}\text{La}_{0.12}\text{TiO}_3$ are closely related to its oxygen deficiency. Thermogravimetric analysis has been conducted to confirm the oxygen deficiencies of the samples. The oxygen deficiency can be calculated from the weight increase of samples annealed in oxygen by Equation 7-12.

$$[V_{O}^{\bullet\bullet}] = \delta = \frac{\Delta m/A_o}{m_{ox}/A_{LaSTO}} \quad \text{Equation 7-12}$$

where δ is the oxygen deficiency per formula unit, m_{ox} is the weight of the oxidized sample after annealing, Δm is the weight gain after annealing the sample in oxygen, A_o is the atomic weight of oxygen, and A_{LaSTO} is the atomic weight of the $Sr_xLa_{0.12}TiO_3$.

The oxygen deficiencies of $Sr_xLa_{0.12}TiO_3$ sintered at 1400 °C and 1600 °C are plotted in Figure 7-12a as a function of x . Similar oxygen deficiency is obtained in the compositions with $x = 0.82$ and 0.86 sintered at 1400 °C. The oxygen deficiency is further reduced with increasing x . All compositions show an increase in oxygen deficiency by increasing the sintering temperature. According to Equation 7-12, the concentration of SrO is proportional to $(0.06 - y/2)$ where $y/2$ is equal to the oxygen deficiency (δ). Therefore, the concentration of SrO in stoichiometric composition can be estimated. The concentration of SrO is increased with increasing amount of excess Sr. Moreover, the concentration of SrO is reduced as excess TiO_2 is added to the stoichiometric composition (Equation 7-13). The amount of the remaining RP phases in TiO_2 -excess compositions depends on the oxygen deficiency and amount of excess TiO_2 .



The concentration of SrO is therefore estimated and plotted versus x in Figure 7-12b. By comparing Figure 7-11 and Figure 7-12, it is clear that the cubic crystal structure observed in the compositions with $0.82 \leq x \leq 0.86$ sintered at 1400 °C and with $0.82 \leq x \leq 0.87$ sintered at 1600 °C is due to the absence of SrO RP phases. The Sr-excess compositions sintered at both temperatures and the stoichiometric composition sintered at 1400 °C show additional reflection peaks due to the presence of SrO. The compositions with intermediate concentration of SrO ($x = 0.87$ sintered at 1400 °C and $x = 0.88$ sintered at 1600 °C) show cubic structure possibly owing to the fact that the amount of SrO is not high enough to be observed by XRD.

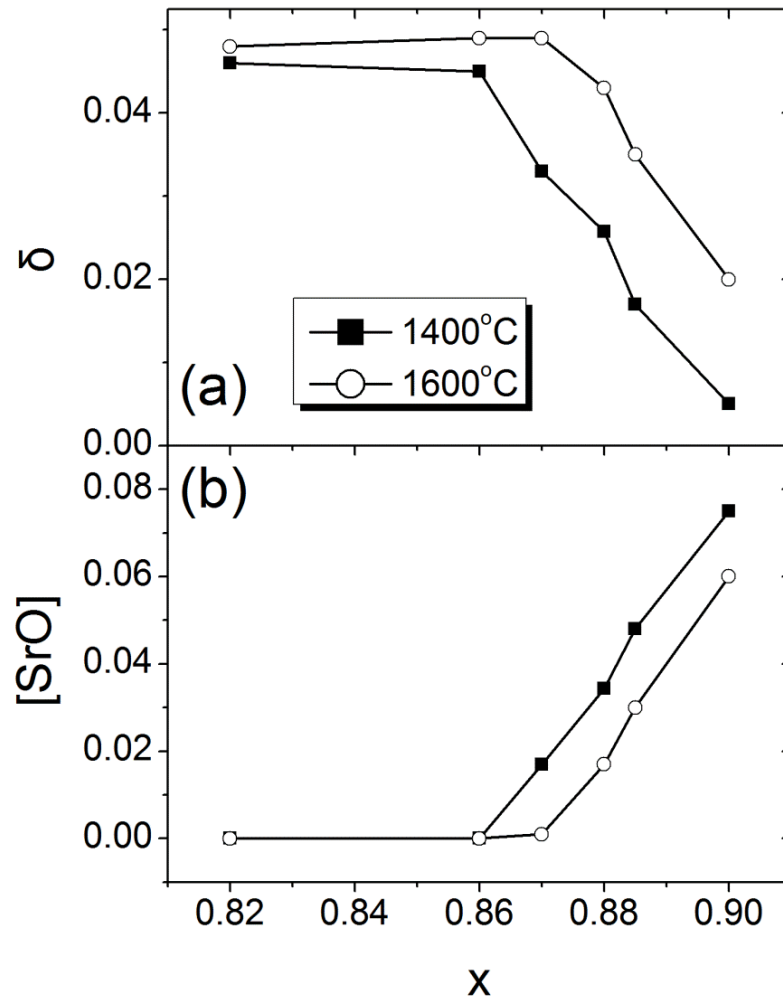


Figure 7-12 (a) Oxygen deficiency (δ) and (b) concentration of SrO ([SrO]) of $\text{Sr}_x\text{La}_{0.12}\text{TiO}_{3-\delta}$ ($x = 0.82, 0.86, 0.87, 0.88, 0.9$) versus x sintered at 1400 and 1600 °C.

Table 7-2 Bulk densities of $\text{Sr}_x\text{La}_{0.12}\text{TiO}_3$ ($x = 0.82, 0.86, 0.87, 0.88, 0.885, 0.90$) sintered at 1400 °C and 1600 °C. Theoretical density is assumed to be 5.12 g/cm³ (JCPDS 73-0661).

x	1400 °C		1600 °C	
	Bulk density (g/cm ³)	Relative density	Bulk density (g/cm ³)	Relative density
0.82	4.94	0.96	5.09	0.99
0.86	4.64	0.91	5.07	0.99
0.87	4.42	0.86	5.00	0.98
0.88	3.62	0.71	4.88	0.95
0.885	3.75	0.73	5.08	0.99
0.90	3.95	0.77	5.07	0.99

The bulk densities of $\text{Sr}_x\text{La}_{0.12}\text{TiO}_3$ are shown in Table 7-2. At both sintering temperatures, the lowest bulk densities are found in the stoichiometric compositions. It

is in good agreement with previous studies reporting that excess TiO_2 or SrO promotes densification of SrTiO_3 during sintering [166,173].

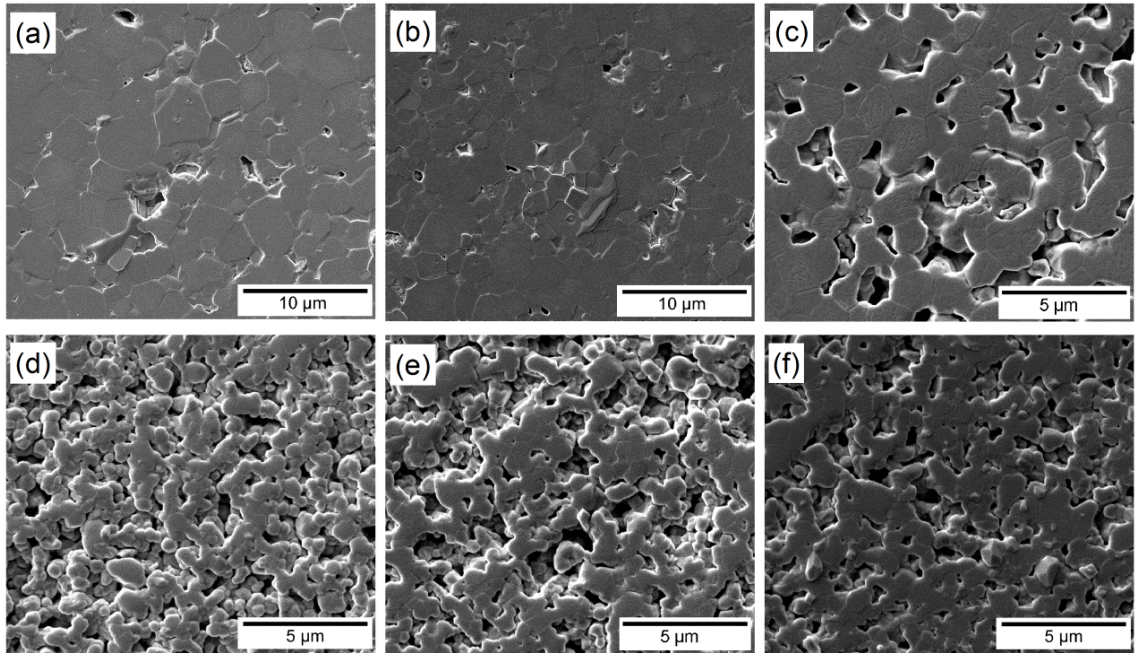


Figure 7-13 SEM micrographs of $\text{Sr}_x\text{La}_{0.12}\text{TiO}_3$ sintered at 1400 °C. (a) $x = 0.82$, (b) $x = 0.86$, (c) $x = 0.87$, (d) $x = 0.88$, (e) $x = 0.885$, and (f) $x = 0.9$.

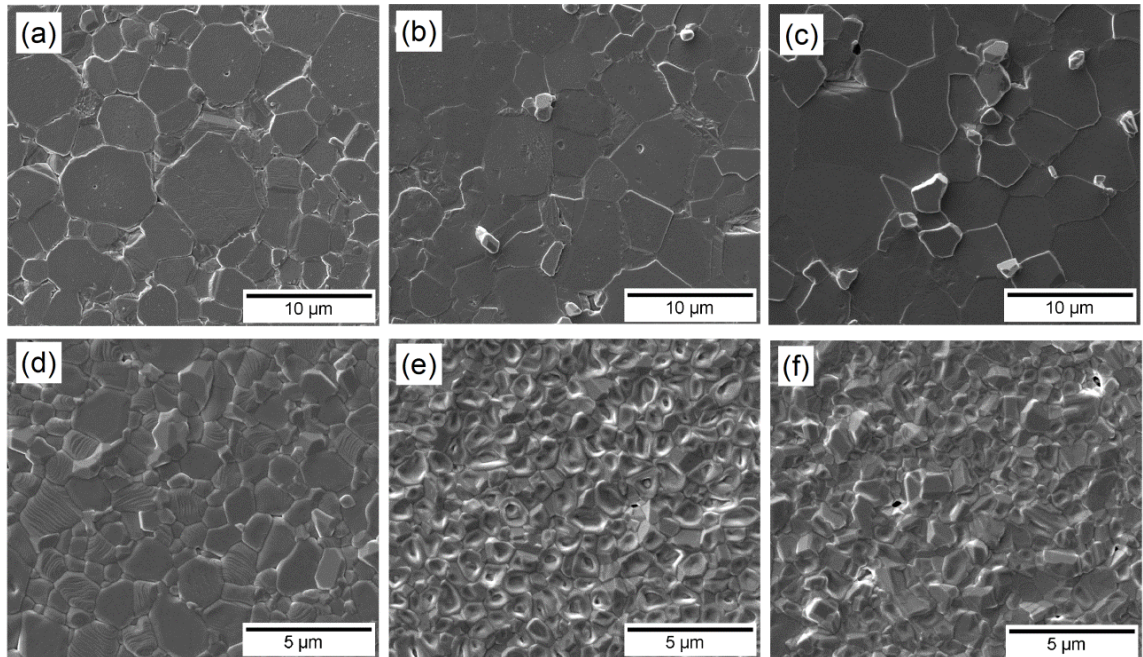


Figure 7-14 SEM micrographs of $\text{Sr}_x\text{La}_{0.12}\text{TiO}_3$ sintered at 1600 °C. (a) $x = 0.82$, (b) $x = 0.86$, (c) $x = 0.87$, (d) $x = 0.88$, (e) $x = 0.885$, and (f) $x = 0.9$.

The SEM micrographs of $\text{Sr}_x\text{La}_{0.12}\text{TiO}_3$ sintered at 1400 and 1600 °C are shown in Figure 7-13 and Figure 7-14, respectively. At a sintering temperature of 1400 °C, only the compositions with $0.82 \leq x \leq 0.86$ show high relative densities. The other samples show reduced relative densities and grain sizes. The relative densities of these samples are much improved by increasing sintering temperature to 1600 °C. At both sintering temperatures, the compositions with the appearance of RP phases, i.e., $0.87 \leq x \leq 0.9$ sintered at 1400 °C and $0.88 \leq x \leq 0.9$ at 1600 °C, show smaller grain sizes relative to the compositions without RP phases.

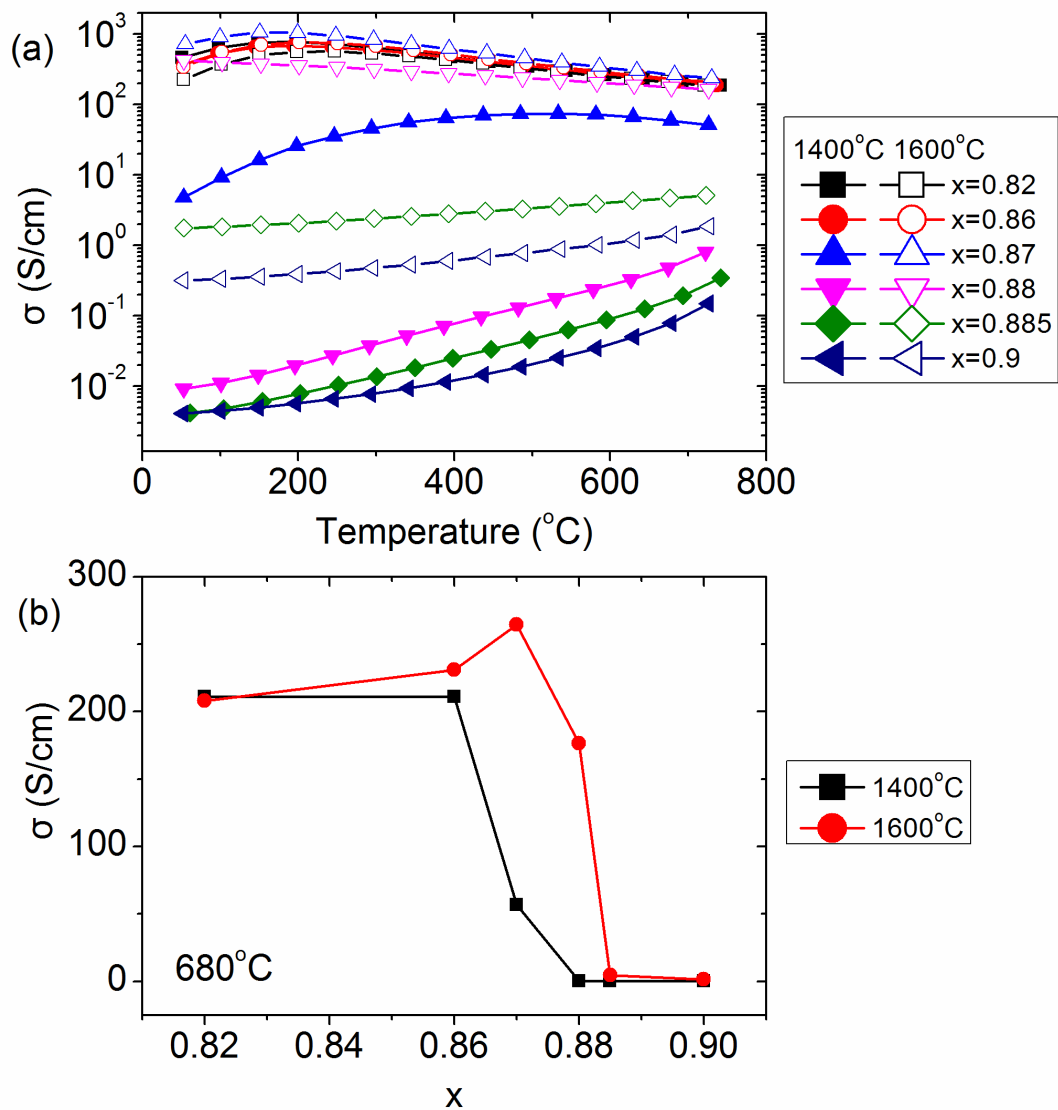


Figure 7-15 (a) Electrical conductivity (σ) versus temperature and (b) σ at 675 °C versus Sr content (x) for $\text{Sr}_x\text{La}_{0.12}\text{TiO}_3$ ($x = 0.82, 0.86, 0.87, 0.88, 0.885, 0.9$) sintered at 1400 and 1600 °C.

As shown in Figure 7-15a, both the compositions with $0.82 \leq x \leq 0.86$ sintered at 1400 °C and the compositions with $0.82 \leq x \leq 0.88$ sintered at 1600 °C exhibit high electrical conductivity ($\sigma \sim 200$ S/cm at 680 °C) and metallic conduction above 150 °C. The sample with $x = 0.87$ sintered at 1400 °C show intermediate electrical conductivity ($\sigma \sim 57$ S/cm at 680 °C) and mixed semiconducting-metallic conduction. With a further increase in x , the electrical conductivity is dramatically reduced and shows semiconducting behavior. The electrical conductivity of most of the samples is improved by increasing the sintering temperature (Figure 7-15b). The electrical conduction mechanisms are discussed in the following.

The electrical conduction in La-doped SrTiO₃ sintered in a reducing atmosphere is contributed by both La substitution and oxygen deficiency, as indicated in Equation 7-14 and Equation 7-15.



The electrons are neutralized by coupling with Ti⁴⁺ ions, forming mixed Ti³⁺/Ti⁴⁺ ions. The Ti³⁺ concentration ($[\text{Ti}^{3+}]$ or $[\text{Ti}'_{\text{Ti}}]$) is therefore equal to the carrier concentration, which can be written as

$$[\text{Ti}'_{\text{Ti}}] = n = [\text{La}_{\text{Sr}}^{\bullet}] + 2[\text{V}_0^{\bullet\bullet}] \quad \text{Equation 7-16}$$

Combining the oxygen deficiencies indicated in Figure 7-12a, the Ti³⁺ concentration of Sr_xLa_{0.12}TiO₃ is calculated and plotted versus x , as shown in

Figure 7-16.

Both the Ti³⁺ concentration of the compositions with $0.82 \leq x \leq 0.86$ sintered at 1400 °C and the compositions with $0.82 \leq x \leq 0.87$ sintered at 1600 °C are higher than the other samples, resulting in enhanced electrical conductivity. With increasing x above these values, the electrical conductivity is reduced. It is due to both the decrease in Ti³⁺

concentration and the presence of insulating SrO layers, which increases the effective conduction band offset of SrTiO₃ in these compositions [179].

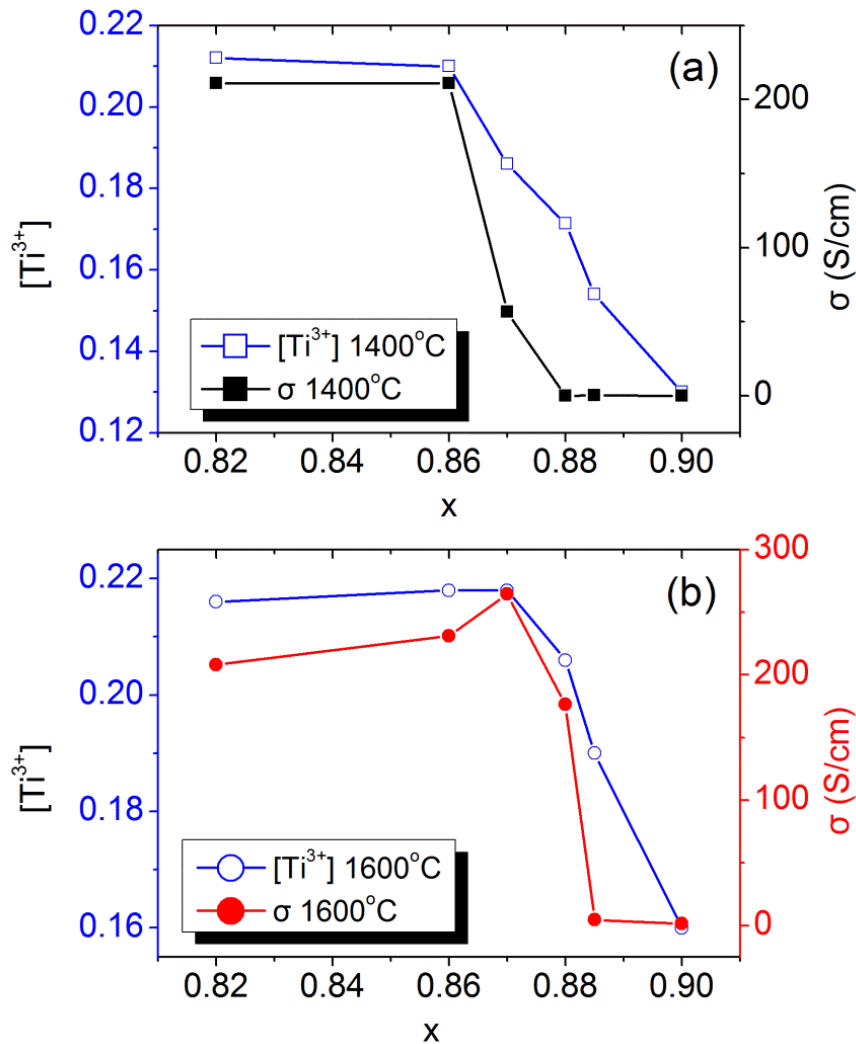


Figure 7-16 Electrical conductivity (σ) at 680 °C and Ti³⁺ concentration ([Ti³⁺]) versus x for Sr_xLa_{0.12}TiO₃ ($x = 0.82, 0.86, 0.87, 0.88, 0.885, 0.9$) sintered at (a) 1400 °C and (b) 1600 °C.

The semiconducting behavior in the compositions with low electrical conductivity is caused by the low Ti³⁺ concentration. A smaller Ti³⁺ concentration results in a smaller overlap of the Ti 3*d* and O 2*p* orbitals and thus localized orbitals. As the Ti³⁺ concentration exceeds a certain value, the orbitals are delocalized, and thus the electrical conductivity are metallic [176]. By increasing sintering temperature, the electrical conductivity of almost all compositions is improved. It is partially due to the increased oxygen deficiency, as indicated in Figure 7-12a. Moreover, the improved

relative density (Table 7-2) contributes to the improvement of the electrical conductivity. However, the electrical conductivity of the composition with $x = 0.82$ is reduced by increasing sintering temperature. The trend is easily to be observed in temperature dependence of the electrical conductivity of the Sr-deficient compositions sintered at both temperatures, as illustrated in Figure 7-17.

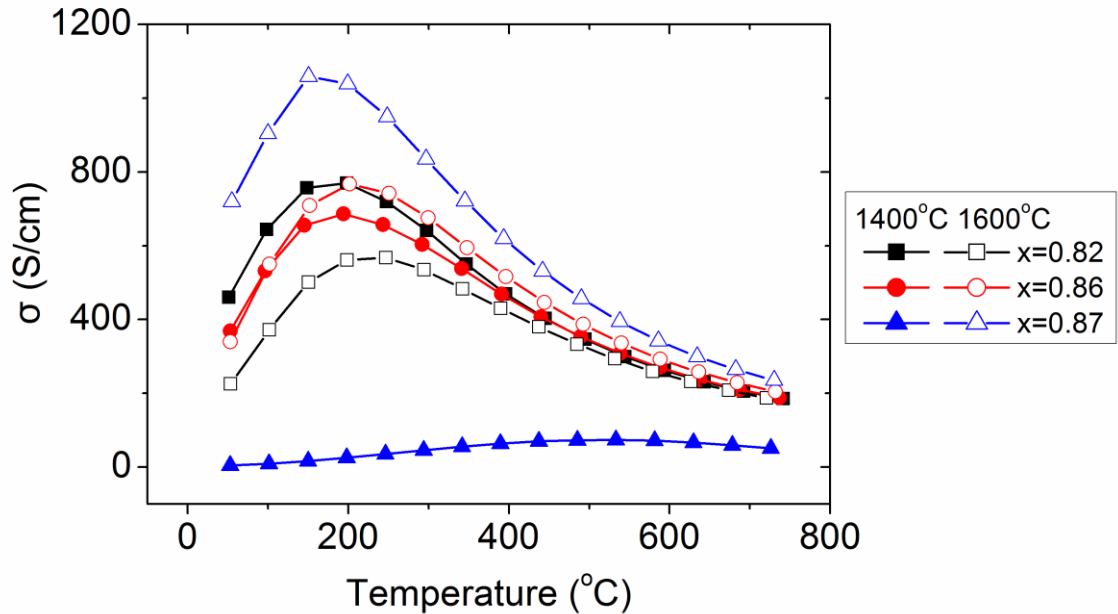


Figure 7-17 Temperature dependent of the electrical conductivity (σ) of $\text{Sr}_x\text{La}_{0.12}\text{TiO}_3$ ($x = 0.82, 0.86, 0.87$) sintered at 1400 °C and 1600 °C.

The composition with $x = 0.86$ exhibits the highest electrical conductivity between 100 °C and 625 °C among the samples sintered at 1400 °C. However, the sample with $x = 0.87$ exhibits the highest electrical conductivity of all compositions sintered at 1600 °C. According to Figure 7-12b, almost no SrO is present in these two compositions. It means that excess TiO_2 is retained in SrTiO_3 if x is lower than the two values. The electrical conductivity decreases with increasing amount of TiO_2 , since Magnéli TiO_2 could block the electrical conduction path [170]. Therefore, the electrical conductivity of the composition with $x = 0.82$ is decreased with increasing sintering temperature due to the increased amount of TiO_2 . It implies that improved electrical conductivity can be achieved by optimizing the amount of excess TiO_2 .

The Seebeck coefficient of $\text{La}_{0.12}\text{Sr}_x\text{TiO}_3$ as a function of temperature is shown in Figure 7-18. The negative Seebeck coefficient indicates electrons are major charge carriers. Although

Figure 7-16 indicates the decreased carrier concentration with increasing x , the absolute value of the Seebeck coefficient decreases with increasing x (Figure 7-19). It appears to be due to the existence of SrO. It was reported that the distortion of TiO_6 octahedra becomes stronger with increasing amount of SrO, resulting in a reduced absolute value of the Seebeck coefficient due to the deterioration of band degeneracy [181].

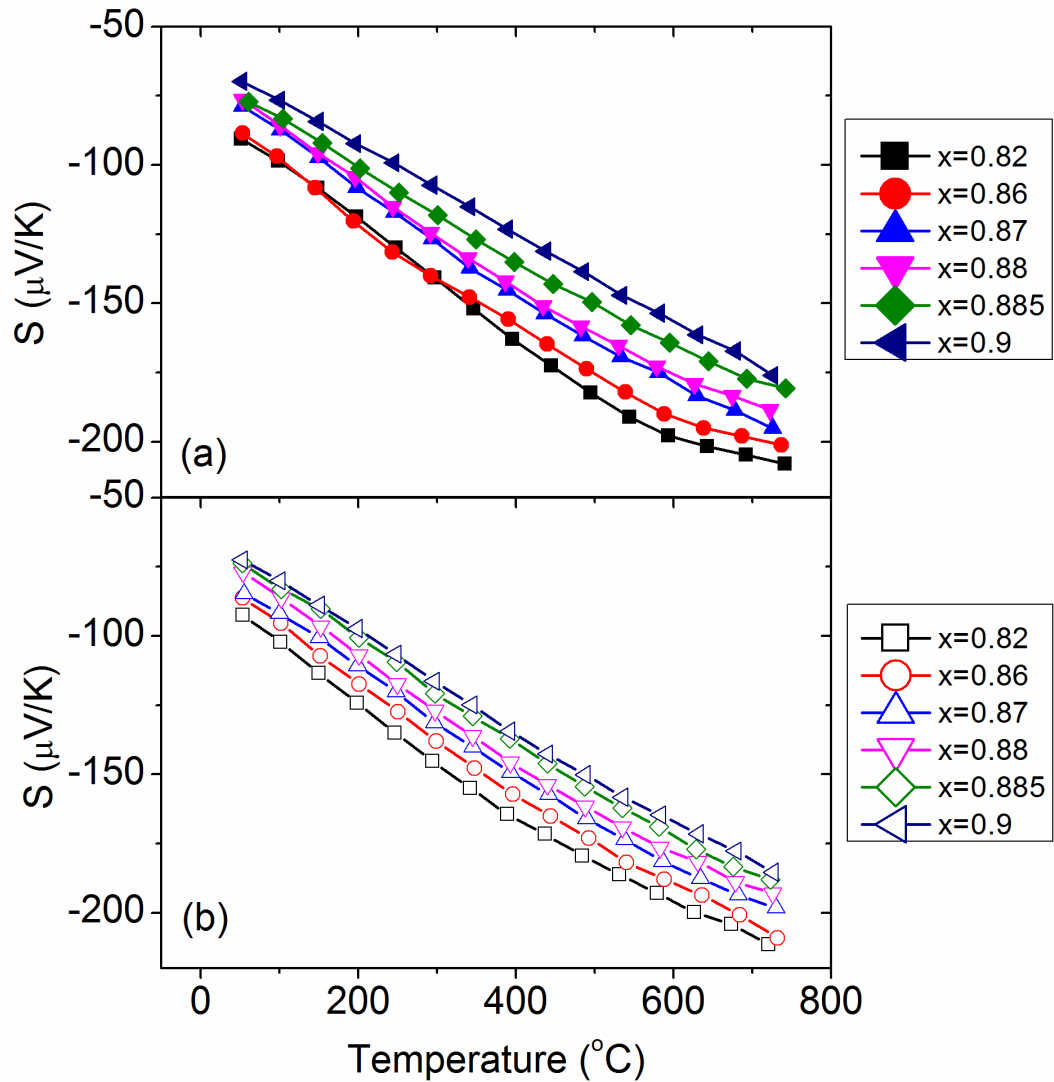


Figure 7-18 Seebeck coefficient (S) versus temperature for $\text{La}_{0.12}\text{Sr}_x\text{TiO}_3$ ($x = 0.82, 0.86, 0.87, 0.88, 0.885, 0.9$) sintered at (a) 1400 and (b) 1600 °C.

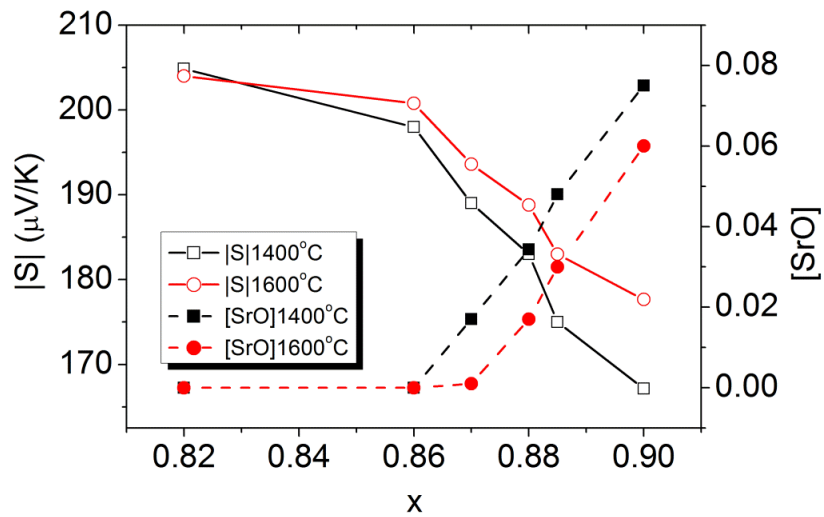


Figure 7-19 Absolute values of the Seebeck coefficient ($|S|$) versus x for $\text{La}_{0.12}\text{Sr}_x\text{TiO}_3$ ($x = 0.82, 0.86, 0.87, 0.88, 0.885, 0.9$) sintered at 1400 and 1600 °C.

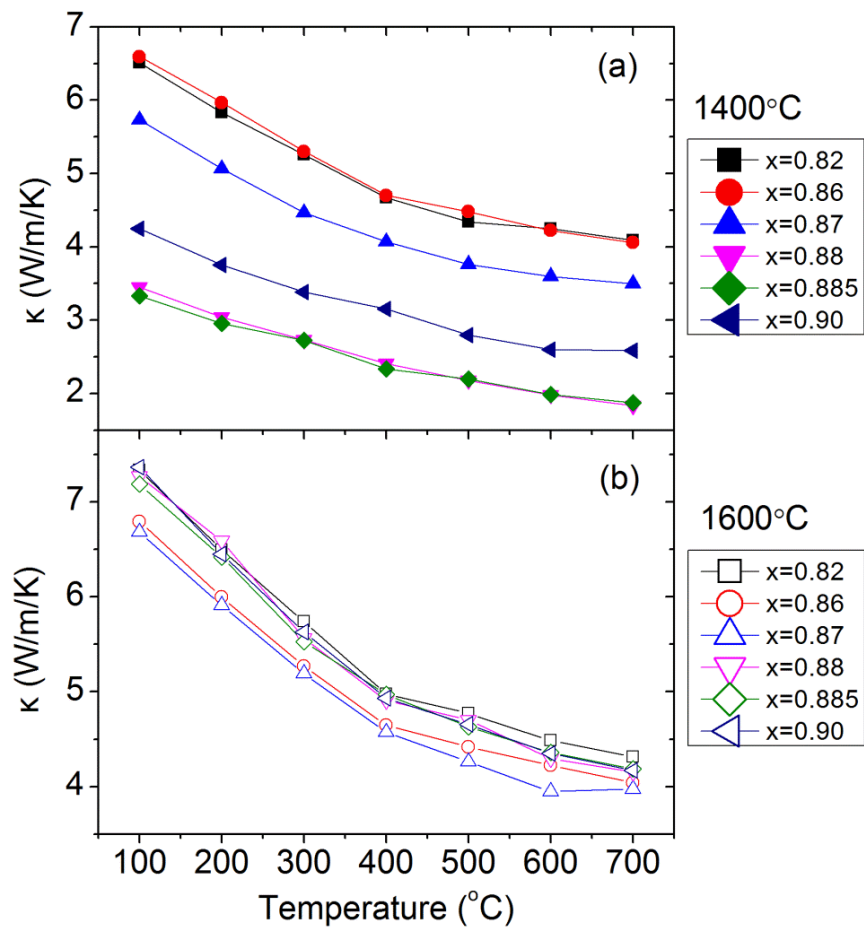


Figure 7-20 Thermal conductivity (κ) versus temperature for $\text{La}_{0.12}\text{Sr}_x\text{TiO}_3$ ($x = 0.82, 0.86, 0.87, 0.88, 0.885, 0.9$) sintered at 1400 and 1600 °C.

Temperature dependence of the thermal conductivity of $\text{La}_{0.12}\text{Sr}_x\text{TiO}_3$ is shown in Figure 7-20. The thermal conductivity decreases with increasing temperature, indicating of the domination of lattice thermal conductivity. Large variation in κ of the samples sintered 1400 °C is observed due to the difference in relative densities shown in Table 7-2. The thermal conductivity is increased by increasing the sintering temperature as a result of improved relative densities. The samples sintered at 1600 °C show similar κ , indicating that the influence of excess TiO_2 or SrO on κ is not obvious.

Figure-of-merit ZT as a function of temperature is shown in Figure 7-21. ZT increases with increasing temperature. ZT values of the TiO_2 excess samples are higher than the stoichiometric and SrO excess samples sintered at both temperatures. Furthermore, ZT is improved by increasing sintering temperature except the composition with $x = 0.82$. It is clear that ZT is largely affected by σ . Highest ZT is achieved in $\text{La}_{0.12}\text{Sr}_{0.87}\text{TiO}_3$ sintered at 1600 °C, ~ 0.245 at 586 °C. At both sintering temperatures, ZT could be improved by adding proper amount of excess TiO_2 in the starting compositions.

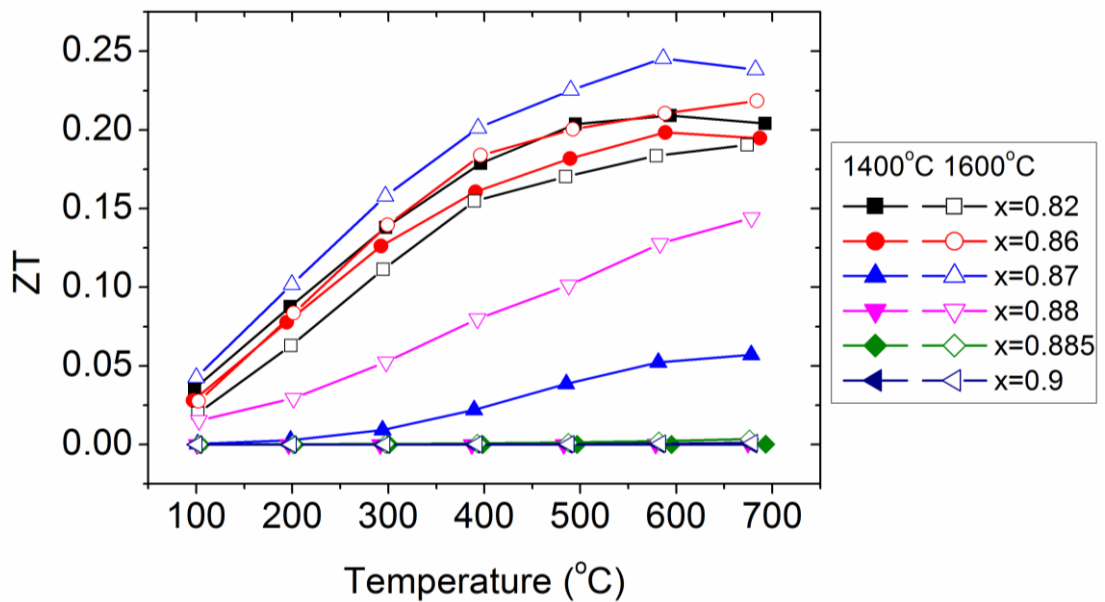


Figure 7-21 Thermoelectric figure-of-merit ZT versus temperature for $\text{La}_{0.12}\text{Sr}_x\text{TiO}_3$ ($x = 0.82, 0.86, 0.87, 0.88, 0.885, 0.9$) sintered at 1400 and 1600 °C.

7.4 Summary

$\text{Sr}_x\text{Y}_{0.04}\text{TiO}_3$ ($x = 0.92, 0.94, 0.95, 0.96, 0.98, 1$) have been prepared and their thermoelectric properties have been studied. The electrical conductivity of the TiO_2 excess compositions ($0.92 \leq x \leq 0.95$) was much higher than that of the stoichiometric and Sr-excess compositions. The Seebeck coefficient was not influenced by the addition of excess TiO_2 , whereas it decreased with increasing amount of excess Sr. Although the stoichiometric composition exhibited the lowest lattice thermal conductivity, its ZT values were very low. All these properties are strongly related to the Ti^{3+} concentration and the defect structure of $\text{Sr}_{0.96}\text{Y}_{0.04}\text{TiO}_3$. Among all the samples prepared under the same condition, $\text{Sr}_{0.94}\text{Y}_{0.04}\text{TiO}_3$ possessed the maximum ZT of 0.183 at 390 °C, which was 8 times as high as that of $\text{Sr}_{0.96}\text{Y}_{0.04}\text{TiO}_3$.

$\text{Sr}_x\text{La}_{0.12}\text{TiO}_3$ ($x = 0.82, 0.86, 0.87, 0.88, 0.885, 0.90$) have been synthesized at two different sintering temperatures. The microstructure and thermoelectric properties have been investigated. At both sintering temperatures, the electrical conductivity of the TiO_2 excess compositions ($0.82 \leq x \leq 0.87$) was much higher than that of the stoichiometric and Sr-excess compositions. Furthermore, the electrical conductivity is closely related to the formation of TiO_2 secondary phase and defect structure of this material. The absolute Seebeck coefficient decreased with increasing x , possibly due to the appearance of SrO. The generation of oxygen vacancies were promoted with increasing sintering temperature, leading to a significantly enhanced electrical conductivity of the compositions with $x = 0.87$ and 0.88 due to the depletion of SrO. The thermal conductivity was greatly affected by the microstructure of the samples. Maximum ZT has been achieved in $\text{La}_{0.12}\text{Sr}_{0.87}\text{TiO}_3$ sintered at 1600 °C, ~ 0.245 at 586 °C.

Chapter 8 Effects of Y and Nb co-doping on the thermoelectric properties of SrTiO₃ and SrTi_{1.01}O₃: a comparative study

8.1 Introduction

SrTiO₃ is intensively studied as an n-type thermoelectric oxide due to its high Seebeck coefficient [27]. However, the figure of merit is limited by its high thermal conductivity caused by its simple cubic crystal structure and light atomic mass. One effective way to reduce its thermal conductivity is to induce a lattice distortion by substituting Sr²⁺ sites with rare-earth elements that possess small ionic radii [25,106]. For example, doping Y³⁺ into Sr²⁺ is found to decrease the thermal conductivity. However, the electrical conductivity of Y-doped SrTiO₃ is lower than that of the other rare-earth element doped samples [104,106]. It is important to maintain its electrical conductivity while decreasing its thermal conductivity. Nb-doped SrTiO₃ is reported to show high electrical conductivity and figure of merit [107]. Therefore, Y and Nb codoped SrTiO₃ has been prepared in this study.

The electrical conductivity of donor-doped SrTiO₃ could be further enhanced by adding excess TiO₂ into the starting composition [28,30]. According to our previous study, the thermoelectric performance of donor-doped SrTiO₃ can be significantly improved by incorporating excess TiO₂. Therefore, excess TiO₂ was added into the samples, with nominal composition Sr_{0.96}Y_{0.04}Ti_{1+z-x}Nb_xO₃ ($x = 0, x = 0.04, x = 0.1, x = 0.2; z = 0, 0.01$). Comparison of the thermoelectric properties between the stoichiometric and TiO₂ excess compositions was made. Maximum ZT was obtained in the TiO₂ excess composition with nominal composition of Sr_{0.96}Y_{0.04}Ti_{0.91}Nb_{0.1}O₃, reaching ~ 0.26 at 685 °C.

8.2 Experimental procedure

Sr_{0.96}Y_{0.04}Ti_{1+z-x}Nb_xO₃ ($x = 0, x = 0.04, x = 0.1, x = 0.2; z = 0, 0.01$) were synthesized by conventional solid-state reaction method. The starting powders were SrCO₃ (99.9%, Sigma Aldrich), TiO₂ (puriss grade, Sigma Aldrich), Y₂O₃ (99.99%, Sigma Aldrich), and Nb₂O₅ (99.9%, Sigma Aldrich). The powders were all baked in

oven at 150 °C for 3 h before use. The powders were then mixed according to the aforementioned nominal compositions. The mixture was ball milled in a planetary ball mill machine (Retsch, PM400) at 150 rpm for 6 h in ethanol with zirconia balls. After drying, the powder was calcined at 1300 °C for 6 h in 5% H₂/Ar. The powder was then ground, and subjected to ball milling again. After drying, the powder was compacted into 20 mm pellets with cold pressing machine under a pressure of 200 MPa with the aid of PVA binder. The pellets were annealed at 500 °C for 0.5 h in air to eliminate the binder. Finally, the pellets were sintered at 1400 °C for 6 h and annealed at 1450 °C for 10 h in 5% H₂/Ar.

X-ray diffraction (XRD) measurement was carried out on the ground powder employing Panalytical X'pert MPD. XRD data were collected between $20^\circ \leq 2\theta \leq 120^\circ$. Rietveld refinements were performed using PANalytical-HighScore Plus software. Density of the pellets was evaluated by Archimedes' principle. Electrical conductivity σ and Seebeck coefficient S were simultaneously measured by the ULVAC-ZEM3 system. Thermal conductivity κ was obtained from the product of the measured density (NETZSCH DIL402PC for the thermal expansion), the specific heat capacity (NETZSCH DSC404C), and the thermal diffusivity (NETZSCH LFA427). Thermogravimetric measurement was carried out employing thermogravimetric analysis (NETZSCH STA 449). The oxygen deficiency was determined by the weight increase upon annealing samples up to 1300 °C in flowing oxygen (50 ml/min).

8.3 Results and discussion

Powder XRD patterns presented in Figure 8-1a confirmed that all compositions have a cubic perovskite structure with the space group $Pm\bar{3}m$. Small amount of impurity phase has been observed in the compositions with nominal composition Sr_{0.96}Y_{0.04}Ti_{0.9}Nb_{0.1}O₃, Sr_{0.96}Y_{0.04}Ti_{0.91}Nb_{0.1}O₃, and Sr_{0.96}Y_{0.04}Ti_{0.8}Nb_{0.2}O₃. However, the impurity phase could not be determined due to the limited intensity of the diffraction peaks.

The lattice parameters have been calculated by performing Rietveld refinement on the XRD patterns. As indicated in Figure 8-1b, the lattice parameter linearly increases with increasing Nb content for both stoichiometric ($z = 0$) and TiO₂ excess ($z = 0.01$) compositions, which is due to the slightly higher ionic radii of Nb⁵⁺ and Ti³⁺

compared with Ti^{4+} . Ti^{3+} is formed as a result of charge neutralization when Nb^{5+} is introduced to Ti^{4+} sites of SrTiO_3 sintered in a reducing atmosphere. Moreover, the lattice parameter shows almost no difference between stoichiometric and TiO_2 excess compositions.

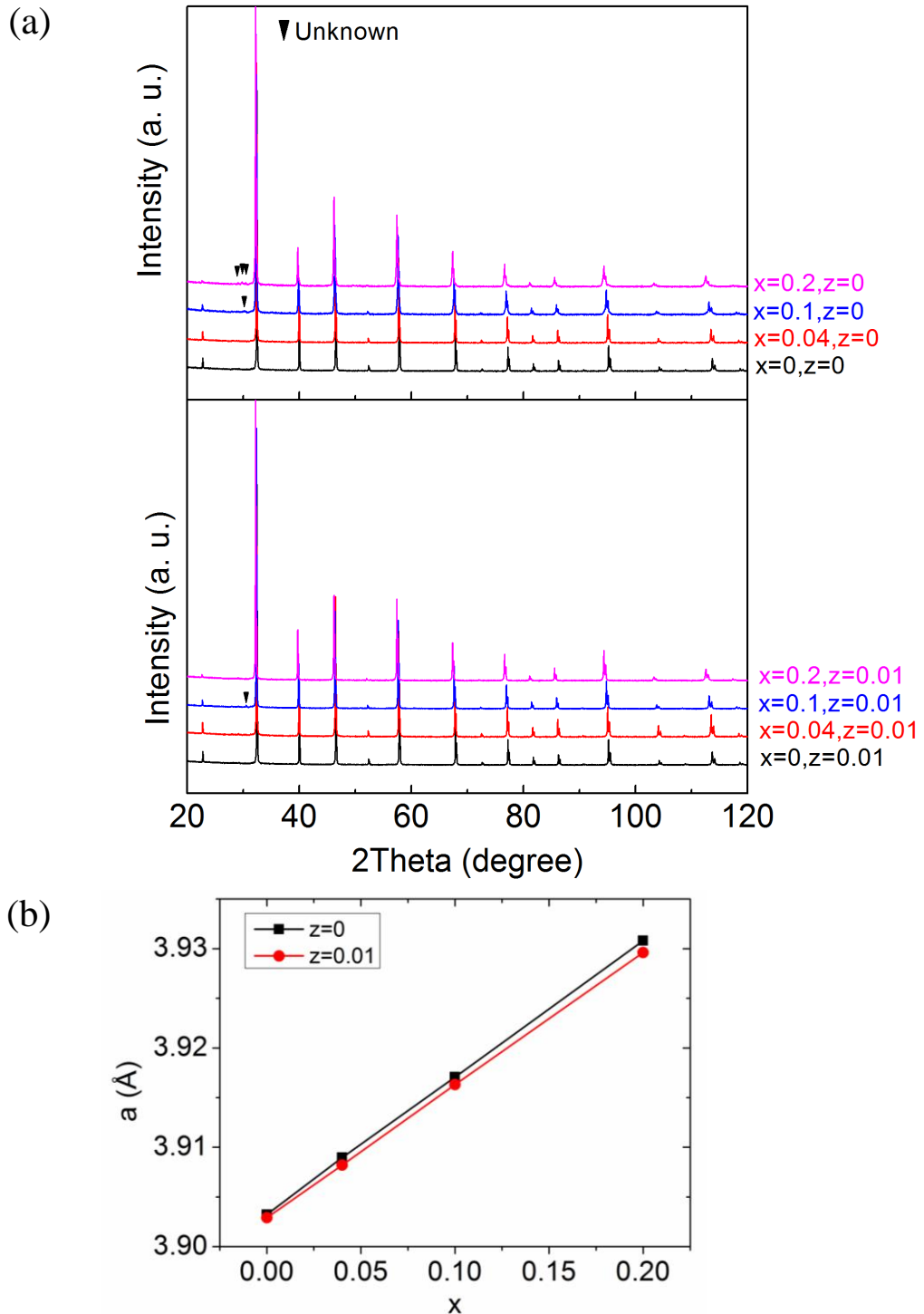


Figure 8-1 (a) XRD patterns and (b) lattice parameter (a) versus x for $\text{Sr}_{0.96}\text{Y}_{0.04}\text{Ti}_{1+z-x}\text{Nb}_x\text{O}_3$ ($x = 0, x = 0.04, x = 0.1, x = 0.2$; $z = 0, 0.01$).

The thermogravimetric curves are shown in Figure 8-2a. The oxidation starts from approximately 400 °C and ends up at 1000 °C. The mass remains unchanged after reaching the equilibrium state. The oxygen deficiency was calculated by the weight increase of a sample after oxidation to an equilibrium state. Introducing Nb into SrTiO₃ promotes the formation of oxygen vacancies as shown in Figure 8-2b. Furthermore, the oxygen deficiency is not obviously affected by the different amount of TiO₂.

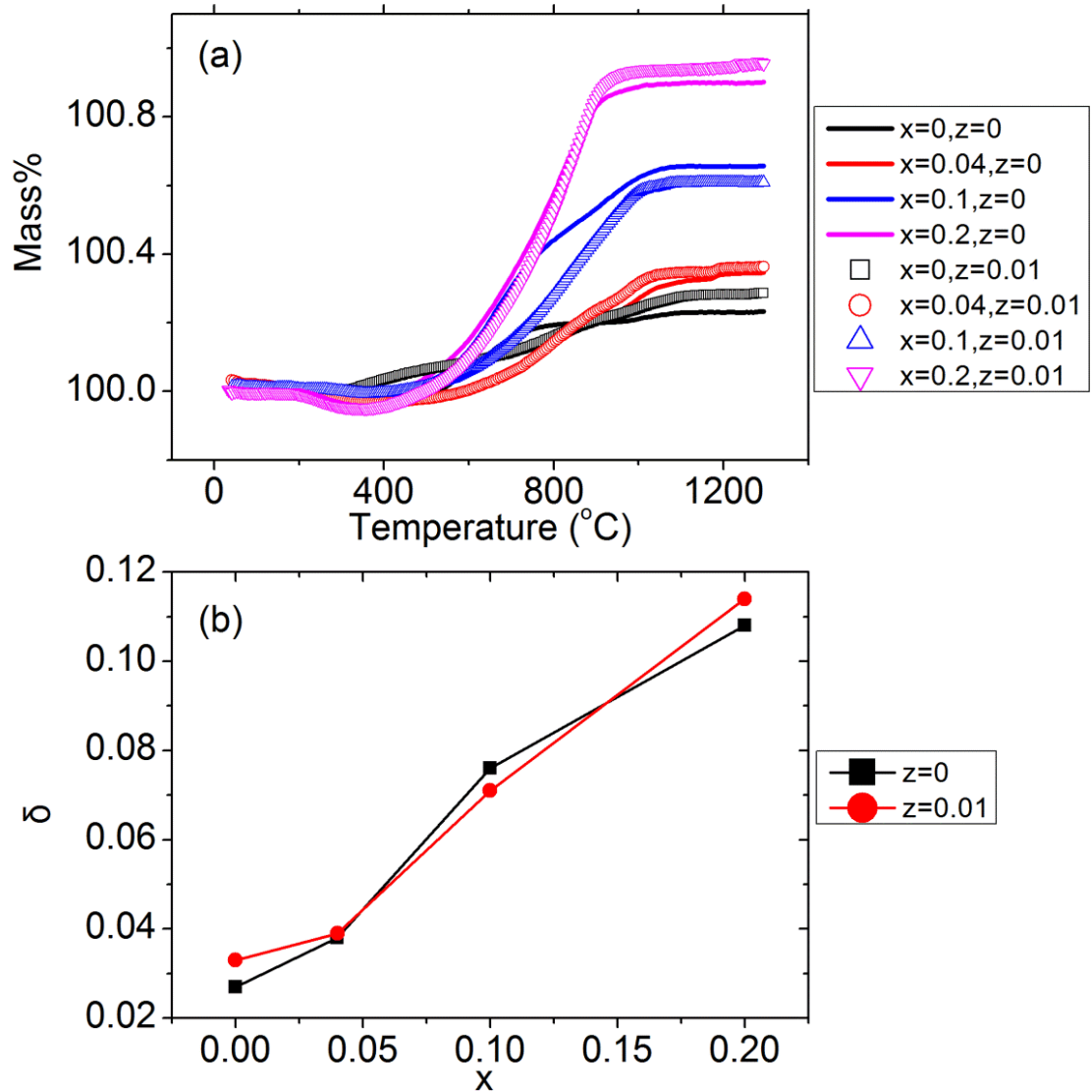


Figure 8-2 (a) Thermogravimetric curve in oxygen (50 ml/min) versus temperature and (b) oxygen deficiency (δ) versus x for Sr_{0.96}Y_{0.04}Ti_{1+z-x}Nb_xO_{3-δ} ($x = 0, x = 0.04, x = 0.1, x = 0.2; z = 0, 0.01$).

The theoretical densities were calculated under the assumption of no oxygen deficiency. The typical SEM micrographs are shown in Figure 8-3. The average grain size is improved with the addition of excess TiO_2 . It is attributed to the fact that excess TiO_2 enhances the bulk diffusion during sintering [166].

Table 8-1 Lattice parameter a , theoretical density, bulk density, and relative density of $\text{Sr}_{0.96}\text{Y}_{0.04}\text{Ti}_{1+z-x}\text{Nb}_x\text{O}_{3-\delta}$ ($x = 0, x = 0.04, x = 0.1, x = 0.2; z = 0, 0.01$).

	x	a (Å)	Theoretical density (g/cm^3)	Bulk density (g/cm^3)	Relative density
$z = 0$	0	3.90323(1)	5.127	4.89	0.95
	0.04	3.90898(2)	5.154	5.04	0.98
	0.1	3.91707(4)	5.197	4.83	0.93
	0.2	3.93079(6)	5.266	4.86	0.92
$z = 0.01$	0	3.90293(1)	5.128	4.9	0.96
	0.04	3.90822(3)	5.158	4.97	0.96
	0.1	3.91630(1)	5.200	4.97	0.96
	0.2	3.92962(3)	5.271	5.05	0.96

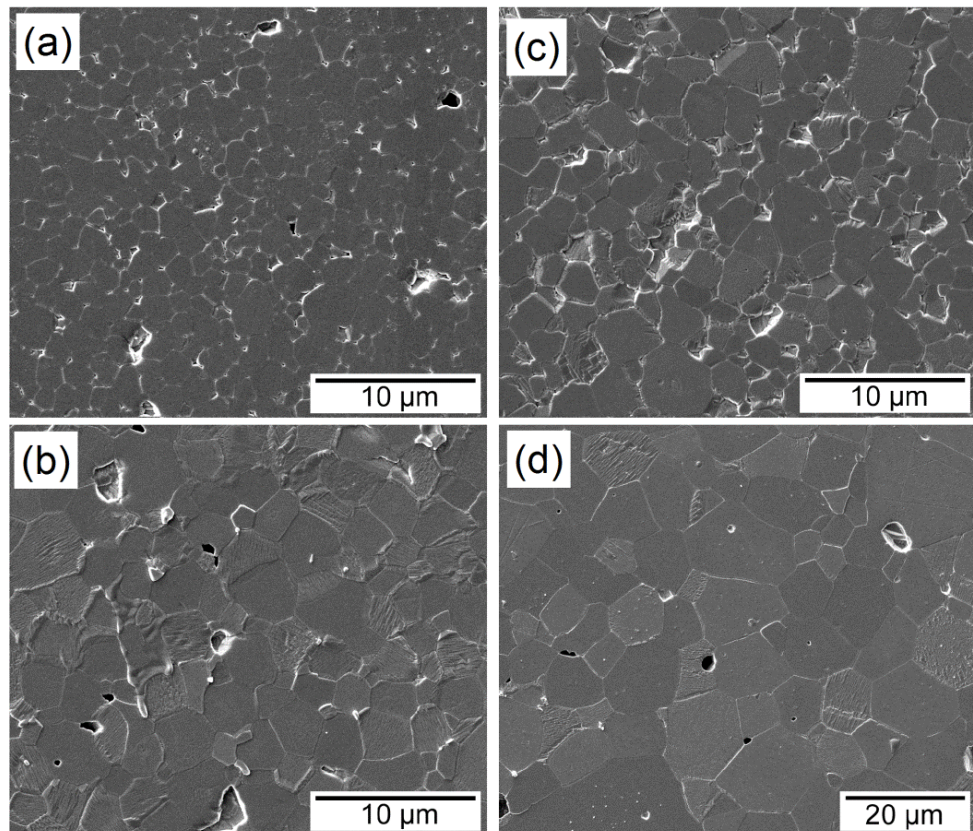


Figure 8-3 SEM micrographs of $\text{Sr}_{0.96}\text{Y}_{0.04}\text{Ti}_{1+z-x}\text{Nb}_x\text{O}_3$. (a) $x = 0, z = 0$, (b) $x = 0.1, z = 0$, (c) $x = 0, z = 0.01$, and (d) $x = 0.1, z = 0.01$.

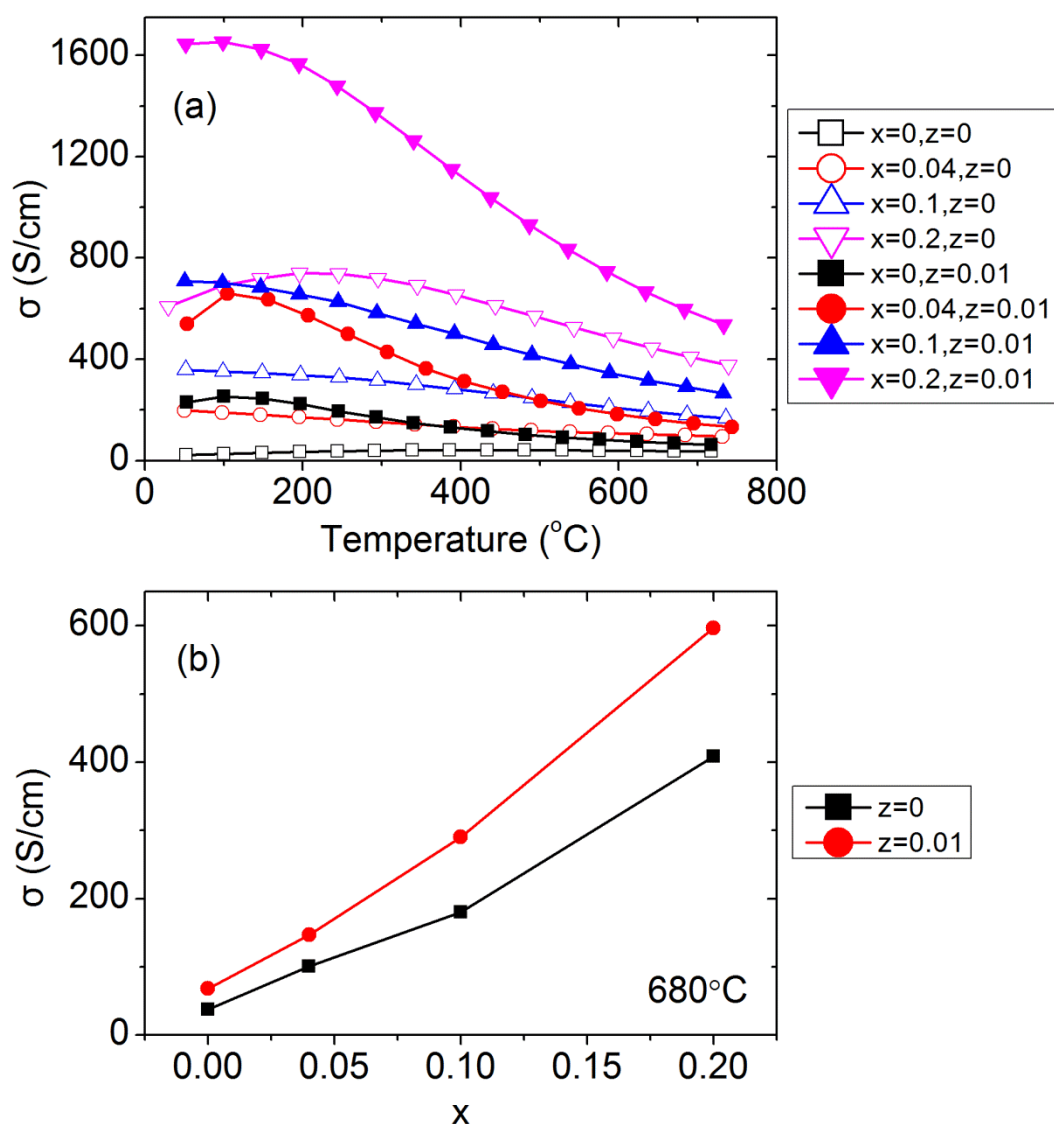


Figure 8-4 The electrical conductivity (σ) of $\text{Sr}_{0.96}\text{Y}_{0.04}\text{Ti}_{1+z-x}\text{Nb}_x\text{O}_3$ ($x = 0, x = 0.04, x = 0.1, x = 0.2; z = 0, 0.01$) versus (a) temperature and (b) Nb content (x).

Most compositions show semiconductor-metal transition in electrical conductivity (Figure 8-4a). The electrical conductivity is improved by increasing Nb content (Figure 8-4b). With the addition of excess TiO_2 , the electrical conductivity is further increased. The electrical conduction is contributed by electrons in donor-doped SrTiO_3 . The carrier concentration n can be approximated by

$$n = [\text{Ti}'_{\text{Ti}}] = [\text{Y}^{\bullet}_{\text{Sr}}] + [\text{Nb}^{\bullet}_{\text{Ti}}] + 2[\text{V}^{\bullet\bullet}_{\text{O}}] \quad \text{Equation 8-1}$$

The concentration of oxygen vacancies is equal to the oxygen deficiency shown in Figure 8-2b. The carrier concentration is therefore calculated and plotted in Figure 8-5. The carrier concentration increases with increasing Nb content, leading to an improved electrical conductivity. Furthermore, it turns out that no obvious difference in the carrier concentration is observed in the stoichiometric and TiO₂ excess compositions.

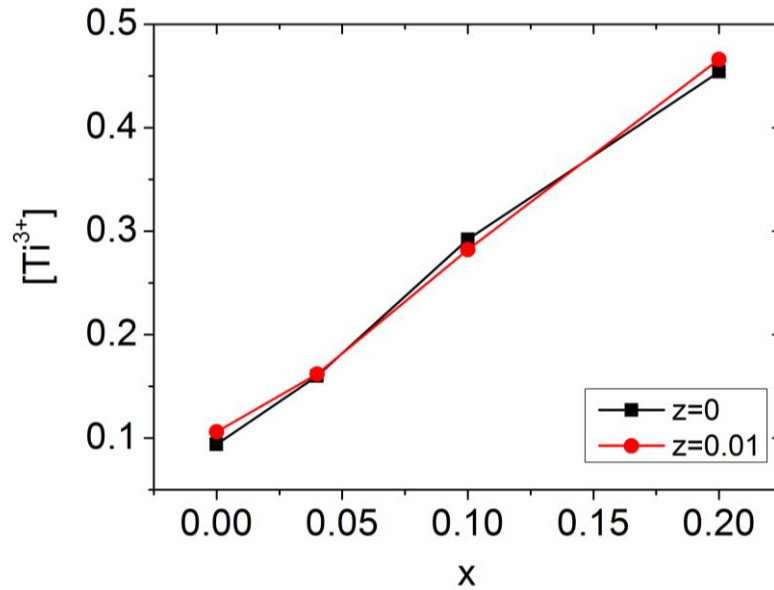
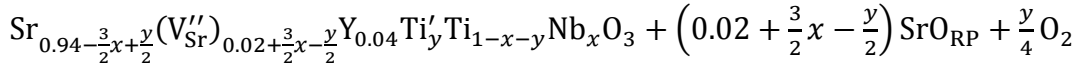
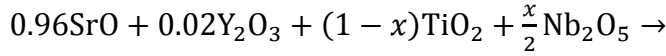


Figure 8-5 Concentration of Ti³⁺ versus x for Sr_{0.96}Y_{0.04}Ti_{1+z-x}Nb_xO₃ ($x = 0, x = 0.04, x = 0.1, x = 0.2; z = 0, 0.01$).

The TiO₂ excess compositions possess higher electrical conductivity than the stoichiometric compositions, which appears to be due to both the change in microstructure and the reduced Ruddlesden-Popper (RP) phases containing SrO potential barriers. The average grain size and relative density are greatly improved in the TiO₂ excess compositions (Figure 8-3), and thus induces an increase in the electrical conductivity. On the other hand, the charge compensation in donor-doped stoichiometric SrTiO₃ sintered in air is achieved by the formation of Sr vacancies and RP phases. Moreover, controlled valency compensation occurs when donor-doped SrTiO₃ is sintered in a reducing atmosphere. Both compensation mechanisms exist when the reducing atmosphere is not strong enough. It has been indicated that even sintering of donor-doped SrTiO₃ in a strong reducing atmosphere cannot completely remove the RP phases SrO [28]. The reaction is expressed in Equation 8-2. The SrO is depleted with the addition of excess TiO₂. Therefore, the electrical conductivity is

increased in the TiO₂ excess compositions partially due to reduced SrO potential barriers.



Equation 8-2

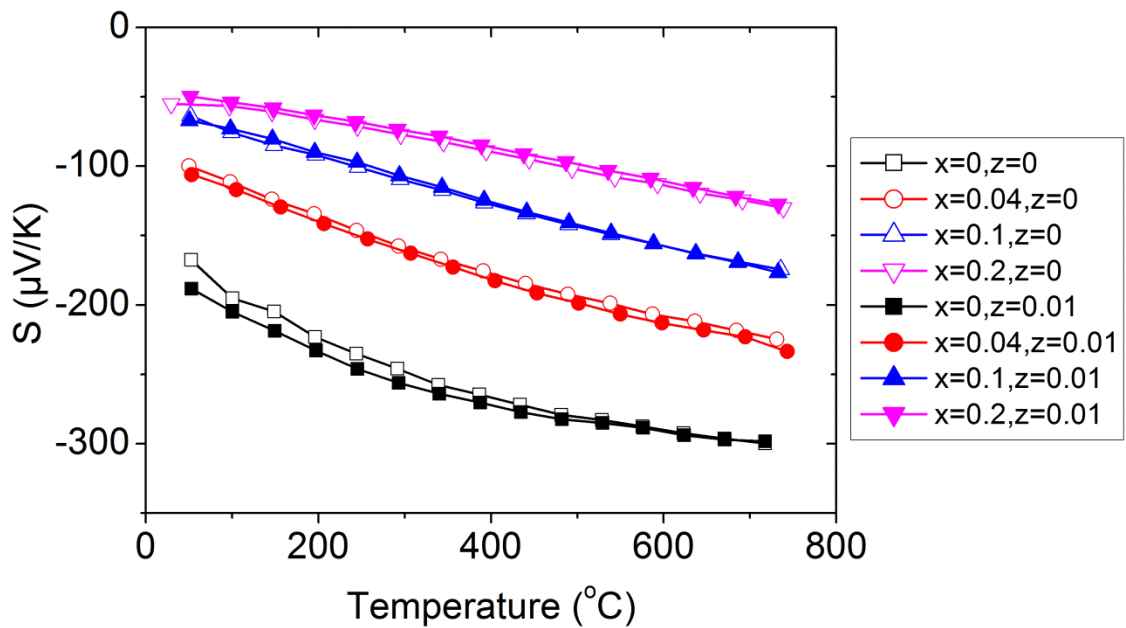


Figure 8-6 Temperature dependence of the Seebeck coefficient (S) of $\text{Sr}_{0.96}\text{Y}_{0.04}\text{Ti}_{1+z-x}\text{Nb}_x\text{O}_3$ ($x = 0, x = 0.04, x = 0.1, x = 0.2; z = 0, 0.01$).

The negative values of the Seebeck coefficient (Figure 8-6) indicate all compositions are n-type semiconductors with electrons being the dominant charge carriers. With increasing doping concentration, the carrier concentration is increased (Figure 8-5), leading to a decrease in the absolute values of the Seebeck coefficient. Moreover, the Seebeck coefficient is not affected by the excess TiO₂.

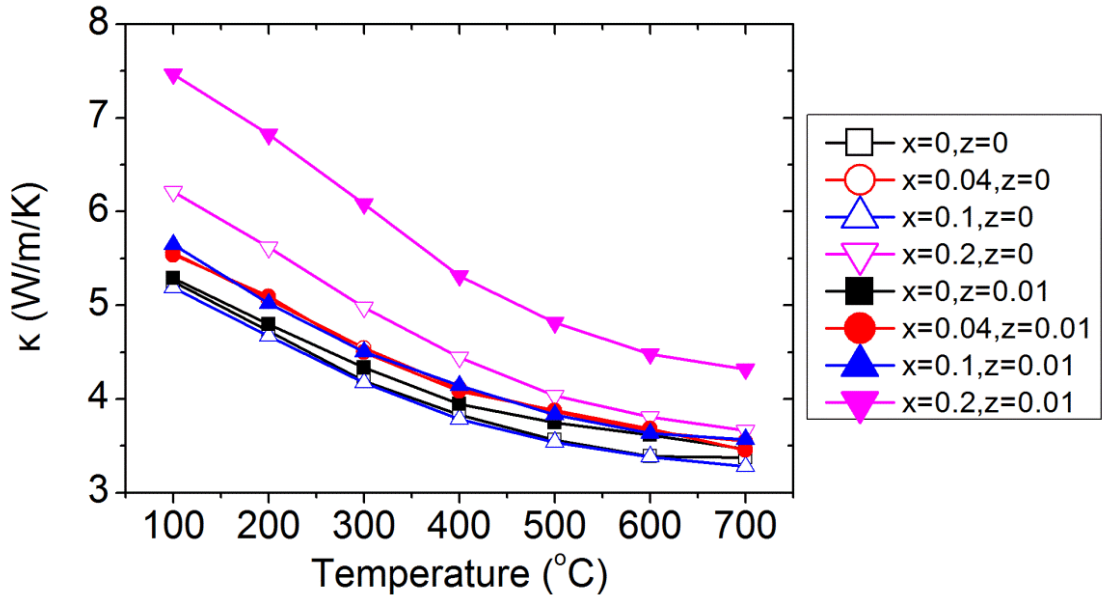


Figure 8-7 Temperature dependence of the thermal conductivity (κ) of $\text{Sr}_{0.96}\text{Y}_{0.04}\text{Ti}_{1+z-x}\text{Nb}_x\text{O}_3$ ($x = 0, x = 0.04, x = 0.1, x = 0.2; z = 0, 0.01$).

As shown in Figure 8-7, the thermal conductivity of all compositions decreases with increasing temperature, indicating the dominated contribution from lattice thermal conductivity. The thermal conductivity was corrected for porosity according to Equation 8-3 [131].

$$\kappa_c = \frac{\kappa}{1 - \frac{3}{2}(1 - RD)} \quad \text{Equation 8-3}$$

where the RD is relative density. The electronic contribution to the thermal conductivity was calculated by the Wiedemann-Franz law (Lorenz number is assumed to be $2.44 \times 10^{-8} \text{ W}\Omega\text{K}^{-2}$). The lattice thermal conductivity is therefore obtained by subtracting the electronic part from the total thermal conductivity. The calculation results are shown in Figure 8-8. The thermal conductivity is increased, while the lattice thermal conductivity is reduced with increasing Nb content. The decrease in the lattice thermal conductivity is likely due to the point defects induced by oxygen vacancies and Nb dopants [160,182].

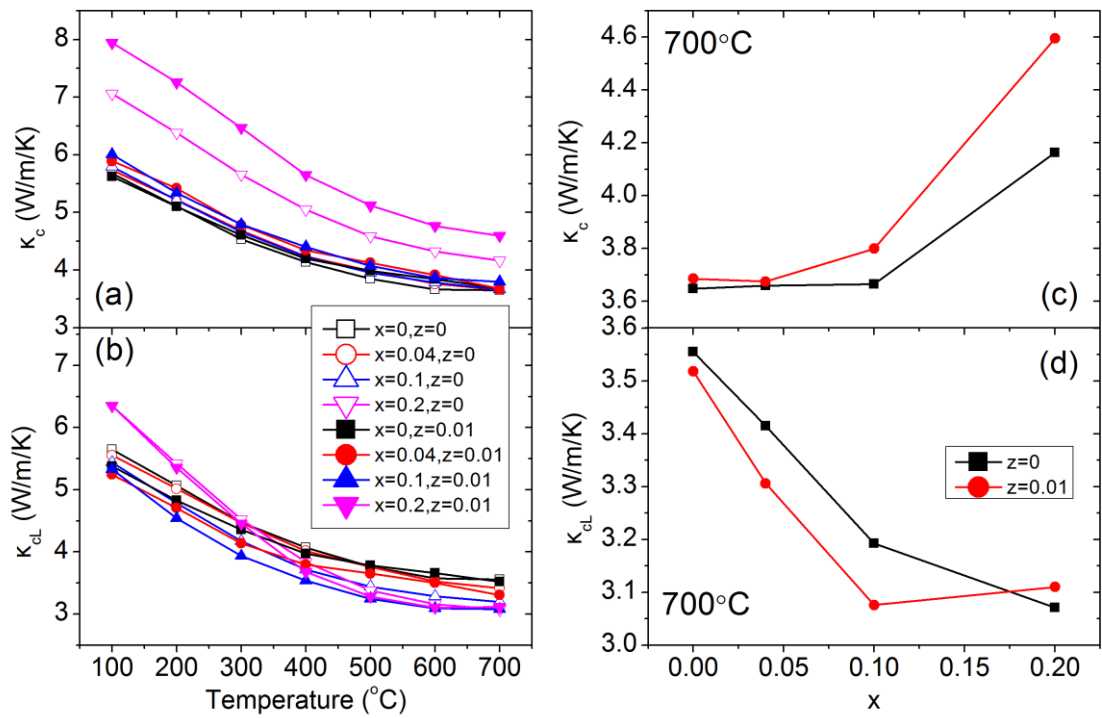


Figure 8-8 Thermal conductivity κ_c of $\text{Sr}_{0.96}\text{Y}_{0.04}\text{Ti}_{1+z-x}\text{Nb}_x\text{O}_3$ ($x = 0, x = 0.04, x = 0.1, x = 0.2; z = 0, 0.01$) versus (a) temperature and (b) Nb content (x). Lattice thermal conductivity κ_{cL} versus (c) temperature and (d) Nb content (x). All values were corrected for porosity.

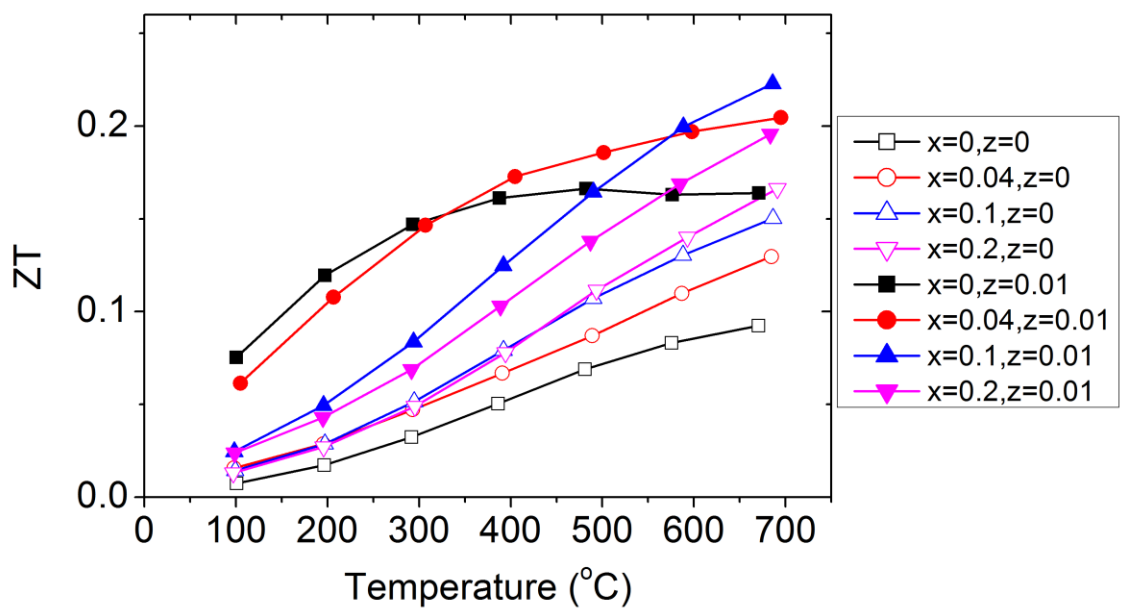


Figure 8-9 Temperature dependence of figure-of-merit ZT of $\text{Sr}_{0.96}\text{Y}_{0.04}\text{Ti}_{1+z-x}\text{Nb}_x\text{O}_3$ ($x = 0, x = 0.04, x = 0.1, x = 0.2; z = 0, 0.01$).

ZT of the stoichiometric compositions increases with both increasing temperature and Nb content. ZT of $\text{Sr}_{0.96}\text{Y}_{0.04}\text{Ti}_{1.01}\text{O}_3$ reaches the maximum at 480 °C. ZT of the other TiO_2 excess compositions increases with increasing temperature. ZT is improved by adding excess TiO_2 into the starting compositions. Below 500 °C, $\text{Sr}_{0.96}\text{Y}_{0.04}\text{Ti}_{0.97}\text{Nb}_{0.04}\text{O}_3$ exhibits high ZT values. Maximum $ZT \sim 0.22$ at 685 °C is found in $\text{Sr}_{0.96}\text{Y}_{0.04}\text{Ti}_{0.91}\text{Nb}_{0.1}\text{O}_3$.

8.4 Summary

The thermoelectric properties of $\text{Sr}_{0.96}\text{Y}_{0.04}\text{Ti}_{1+z-x}\text{Nb}_x\text{O}_3$ ($x = 0, x = 0.04, x = 0.1, x = 0.2; z = 0, 0.01$) prepared by conventional solid-state reaction were studied. The electrical conductivity increased and the absolute value of the Seebeck coefficient decreased with increasing Nb content due to increased carrier concentration. Incorporation of excess TiO_2 improved the electrical conductivity of $\text{Sr}_{0.96}\text{Y}_{0.04}\text{Ti}_{1+z-x}\text{Nb}_x\text{O}_3$ due to the change in microstructure and the reduced SrO potential barrier. However, no change in the Seebeck coefficient was observed with different TiO_2 content. The lattice thermal conductivity was decreased with increasing Nb content, which is attributed to the increased point defect scattering due to increased oxygen deficiency and Nb dopants. Maximum ZT was obtained in $\text{Sr}_{0.96}\text{Y}_{0.04}\text{Ti}_{0.91}\text{Nb}_{0.1}\text{O}_3$, ~ 0.22 at 685 °C.

Chapter 9 Conclusions and future work

9.1 Conclusions

In this thesis, the structural and thermoelectric properties of p-type Na_xCoO_2 and n-type SrTiO_3 have been examined. Na_xCoO_2 was synthesized by solid-state reaction combined with spark plasma sintering. Nearly full densification was achieved by the use of spark plasma sintering. The effects of spark plasma sintering temperature and dwell time on the thermoelectric properties of $\text{Na}_x\text{CoO}_2/\text{Ca}_3\text{Co}_4\text{O}_9$ composites were determined. The thermoelectric properties and chemical stability of $\text{Na}_x\text{CoO}_2/\text{Ca}_3\text{Co}_4\text{O}_9$ with different volume ratios were compared. Moreover, the thermoelectric properties of Na_xCoO_2 were adjusted by doping transition metal ion (Fe^{3+}) into Co sites. On the other hand, donor-doped SrTiO_3 was synthesized by conventional solid-state reaction method. The influences of Y and La content on the structural and thermoelectric properties of A-site deficient SrTiO_3 were investigated. Furthermore, the Y and La-doped SrTiO_3 with different Sr content were studied in terms of crystal phase, microstructure, and thermoelectric properties. The thermoelectric properties of Y and Nb co-doped SrTiO_3 and $\text{SrTi}_{1.01}\text{O}_3$ were compared.

Single-phase $\text{Na}_{0.8}\text{Co}_{1-x}\text{Fe}_x\text{O}_2$ with high relative density were successfully prepared by solid-state reaction and spark plasma sintering. Both the electrical resistivity and the Seebeck coefficient of $\text{Na}_{0.8}\text{Co}_{1-x}\text{Fe}_x\text{O}_2$ were increased with increasing Fe content, which is likely caused by an increase in the effective mass and/or a decrease in the carrier concentration induced by Fe doping on Co sites. $\text{Na}_{0.8}\text{Co}_{1-x}\text{Fe}_x\text{O}_2$ with $0.25\% \leq x \leq 1\%$ exhibited a decrease in thermal conductivity. ZT was improved by substituting Co with Fe, reaching ~ 0.40 at 680°C in $\text{Na}_{0.8}\text{Co}_{0.99}\text{Fe}_{0.01}\text{O}_2$.

Although Na_xCoO_2 possesses good thermoelectric properties, its poor chemical stability in air poses a limitation on its realistic application. We have found out that the chemical stability of $\text{Na}_{0.77}\text{CoO}_2$ could be improved while maintaining its thermoelectric performance by adding up to 30% volume fraction of $\text{Ca}_3\text{Co}_4\text{O}_9$. Moreover, the electrical resistivities of the composites were compared with the theoretical values from the modified Landauer's model and a resistor network model. The experimental values were larger than the theoretical values. Furthermore, an enhanced Seebeck coefficient was observed in the composites, which were higher than the Seebeck coefficient of both

single-phase $\text{Na}_{0.77}\text{CoO}_2$ and $\text{Ca}_3\text{Co}_4\text{O}_9$. The behavior of both the electrical resistivity and the Seebeck coefficient is attributed to the compressive strain on $\text{Ca}_3\text{Co}_4\text{O}_9$ originating from the mismatch of the thermal expansion coefficients between $\text{Ca}_3\text{Co}_4\text{O}_9$ and $\text{Na}_{0.77}\text{CoO}_2$. In addition, the effects of spark plasma sintering temperature and time on the thermoelectric properties of $\text{Na}_{0.77}\text{CoO}_2/\text{Ca}_3\text{Co}_4\text{O}_9$ composites were studied. No solid-state reaction was observed between the two phases during spark plasma sintering up to 700 °C and 1 hour. The thermoelectric properties of the composites were improved by increasing sintering temperature (500 °C – 700 °C) due to improved relative density. The dwell time (10 min – 60 min, at 700 °C) had no obvious effect on the thermoelectric performance of the composites.

The thermoelectric properties of Sr-deficient Y or La-doped SrTiO_3 with nominal composition $\text{Sr}_{1-1.5x}\text{M}_x\text{TiO}_3$ ($M = \text{Y}, \text{La}$) were studied. High relative densities were obtained in all compositions. ZT was found to increase with increasing dopant content up to $x = 0.08$ and $x = 0.12$ for Y and La, respectively. Below these two values, the electrical conductivity and the Seebeck coefficient increased with increasing doping content due to increased concentration of Ti^{3+} contributed by both dopants and oxygen vacancies. $\text{Y}_2\text{Ti}_2\text{O}_7$ was formed in $\text{Sr}_{1-1.5x}\text{Y}_x\text{TiO}_3$ with $x \geq 0.08$, which led to a decrease in both the electrical and thermal conductivity. The crystal structure of $\text{Sr}_{1-1.5x}\text{La}_x\text{TiO}_3$ changed from cubic to tetragonal as x was increased above $x = 0.12$ possibly due to the formation of $\text{La}_2\text{Ti}_2\text{O}_7$ -like lamellar compounds. Decreased electrical and thermal conductivity were observed in $\text{Sr}_{0.4}\text{La}_{0.4}\text{TiO}_3$, which appeared to be due to the lamellar phases. The highest ZT values of 0.20 and 0.23 were achieved at ~ 680 °C for $\text{Sr}_{0.88}\text{Y}_{0.08}\text{TiO}_3$ and $\text{Sr}_{0.82}\text{La}_{0.12}\text{TiO}_3$, respectively.

The Sr/Ti cationic ratio influences the phase composition, microstructure, and thermoelectric properties of Y and La doped SrTiO_3 . The existence of Magnéli phases TiO_2 was confirmed in the Sr-deficient $\text{Sr}_x\text{Y}_{0.04}\text{TiO}_3$ ($0.92 \leq x \leq 0.95$). Y_2O_3 was found in the Sr-excess compositions, indicating that Sr has the preference to occupy A-site of SrTiO_3 . The Sr-deficient compositions showed much higher electrical conductivity than the stoichiometric ($x = 0.96$) and Sr-excess ($0.98 \leq x \leq 1$) compositions. The Seebeck coefficient of the Sr-deficient and stoichiometric compositions were similar and decreased with increasing amount of excess Sr. The carrier concentration or Ti^{3+} concentration remained similar in the Sr-deficient and stoichiometric compositions and decreased with increasing x above $x = 0.96$. The low electrical conductivity in

stoichiometric composition was likely due to the presence of Ruddlesden-Popper phases SrO. Highest ZT was obtained $\text{Sr}_{0.94}\text{Y}_{0.04}\text{TiO}_3$, reaching 0.183 at 390 °C, 8 times as high as that of $\text{Sr}_{0.96}\text{Y}_{0.04}\text{TiO}_3$.

The thermoelectric properties of $\text{Sr}_x\text{La}_{0.12}\text{TiO}_3$ ($0.82 \leq x \leq 0.90$) sintered at 1400 °C and 1600 °C were studied. The formation of SrO Ruddlesden-Popper phase was confirmed in the compositions with $0.88 \leq x \leq 0.90$ sintered at 1400 °C and $0.885 \leq x \leq 0.90$ sintered at 1600 °C. Therefore the electrical conductivity of the Sr-deficient compositions was much higher than that of the Sr-excess compositions. Furthermore, the electrical conductivity was reduced with increasing excess TiO_2 in Sr-deficient compositions. The absolute value of the Seebeck coefficient decreased with increasing x , which is likely due to the deterioration of band degeneracy caused by the SrO phases. The oxygen deficiency was increased with increasing sintering temperature, leading to significantly enhanced electrical conductivity of compositions with $x = 0.87$ and 0.88 due to the depletion of SrO. Highest ZT was found in $\text{La}_{0.12}\text{Sr}_{0.87}\text{TiO}_3$ sintered at 1600 °C, ~ 0.245 at 586 °C.

The structural and thermoelectric properties of stoichiometric and Ti-excess $\text{Sr}_{0.96}\text{Y}_{0.04}\text{Ti}_{1+z-x}\text{Nb}_x\text{O}_3$ were compared. An increase in the electrical conductivity and the Seebeck coefficient was observed with increasing Nb content. The Ti-excess compositions showed higher electrical conductivity than the stoichiometric compositions due to the change in microstructure and the reduced SrO potential barrier. The Seebeck coefficient was not influenced by the Ti content. Nb dopants were effective in reducing the lattice thermal conductivity, which is associated with the increased point defects from the oxygen vacancies and Nb substitution. The highest ZT was found in $\text{Sr}_{0.96}\text{Y}_{0.04}\text{Ti}_{0.91}\text{Nb}_{0.1}\text{O}_3$, reaching 0.22 at 685 °C.

9.2 Future work

Both p-type Na_xCoO_2 and n-type SrTiO_3 show promising thermoelectric performance. The temperature dependent electrical conductivity and Seebeck coefficient of Na_xCoO_2 and SrTiO_3 were measured in low-pressure helium atmosphere, in order to protect parts of the furnace chamber which are prone to be oxidized at elevated temperatures. The lattice oxygen tends to lose with both increasing temperature and reducing oxygen partial pressure. The measured results can be used for comparison,

since all samples were prepared with the same preparation method and measured with the same program. Nonetheless, it is important to understand the transport properties as a function of oxygen partial pressure, since oxygen nonstoichiometry has a significant effect on the chemical and physical properties of thermoelectric oxides [70,128-130,172]. Further measurement of their thermoelectric properties in air is needed to examine their suitability for operation in air.

Although the lattice thermal conductivity of SrTiO_3 was effectively reduced by substituting Sr^{2+} with Y^{3+} , there is still room for reducing the thermal conductivity through improving synthesis methods and nanostructuring approach. Different synthesis methods, e.g., sol-gel method combined with spark plasma sintering, might be explored as a way to reduce the thermal conductivity due to the fine grain size. It is also interesting to know the effects of nanosized- TiO_2 dispersion on the thermoelectric properties of donor-doped SrTiO_3 . Further study is required to examine the physical and mechanical reliability related to high operation temperatures and thermal cycling for the application of such materials. For example, it is worthwhile to investigate the degradation of thermoelectric properties due to continuous high-temperature exposure and thermal cycles. Furthermore, high mechanical strength, especially the compressive strength, is required to avoid the mechanical failure during assembly and operation of thermoelectric modules. Therefore, it is interesting to carry out mechanical testing of the thermoelectric materials and improve the synthesis methods to achieve high mechanical strength.

References

- [1] U.S.E.I. Administration, AEO2914 early release overview-Energy consumption by primary fuel, http://www.eia.gov/forecasts/aeo/er/early_fuel.cfm.
- [2] T.C. Jean-Pierre Fleurial, Bill J. Nesmith, David F. Woerner, Jack F. Mondt, and Gerhard Stapfer, High Reliability High Temperature Thermoelectric Power Generation Materials and Technologies, <http://energy.gov/sites/prod/files/2014/03/f10/fleurial.pdf>.
- [3] D. Kraemer, B. Poudel, H.P. Feng, J.C. Caylor, B. Yu, X. Yan, Y. Ma, X.W. Wang, D.Z. Wang, A. Muto, K. McEnaney, M. Chiesa, Z.F. Ren, G. Chen, *Nat. Mater.*, 10 (2011) 532-538.
- [4] W.J. Xie, X.F. Tang, Y.G. Yan, Q.J. Zhang, T.M. Tritt, *Appl. Phys. Lett.*, 94 (2009) 102111.
- [5] J.P. Heremans, V. Jovovic, E.S. Toberer, A. Saramat, K. Kurosaki, A. Charoenphakdee, S. Yamanaka, G.J. Snyder, *Science*, 321 (2008) 554-557.
- [6] J.R. Sootsman, H. Kong, C. Uher, J.J. D'Angelo, C.I. Wu, T.P. Hogan, T. Caillat, M.G. Kanatzidis, *Angew. Chem. Int. Edit.*, 47 (2008) 8618-8622.
- [7] S.H. Yang, T.J. Zhu, T. Sun, S.N. Zhang, X.B. Zhao, J. He, *Nanotechnology*, 19 (2008) 245707.
- [8] G. Joshi, H. Lee, Y.C. Lan, X.W. Wang, G.H. Zhu, D.Z. Wang, R.W. Gould, D.C. Cuff, M.Y. Tang, M.S. Dresselhaus, G. Chen, Z.F. Ren, *Nano Lett.*, 8 (2008) 4670-4674.
- [9] X.W. Wang, H. Lee, Y.C. Lan, G.H. Zhu, G. Joshi, D.Z. Wang, J. Yang, A.J. Muto, M.Y. Tang, J. Klatsky, S. Song, M.S. Dresselhaus, G. Chen, Z.F. Ren, *Appl. Phys. Lett.*, 93 (2008) 193121
- [10] U.S.G. Survey, Selenium and Tellurium Statistics and Information, Aug 11, 2014, <http://minerals.usgs.gov/minerals/pubs/commodity/selenium/>.
- [11] U.S.G. Survey, Germanium Statistics and Information, Aug 11, 2014, <http://minerals.usgs.gov/minerals/pubs/commodity/germanium/>.
- [12] I. Terasaki, Y. Sasago, K. Uchinokura, *Phys. Rev. B*, 56 (1997) R12685.
- [13] K. Fujita, T. Mochida, K. Nakamura, *Jpn. J. Appl. Phys., Part 1*, 40 (2001) 4644-4647.
- [14] W. Koshibae, K. Tsutsui, S. Maekawa, *Phys. Rev. B*, 62 (2000) 6869-6872.
- [15] J. He, Y. Liu, R. Funahashi, *J. Mater. Res.*, 26 (2011) 1762-1772
- [16] Z.P. Xu, H.C. Zeng, *J. Mater. Chem.*, 8 (1998) 2499-2506.

- [17] A.C. Masset, C. Michel, A. Maignan, M. Hervieu, O. Toulemonde, F. Studer, B. Raveau, J. Hejtmanek, *Phys. Rev. B*, 62 (2000) 166-175.
- [18] K. Koumoto, I. Terasaki, R. Funahashi, *MRS Bull.*, 31 (2006) 206-210.
- [19] S.W. Li, R. Funahashi, I. Matsubara, K. Ueno, S. Sodeoka, H. Yamada, *Chem. Mater.*, 12 (2000) 2424-2427.
- [20] G.J. Xu, R. Funahashi, M. Shikano, I. Matsubara, Y.Q. Zhou, *Appl. Phys. Lett.*, 80 (2002) 3760-3762.
- [21] H.M. Su, Y. Jiang, X.Z. Lan, X.M. Liu, H.H. Zhong, D.B. Yu, *Phys. Status Solidi A-Appl. Mat.*, 208 (2011) 147-155.
- [22] N.V. Nong, N. Pryds, S. Linderoth, M. Ohtaki, *Adv. Mater.*, 23 (2011) 2484-2490.
- [23] T. Okuda, K. Nakanishi, S. Miyasaka, Y. Tokura, *Phys. Rev. B*, 63 (2001) 113104.
- [24] S. Ohta, T. Nomura, H. Ohta, K. Koumoto, *J. Appl. Phys.*, 97 (2005) 034106.
- [25] H. Muta, K. Kurosaki, S. Yamanaka, *J. Alloys Compd.*, 350 (2003) 292-295.
- [26] J.W. Fergus, *J. Eur. Ceram. Soc.*, 32 (2012) 525-540.
- [27] H. Ohta, S. Kim, Y. Mune, T. Mizoguchi, K. Nomura, S. Ohta, T. Nomura, Y. Nakanishi, Y. Ikuhara, M. Hirano, H. Hosono, K. Koumoto, *Nat. Mater.*, 6 (2007) 129-134.
- [28] S.Q. Hui, A. Petric, *J. Electrochem. Soc.*, 149 (2002) J1-J10.
- [29] Q.X. Fu, S.B. Mi, E. Wessel, F. Tietz, *J. Eur. Ceram. Soc.*, 28 (2008) 811-820.
- [30] B. Bochentyn, J. Karczewski, T. Miruszewski, A. Krupa, M. Gazda, P. Jasinski, B. Kusz, *Solid State Ionics*, 225 (2012) 118-123.
- [31] G.J. Snyder, E.S. Toberer, *Nat. Mater.*, 7 (2008) 105-114.
- [32] T.M. Tritt, M.A. Subramanian, *MRS Bull.*, 31 (2006) 188-194.
- [33] A.F. Ioffe, *Semiconductor thermoelements, and Thermoelectric cooling*, Infosearch, Ltd., 1957.
- [34] D.M. Rowe, *General Principles and Basic Considerations*, in: *Thermoelectrics Handbook*, CRC Press, 2005, pp. 1-1-1-14.
- [35] I. Terasaki, *Thermal conductivity and thermoelectric power of semiconductors*, in: H. Kamimura (Ed.) *Comprehensive Semiconductor Science and Technology*, Elsevier Science, 2011.
- [36] M.S. Dresselhaus, G. Chen, M.Y. Tang, R.G. Yang, H. Lee, D.Z. Wang, Z.F. Ren, J.P. Fleurial, P. Gogna, *Adv. Mater.*, 19 (2007) 1043-1053.
- [37] A. Popescu, L.M. Woods, *Appl. Phys. Lett.*, 97 (2010) 052102.

- [38] Y. Pei, X. Shi, A. LaLonde, H. Wang, L. Chen, G.J. Snyder, *Nature*, 473 (2011) 66-69.
- [39] A.J. Minnich, M.S. Dresselhaus, Z.F. Ren, G. Chen, *Energ. Environ. Sci.*, 2 (2009) 466-479.
- [40] R.R. Heikes, W.D. Johnston, *J. Chem. Phys.*, 26 (1957) 582-587.
- [41] P.M. Chaikin, G. Beni, *Phys. Rev. B*, 13 (1976) 647-651.
- [42] B. Poudel, Q. Hao, Y. Ma, Y. Lan, A. Minnich, B. Yu, X. Yan, D. Wang, A. Muto, D. Vashaee, X. Chen, J. Liu, M.S. Dresselhaus, G. Chen, Z. Ren, *Science*, 320 (2008) 634-638.
- [43] P.G. Klemens, *Proceedings of the Physical Society of London Section A*, 68 (1955) 1113-1128.
- [44] B. Abeles, *Phys. Rev.*, 131 (1963) 1906-1911.
- [45] C. Wood, *Reports on Progress in Physics*, 51 (1988) 459.
- [46] B. Poudel, Q. Hao, Y. Ma, Y.C. Lan, A. Minnich, B. Yu, X.A. Yan, D.Z. Wang, A. Muto, D. Vashaee, X.Y. Chen, J.M. Liu, M.S. Dresselhaus, G. Chen, Z.F. Ren, *Science*, 320 (2008) 634-638.
- [47] D.Y. Chung, T. Hogan, P. Brazis, M. Rocci-Lane, C. Kannewurf, M. Bastea, C. Uher, M.G. Kanatzidis, *Science*, 287 (2000) 1024-1027.
- [48] J. Androulakis, K.F. Hsu, R. Pcionek, H. Kong, C. Uher, J.J. Dangelo, A. Downey, T. Hogan, M.G. Kanatzidis, *Adv. Mater.*, 18 (2006) 1170-1173.
- [49] K.F. Hsu, S. Loo, F. Guo, W. Chen, J.S. Dyck, C. Uher, T. Hogan, E.K. Polychroniadis, M.G. Kanatzidis, *Science*, 303 (2004) 818-821.
- [50] X. Shi, J. Yang, J.R. Salvador, M. Chi, J.Y. Cho, H. Wang, S. Bai, J. Yang, W. Zhang, L. Chen, *J. Am. Chem. Soc.*, 133 (2011) 7837-7846.
- [51] R.W. Rice, *J. Mater. Sci.*, 31 (1996) 1509-1528.
- [52] A. Saramat, G. Svensson, A.E.C. Palmqvist, C. Stiewe, E. Mueller, D. Platzek, S.G.K. Williams, D.M. Rowe, J.D. Bryan, G.D. Stucky, *J. Appl. Phys.*, 99 (2006) 023708-023705.
- [53] S.R. Brown, S.M. Kauzlarich, F. Gascoin, G.J. Snyder, *Chem. Mat.*, 18 (2006) 1873-1877.
- [54] S.R. Culp, S.J. Poon, N. Hickman, T.M. Tritt, J. Blumm, *Appl. Phys. Lett.*, 88 (2006) 042106.
- [55] G. Joshi, X. Yan, H.Z. Wang, W.S. Liu, G. Chen, Z.F. Ren, *Adv. Energy Mater.*, 1 (2011) 643-647.

- [56] X.A. Yan, G. Joshi, W.S. Liu, Y.C. Lan, H. Wang, S. Lee, J.W. Simonson, S.J. Poon, T.M. Tritt, G. Chen, Z.F. Ren, *Nano Lett.*, 11 (2011) 556-560.
- [57] A.F. May, E. Flage-Larsen, G.J. Snyder, *Phys. Rev. B.*, 81 (2010) 125205.
- [58] M. Ito, T. Nagira, D. Furumoto, S. Katsuyama, H. Nagai, *Scripta Mater.*, 48 (2003) 403-408.
- [59] M. Ohtaki, T. Tsubota, K. Eguchi, H. Arai, *J. Appl. Phys.*, 79 (1996) 1816-1818.
- [60] L. Bocher, M.H. Aguirre, D. Logvinovich, A. Shkabko, R. Robert, M. Trottmann, A. Weidenkaff, *Inorg. Chem.*, 47 (2008) 8077-8085.
- [61] S. Ohta, T. Nomura, H. Ohta, M. Hirano, H. Hosono, K. Koumoto, *Appl. Phys. Lett.*, 87 (2005) 092108.
- [62] Y. Wang, H.J. Fan, *Scr. Mater.*, 65 (2011) 190-193.
- [63] K. Takada, H. Sakurai, E. Takayama-Muromachi, F. Izumi, R.A. Dilanian, T. Sasaki, *Nature*, 422 (2003) 53-55.
- [64] M.L. Foo, Y. Wang, S. Watauchi, H.W. Zandbergen, T. He, R.J. Cava, N.P. Ong, *Phys. Rev. Lett.*, 92 (2004) 247001.
- [65] T. Motohashi, R. Ueda, E. Naujalis, T. Tojo, I. Terasaki, T. Atake, M. Karppinen, H. Yamauchi, *Phys. Rev. B*, 67 (2003) 064406.
- [66] L. Viciu, J.W.G. Bos, H.W. Zandbergen, Q. Huang, M.L. Foo, S. Ishiwata, A.P. Ramirez, M. Lee, N.P. Ong, R.J. Cava, *Phys. Rev. B*, 73 (2006) 174104.
- [67] T. Motohashi, M. Karppinen, H. Yamauchi, Sodium and oxygen nonstoichiometry, and thermoelectric properties of $\text{Na}_x\text{CoO}_{2+\delta}$, in: *Oxide Thermoelectrics (Research Signpost)*, India, 2002, pp. 73-81.
- [68] H. Sakurai, S. Takenouchi, N. Tsujii, E. Takayama-Muromachi, *J. Phys. Soc. Jpn.*, 73 (2004) 2081-2084.
- [69] G.J. Shu, F.C. Chou, *Phys. Rev. B*, 78 (2008) 052101.
- [70] G.J. Shu, W.L. Lee, F.T. Huang, M.W. Chu, P.A. Lee, F.C. Chou, *Phys. Rev. B*, 82 (2010) 054106.
- [71] Q. Huang, M.L. Foo, R.A. Pascal, J.W. Lynn, B.H. Toby, T. He, H.W. Zandbergen, R.J. Cava, *Phys. Rev. B*, 70 (2004) 184110.
- [72] Y. Miyazaki, *Solid State Ionics*, 172 (2004) 463-467.
- [73] D.J. Singh, *Phys. Rev. B*, 61 (2000) 13397-13402.
- [74] H.B. Yang, Z.H. Pan, A.K.P. Sekharan, T. Sato, S. Souma, T. Takahashi, R. Jin, B.C. Sales, D. Mandrus, A.V. Fedorov, Z. Wang, H. Ding, *Phys. Rev. Lett.*, 95 (2005) 146401.

- [75] A. Rebola, R. Klie, P. Zapol, S. Ogut, *Phys. Rev. B*, 85 (2012) 10.
- [76] M. Schrade, S. Casolo, P.J. Graham, C. Ulrich, S. Li, O.-M. Løvvik, T.G. Finstad, T. Norby, *The Journal of Physical Chemistry C*, 118 (2014) 18899-18907.
- [77] T. Takeuchi, T. Kitao, T. Kondo, M. Mikami, Electronic structure and its contribution to the thermoelectric power of $\text{Ca}_3\text{Co}_4\text{O}_9$ and Na_xCoO_2 layered cobalt oxides, in: *Thermoelectrics, 2005. ICT 2005. 24th International Conference on*, 2005, pp. 488-491.
- [78] G. Yang, Q. Ramasse, R.F. Klie, *Phys. Rev. B*, 78 (2008) 4.
- [79] T. Takeuchi, T. Kondo, T. Takami, H. Takahashi, H. Ikuta, U. Mizutani, K. Soda, R. Funahashi, M. Shikano, M. Mikami, S. Tsuda, T. Yokoya, S. Shin, T. Muro, *Phys. Rev. B*, 69 (2004) 125410.
- [80] A. Oguri, S. Maekawa, *Phys. Rev. B*, 41 (1990) 6977-6988.
- [81] A. Satake, H. Tanaka, T. Ohkawa, T. Fujii, I. Terasaki, *J. Appl. Phys.*, 96 (2004) 931-933.
- [82] J. Soret, M.-B. Lepetit, *Phys. Rev. B*, 85 (2012) 165145.
- [83] M. Shikano, R. Funahashi, *Appl. Phys. Lett.*, 82 (2003) 1851-1853.
- [84] T. Kawata, Y. Iguchi, T. Itoh, K. Takahata, I. Terasaki, *Phys. Rev. B*, 60 (1999) 10584.
- [85] T. Nagira, M. Ito, S. Katsuyama, K. Majima, H. Nagai, *J. Alloys Compd.*, 348 (2003) 263-269.
- [86] I. Terasaki, Y. Ishii, D. Tanaka, K. Takahata, Y. Iguchi, *Jpn. J. Appl. Phys., Part 2*, 40 (2001) L65-L67.
- [87] K. Park, K.U. Jang, H.C. Kwon, J.G. Kim, W.S. Cho, *J. Alloys Compd.*, 419 (2006) 213-219.
- [88] M. Ito, T. Nagira, Y. Oda, S. Katsuyama, K. Majima, H. Nagai, *Mater. Trans.*, 43 (2002) 601-607.
- [89] P.H. Tsai, T.S. Zhang, R. Donelson, T.T. Tan, S. Li, *J. Alloys Compd.*, 509 (2011) 5183-5186.
- [90] Z.P. Guo, Y.G. Zhao, W.Y. Zhang, L. Cui, S.M. Guo, L.B. Luo, *J. Phys.: Condens. Matter*, 18 (2006) 4381.
- [91] W.Y. Zhang, Y.G. Zhao, Z.P. Guo, P.T. Qiao, L. Cui, L.B. Luo, X.P. Zhang, H.C. Yu, Y.G. Shi, S.Y. Zhang, T.Y. Zhao, J.Q. Li, *Solid State Commun.*, 135 (2005) 480-484.
- [92] T. Seetawan, V. Amornkitbamrung, T. Burinprakhon, S. Maensiri, K. Kurosaki, H. Muta, M. Uno, S. Yamanaka, *J. Alloys Compd.*, 407 (2006) 314-317.

- [93] T. Seetawan, V. Amornkitbamrung, T. Burinprakhon, S. Maensiri, K. Kurosaki, H. Muta, M. Uno, S. Yamanaka, *J. Alloys Compd.*, 414 (2006) 293-297.
- [94] B. Dutta, J. Battogtokh, D. McKewon, I. Vidensky, N. Dutta, I.L. Pegg, *J. Electron. Mater.*, 36 (2007) 746-752.
- [95] S.W. Li, R. Funahashi, I. Matsubara, S. Sodeoka, *Mater. Res. Bull.*, 35 (2000) 2371-2378.
- [96] R. Kitawaki, I. Terasaki, *J. Phys.: Condens. Matter*, 14 (2002) 12495.
- [97] Y. Wang, K.H. Lee, H. Ohta, K. Koumoto, *J. Appl. Phys.*, 105 (2009) 103701.
- [98] N. Shanthi, D.D. Sarma, *Phys. Rev. B*, 57 (1998) 2153-2158.
- [99] K. van Benthem, C. Elsasser, R.H. French, *J. Appl. Phys.*, 90 (2001) 6156-6164.
- [100] S. Piskunov, E. Heifets, R.I. Eglitis, G. Borstel, *Computational Materials Science*, 29 (2004) 165-178.
- [101] A. Kinaci, C. Sevik, T. Cagin, *Phys. Rev. B*, 82 (2010) 155114.
- [102] C.R.R. E. M. Levin, and H. F. McMurdie, *Phase diagrams for ceramists 1969 Supplement*, The American Ceramic Society, Inc. Columbus, Ohio, 1969.
- [103] S. Witek, D.M. Smyth, H. Pickup, *J. Am. Ceram. Soc.*, 67 (1984) 372-375.
- [104] L. Zhang, T. Tosh, N. Okinaka, T. Akiyama, *Mater. Trans.*, 48 (2007) 2088-2093.
- [105] N. Okinaka, L. Zhang, T. Akiyama, *Isij Int.*, 50 (2010) 1300-1304.
- [106] J. Liu, C.L. Wang, Y. Li, W.B. Su, Y.H. Zhu, J.C. Li, L.M. Mei, *J. Appl. Phys.*, 114 (2013) 223714.
- [107] S. Ohta, H. Ohta, K. Koumoto, *J. Ceram. Soc. Jpn.*, 114 (2006) 102-105.
- [108] Y.J. Cui, J. He, G. Amow, H. Kleinke, *Dalton Trans.*, 39 (2010) 1031-1035.
- [109] A.V. Kovalevsky, A.A. Yaremchenko, S. Populoh, A. Weidenkaff, J.R. Frade, *J. Phys. Chem. C*, 118 (2014) 4596-4606.
- [110] H. Muta, K. Kurosaki, S. Yamanaka, *J. Alloys Compd.*, 392 (2005) 306-309.
- [111] T. Teranishi, Y. Ishikawa, H. Hayashi, A. Kishimoto, M. Katayama, Y. Inada, *J. Am. Ceram. Soc.*, 96 (2013) 2852-2856.
- [112] Y. Wang, X. Zhang, L. Shen, N. Bao, C. Wan, N.-H. Park, K. Koumoto, A. Gupta, *J. Power Sources*, 241 (2013) 255-258.
- [113] R.-z. Zhang, K. Koumoto, *J. Electron. Mater.*, 42 (2013) 1568-1572.
- [114] T. Motohashi, E. Naujalis, R. Ueda, K. Isawa, M. Karppinen, H. Yamauchi, *Appl. Phys. Lett.*, 79 (2001) 1480-1482.

- [115] M. Tokita, Mechanism of spark plasma sintering, in: S.M.a.M. Samandi (Ed.) Proceedings of the International Symposium on Microwave, Plasma and Thermochemical Processing of Advanced Materials, JWRI, Osaka Universities, Japan, 1997, pp. 69-76.
- [116] Z.A. Munir, U. Anselmi-Tamburini, M. Ohyanagi, *J. Mater. Sci.*, 41 (2006) 763-777.
- [117] Z.A. Munir, D.V. Quach, M. Ohyanagi, *J. Am. Ceram. Soc.*, 94 (2011) 1-19.
- [118] V. Petricek, M. Dusek, L. Palatinus, *Z. Kristallogr.*, 229 (2014) 345-352.
- [119] J. Hutton, R.J. Nelmes, *J. Phys. C.*, 14 (1981) 1713.
- [120] W. Jauch, A. Palmer, *Phys. Rev. B*, 60 (1999) 2961-2963.
- [121] NETZSCH, DSC 404 F1 Pegasus® - High-Temperature DSC, Aug 13, 2014, <http://www.netzsch-thermal-analysis.com/en/products-solutions/differential-scanning-calorimetry/dsc-404-f1-pegasus.html#!tabs/literature>.
- [122] NETZSCH, STA 449 F1 Jupiter® – Simultaneous TGA-DSC, Aug 13, 2014, <http://www.netzsch-thermal-analysis.com/en/products-solutions/simultaneous-thermogravimetry-differential-scanning-calorimetry/sta-449-f1-jupiter.html#!tabs/literature>.
- [123] N. Gayathri, A. Bharathi, V.S. Sastry, C.S. Sundar, Y. Hariharan, *Solid State Commun.*, 138 (2006) 489-493.
- [124] I. Terasaki, I. Tsukada, Y. Iguchi, *Phys. Rev. B*, 65 (2002) 195106.
- [125] C.J. Liu, L.C. Huang, J.S. Wang, *Appl. Phys. Lett.*, 89 (2006) 204102.
- [126] Y. Wang, Y. Sui, X.J. Wang, W.H. Su, X.Y. Liu, *J. Appl. Phys.*, 107 (2010) 033708.
- [127] Q. Yao, D.L. Wang, L.D. Chen, X. Shi, M. Zhou, *J. Appl. Phys.*, 97 (2005) 103905.
- [128] J. Shimoyama, S. Horii, K. Otschi, M. Sano, K. Kishio, *Jpn. J. Appl. Phys., Part 2*, 42 (2003) L194-L197.
- [129] J. Shimoyama, Y. Yokota, M. Shiraki, Y. Sugiura, S. Horii, K. Kishio, Oxygen nonstoichiometry of various functional layered oxides, in: J. Li, N.E. Brese, M.G. Kanatzidis, M. Jansen (Eds.) *Solid-State Chemistry of Inorganic Materials V*, 2005, pp. 523-527.
- [130] P.H. Tsai, T. Norby, T.T. Tan, R. Donelson, Z.D. Chen, S. Li, *Appl. Phys. Lett.*, 96 (2010) 141905.
- [131] K.W. Schlichting, N.P. Padture, P.G. Klemens, *J. Mater. Sci.*, 36 (2001) 3003-3010.

- [132] G.D. Tang, X.N. Xu, C.P. Tang, L. Qiu, L.Y. Lv, Z.H. Wang, Y.W. Du, *J. Appl. Phys.*, 107 (2010) 093707.
- [133] M. Sternitzke, *J. Eur. Ceram. Soc.*, 17 (1997) 1061-1082.
- [134] J.H. Zhao, L.C. Stearns, M.P. Harmer, H.M. Chan, G.A. Miller, R.F. Cook, *J. Am. Ceram. Soc.*, 76 (1993) 503-510.
- [135] J. Meyer, *Polym. Eng. Sci.*, 14 (1974) 706-716.
- [136] S. Jagtap, S. Rane, D. Amalnerkar, *Microelectron. Eng.*, 86 (2009) 2026-2029.
- [137] C. Richard, H.S. Lee, D. Guyomar, *Ultrasonics*, 42 (2004) 417-424.
- [138] D.W. Dees, T.D. Claar, T.E. Easler, D.C. Fee, F.C. Mrazek, *J. Electrochem. Soc.*, 134 (1987) 2141-2146.
- [139] J.S. Chen, R.J. Young, T.B. Wu, *J. Am. Ceram. Soc.*, 70 (1987) C260-C264.
- [140] Z. He, C. Stiewe, D. Platzek, G. Karpinski, E. Muller, S. Li, M. Toprak, M. Muhammed, *J. Appl. Phys.*, 101 (2007) 043707-043707.
- [141] X.Y. Zhao, X. Shi, L.D. Chen, W.Q. Zhang, S.Q. Bai, Y.Z. Pei, X.Y. Li, T. Goto, *Appl. Phys. Lett.*, 89 (2006) 092121-092123.
- [142] J. Martin, L. Wang, L. Chen, G.S. Nolas, *Phys. Rev. B*, 79 (2009) 115311.
- [143] H. Odahara, O. Yamashita, K. Satou, S. Tomiyoshi, J. Tani, H. Kido, *J. Appl. Phys.*, 97 (2005) 103722.
- [144] D. Carlier, M. Blangero, M. Menetrier, M. Pollet, J.P. Doumerc, C. Delmas, *Inorg. Chem.*, 48 (2009) 7018-7025.
- [145] K. Matsugi, H. Kuramoto, T. Hatayama, O. Yanagisawa, *J. Mater. Process. Technol.*, 134 (2003) 225-232.
- [146] X.-D. Zhou, L.R. Pederson, E. Thomsen, Z. Nie, G. Coffey, *Electrochem. Solid-State Lett.*, 12 (2009) F1-F3.
- [147] N.V. Nong, A.J. Samson, N. Pryds, S. Linderoth, *J. Electron. Mater.*, 41 (2012) 1280-1285.
- [148] R. Landauer, *J. Appl. Phys.*, 23 (1952) 779-784.
- [149] D.J. Bergman, O. Levy, *J. Appl. Phys.*, 70 (1991) 6821-6833.
- [150] J. Liu, X. Huang, Z. Sun, R. Liu, L. Chen, *CrystEngComm*, 12 (2010) 4080-4083.
- [151] I. Matsubara, R. Funahashi, M. Shikano, K. Sasaki, H. Enomoto, *Appl. Phys. Lett.*, 80 (2002) 4729-4731.
- [152] X. Kleber, P. Roux, M. Morin, *Philos. Mag. Lett.*, 89 (2009) 565-572.

- [153] H. Obara, A. Yamamoto, C.H. Lee, K. Kobayashi, A. Matsumoto, R. Funahashi, *Jpn. J. Appl. Phys. Part 2 - Lett. Express Lett.*, 43 (2004) L540-L542.
- [154] D.L. Medlin, G.J. Snyder, *Curr. Opin. Colloid Interface Sci.*, 14 (2009) 226-235.
- [155] N. Wang, H.J. Chen, H.C. He, W. Norimatsu, M. Kusunoki, K. Koumoto, *Sci. Rep.*, 3 (2013) 3449.
- [156] F. Tang, D.S. Gianola, M.P. Moody, K.J. Hemker, J.M. Cairney, *Acta Mater.*, 60 (2012) 1038-1047.
- [157] U. Balachandran, N.G. Eror, *J. Am. Ceram. Soc.*, 64 (1981) C75-C76.
- [158] Y. Tokura, Y. Taguchi, Y. Okada, Y. Fujishima, T. Arima, K. Kumagai, Y. Iye, *Phys. Rev. Lett.*, 70 (1993) 2126-2129.
- [159] S. Yamaguchi, K. Kobayashi, K. Abe, S. Yamazaki, Y. Iguchi, *Solid State Ionics*, 113-115 (1998) 393-402.
- [160] C. Yu, M.L. Scullin, M. Huijben, R. Ramesh, A. Majumdar, *Appl. Phys. Lett.*, 92 (2008) 191911.
- [161] S.R.S. Kumar, A.Z. Barasheed, H.N. Alshareef, *ACS Appl. Mater. Interfaces*, 5 (2013) 7268-7273.
- [162] M. Ito, T. Matsuda, *J. Alloys Compd.*, 477 (2009) 473-477.
- [163] C. Perillat-Merceroz, P. Roussel, M. Huve, E. Capoen, R.-N. Vannier, G. Gauthier, *Solid State Ionics*, 247 (2013) 76-85.
- [164] D. Neagu, J.T.S. Irvine, *Chem. Mater.*, 22 (2010) 5042-5053.
- [165] M. Baurer, H. Kungl, M.J. Hoffmann, *J. Am. Ceram. Soc.*, 92 (2009) 601-606.
- [166] L. Amaral, A.M.R. Senos, P.M. Vilarinho, *Mater. Res. Bull.*, 44 (2009) 263-270.
- [167] N.H. Chan, R.K. Sharma, D.M. Smyth, *J. Electrochem. Soc.*, 128 (1981) 1762-1769.
- [168] N.G. Eror, U. Balachandran, *J. Solid State Chem.*, 42 (1982) 227-241.
- [169] A. Tkach, P.M. Vilarinho, A.M.R. Senos, A.L. Kholkin, *J. Eur. Ceram. Soc.*, 25 (2005) 2769-2772.
- [170] Q.L. Ma, F. Tietz, D. Stover, *Solid State Ionics*, 192 (2011) 535-539.
- [171] S.N. Ruddlesden, P. Popper, *Acta Crystallogr.*, 11 (1958) 54-55.
- [172] L. Sagarna, S. Populoh, A. Shkabko, J. Eilertsen, A.E. Maegli, R. Hauert, M. Schrade, L. Karvonen, A. Weidenkaff, *J. Phys. Chem. C*, 118 (2014) 7821-7831.
- [173] C.F. Kao, W.D. Yang, *Mater. Trans., JIM*, 37 (1996) 142-149.

- [174] A. Fujimori, *J. Phys. Chem. Solids*, 53 (1992) 1595-1602.
- [175] A.H. Kahn, A.J. Leyendecker, *Phys. Rev.*, 135 (1964) A1321-A1325.
- [176] W. Luo, W. Duan, S.G. Louie, M.L. Cohen, *Phys. Rev. B*, 70 (2004) 214109.
- [177] B. Odekirk, U. Balachandran, N.G. Eror, J.S. Blakemore, *J. Am. Ceram. Soc.*, 66 (1983) C22-C24.
- [178] U. Balachandran, N.G. Eror, *J. Electrochem. Soc.*, 129 (1982) 1021-1026.
- [179] T. Schimizu, T. Yamaguchi, *Appl. Phys. Lett.*, 85 (2004) 1167-1168.
- [180] K.H. Lee, S.W. Kim, H. Ohta, K. Koumoto, *J. Appl. Phys.*, 100 (2006) 063717.
- [181] Y.F. Wang, C.L. Wan, X.Y. Zhang, L.M. Shen, K. Koumoto, A. Gupta, N.Z. Bao, *Appl. Phys. Lett.*, 102 (2013) 183905.
- [182] Y. Wang, F. Li, L.X. Xu, Y. Sui, X.J. Wang, W.H. Su, X.Y. Liu, *Inorg. Chem.*, 50 (2011) 4412-4416.
- [183] N.G. Eror, U. Balachandran, *J. Solid State Chem.*, 40 (1981) 85-91.